INFORMATION TO USERS

This manuscript has been reproduced from the microfilm master. UMI films the text directly from the original or copy submitted. Thus, some thesis and dissertation copies are in typewriter face, while others may be from any type of computer printer.

The quality of this reproduction is dependent upon the quality of the copy submitted. Broken or indistinct print, colored or poor quality illustrations and photographs, print bleedthrough, substandard margins, and improper alignment can adversely affect reproduction.

In the unlikely event that the author did not send UMI a complete manuscript and there are missing pages, these will be noted. Also, if unauthorized copyright material had to be removed, a note will indicate the deletion.

Oversize materials (e.g., maps, drawings, charts) are reproduced by sectioning the original, beginning at the upper left-hand corner and continuing from left to right in equal sections with small overlaps.

Photographs included in the original manuscript have been reproduced xerographically in this copy. Higher quality 6" x 9" black and white photographic prints are available for any photographs or illustrations appearing in this copy for an additional charge. Contact UMI directly to order.

ProQuest Information and Learning
300 North Zeeb Road, Ann Arbor, MI 48106-1346 USA
800-521-0600

MAGNETIC FRUSTRATION IN TRANSITION METAL OXIDES WITH TRIANGULAR, TETRAHEDRAL AND SQUARE PLANAR MAGNETIC SUBLATTICES

By

MARIO BIERINGER, Dipl.-Chem.

A Thesis
Submitted to the School of Graduate Studies
in Partial Fulfilment of the Requirements
for the Degree
Doctor of Philosophy

McMaster University

MAGNETIC FRUSTRATION IN TRANSITION METAL OXIDES WITH TRIANGULAR, TETRAHEDRAL AND SQUARE PLANAR MAGNETIC SUBLATTICES

Doctor of Philosophy (2000)
(Chemistry)

McMaster University
Hamilton, Ontario

TITLE:	Magnetic Frustration in Transition Metal Oxides with Triangular, Tetrahedral and Square Planar Magnetic Sublattices
AUTHOR:	Mario Bieringer, Dipl.-Chem. (Gerhard-Mercator-Universität Duisburg)
SUPERVISOR:	Professor J.E. Greedan
NUMBER OF PAGES:	xxviii, 205

Hoffnung

Schaff, das Tagwerk meiner Hände,
Hohes Glück, daß ichs vollende!
Laß, o laß mich nicht ermatten!
Nein, es sind nicht leere Träume:
Jetzt nur Stangen, diese Bäume
Geben einst noch Frucht und Schatten.

Johann Wolfgang von Goethe

Abstract

The solid solution $Lu_xSc_{(1-x)}MnO_3$ has been prepared for $0.00 \leq x \leq 1.00$. All members crystallize in space group $P6_3cm$. The triangular antiferromagnets form 120° spin structures with Néel temperatures between 91K and 130K. Below T_N all samples show evidence of out of plane spin canting. With the exception of $LuMnO_3$ for all compositions an in-plane spin-reorientation transition is found at low temperatures. The chiralities of the magnetic structures were determined from neutron powder diffraction data. In the vicinity of T_N 2-dimensional magnetic short range order is found.

The solid solution $Ba_xSr_{(1-x)}LaMnO_4$ crystallizes in the K_2NiF_4 structure, space group $I4/mmm$. The magnetic structures were determined from neutron powder diffraction experiments, where Néel ground states were found for $x \leq 0.20$. The magnetic moment magnitude decreases with increasing x. The disappearance of magnetic long range ordering for $x > 0.20$ is rationalized in terms of intralayer and interlayer magnetic coupling constants. 2-dimensional magnetic short range order is found in the vicinity of the Néel temperatures.

Polycrystalline Li_4MgReO_6 was prepared and investigated by means of neutron powder diffraction experiments. Li_4MgReO_6 crystallizes in space group C2/m and forms an ordered rock salt structure. The Re^{6+} sublattice consists of distorted face-sharing tetrahedra. Neutron diffraction, heat capacity, bulk magnetic susceptibility, magnetic relaxation and muon spin relaxation measurements reveal a spin glass ground state with T_f=12K. The spin glass ground state is rationalized in terms of Li-Mg disorder. At 2.5K all magnetic moments are static.

Acknowledgements

I would like to express my gratitude to all the supportive people I met while I was carrying out my research at McMaster University as well as at several other research facilities. Foremost, I thank my supervisor, Dr. John E. Greedan, for his guidance, encouragement and all the research opportunities he provided me with throughout my Ph.D. project. I would like to thank Dr. Graeme M. Luke for his help with the muon spin relaxation measurements. I am also grateful to Dr. Raju P. Nandyala for introducing me to magnetic measurements and assistance with heat capacity measurements. Special thanks go to Andrew Wills for his intriguing scientific input and his friendship during the time he worked at McMaster University and beyond. Furthermore, I would like to thank Dr. Hanna Dabkowska and Dr. Anton Dabkowski for their help regarding sample preparation and single crystal growth. I thank Jim Garrett and Bruce Collier for helping me to solve practical problems, giving me access to a large variety of instrumentation, and making so many experiments work. Furthermore, I would like to extend my thanks to fellow students in the research group, Craig Bridges, Chris Wiebe, David Levy and so many thesis and exchange students.

Quite a few experiments were carried out at external facilities. I am grateful to all people who were so supportive during these experiments; in particular, Dr. Jason Gardner, Dr. Ian Swainson and Ron Donnaberger at NRC in Chalk River. Furthermore, I would like to express my gratitude to Simine Short at IPNS in Argonne and to Dr. Thomas Hansen at ILL in Grenoble.

Finally, I would like to extend my gratitude to Dr. Bruce D. Gaulin and

Dr. Jacques Barbier for being on my supervisory committee.

I would like to thank my friends Rodica, Klaus, Heidi, Ayumi, Craig and Andrew for making my time in Hamilton and our weekend trips so enjoyable.

Special thanks go to my parents, who were so encouraging and supportive during my time as a Ph.D. student in Hamilton.

Table of Contents

List of Tables

List of Figures

Chapter 1

Introduction

1.1 Objective and Background

Transition metal oxides exhibit a wide variety of electronic and magnetic properties, thus presenting an exciting field for the investigation of structure property relations. The various properties are due to the outer d-electrons of the transition metals. However, there is no comprehensive theory summarizing the properties of these materials. Transition metal oxides are found in all kinds of crytallographic structures, covering 1-, 2- and 3-dimensional networks of transition metal ions. Transition metal oxide polyhedra can be connected via corners, edges and faces. Furthermore, interstitial diamagnetic ions and substitution of paramagnetic ions with diamagnetic ions allow the engineering of materials with particular properties. Recently, a lot of work has been focused on systems exhibiting high temperature superconductivity and in particular magnetoresistance [Gre94] [Rao99].

The class of magnetic insulators is particularly useful, as they give insight into magnetic exchange and in particular the effect of competing interactions on a magnetic lattice. The dimensionality and the topology of the magnetic sublattices

allow the investigation of interesting effects. Furthermore, the spin quantum number, S, for a particular sublattice topology can strongly influence possible ground states. In general the main focus is the investigation of magnetic ground states based on the above mentioned criteria.

A particularly interesting transition metal is manganese. Manganese occurs in a wide variety of oxidation states, resulting in a wide variety of magnetic properties for its oxides. This work is primarily aimed at the investigation of transition metal oxides showing geometric magnetic frustration. All the compounds under investigation are electronic insulators and contain only one kind of paramagnetic ion each. Magnetic long range order, magnetic short range order and a randomly frozen spin system will be presented.

Chapter 1 gives an introduction for the theoretical concepts and chapter 2 covers experimental techniques. In chapter 3 the triangular antiferromagnets $ScMnO_3$ and $LuMnO_3$ will be investigated. Chapter 4 will present the square planar antiferromagnets $SrLaMnO_4$ and $BaLaMnO_4$ with emphasis on interlayer interactions and associated consequences regarding the magnetic ground state. In chapter 5 Li_4MgReO_6, a new spin glass with a tetrahedral magnetic sublattice will be presented. Finally, in chapter 6 the different systems will be summarized and compared.

1.2 Magnetism

1.2.1 Atomic Moments

Paramagnetism originates from unpaired electronic spins as well as any associated orbital angular momentum. If the the spin orbit coupling is negligible

the total magnetic moment is given by equation 1.2.1.

$$\vec{\mu} = -\mu_B \left(\vec{L} + g_s \vec{S} \right) \tag{1.2.1}$$

Where $\vec{\mu}$ is the magnetic moment, μ_B = Bohr magneton, $\vec{L}$ is the orbital and $\vec{S}$ is the spin angular momentum, for a free electron g_s equals 2. However, for the case of considerable spin orbit coupling equation 1.2.2 is required to describe the total magnetic momentum properly.

$$\vec{\mu} = -\mu_B g_J \vec{J} \tag{1.2.2}$$

$\vec{J}$ is the total angular momentum and g_J (the Landé g factor) is given by 1.2.3.

$$g_J = \frac{2}{3} + \frac{S(S+1) - L(L-1)}{2J(J+1)} \tag{1.2.3}$$

Whereas, core diamagnetism is caused by paired electrons. For compounds with small molecular masses the diamagnetic contribution is a few orders of magnitude smaller than the paramagnetic part. Such diamagnetism is due to induced charge density currents and is temperature independent [CvD77].

1.2.2 The Curie-Weiss law

Paramagnetism consists of temperature dependent and independent contributions. According to a Boltzmann distribution several magnetic states can be accessed, which are weighted according to the population of states. Perturbation theory results in van Vleck's equation, which describes the magnetic susceptibility χ as a function of temperature T.

$$\chi = \frac{<\mu>}{H} = \frac{\sum_n \left(\frac{E_n^{(1)^2}}{kT} - 2E_n^{(2)} \right) \exp\left(-E_n^{\circ}/kT\right)}{\sum_n \exp\left(-E_n^{\circ}/kT\right)} \tag{1.2.4}$$

Where $< \mu >$ is the average magnetization, H is the external magnetic field, E is the energy and the superscripts in brackets denote the order of the corresponding terms according to perturbation theory. k is Boltzmann's constant and the index n denotes accessible states. The high temperature expansion of van Vleck's equation leads to the Curie law, which describes the temperature dependent paramagnetism with no interactions between paramagnetic moments.

$$\chi = \frac{C}{T} \tag{1.2.5}$$

The Curie law is valid for sufficiently small magnetic fields H and under the condition that there are no thermally accessible states whose populations change with changing temperature. Considering the temperature independent contribution results in an additive term α:

$$\chi = \frac{C}{T} + \alpha \tag{1.2.6}$$

For spin-only magnetic moments the Curie constant C is defined by equation 1.2.7.

$$C = \frac{Ng^2\mu_B^2 S\ (S+1)}{3k} \tag{1.2.7}$$

Introducing the effective magnetic moment $\mu_{eff} = g\sqrt{(S\ (S+1)}\ \mu_B$ results in equation 1.2.8.

$$C = \frac{N\mu_{eff}^2}{3k} = \frac{\mu_{eff}^2}{8} \tag{1.2.8}$$

Interactions between paramagnetic moments in the paramagnetic state can be incorporated into the Curie law by using an effective temperature (T-θ), where θ is the Weiss temperature. Thus equation 1.2.6 is rewritten:

$$\chi = \frac{C}{T-\theta} + \alpha \tag{1.2.9}$$

Equation 1.2.9 is commonly known as the Curie-Weiss law including the temperature independent term. θ is negative for overall antiferromagnetic interactions and positive for overall ferromagnetic interactions [Kit76].

1.2.3 Cooperative Magnetism and Magnetic Exchange

Magnetic exchange can be described in terms of electron transfer and interaction between ions [Kra34]. For simple cases basic rules like Hund's rule and the Pauli principle allow the prediction of the sign of the exchange interaction. The so called Kanamori & Goodenough rules are well described in [Goo63][Kan59]. Magnetic exchange has been treated for cation-cation interactions, cation-anion-cation interactions as well as cation-anion-anion-cation interactions. However, reliable predictions regarding the sign of the coupling constants are only obtained for simple cases, i.e. 180° and 90° overlap. Due to several competing interactions exchange for intermediate angles is difficult to estimate and would require sound quantification. The two important concepts for spin-spin interactions for cation-anion-cation exchange are called super-exchange and double-exchange, and will be presented in the following two paragraphs.

Super Exchange

The spin alignment on the two cation sites is governed by a hypothetical electron transfer from the bridging anion to one of the cations. Formally, one cation is reduced and the anion oxidized. Whether the spin state of the virtually transferred electron is up or down depends on Hund's rule and the "Aufbauprinzip". The spin is not allowed to undergo a spin flip during transfer, consequently the spin orientation on the cation and the anion are identical. This "Gedankenexperiment" is carried out

with all cations around the anion of interest. One pathway for the super-exchange for a 180° arrangement of Mn^{3+}-O^{2-}-Mn^{3+} is demonstrated in figure 1.1. The sign

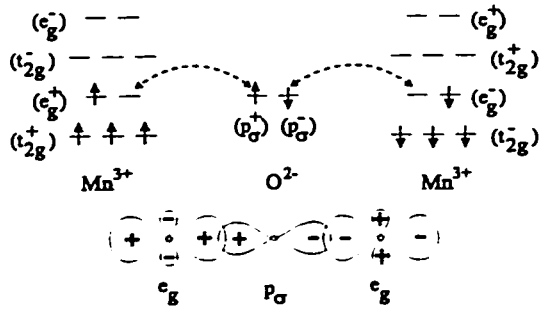

Figure 1.1: Super exchange for Mn^{3+}-O^{2-}-Mn^{3+} with a 180° bonding angle and Mn in an octahedral crystal field. The t_{2g} and e_g orbitals are for one spin orientation each. The orbital overlap for the contributing orbitals is shown at the bottom. The super exchange results in antiferromagnetic coupling.

of the exchange interaction is negative, thus antiferromagnetic.

Double Exchange

Double exchange is important for systems with identical cations in different oxidation states. The hypothetical mechanism consists of an electron transfer from the anion to the more oxidized cation and the anion receives an electron from the more reduced cation. Overall, an electron is transferred from the reduced cation to the oxidized cation and the oxidation states change accordingly. For one pathway this situation is illustrated in figure 1.2 for the case of $Mn(1)^{3+}$-O^{2-}-$Mn(2)^{4+}$ with a 180° bond angle. The result is ferromagnetic exchange between Mn^{3+} and Mn^{4+} ions, more details can be found in [Goo63].

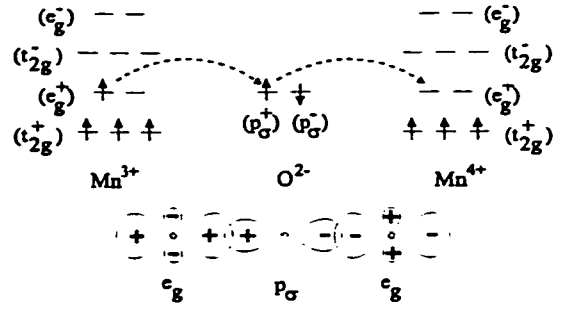

Figure 1.2: Double exchange for $Mn(1)^{3+}$-O^{2-}-$Mn(2)^{4+}$ with 180° bonding angle, resulting in ferromagnetic exchange interaction. Where Mn is octahedrally coordinated by oxygen. The overlap for the contributing orbitals is shown at the bottom.

1.2.4 Characterization of Magnetic Systems

For quantitative evaluations a more sophisticated treatment than the qualitative description in section 1.2.3 is required. The magnetic ground state can be determined by minimizing the total energy of the system. The corresponding Hamiltonian $\mathcal{H}$ for magnetic insulators with localized magnetic moments describing the underlying magnetic interactions is given in equation 1.2.10.

$$\mathcal{H} = -2 \sum_{<i,j>} J_{ij} \left(a\, S_i^z\, S_j^z + b \left(S_i^x\, S_j^x + S_i^y \cdot S_j^y \right) \right) - g\mu_B \mathbf{H} \cdot \sum_i \mathbf{S_i} \qquad (1.2.10)$$

In the above J_{ij} is the coupling constant between site i and j. The coefficients a and b allow one to distinguish between the isotropic Heisenberg model (a=b), the XY-model (a=0, b=1) and the Ising model (a=1, b=0). More regarding the dimensionality of spin systems can be found in section 1.2.5. The last term in equation 1.2.10 accounts for the presence of a uniform external magnetic field of strength $\mathbf{H}$ and its effect on the localized magnetic moments on the lattice.

1.2.5 Dimensionality of Magnetic Lattices

Magnetic systems can be categorized according to the lattice dimensionality, d, and the dimensionality of the magnetic moments, D. The dimensionality d is related to the crystallographic structure, more precisely of the magnetic sublattice, of the system under investigation. The distinction between 1-dimensional (chain like), 2-dimensional (layered) and 3-dimensional (3-d networks) is made. Whereas, the dimensionality D describes the symmetry or geometric restrictions of the magnetic moments involved, thus it refers to the anisotropy of the magnetic spin system. For the standard models three cases are known. D=1 are Ising spin systems with only one reference axis (e.g. z-axis), i.e. the spins only point up or down but do not deviate from the reference axis. The family of XY-magnets are characterized by the orientation of the magnetic moment in only one defined plane, but no magnetic components perpendicular to this reference plane are observed, D=2. The D=3 systems are called Heisenberg magnets, where the spins are allowed to point in any direction, Heisenberg spins are isotropic. The Hamiltonian (equation 1.2.10) presented in section 1.2.4 (page 7) can account for all three models through the coefficients a and b. However, not all combinations of d and D lead to an uniquely defined long range ordered ground state, table 1.1 presents the possible combinations of crystallographic and magnetic dimensionalities. The table also represents the universality class notation for D=1 to D=3. Crystallographic systems with d=3 exist as Ising, XY and Heisenberg magnets. No true d=1 system is known to exhibit a transition to a magnetic long range ordered state for any spin dimensionality, D. Where systems with d=2 exist as Ising but not as Heisenberg magnets the case d=2, D=2 is particularly interesting as it forms the borderline. A large body of

Table 1.1: Stability of magnetic systems based on the two parameters d and D. Where o = not allowed, • = allowed and ? = not known.

		universality	d=1	d=2	d=3
Ising	D=1	S_0	o	•	•
XY	D=2	S_1	o	?	•
Heisenberg	D=3	S_2	o	o	•

research is being carried out on the combination D=2 and d=2 and related systems. All these models are commonly referred to as standard models, however systems beyond the standard models exist. In 1985 Kawamura reported that there are more universality classes, since triangular antiferromagnets do not fall in any of the above mentioned classes. Two relevant classes have been added since 1985, the $Z_2 \times S_1$ and the SO(3) classes [Kaw85]. The universality classes are characterized by their critical exponents. These are obtained from power laws, which are satisfied in the vicinity of a transition. Here the focus is on magnetic transitions, thus only the relevant critical exponents will be discussed. The expression for a general critical exponent λ for the function F(t) is given in the following equation:

$$F(t) \propto |t|^{\pm\lambda} \tag{1.2.11}$$

Where t is the reduced temperature, which is related to the thermodynamic temperature T and the critical temperature T_c by equation 1.2.12

$$t = \frac{T - T_c}{T_c} \tag{1.2.12}$$

For an antiferromagnetic system T_c is the Néel temperature (T_N). Commonly used critical exponents are related to the zero field magnetization M, magnetic susceptibility χ, the magnetic correlation length ξ and the heat capacity C_p. These are

presented in equations 1.2.13 to 1.2.16:

$$M \propto \left(\frac{T_c - T}{T_c}\right)^{\beta} \tag{1.2.13}$$

$$\chi = \chi_0 \pm \left(\frac{T_c - T}{T_c}\right)^{-\gamma} \tag{1.2.14}$$

$$\xi = \xi_0 \pm \left(\frac{T_c - T}{T_c}\right)^{-\nu} \tag{1.2.15}$$

$$C_p = C_0 \pm \left(\frac{T_c - T}{T_c}\right)^{-\alpha} \tag{1.2.16}$$

Equations 1.2.14 to 1.2.16 are valid above and below the transition at T_c, whereas equation 1.2.13 is only valid below T_c. Within one universality class the critical exponents satisfy certain relationships (equation 1.2.17 and 1.2.18), thus providing a good tool to confirm that a compound belongs to a certain universality class.

$$\gamma + \alpha + 2\beta = 2 \tag{1.2.17}$$

$$D\nu = 2 - \alpha \tag{1.2.18}$$

where D is the spatial dimensionality of the system. Scaling relations involving the spatial dimensionality, D, are referred to as hyperscaling relations [Gau94]. Table 1.2 shows well established critical exponents for various systems [Col89].

1.3 Conventional Magnetic Ground States

The classical examples of systems establishing magnetic long range order at low temperature involve the ferromagnetic, the antiferromagnetic and the ferrimagnetic states.

Table 1.2: Calculated critical exponents for different combinations of d and D, the data are taken from [Col89], [Gau94], [Kaw88] and[Mas90].

Model	α	β	γ	ν
Mean field	-	1/2	1	1/2
2d-Ising	0	1/8	7/4	1
3d-Ising	0.106	0.326	1.2378	0.6312
3d-XY	-0.01	0.345	1.316	0.669
3d-Heisenberg	-0.121	0.367	1.388	0.707
SO(3)	0.34	0.28	1.1	0.55
$Z_2 \times S_1$	0.40	0.25	1.1	0.53

The ferromagnetic state is characterized by the parallel alignment of magnetic moments resulting in large net magnetization which is proportional to the total magnetic moment, JS or $g_J J$ and the moment density. Bulk magnetization measurements show hysteresis behaviour and a large saturation at low temperatures.

Antiferromagnets consist of two interpenetrating magnetic sublattices, with magnetic moments aligned antiparallel. Consequently, the net magnetization is zero, apart from small contributions from thermal excitations.

Ferrimagnets consist of two or more magnetic sublattices with opposing magnetic moment orientations, but where the sublattice magnetizations do not cancel, thus creating a net magnetic moment, which follows the characteristics of a ferromagnet.

1.4 Magnetic Frustration

Magnetic frustration is caused by competing interactions which prevent all of the magnetic exchange constraints at a given site to be satisfied simultaneously.

Equivalently, not all terms of the describing Hamilton can be minimized simultaneously. When the competition results exclusively from the geometry or topology of the lattice, this is known as geometric frustration, which is illustrated for a triangular antiferromagnet as shown in the upper left corner of figure 1.3. Antiferromagnetic

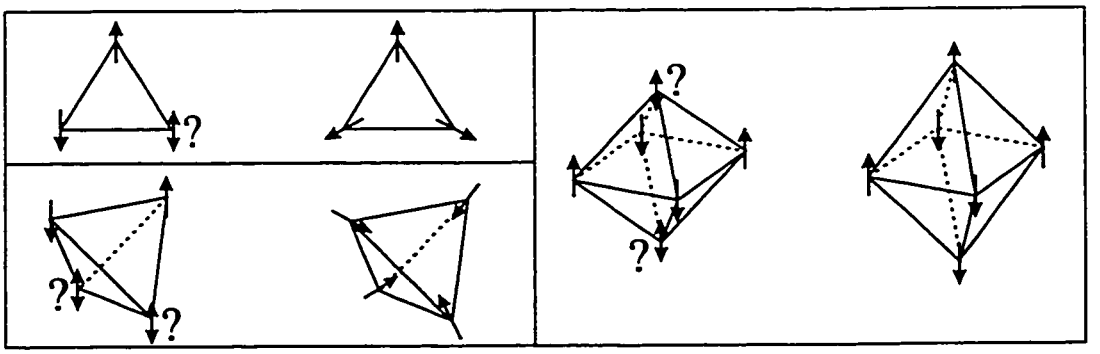

Figure 1.3: Illustration of a magnetically frustrated triangular lattice (left upper figure) with antiferromagnetic coupling constant J_1. Only two of the spins can align antiparallely, whereas the third spin is frustrated. The figure in the lower left shows the geometrically frustrated situation on the 4 vertices of a tetrahedron. The right sketch illustrates geometric frustration for an octahedral lattice.

exchange coupling between nearest neighbors on an equilateral triangle is a sufficient condition for magnetic frustration. Extended 2-dimensional lattices can be based on corner connected triangles (this is the Kagomé structure) or on edge sharing; the latter case is the focus of chapter 3. A tetrahedral arrangement of magnetic ions also shows frustration for antiferromagnetic exchange, this is shown in figure 1.3, lower left hand. Connecting the tetrahedra results in 3-dimensional sublattices. In pyrochlore and spinel phases the tetrahedra are linked by corners, whereas edge sharing is found for face-centered cubic lattices. Ordered rock salt structures with monoclinic distortion can result in face shared tetrahedral sublattices, Li_4MgReO_6 shows this topology and is presented in chapter 5. The body-centered tetragonal

lattice consists of octahedral units. The octahedral topology also shows geometric frustration for antiferromagnetic exchange, which is illustrated on the right in figure 1.3. However, infinitely elongated octahedra only show 2-dimensional interactions, thus are better described as a square planar lattice with no frustration. This cross over from three to two dimensions is well known for the K_2NiF_4 structure. Indeed both dimensionalities have been reported [BSS71] [BGS73]. The systems presented in chapter 4 show the body-centered (or octahedral) topology.

The degree of frustration can be quantified using the definition introduced by Lacorre [Lac87]. Lacorre proposed the calculation of a constraint function, F_c, which is the ratio between the energy per spin and the base energy per spin of a magnetic system. The base energy is the independent sum of all exchange energies present, i.e. frustration is not taken into account. In contrast the total energy is the sum of all interactions and considers the increase of energy due to frustration. Equation 1.4.1 is used to determine the constraint function F_c.

$$F_c = -\frac{E}{E_b} = -\frac{\sum_{k=1}^{n} J_k S_{k1} \cdot S_{k2}}{\sum_{k=1}^{n} |J_k||S_{k1}||S_{k2}|} \tag{1.4.1}$$

The summation is performed over the products of all n coupling constants J_k with the dot-product of spins S_{k1} and S_{k2}. F_c can take values between 1.0 (fully frustrated) and -1.0 (non-frustrated). Using equation 1.4.1 and assuming only identical exchange constants the following results are obtained for an equilateral triangle and a regular tetrahedron F_c values of -0.5 and -0.333, respectively. According to the above definition, the tetrahedral spin system is more frustrated since its constraint function is less negative than for the triangular spin lattice. Furthermore, for a planar triangular system the constraint angle, θ_c, describes the deviation of the two

spins from collinearity.

$$\theta_c = \cos^{-1}(F_c) \tag{1.4.2}$$

The following paragraph focuses on triangular platelets of spins having two exchange coupling constants J' and J, where J' only occurs once but J is identical for the two remaining exchange paths. J is always negative as it is an antiferromagnetic coupling constant. The constraint function $F(X)$ with $X = J'/J$ can be derived using equation 1.4.1. Using equation 1.4.3 the angle between the magnetic moments coupled via J' can be computed. The angle $\alpha = 2\theta_c$ is defined in the inset of figure 1.4 and can take values from α=0° for parallel alignment to α=180° for antiparallel alignment.

$$\begin{aligned} \alpha &= 0 && \text{if:} \quad -\infty < X < 1/2 \\ \alpha &= 2\cos^{-1}\left(\tfrac{1}{2X}\right) && \text{if:} \quad X \geq 1/2 \end{aligned} \tag{1.4.3}$$

Figure 1.4 shows the function $\alpha(X)$. The function $\alpha(X)$ behaves asymptotically for $X \to \infty$ causing an antiferromagnetic alignment of the spins coupled via J'. Whereas, at $X \leq 1/2$ the same spins align ferromagnetically and here the interaction J' is negligible. In contrast the asymptotic limit disregards the coupling constant J, consequently, the predominance of J' causes an antiparallel arrangement of the spins coupled via J'. The intermediate X-values are very interesting, all possible spin orientations between the limits α=0° and α=180° are accessible. The true 120° structure is predicted for X=1 (i.e. J'=J) [Vil79].

1.4.1 Magnetic Ground States for Frustrated Systems

After introducing the concept of magnetic frustration different possible magnetic ground states should be considered and compared. Three ground states are of

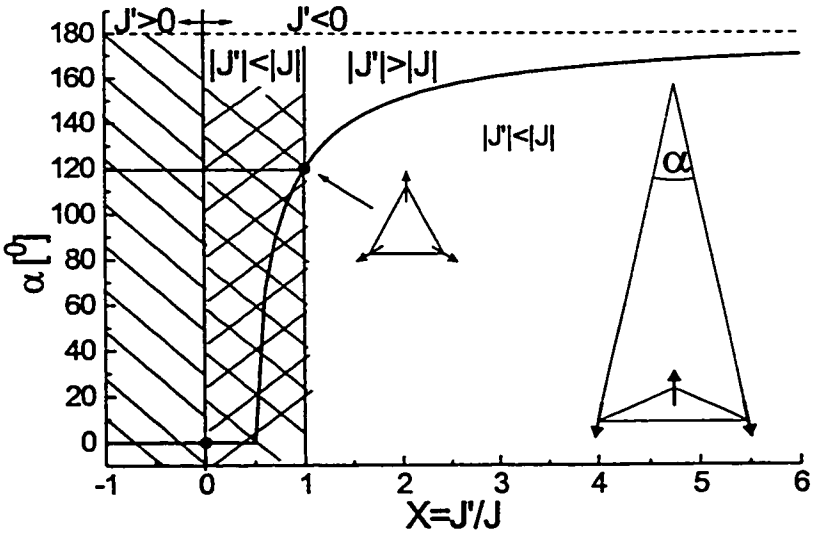

Figure 1.4: The function $\alpha(X)$ (equation 1.4.3)is shown for a triangular system with the constraint that J is an antiferromagnetic exchange constant. The angle α is depicted in the inset. Note that for X$\leq$0 the system is not frustrated (θ_c is positive).

particular interest, magnetic long range order forming a Néel state, the spin glass ground state and the spin liquid state.

The Néel State

The Néel state represents true magnetic long range order and is best described by a compromise between competing interactions. For the triangular antiferromagnets a 120° structure can be found, where the magnetic moments on a triangle form 120° angles with respect to each other. This is no true antiferromagnetic state, since the spin vectors are not collinear, but as for an antiferromagnet

the net moment is zero [1]. Furthermore, the 120° structure has three interpenetrating magnetic sublattices, in contrast to two for a true antiferromagnet. The magnetic sublattices can be determined with neutron diffraction experiments. The magnetic susceptibility for a 120° structure shows an inflection point at the ordering temperature, whereas an antiferromagnet like MnO shows a maximum close to T_N. Furthermore, the ordering temperature is usually rather low for a frustrated system when compared with the non-frustrated antiferromagnet. For a frustrated antiferromagnet a Néel state is only expected for a large spin quantum number, S.

An equilateral triangular arrangement of magnetic moments has two chiral solutions labeled (+) and (-). Furthermore, by rotating all magnetic moments simultaneously in the plane of the paper an infinite number of degenerate states can be accessed. Four degenerate states are compared in figure 1.5. Similar spin

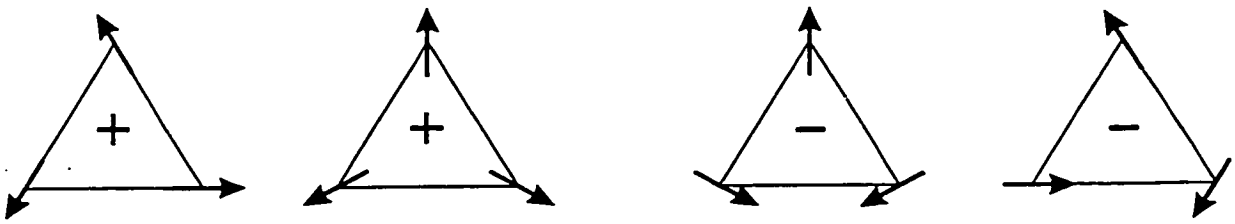

Figure 1.5: Comparison of the two chiral 120° magnetic structures on a triangular lattice. The two left images show one chiral form (labeled (+)), the only difference between these is a simultaneous spin rotation by 30°. The two figures on the right show the same cases for the opposite chirality (labeled (-)). All structures have a zero net magnetic moment.

structures can be constructed for tetrahedral antiferromagnets.

[1] The term antiferromagnet for the 120° structure refers to the antiferromagnetic coupling constants between magnetic moments.

The Spin Glass State

The spin glass state is best described as a magnetic ground state based on magnetic short range order only. Due to the absence of a periodic spin structure, no Bragg peaks will be found in diffraction patterns. The overall spin orientations are random and static or almost static. Averaging over all random spin orientations in the sample results in a zero net magnetic moment. Spin glasses are very often identified by a cusp at low temperature in the magnetic susceptibility data. This cusp is common but not always found. However, a divergence between zero field and field cooled magnetic susceptibilities is expected due to the cooperative nature of the magnetism, thus providing information regarding the freezing temperature T_f. Heat capacity measurements and in particular muon spin relaxation measurements are powerful tools for the investigation of spin glasses. Commonly, the heat capacity measurements reveal a significant fraction of entropy removal above the freezing temperature and a large electronic contribution at low temperature. Muon relaxation measurements can provide a window on the freezing process as the spin dynamics are mapped. Furthermore, time dependent phenomena are often seen in d.c. magnetization measurements. In general, a.c. susceptibility measurements show a frequency dependence for the maximum in χ' for spin glasses. Consequently, many different experiments are required to identify a spin glass and to rule out other ground states.

The Spin Liquid State

The existence of spin liquids is somewhat disputed in the scientific community. Here only a general introduction to the resonating bond valence model

as proposed by Anderson [And73] is presented. For more details the reader is referred to [And73], [FA74]. Instead of minimizing the total energy of the magnetic lattice by finding a compromise structure a large number of equivalent states are generated. These states are based on spin-pairs, which couple antiferromagnetically (truly collinear) and by carrying out a 180° spin flip on such a pair a degenerate state is formed, where the previously antiparallel alignments to nearest neighbors are now parallel and vice versa. This pair formation is schematically shown in figure 1.6. Anderson considers fluctuations between all possible degenerate states. If these

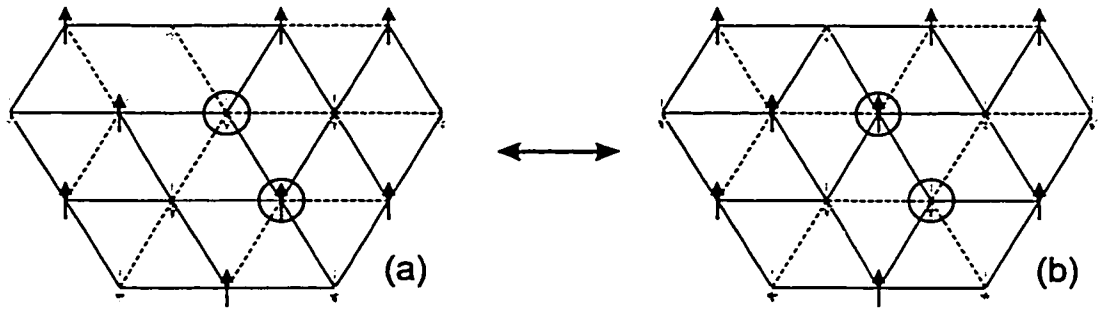

Figure 1.6: Illustration of pair formation and conservation of total energy for a spin liquid. The two spin structures (a) and (b) are only different in that the two circled moments are flipped by 180°. Parallel and antiparallel alignment is shown as dashed and solid lines, respectively. For an infinitely large magnetic lattice the total number of antiferromagnetic and ferromagnetic interactions is constant upon changing the orientation of any spin pair.

fluctuations are real classical fluctuations, then these should be measurable with muon spin relaxation or at least no freezing should be observed. However, if quantum fluctuations are considered the spin dynamics can not be observed. These two interpretations are disputed. However, there has been reported the first experimental examples of significant spin dynamics far below a potential freezing temperature [UKK+94].

1.5 Theory of Diffraction

1.5.1 Introduction

In order to investigate the atomic scale structure of solids diffraction methods are employed. In particular x-ray diffraction on powders as well as on single crystals is widely used. The widespread use of these two techniques is due to the widespread availability of instrumentation equipped with common laboratory x-ray sources. Whereas, synchrotron sources provide brighter x-ray beams and tunable wavelengths, synchrotron experiments must be carried out at large facilities making access less available. But there are experiments which require the high resolution and brightness or the tunable wavelength characteristics of a synchrotron source. Electron diffraction techniques are easily accessible, but electrons interact strongly with matter, such that multiple diffraction occurs in most samples, which is problematic for structural work. However, electron diffraction is a very powerful tool in order to investigate symmetry and single micro-crystals. The direct space imaging of objects on the Å scale also makes it an interesting and powerful tool. The third diffraction technique is neutron diffraction. In general neutrons interact rather weakly with matter and neutron beams are not as bright as electron and x-ray beams. Thus, neutron diffraction experiments require considerably larger samples than the other two techniques but there are compensatory advantages. Neutron and x-ray diffraction are complementary. X-ray diffraction can map the electron density, whereas neutrons locate the nuclear positions, and, as will be discussed later, neutrons are much more sensitive to magnetic moment density.

1.5.2 Diffraction Theory

Diffraction from a periodic lattice is explained according to Bragg's theory. The incident beam is scattered from crystallographic planes separated by distance, $d_{(hkl)}$. For constructive interference the path difference between two rays scattered from two successive planes is $2d_{(hkl)} \sin\theta$. The requirement for a sharp peak in the scattered radiation is that the angle of incidence must equal the angle of reflection, i.e., that the rays from successive layers interfere constructively. Bragg reflection according to equation 1.5.1 is illustrated in figure 1.7.

$$\lambda = 2d_{(hkl)} \sin\theta \tag{1.5.1}$$

Where λ is the wavelength of the incident beam and θ is the diffraction angle. The

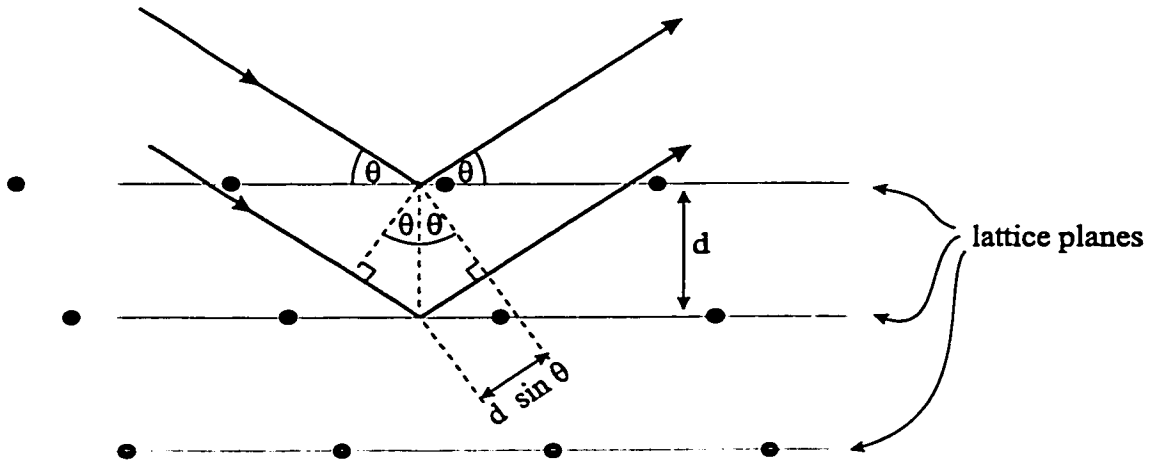

Figure 1.7: Bragg reflection from a set of lattice planes.

structure factor, $F_{(hkl)}$, for a reflection with Miller indices (hkl) is given by equation 1.5.2.

$$F_{hkl} = \sum_{n=1}^{N} f_n(2\theta)\ \exp\left[i\ 2\pi(hx_n + ky_n + lz_n)\right] \tag{1.5.2}$$

Where $f_n(2\theta)$ is the atomic form factor which is a function of 2θ for the case of x-ray diffraction [2], h,k and l are the Miller indices and x_n, y_n and z_n are the fractional coordinates of atom (or ion) n. The summation is carried out over all N atoms in the unit cell. The intensity, I_{hkl}, is related to the structure factor by equation 1.5.3

$$I_{hkl} \propto F_{hkl}^2 \tag{1.5.3}$$

1.5.3 Neutron Diffraction

A neutron is a neutral particle and possesses a magnetic moment of $1.891\mu_N$, where μ_N is the nuclear magneton. According to the de Broglie equation 1.5.4 the neutron wavelength λ is inversely proportional to the particle velocity, v.

$$\lambda = \frac{h}{mv} \tag{1.5.4}$$

Where h is Planck's constant and m is the mass of the neutron. Neutrons can be regarded as an ideal gas in thermal equilibrium with the moderator. Thus, knowing the moderator temperature, the velocity distribution can be described with a Maxwellian distribution function. Consequently, the maximum of the distribution function can be shifted by passing the neutrons through a medium of a particular temperature. For slow neutrons liquid deuterium or hydrogen (T≈10K) is used, whereas fast neutrons are obtained using heated graphite (T≈2000K). Figure 1.8 illustrates the wavelength distribution for two moderator temperatures.

Neutrons are generated using two methods. Using a nuclear reactor, neutrons are made available through the fission reaction of U^{235} with thermal neutrons. An alternative mode of neutron production consists of directing a beam of high

[2]For neutron diffraction b (neutron scattering length) is the equivalent to f_n for x-rays. The neutron scattering length b is independent of the diffraction angle 2θ.

energy particles (e.g. protons), which are supplied by a particle accelerator, at a heavy metal target (e.g. W, Hg). The heavy metal target nuclei are activated and neutrons are released upon nuclear decay. This process is called spallation and one characteristic of spallation sources is that the pulse repetition rate of the particle accelerator (usually in the order of 50 to 60Hz) imposes a time structure on the resulting neutron beam. The velocity distribution of neutrons from a spallation source shows a thermal component of the Maxwellian type, but there is an additional epithermal (i.e. high energy neutrons) impurity. Figure 1.8 shows the distribution functions for the two types of neutron sources. The different characteristics of these

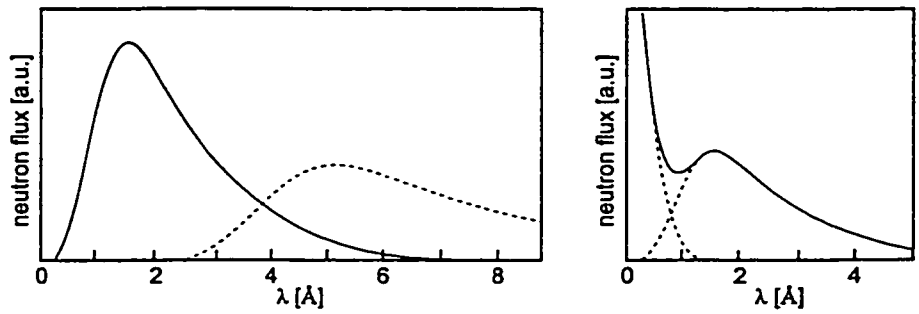

Figure 1.8: The left figure shows the neutron wavelength distributions for a reactor source for two temperatures; solid line approximately room temperature, dashed line low temperature (T≈10K). The right figure represents a typical wavelength distribution for a spallation source with the presence of epithermal neutrons at small wavelengths, the dashed lines show the components of the total distribution function.

neutron sources contribute significantly to the background functions and peak shape functions of powder diffraction patterns.

Interaction of Neutrons with Matter

Neutrons interact with the nuclei of atoms as well as with electronic magnetic moments. For a neutron diffraction experiment the incident and scattered neutrons are described by wave vector $\vec{k}$ and $\vec{k}'$, respectively. For an elastic scattering event equation 1.5.5 is valid.

$$\lambda = \frac{2\pi}{|\vec{k}|} = \frac{2\pi}{|\vec{k}'|} \tag{1.5.5}$$

According to equation 1.5.6 the scattering process is characterized by scattering vector $\vec{Q}$, the three participating vectors are illustrated in figure 1.9.

$$\vec{Q} = \vec{k}' - \vec{k} \tag{1.5.6}$$

Combination of equations 1.5.5 and 1.5.6 yields equation 1.5.7.

$$\vec{Q} = \frac{4\pi \sin\theta}{\lambda} \tag{1.5.7}$$

The sample is immersed in a monochromatic beam of incident neutrons, which are scattered with probability σ, which is called the cross section. Scattered neutrons are detected for a solid angle $d\Omega$. The differential cross section $\frac{d\sigma}{d\Omega}d\Omega$ is the probability of scattering a neutron into the region of solid angle $d\Omega$. The relations between the intensity of the incident beam and the scattered beam as well as the associated wave vectors and scattering vector are shown in figure 1.9. The total cross section σ_{tot} is the sum of several contributions, the absorption cross section σ_{abs}, the coherent σ_{coh} and incoherent scattering cross section σ_{incoh}. The neutron scattering length b is related to the cross section σ by equation 1.5.8.

$$\sigma = 4\pi b^2 \tag{1.5.8}$$

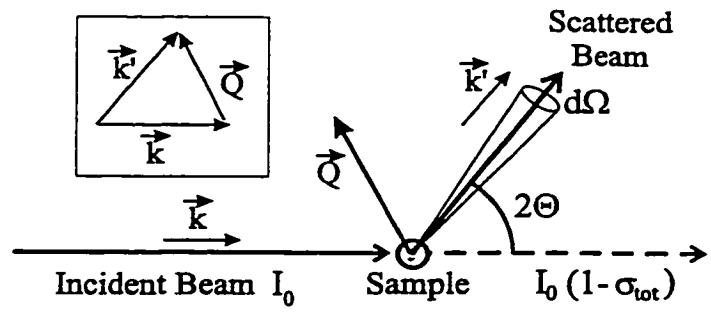

Figure 1.9: Schematic presentation of an elastic scattering experiment. The inset demonstrates the relation between $\vec{k}$, $\vec{k}'$ and $\vec{Q}$

In contrast to the atomic form factor for x-rays, $f(2\theta)$, b is independent of the scattering angle as the nuclei can be regarded as point scatterers. The structure factor for x-ray diffraction (equation 1.5.2) is rewritten for nuclear neutron diffraction.

$$F_{hkl} = \sum_{n=1}^{N} b \ \exp\left[i\ 2\pi(hx_n + ky_n + lz_n)\right] \tag{1.5.9}$$

1.5.4 Magnetic Neutron Diffraction

As already mentioned in section 1.5.3 neutrons can probe magnetic moments. This property is particularly useful for systems showing magnetic long range ordering. However, the best way of considering magnetic neutron scattering is by considering the scattering from paramagnetic ions first.

Paramagnetic Neutron Scattering

As the paramagnetic ions are ideally independent of each other no periodicity is associated with this state. Therefore, the differential neutron scattering cross section $d\sigma_{pm}$ is a function of the magnetic moment density. Halpern and Johnson derived the differential scattering cross section (equation 1.5.10) for paramagnetic

neutron scattering [HJ39].

$$d\sigma_{pm} = \frac{2}{3}S(S+1)\left(\frac{e^2\gamma}{mc^2}\right)^2 f^2 \tag{1.5.10}$$

Where S is the spin quantum number, m is the electron mass, e its charge, c is the speed of light, γ is the magnetic moment of the neutron expressed in terms of nuclear magnetons and f is the magnetic form factor. The magnetic form factors for magnetic neutron scattering are similar to x-ray form factors and are tabulated in [Wil92]. However, since only the "outer" electrons contribute to the paramagnetism, these form factors fall off much more rapidly as a function of the scattering angle than for the case of x-rays. Due to the randomness of the magnetic moments for the paramagnetic state no Bragg peaks are observed, but a broad background contribution, which decreases rapidly with $\sin\theta/\lambda$ is seen at low diffraction angles.

Neutron Diffraction from Ordered Moments

As the magnetic moments order periodically Bragg's condition (equation 1.5.1) for diffraction can be satisfied and consequently the periodicity of the magnetic moments, i.e. the magnetic structure, can be determined. The differential magnetic scattering cross section is described in equation 1.5.11 [3].

$$d\sigma_m = q^2S^2\left(\frac{e^2\gamma}{mc^2}\right)^2 f^2 = q^2p^2 \tag{1.5.11}$$

p is the magnetic counterpart to the nuclear scattering length b. The definition of p is given in equation 1.5.12,

$$p = \left(\frac{e^2\gamma}{mc^2}\right)Sf \tag{1.5.12}$$

[3]Note the difference between equation 1.5.11 and 1.5.10, for paramagnetic scattering $d\sigma_{pm}$ is proportional to $S(S+1)$, whereas for the ordered state $d\sigma_m$ is proportional to S^2.

and q is the magnetic interaction vector (equation 1.5.13).

$$\vec{q} = \vec{\epsilon}\left(\vec{\epsilon} \cdot \vec{K}\right) - \vec{K} \tag{1.5.13}$$

$\vec{\epsilon}$ is the scattering vector (perpendicular to the reflection plane) and $\vec{K}$ is the magnetic moment vector. The contributing unit vectors are illustrated in figure 1.10. Due to the rapid drop off of the magnetic form factor, magnetic Bragg peaks are

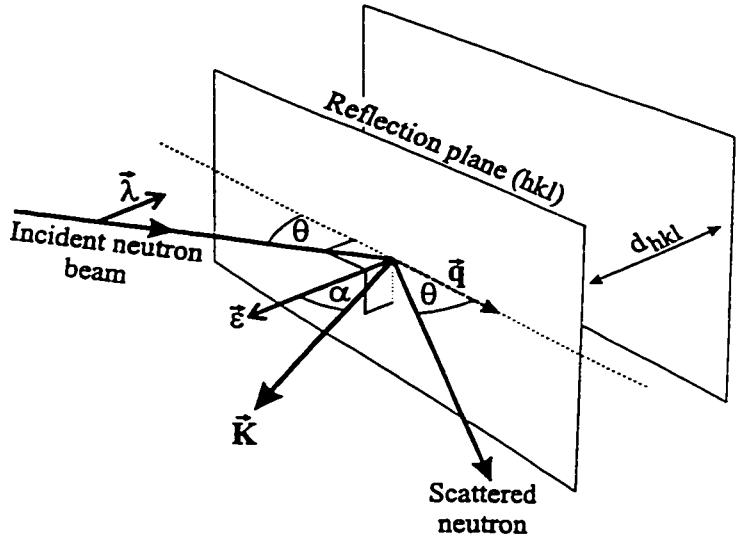

Figure 1.10: Schematic description of contributing unit vectors to a magnetic neutron scattering event. $\vec{\lambda}$ is the polarization vector of the incident neutron beam, $\vec{\epsilon}$ is the scattering vector, $\vec{K}$ is the magnetic moment and $\vec{q}$ is the magnetic interaction vector with a magnitude dependence of $|\vec{q}| = \sin\alpha$.

found at small diffraction angles. It is important to mention that there is no coherence between nuclear and magnetic scattering unless the neutron beam is polarized, consequently the diffraction intensities are additive, as shown in equation 1.5.14.

$$|F_{hkl}|^2 = |F_{nucl}|^2 + |F_{mag}|^2 \tag{1.5.14}$$

Where the magnetic structure factor is given in equation 1.5.15.

$$\vec{F}_{mag} = \sum_{n}^{N} \vec{q}_n p_n \exp\left[i\ 2\pi\left(hx_n + ky_n + lz_n\right)\right] \qquad (1.5.15)$$

The same notation as in equation 1.5.2 is used and the parameters $\vec{q}$ and p were defined above. The magnetic structure factor in equation 1.5.15 is a vector property, each magnetic sublattice contributes to the structure factor and thus, there is an orientational dependence. Only magnetic moment components in the reflection plane contribute to the magnetic structure factors, consequently, the magnetic moment orientation as well as the magnitude can be determined from neutron diffraction experiments. Because of the form factor dependence and the change of paramagnetic background intensity as the Bragg peaks develop, the magnetic diffraction peaks can be identified.

The Ordering Vector

As the magnetic moment is a vector, the symmetry describing a crystallographic lattice is not necessarily sufficient to describe the magnetic lattice. Ferromagnetic structures are compatible with the crystallographic unit cell and symmetry[4]. Consequently, the magnetic diffraction peaks will be located at the positions of the crystallographic peaks and thus, only the intensities of the powder pattern will change. In contrast, an antiferromagnetic structure is described by at least one symmetry element which reverses the orientation of the magnetic vectors between different sites of the paramagnetic sublattice. Therefore, the paramagnetic lattice is split into two or more sublattices, each describing the orientation of one set of

[4]For all paramagnetic ions the same magnetic vector orientation is found and therefore no symmetry element in addition to the symmetry elements describing the crystallographic structure is required.

magnetic moments. As a result the unit cell describing the magnetic structure might be larger than the crystallographic unit cell and additional Bragg peaks (with respect to the crystallographic pattern) might be found in the diffraction pattern. In particular diffraction peaks with non-integer Miller indices (when indexed on the crystallographic unit cell) are indicative for antiferromagnetic ordering. However, if the crystallographic phase is of low symmetry and the unit cell is large, it might be possible that the magnetic unit cell and the crystallographic unit cell are identical. The lack of additional peaks does not mean that the phase is not antiferromagnetically ordered. Commonly, magnetic structures are described with respect to the crystallographic phase using the "magnetic reciprocal lattice translation vector" $\underline{\mathbf{k}}$. This is a translation vector which locates the magnetic reflections in reciprocal space. If the magnetic reflections occur at the same positions as the crystallographic peaks, then $\underline{\mathbf{k}}$=0. Whereas, an antiferromagnetic structure yielding Bragg reflections with non-integer Miller indices (e.g. (1/2, 0, 0)) requires a reciprocal translation vector of $\underline{\mathbf{k}}$=(1/2 0 0). Therefore, the $\underline{\mathbf{k}}$ is defined as through the vector sum in equation 1.5.16.

$$\vec{\epsilon} = \vec{G} + \underline{\mathbf{k}} \tag{1.5.16}$$

where $\vec{G}$ is the reciprocal lattice translation vector describing the crystallographic unit cell and $\vec{\epsilon}$ is the scattering vector as defined earlier.

Magnetic Short Range Order

Magnetic short range order can be identified by the temperature dependence of broad features at low diffraction angles. The widths of these broad features allow the determination of magnetic correlation lengths. Whereas, the profile shape

indicates the dimensionality of the magnetic domains. 3-dimensional short range order causes symmetrical features, whereas 2-dimensional domains produce asymmetric peaks with a steep rise on the low angle side and a more gradual rise on the high angle side. The Warren-line shape describes 2-dimensional short range order and is given in equation 1.5.17.

$$P_{2\theta} = K\ m\frac{F_{hk}^2\,(1+\cos^2 2\theta)}{2\,(\sin\theta)^{3/2}}\frac{(\xi_{2D})^{1/2}}{\pi\lambda}F(a) \qquad (1.5.17)$$

where a=$(2\pi\sqrt{\pi}L/\lambda)(\sin\theta - \sin\theta_0)$, K is a constant, m is the multiplicity, F_{hk} is the two-dimensional structure factor, λ is the wavelength, ξ_{2D} is a two-dimensional correlation length, and θ_0 is the peak position. The function $F(a)$ is tabulated [War41]. Furthermore, the peak maximum is shifted with respect to the Bragg position. Equation 1.5.18 is the quantitative expression for the shift of the maximum as derived by Warren [War41].

$$\sin\theta_m - \sin\theta_\circ = 0.16\frac{\lambda}{\xi_{2D}} \qquad (1.5.18)$$

Where θ_m is the observed maximum of the broad peak caused by 2-dimensional short range order and $\theta_\circ$ is the expected peak position for a sharp Bragg peak with an infinite correlation length, ξ_{2D}. Consequently, the peak position can give an estimate for the correlation length even if no full peak profile fit is carried out. More details will be presented in chapter 3.10 and 4.9.

1.6 Data Analysis

1.6.1 Rietveld Refinement

Crystal structures can be refined from powder diffraction data by means of the Rietveld refinement method [Rie69]. Diffraction patterns from polycrystalline

samples show severe peak overlap. Consequently, instead of using individual peak intensities, profile points of the total diffraction pattern are used for the refinement of the structure, where the intensity at each data point, $y(2\theta)$, is the sum of the contributions from a number of neighboring Bragg peaks.

The relation between a reciprocal lattice, as obtained from a single crystal diffraction experiment, and the corresponding powder diffraction pattern is illustrated in figure 1.11. Starting with a 3-dimensional reciprocal lattice (figure 1.11 (a)) all intensities are projected on a common reciprocal axis with dimension 1/d. In figure 1.11 (b) the integrated intensities are shown as δ-functions which are convoluted with a peak shape function as shown in (c). In figure 1.11 (d) the profile is digitized and the resulting points represent the powder diffraction pattern. As illustrated in figure 1.11 (e) the powder pattern shows severe overlap for the (100) and (010) peaks, whereas these peaks are well separated on the 3-dimensional reciprocal lattice. The same is true for the barely resolved peaks in figure 1.11 (f).

The least squares refinement method is based on a curve fitting procedure by minimizing equation 1.6.1.

$$M = \sum_{i}^{N} w_i \left[y_i(obs) - y_i(calc) \right]^2 \qquad (1.6.1)$$

where w_i is a weighting factor which is based on the counting statistics ($w_i = 1/y_i(obs)$), $y_i(obs)$ is the observed intensity and $y_i(calc)$ is the calculated intensity at the i^{th} step. A starting structural model is required for the determination of the calculated profile points, during the course of the refinement the structural model is adjusted until the best agreement between observed and calculated patterns is reached. In addition to the structural parameters instrumental parameters are required in order to describe the diffraction pattern properly. Among these are

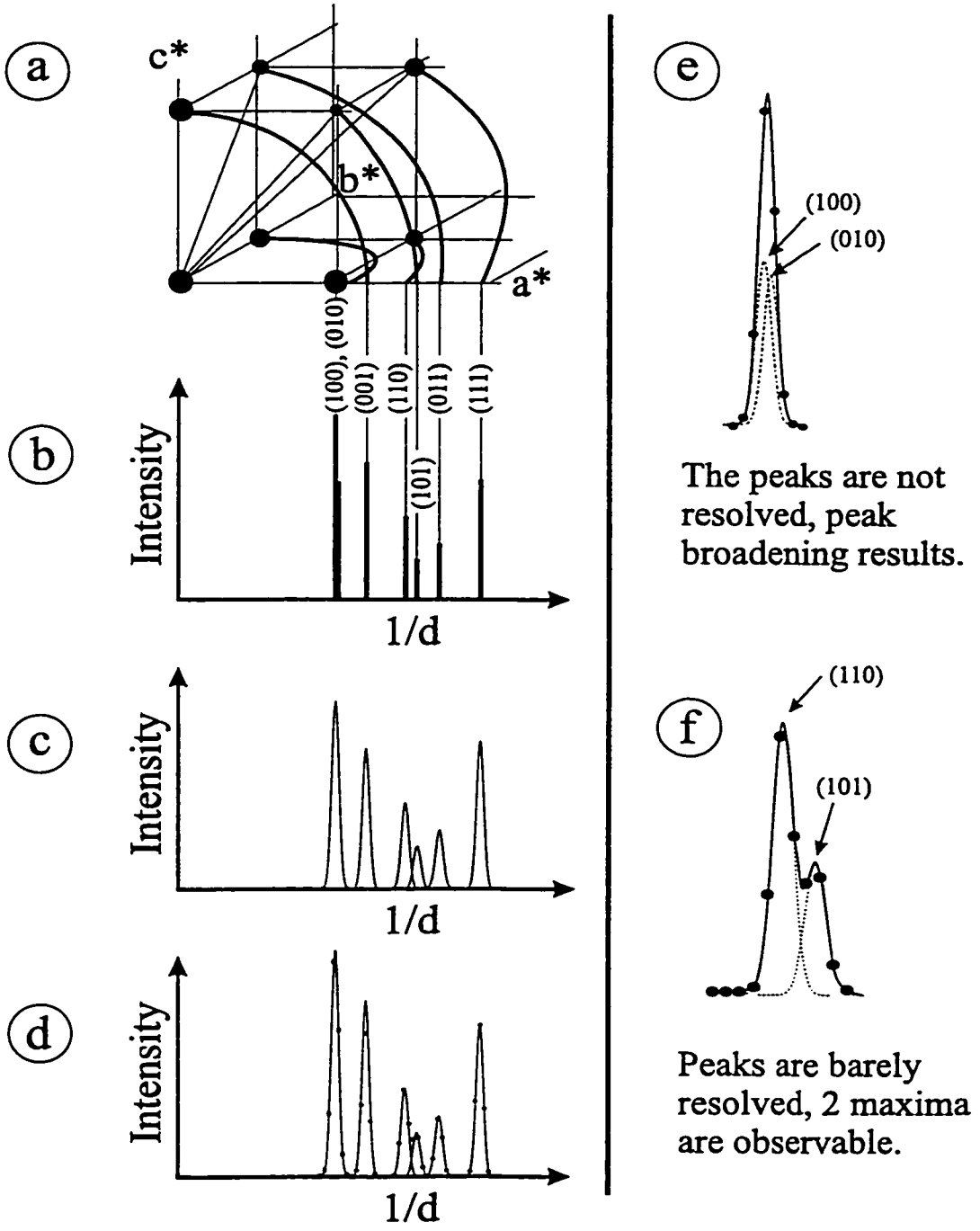

Figure 1.11: Illustration of the relation between a 3-dimensional reciprocal lattice (a^*, b^* and c^* are the reciprocal lattice vectors) and the corresponding powder diffraction pattern. The figure is discussed in the text.

the zero point, peak asymmetry, preferred orientation, the instrumental resolution function and the peak shape function. The resolution function is described by three parameters U, V and W which give the full width at half maximum (FWHM), $H^2_{(hkl)}$, of a reflection at an angle, θ, where,

$$H^2_{(hkl)} = U \tan^2\theta + V \tan\theta + W \tag{1.6.2}$$

U is related to the wavelength resolution, $\Delta\lambda/\lambda$, V is due to beam divergence and mosaic spread of the sample and the parameter W is defined by the incident beam cross section and sample diameter [CPR58]. For continuous wave neutron sources the peak shape can be described to a good first approximation by a simple Gaussian function. The profile of such a powder diffraction line is given in equation 1.6.3.

$$y_i = t\ F^2_{(hkl)}\ j_{(hkl)}\ L_{(hkl)} \frac{2\sqrt{\ln 2}}{H_{(hkl)}\sqrt{\pi}} \exp\left[-\frac{4\ln 2\left(2\theta_i - 2\theta_{(hkl)}\right)^2}{H^2_{(hkl)}}\right] \tag{1.6.3}$$

where t = step width of the counter, $F_{(hkl)}$ = the structure factor of the reflection, $j_{(hkl)}$ = the multiplicity of the reflection, $L_{(hkl)}$ = the Lorentz factor and $\theta_{(hkl)}$ the Bragg angle. The peak shape functions for powder x-ray diffraction and time of flight neutron diffraction experiments are not adequately described by a Gaussian. More sophisticated peak shapes have been suggested for these purposes, such as Cauchy, modified Lorentzian, pseudo-Voigt, Pearson VII and several more [RC98], [You93].

The quality of the fit of the calculated model to the observed intensities is indicated by the following agreement factors.

$$R_p = 100\ \frac{\sum_i |y_i(obs) - y_i(calc)|}{\sum_i |y_i(obs)|} \tag{1.6.4}$$

$$R_{wp} = 100\ \sqrt{\frac{\sum_i w_i\left[y_i(obs) - y_i(calc)\right]^2}{\sum_i w_i (y_i(calc))^2}} \tag{1.6.5}$$

$$R_{exp} = 100 \sqrt{\frac{[N - P + C]}{\sum_i w_i (y_i(obs))^2}} \tag{1.6.6}$$

$$\chi^2 = \frac{R_{wp}^2}{R_{expected}^2} \tag{1.6.7}$$

$$R_{Bragg} = 100 \frac{\sum_k |I_k(obs) - I_k(calc)|}{\sum_k |I_k(obs)|} \tag{1.6.8}$$

Where R_p is the profile R-value, R_{wp} is the weighted R-value, R_{exp} is the expected R-value, χ^2 is called the goodness of fit and R_{Bragg} is the Bragg R-factor. N is the number of data points, P the number of refined parameters and C the number of constraints.

1.6.2 The Bond Valence Method

The bond valence method is a powerful tool to check the correctness of a proposed crystallographic structure [M.O89] [BM97]. The premise is that the sum over all bond valences, S_{ij}, originating at ion j should be equal to the oxidation state or the valence, V_j, of the atom or ion j. Strictly speaking the bond valence sum should include the whole coordination sphere.

$$V_j = \sum_i^n S_{ij} \tag{1.6.9}$$

The summation is carried out over all n contributing bonds, i, originating at ion j. Bond valences are inversely related to the corresponding bond distances by the empirical expression 1.6.10 which was introduced by Brown [Bro92].

$$S_{ij} = \exp \frac{(R_o - R_{ij})}{b} \tag{1.6.10}$$

Here R_o is the bond length for unity valence and b is the slope of the correlation curve. These values have been determined for each ion, oxidation state and coordination from well known crystal structures. These parameters are tabulated [BA85] [BM97] and are easily used with program ValList [WB99]. The parameter b is close to 0.37Å [BA85]. R_{ij} is the actual length of bond i originating at ion j. Combining equations 1.6.9 and 1.6.10 results in:

$$V_j = \sum_i^n \exp \frac{(R_o - R_{ij})}{b} \tag{1.6.11}$$

The oxidation state, $V_j(assumed)$, and calculated bond valence sum, V_j, for any ion j should be similar. Any large deviation should prompt a careful reconsideration of the structure. The "Global Instability Index" $R1$ (equation 1.6.12) compares the assumed oxidation states with the calculated bond valence sums in the formula unit. $R1$ serves as a useful measure for assessing the "reasonable" correctness of a crystal structure and should be less than 0.2 for a correct structure [ASJMJCRP92].

$$R1 = \sqrt{\frac{\sum_j^m \left(\sum_{ij}^n S - V_k(assumed)\right)^2}{m}} \tag{1.6.12}$$

The summation is carried out over all m atoms j and all n bonds i.

Furthermore, disorder of two ions with different oxidation states (V_{A1} and V_{A2}) on a common crystallographic site can be determined using equation 1.6.13 [SI90].

$$x \sum s_{A1} + y \sum s_{A2} = x\ V_{A1} + y\ V_{A2} \tag{1.6.13}$$

Where the condition $1 = x + y$ must be satisfied for a fully occupied site.

Chapter 2

Experimental Techniques

2.1 SQUID DC-Susceptibilities

Magnetic susceptibilities are commonly measured using a dc-SQUID magnetometer. The SQUID (Superconducting QUantum Interference Device) consists of a sample translation system of high accuracy and reproducibility, a superconducting magnet to apply an adjustable external magnetic field and a pick-up coil coupled to Josephson junctions for high sensitivity. The external field strengths can be varied continuously between -5.5T and 5.5T. The temperature controller allows sample temperatures between 2K and 350K (±0.5%). High temperature measurements can be carried out using an additional furnace, which can cover the temperature range 300K to 600K (±0.5%). For all experiments presented here a sample translation of 6cm was used. At low temperatures samples were measured in gelatine capsules, which are held in a plastic straw. High temperature measurements were carried out in quartz tubes with 1mm inner diameter. Typical sample masses vary between 20mg and 200mg, where the mass depends on the spin system and sample availability. A conventional experiment consists of both zero field cooled (ZFC) and field cooled (FC) runs. For the ZFC measurement the magnet is switched on at the lowest

temperature after equilibration, and followed by measuring the magnetic susceptibility with increasing temperature. For the FC run the sample is cooled down in the presence of the magnetic field and the measurements are repeated upon heating. The detection system consists of 3 serial pick up coils, called a 2^{nd} derivative coil configuration. The main pick up coil is in the center and above and below are coils, with only half as many windings, which are wound in the opposite direction to the main central coil. A schematic of the experimental set-up and the recorded signal is shown in figure 2.1. Each magnetic susceptibility measurement at a temperature

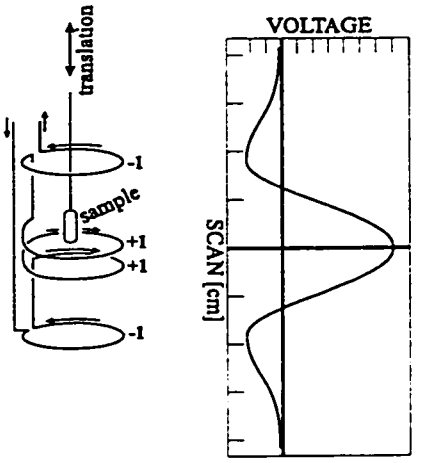

Figure 2.1: Left: Sample translation inside the pick-up coils of a SQUID magnetometer, the -1 and +1 indicate the winding orientation of the coils. Right: Voltage signal of a sample translated through the pick-up coils as a function of the scan position. For sake of comparison the scan axis of the left figure and the positions of the coils (right figure) use a common length scale.

consists of two independent scans with each scan consisting of 25 data points over the whole scan length. These data points are fitted to a function describing the voltage signal expected from the coil geometry [Des94].

2.2 Heat Capacity Measurements

Heat capacity measurements provide unique information on the ground electronic state. Phase transitions to a long range ordered state are identified by a so called λ-anomaly, which is a sharp feature. Broad features, called Schottky anomalies, provide information on energy differences between low lying electronic levels. Even if no C_p versus T anomaly is observed, the temperature dependence of the heat capacity allows conclusions regarding the magnetic state. Spin glasses usually show a linear temperature dependent contribution. Furthermore, no specific heat anomaly is found at the freezing temperature, T_f. For spin glasses it is observed that a considerable amount of the entropy (more than 70%) is removed above the T_f [FH91] [Myd93]. The lattice contribution to the heat capacity, which follows a T^3 dependence, must be subtracted before the electronic contribution can be evaluated.

Heat capacities for the temperature range from liquid nitrogen to 1300K are measured with commercial differential scanning calorimeters. In contrast low temperature calorimetry is rather sophisticated, since thermal insulation becomes crucial for adiabatic calorimeters. Thermal insulation is usually established with several heat shields, which might be temperature controlled such that the temperature gradient between the sample and the shields is as low as possible. The most common method for the investigation of small sample masses is the pulse method in conjunction with a quasi-adiabatic calorimeter. The experiments presented in this work were carried out in a ^{3}He cryostat, since temperatures as low as 0.5K were of interest. The sample is prepared in form of a pellet, which is placed on a sapphire stage using apiezon grease to assure thermal contact to the heater. The sapphire

stage is held in place with nylon threads. The sample can be heated using a resistive heater and the temperature is monitored using a RuO_2 resistive thermometer. The sample chamber is surrounded by two thermal shields in order to approximate adiabatic conditions. The sample temperature is equilibrated and a heat pulse of known energy is supplied to the sample. The temperature is followed as a function of time. Extrapolating the initial readings (before sending the heat pulse) and extrapolating the final temperature readings allows determination of the initial and final temperatures, respectively. A typical temperature profile is shown in figure 2.2. The heat capacity can be determined from the supplied heat [1], the sample mass,

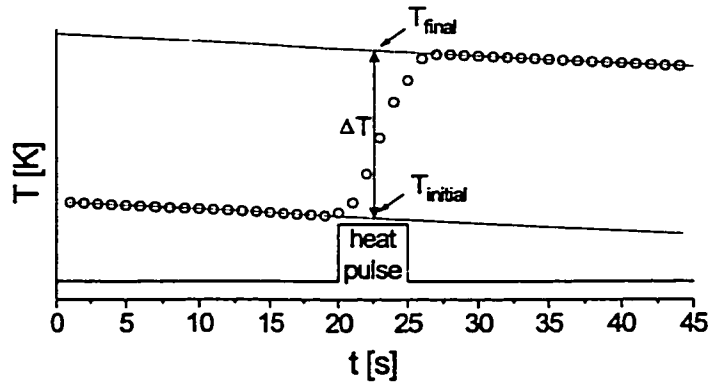

Figure 2.2: Illustration of a typical temperature profile for a heat capacity measurement using the pulse method. The lower line shows the status of the heater, low value=off, high value=on.

the heat capacity of the instrument [2] and the temperature difference.

In fact the pulse-heating method is the direct transposition of the definition

[1]The supplied heat is simply $Q = U\ I\ t$ where U is the voltage, I is the current and t is the heating time.

[2]The heat capacity of the instrument, including heat shields, sample holder, thermometer and heater is called the addendum and is determined in a separate experiment.

of the specific heat c_p as given in equation 2.2.1 [Gme87].

$$c_p(T) = \lim_{\Delta T \to 0} \frac{Q}{\Delta T} \tag{2.2.1}$$

2.3 Neutron Diffraction Experiments

2.3.1 Continuous Wave Powder Neutron Experiments

For an elastic neutron powder scattering experiment a narrow wavelength band is selected using a monochromator crystal. The monochromator take off angle $2\theta_M$ limits the resolution of the experiment. The monochromatic beam hits the sample and the diffracted neutrons are counted using for instance a position sensitive detector. The oscillating collimator excludes peaks which are due to experimental equipment which is close to the sample (e.g. cryostats). Figure 2.3 shows a schematic diagram for a powder diffractometer for a continuous wave neutron source. Most of the neutron experiments presented in this work were carried out using continuous wave double axis powder diffractometers, including the diffractometer at the McMaster nuclear reactor, the high resolution diffractometer C2 at Chalk River and low resolution instrument D1B at the Institute Laue-Langevin in Grenoble. D1B is not equipped with an oscillation collimator, whereas the other two instruments are.

2.3.2 The Time of Flight Experiment

Neutron spallation sources provide the full wavelength distribution of neutrons when the proton beam hits the target. This "white" beam is used and analyzed as a function of time. After diffraction takes place at the sample the scattered neutrons are detected using a fixed single counter, as a function of the time of flight, t, rather than the diffraction angle, 2θ, as for the case of monochromatic neutrons.

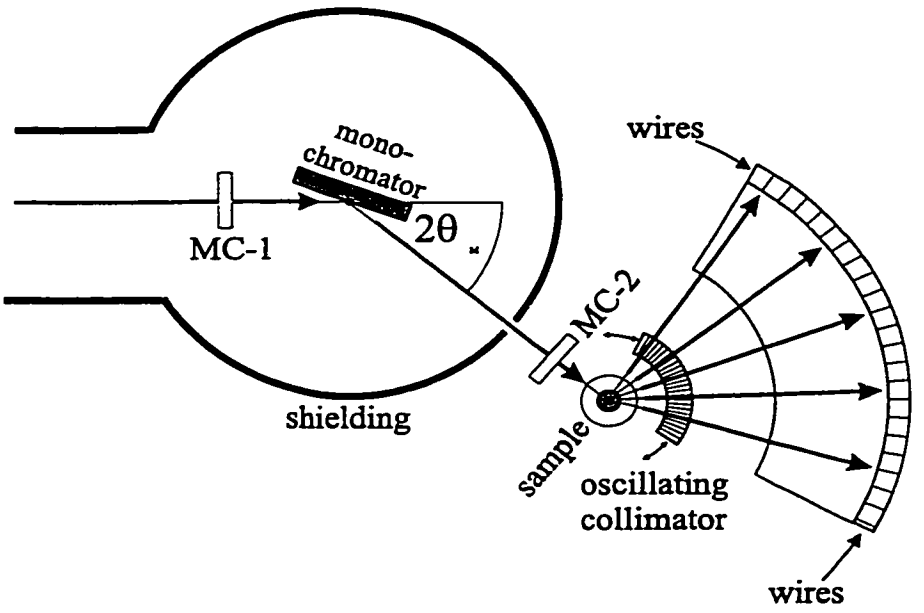

Figure 2.3: Powder diffractometer setup for a reactor source. MC-1 and MC-2 are monitor counters, which are required to normalize data sets.

The experimental setup is shown in figure 2.4. The clock starts when the neutrons are released from the target. Using equation 1.5.4, 1.5.1 and the length l of the total flight path, equation 2.3.1 is obtained which shows the proportionality between time of flight, t, and lattice spacing, d.

$$t = \frac{2d\ m\ l \sin\theta_T}{h} \tag{2.3.1}$$

Here m is the neutron mass and θ_T is the take off angle which determines the accessible range of d-spacings and the associated resolution. Usually, several detector banks having different θ_T-angles are used and each detector bank collects an independent diffraction pattern. The TOF neutron diffraction data presented in this work were collected at IPNS (Argonne National Laboratory) on high resolution

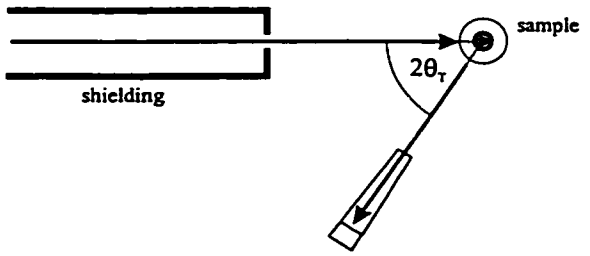

Figure 2.4: Experimental setup of a time of flight powder diffractometer at a neutron spallation source.

instrument SEPD [JFC+89]. The diffraction peaks show a high degree of asymmetry and require a rather sophisticated peak shape function in order to carry out meaningful data analysis [DJW82].

2.4 Powder X-ray Diffraction

Powder x-ray diffraction experiments are commonly carried out using conventional laboratory x-ray sources. The x-ray beam is scattered by the sample and the resulting Bragg peaks are detected using a scintillation counter, which scans along the 2-θ circle of the diffractometer. Alternatively, film techniques are used. A particularly useful device is the focussing Guinier Hägg camera, since it provides an outstandingly high resolution. The exposed film can be scanned afterwards and analyzed using a least square fitting program. The distinction between transmission (e.g. Debye-Scherrer geometry) and reflection (Bragg-Brentano setup) is particularly important for x-ray experiments, due to the absorption characteristics of x-rays. The focussing geometry which allows the high resolution for the Guinier Hägg camera is shown in figure 2.5.

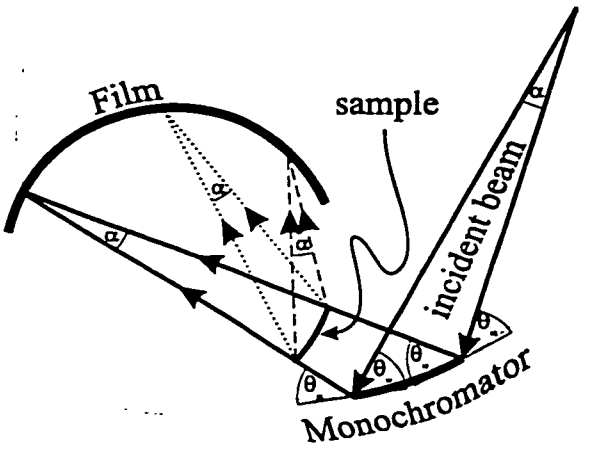

Figure 2.5: Geometry of the focussing Guinier Hägg camera, the divergent incident beam is focussed by the curved monochromator. The convergent beam then hits the sample and exposes the photographic film, which is placed on a common circle of focal points. The large grey circles are the extended circles of the curved monochromator and of the camera.

2.5 Muon Spin Relaxation Spectroscopy

Diffraction methods give information on the average or long range magnetic structure, whereas muon spin relaxation is an excellent, complementary technique which probes local magnetic fields. A muon is an elementary particle [3] with a magnetic moment which is approximately 3.18 times that of the proton [ea96]. The magnetic moment of the muon interacts with the local magnetic fields in the sample from which information on such fields can be obtained. Muons are produced in a multi step process which is described here and illustrated in figure 2.6 [Bre94], [Cox87] and [dRY97]. The first step consists of a high energy proton beam hitting a target made out of light elements, e.g. carbon. Equations 2.5.1, 2.5.2 and 2.5.3 show three possible pion (π^+ or π^-) producing reactions, as the proton beam hits a

[3] Muons belong to the family of leptons.

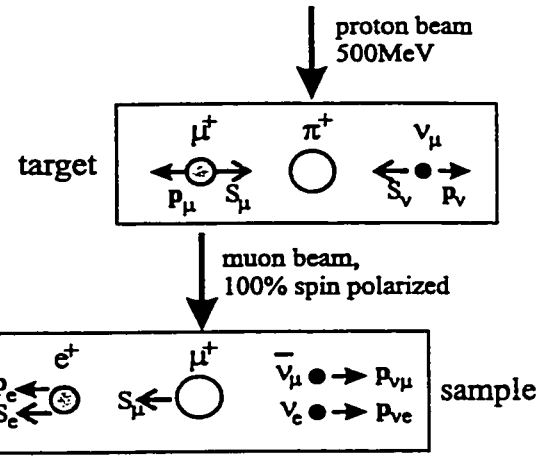

Figure 2.6: Illustration of the cascade process leading to the generation of muons. In each box the central particle decays into the particles shown to the left and right of it. The momentum (p) and the spin (S) is indicated for each produced particle.

proton or a neutron in the target.

$$p + p \rightarrow p + n + \pi^+ \tag{2.5.1}$$

$$p + n \rightarrow n + n + \pi^+ \tag{2.5.2}$$

$$p + n \rightarrow p + n + \pi^- \tag{2.5.3}$$

In the next step the π^+ decays with a half life of $\tau_\pi = 26$ns. According to equation 2.5.4 the π^+ decays into a muon (μ^+) and a neutrino (ν_μ).

$$\pi^+ \rightarrow \mu^+ + \nu_\mu \tag{2.5.4}$$

The produced muon beam is 100% spin polarized. When the polarized μ^+ beam hits the sample the muons are slowed down and reside on interstitial sites in the sample. The magnetic moments of the muons interact with the local magnetic fields

and the beam depolarizes as a function of time. Analyzing the depolarization of the muons allows determination of the local magnetic fields. The next step is the detection of the orientation of the magnetic moments of the muons in the sample. A muon undergoes decay with a life time of τ_μ=2.2μs producing a positron (e^+), a neutrino (ν_e) and an anti-neutrino ($\bar{\nu}_\mu$) (equation 2.5.5).

$$\mu^+ \rightarrow e^+ + \nu_e + \bar{\nu}_\mu \tag{2.5.5}$$

It is the fact that the positron is emitted along the direction of the spin of the decaying muon which makes this technique so powerful. Finally the positron is detected using detectors placed around the sample and the time of detection is recorded. The depolarization of the muons in the sample is determined from a large number of events and this is described by a time dependent relaxation function.

2.5.1 Muon Detection and Data Treatment

Muon relaxation spectra can be recorded using two counters and a trigger to start the experimental clock. The geometry of the detection system is shown in figure 2.7. The muons strike the sample, reside on interstitial sites and emit positrons at the time of muon decay. The muon is detected on the backward counter (B-counter) or on the forward counter (F-counter). Each data bin represents a fixed time difference between starting the trigger and detection. A large enough number of positron events is recorded assuring good counting statistics. Quite a few corrections for counter efficiency, sample and target size, absorptions of beams as well as geometric effects are required and can be carried out using calibration standards as well as fitting routines for different experimental set ups. Details can be found in the following monograph [Bre94].

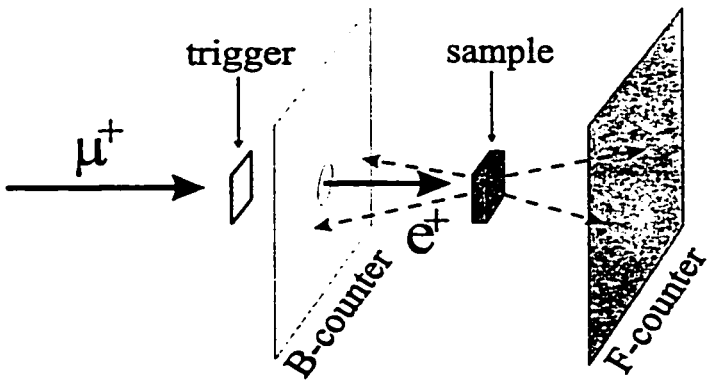

Figure 2.7: The muons pass the trigger before hitting the sample. Upon decay (refer to equation 2.5.5) a positron (dashed line) is emitted and detected on either the backward counter (B-counter) or the forward counter (F-counter). A 100% spin polarized muon beam in the sample should show only detection on the forward counter, whereas a depolarized beam shows a distribution of counts recorded on the B-counter and the F-counter.

2.5.2 The Muon in the Sample

Due to its magnetic moment the muon interacts with the local magnetic fields in the sample as well as external fields. In the presence of a strong enough transverse magnetic field (perpendicular to the initial polarization of the muon spins) precession is observed. The precession frequency (Larmor frequency) can be extracted and analyzed. In the case of random magnetic fields the relaxation function describing the depolarization is used to evaluate the local magnetic fields, field distribution and dynamics of the magnetic moments of the samples. A common problem is that the muon residence site is very often not known and that several sites might be accessed, which can lead to broadened distribution functions. The longitudinal and zero field relaxation function ($P_z(t)$) can be obtained most reliably by considering the backward and the forward counter (equation 2.5.6). The z-axis

is the direction of the external field and the initial spin polarization of the muon beam.

$$G_z(t) = \frac{P_z(t)}{P_z(0)} \propto \frac{F(t) - \alpha\ B(t)}{F(t) + \alpha\ B(t)} \tag{2.5.6}$$

The function $F(t)$ and $B(t)$ are shown in equation 2.5.7 and 2.5.8, respectively.

$$F(t) \propto \exp(-t/\tau_\mu)(1 + A_F P_z(t)) \tag{2.5.7}$$

$$B(t) \propto \exp(-t/\tau_\mu)(1 - A_B P_z(t)) \tag{2.5.8}$$

where t is the time and $\alpha = A_F/A_B$ and corrects for the different counting efficiencies between the two counters.

2.5.3 Muon Relaxation Functions

The exact form for polycrystalline samples in zero field is known as the Kubo-Toyabe function (equation 2.5.9).

$$G_z(t) = \frac{1}{3} + \frac{2}{3}\left(1 - \sigma^2 t^2\right) \exp\left(\frac{-\sigma^2 t^2}{2}\right) \tag{2.5.9}$$

Where σ describes the halfwidth of the gaussian distribution. The function is illustrated in figure 2.8 a), the initial decay is described by gaussian behavior and is due to static random internal fields. At large times a recovery to 1/3 is observed, which is due to the static nature of the fields. Fast dynamical internal fields show a square-root exponential decay (equation 2.5.10) for dilute moments, which is shown in figure 2.8 b) [Cox87].

$$G_z(t) \propto \exp\left(-\lambda t\right)^{1/2} \tag{2.5.10}$$

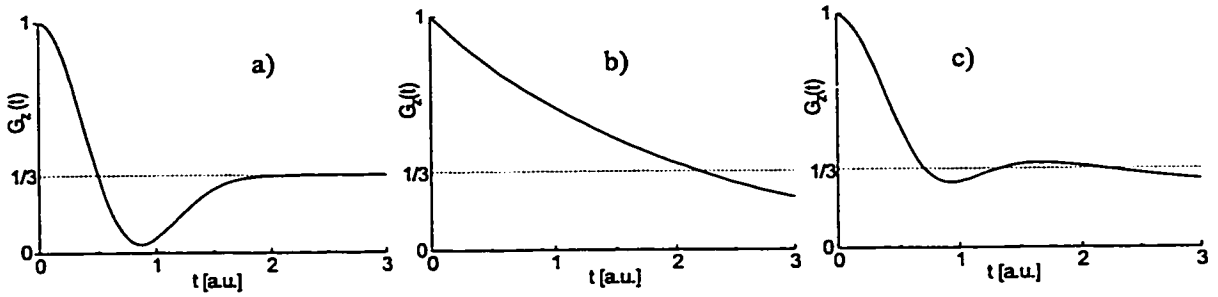

Figure 2.8: Illustration of three different relaxation functions. Where a) shows the muon relaxation function for random static fields according to 2.5.9, b) shows the case for fast fluctuating fields (equation 2.5.10). Figure c) illustrates the onset of fluctuations.

where λ is the relaxation rate. Figure 2.8 c) shows the decrease of the 1/3-recovery due to the onset of fluctuating magnetic fields. In conclusion muon spin relaxation measurements are very suitable to investigate spin dynamics and local magnetic properties [Bre94] [Cox87] [dRY97].

Chapter 3

The Triangular Antiferromagnets $AMnO_3$

3.1 Introduction

This chapter is focused on the investigation of the hexagonal manganates of composition $AMnO_3$. Primarily, the compounds $LuMnO_3$, $ScMnO_3$ and the solid solution $Lu_xSc_{(1-x)}MnO_3$ will be presented in terms of crystallographic structures and magnetic properties. The above mentioned compounds belong to the class of planar triangular antiferromagnets and show severe geometric magnetic frustration.

3.1.1 The series $AMnO_3$

The manganates of composition $AMnO_3$ are known for all trivalent lanthanide cations as well as Y^{3+}, In^{3+} and Sc^{3+}. The early lanthanide cations form orthorhombic perovskite phases [PV70], whereas the later Ln^{3+}-cations as well as In^{3+} and Sc^{3+} form hexagonal structures of $LuMnO_3$ type. If the A-cation radius decreases further along the lanthanide series the orthorhombic structure destabilizes and hexagonal structures are formed. The Goldschmidt tolerance factor (equation

3.1.1) is a well established criterion for the phase stability of perovskites [Gol26].

$$t = \frac{r_A + r_O}{\sqrt{2}\,(r_B + r_O)} \tag{3.1.1}$$

Where r_A, r_B and r_O are the ionic radii for the A, B and O ions, respectively. The perovskite phases are stable for the range $0.8 \leq t \leq 1.0$. For t smaller than 0.8 the coordination numbers for the cations decrease and structures like ilmenite and bixbyite besides others are often found [GzL94]. For the series $AMnO_3$ the decrease of the radius of A^{3+} results in the formation of hexagonal phases where the A^{3+}-cation is 7-fold and Mn^{3+} is 5-fold coordinated by oxygen. A more detailed discussion regarding the phase stability of ABO_3 systems can be found in [GzL94].

3.1.2 The series $Lu_xSc_{(1-x)}MnO_3$

The hexagonal phases of composition $AMnO_3$ (A = Ho^{3+} - Lu^{3+}, Y^{3+}, In^{3+} and Sc^{3+}) crystallize in space group $P6_3cm$. The lanthanide containing compounds were prepared and reported in the 1960's [YKBF63]. $InMnO_3$ was reported in 1992 by Giaquinta et al. [GzL92]. From a single crystal x-ray study the authors assigned the space group $P6_3/mmc$ to $InMnO_3$. However, in 1995 Greedan et al. [GBJ+95] proposed the space group $P6_3cm$, as determined from neutron and x-ray powder diffraction data and it was established that $InMnO_3$ is isostructural with $LuMnO_3$. In 1965 Komissarova [KPS66] reported the phase diagram for $ScMnO_3$, which gives the maximum preparation temperature for $ScMnO_3$ in air as 1350(20)K. Above 1350K irreversible decomposition into Sc_2O_3 and Mn_3O_4 is observed. Norrestam [Nor65] reported that $ScMnO_3$ is isostructural with $LuMnO_3$. However, the single crystal x-ray structure of $ScMnO_3$ was not published until 1995 [GBJ+95], the preparation of (nano)crystalline $ScMnO_3$ using a liquid-mix citrate synthetic route was reported

in 1998 [KW98]. Figure 3.1 illustrates the unit cell dimensions as a function of the ionic radii for Ln^{3+} and a clear linear correlation exists with the exception of $InMnO_3$, which shows an anomalously long c-axis. At this point it should be already

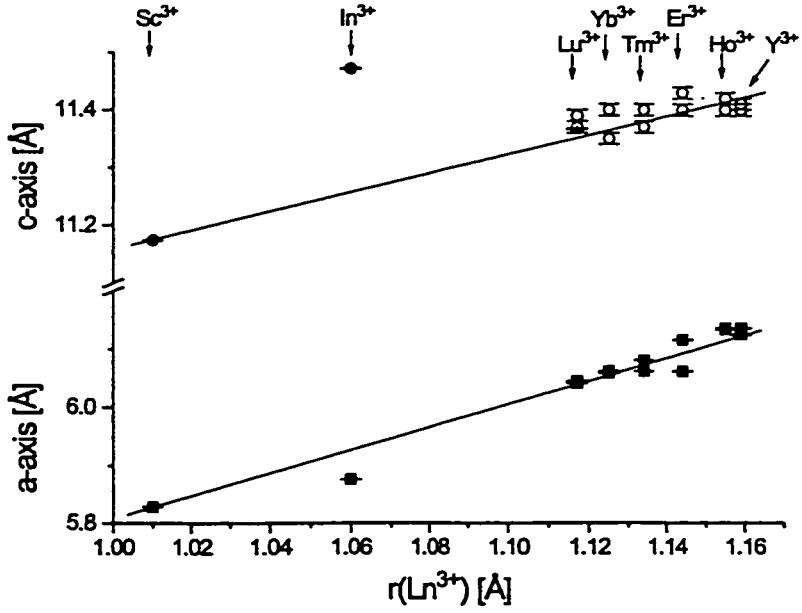

Figure 3.1: Relation between Shannon ionic radii [Sha76] for the trivalent lanthanide cations and the unit cell axes a and c for the hexagonal $AMnO_3$ phases. Different unit cell constants were reported for the same compounds, the data are taken from references [YKBF63] [GBJ+95] [JI98].

mentioned that $InMnO_3$ shows the most distinct magnetic properties, whereas the remaining materials show more similarities with respect to each other.

In 1964 Koehler et al. [KWYC64] reported the magnetic properties of the series $AMnO_3$ for A=Ho^{3+} - Lu^{3+}. The magnetic structures at 4.2K were reported based on powder neutron diffraction data. The magnetic structure of $ScMnO_3$ was reported in 1999 by Bieringer and Greedan [BG99], whereas the magnetic structure

of $InMnO_3$ has not been solved to date. However, in 1995 Greedan [GBJ+95] reported an ordering vector $\underline{k}$=(0,0,1/2) for $InMnO_3$, while all other members of the series show $\underline{k}$=(0,0,0), i.e. the crystallographic and magnetic unit cells are identical. For the $\underline{k}$=(0,0,0) structures true magnetic long range order is found, as the magnetic Bragg peaks are resolution limited. In contrast for $InMnO_3$ ($\underline{k}$=(0,0,1/2)), the magnetic reflections are significantly broader, indicating finite range magnetic order. In addition two compounds of the $AMnO_3$ family are known to exhibit an in-plane spin-reorientation transition at low temperatures, namely $HoMnO_3$ [KWYC64] and $ScMnO_3$[BG99].

The details of the crystallographic structures of the above mentioned compounds are required in order to make any meaningful statement regarding the different magnetic properties. The Mn^{3+}-ions ($d^4 \rightarrow$ S=2) are the only paramagnetic ions, which are located on position 6c, ($P6_3cm$), (x,0,z). Due to the 6_3 screw axis the separation of the Mn^{3+} layers will always be 0.5×c, while, the triangular planar lattice topology depends on the x-parameter for the Mn^{3+} position. For x=1/3 perfect equilateral triangular sheets are found, whereas any deviation from this position creates a set of long and short Mn-Mn distances thus destroying the high symmetry of the magnetic sublattice. In any case there is always one equilateral triangle per Mn-layer per unit cell present. This triangular Mn^{3+}-arrangement in conjunction with antiferromagnetic exchange between adjacent paramagnetic ions is a sufficient condition for geometric magnetic frustration. In figure 3.2 the perfectly regular lattice is compared with the distorted triangular lattice. Secondly, due to the $\cdots$ABAB$\cdots$ layer stacking competing interactions can also occur between Mn^{3+} layers. Thus, the magnetic frustration is essentially 3-dimensional. Truly equivalent

interlayer exchange paths are only expected if the Mn^{3+} ions are located at exactly 1/3, 0, z. Whereas any deviation from x=1/3 will create a set of long and short distances in the c-direction, thus removing the equivalence of the three bond paths. Furthermore it is important to consider the local environment of the Mn^{3+} ions,

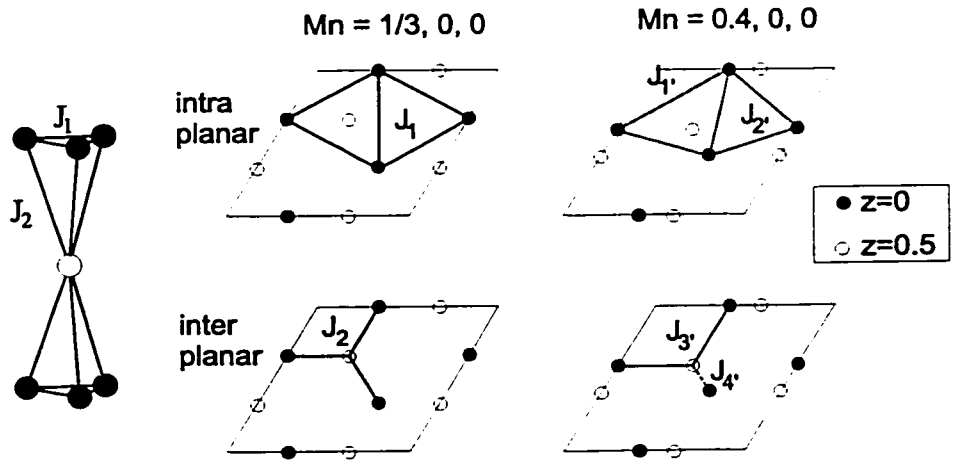

Figure 3.2: Illustration of the magnetic sublattice, the left figure shows the non-distorted Mn^{3+}-sublattice from the side. The remaining figures show the projection of the Mn^{3+} ions onto the ab-plane. In the middle the perfectly triangular arrangement of Mn^{3+}-cations is shown (x=1/3), whereas the right side emphasizes the distortion for x=0.4. The two upper sketches emphasize the intraplanar coupling constants and the lower figures show the consequences for the interplanar couplings.

including the exchange paths and the crystal field effects. The ratio between intraplanar and interplanar coupling constants is important. Long range order is not generally possible in two spatial dimensions but it can be stabilized by interplanar coupling. Due to the larger distances and more complex exchange pathways along the c-direction the interplanar coupling constants are rather weak compared to the intraplanar exchange couplings.

This section will investigate the crystal structures of the solid solution

$Lu_xSc_{(1-x)}MnO_3$ ($0 \leq x \leq 1.0$), the bulk magnetic properties and the magnetic structures as a function of the temperature. This includes an interesting in-plane spin-reorientation transition at low temperatures. The presence of magnetic short range order will also be discussed.

3.2 Sample Preparation

3.2.1 Polycrystalline Samples

According to equation 3.2.1 all polycrystalline samples were prepared from Sc_2O_3 (Alfa Aesar $\geq$99.9%), Lu_2O_3 (Alfa Aesar $\geq$99.9%) and Mn_2O_3 (Cerac $\geq$99.9%).

$$\frac{x}{2}Lu_2O_3 + \frac{(1-x)}{2}Sc_2O_3 + \frac{1}{2}Mn_2O_3 \xrightarrow{1320°C} Lu_xSc_{(1-x)}MnO_3 \qquad (3.2.1)$$

Stochiometric amounts of the starting materials were mixed, ground in acetone using an agate mortar und pestle and pressed into a pellet or rod of approximately 4g. The samples were wrapped in Pt-foil, placed on an alumina boat and heated to 1200°C in air and kept at this temperature for 48h. All samples showed line broadening on the x-ray films and were refired for 48h at 1320°C in air resulting in x-ray diffraction line narrowing. All products were black and single phase, except $ScMnO_3$ which contained 4% Mn_3O_4, according to Guinier x-ray diffraction data. Two point resistivity measurements showed that all products are poor electronic conductors.

3.2.2 Single Crystal Growth

This work presents the preparation of high quality single crystals of $ScMnO_3$, which were obtained by flux growth in air. The flux is based on a recipe for the growth of $ErMnO_3$ published in 1972 [Wan72] and consists of PbF_2, PbO, PbO_2

and B_2O_3. Sc_2O_3 (Alfa Aesar $\geq$99.9%), Lu_2O_3 (Alfa Aesar $\geq$99.9%) and MnO (Cerac $\geq$99.5%) were used as starting materials. The temperature program consists of heating to 1280°C, soaking for 2h, cooling at 1.0°C/h to 1020°C, cooling further to 1000°C at 0.5°C/h. No hot pour was necessary as most of the flux evaporated during the experiment. The single crystals were freed from flux using warm 10% HNO_3. The crystals did not show any evidence of etching. The shiny, black, hexagonal plates have dimensions of up to 4mm × 4mm × 5μm. EDX analysis did not show any evidence of impurities originating from the crucible (Pt) or the flux (Pb).

3.3 Crystallographic Structures

3.3.1 $LuMnO_3$ at Room Temperature

Room temperature powder neutron diffraction data were collected at Chalk River on diffractometer C2 and the data and the best fit are shown in figure 3.3. The crystallographic refinement was carried out using the Rietveld refinement package GSAS [LD94]. The two data sets collected at low and high angle have been refined as two independent histograms instead of merging the data sets. The refinement results are displayed in table 3.1 along with derived bond distances and angles and bond valence sums. The unit cell dimensions are in agreement with high resolution powder X-ray diffraction experiments (a_{x-ray}=6.0415(3)Å and c_{x-ray}=11.3671(6)Å). The crystallographic structure determined from powder neutron diffraction data is consistent with the structure obtained from single crystal x-ray diffraction data by Yakel et. al. [YKBF63]. The only disagreement is observed for the x-parameter for Mn^{3+}. Yakel et al. reported x=0.3212 [1], whereas our value is x = 0.3319(27).

[1] No error was reported.

Table 3.1: Agreement factors and refined lattice parameters for $LuMnO_3$ as determined from Rietveld refinement of room temperature powder neutron diffraction data. The lower two tables show the crystallographic data, bond distances, bond angles and bond valence sums for $LuMnO_3$ at room temperature.

Number of data points	: 1579	Space group	: $P6_3cm$
Number of parameters	: 87	a [Å]	: 6.04204(16)
R_{wp}	: 4.77	c [Å]	: 11.36715(32)
R_p	: 3.53	V [Å^3]	: 359.376(17)
$reduced\chi^2$	: 14.7		

Atom	x	y	z	$U_{iso}/U_e \times 100$	Occupancy
Lu(1)	0	0	0.27539(71)	0.24(18)	1
Lu(2)	1/3	2/3	0.23155(34)	0.27(11)	1
Mn	0.3319(27)	0	0	0.28(6)	1
O(1)	0.3048(9)	0	0.1639(7)	0.35(18)	1
O(2)	0.6398(7)	0	0.3368(8)	0.13(17)	1
O(3)	0	0	0.4757(9)	0.30(22)	1
O(4)	1/3	2/3	0.0204(4)	0.29(14)	1

	distance [Å]		angle [°]
Mn-O(1)	1.868(14)	O(1)-Mn-O(2)	179.2(4)
Mn-O(2)	1.866(14)	O(1)-Mn-O(3)	92.9(9)
Mn-O(3)	2.025(18)	O(2)-Mn-O(3)	87.3(11)
Mn-O(4) × 2	2.031(9)	O(3)-Mn-O(4)	120.7(4)
<Mn-O>	1.96(9)	O(4)-Mn-O(4)	118.3(9)
$\sum$radii	1.96		
Mn-Mn (intraplanar)	3.496(3)		
Mn-Mn (interplanar)	6.027(1)	Atom	bond valence sum
		$Lu^{3+}(1)$	3.188
Lu(1)-(O1) ×3	2.235(12)	$Lu^{3+}(2)$	3.068
Lu(1)-(O2) ×3	2.285(9)	Mn^{3+}	2.949
Lu(1)-(O3)	2.277(11)		
Lu(2)-(O1) ×3	2.242(5)		
Lu(2)-(O2) ×3	2.277(7)		
Lu(2)-(O4)	2.400(7)		

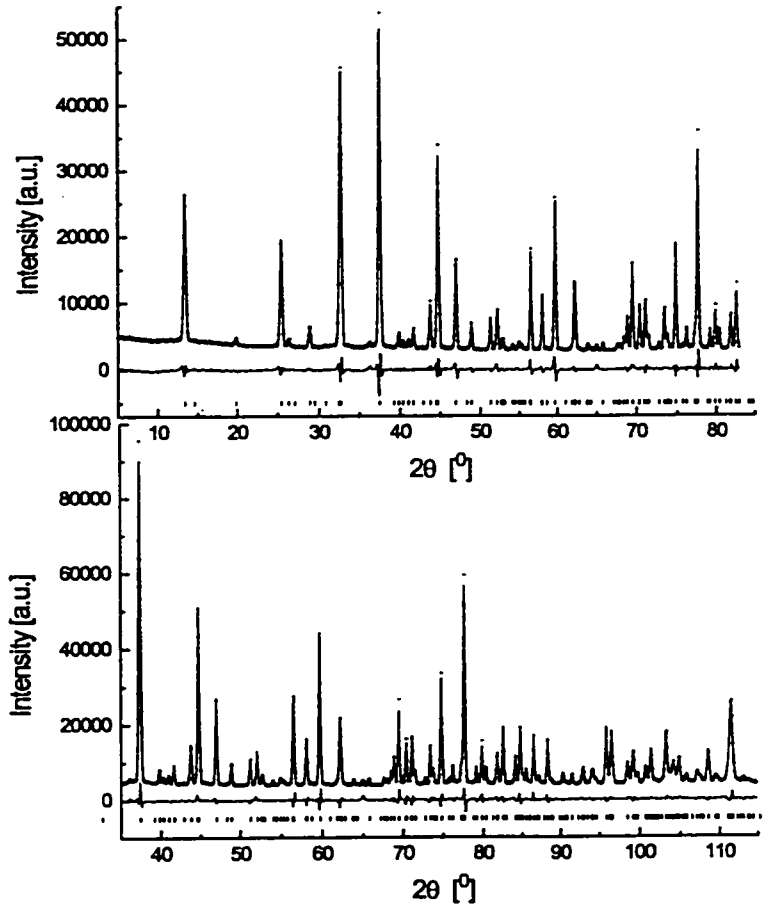

Figure 3.3: Refined neutron powder diffraction data for $LuMnO_3$ collected at room temperature, λ=1.32827(1)Å.

As a result the Mn^{3+} cations form perfect equilateral triangular layers. The crystal structure of $LuMnO_3$ is shown in figure 3.4. The bond valence sums are very close to the expected oxidation states of the cations, thus confirming a reasonable crystallographic solution. The Mn-O triangular bipyramid shows 3 long axes in the ab-plane and 2 short contacts along the c direction. The ratio of the averaged axial over the averaged equatorial bond lengths can serve as a distortion index,

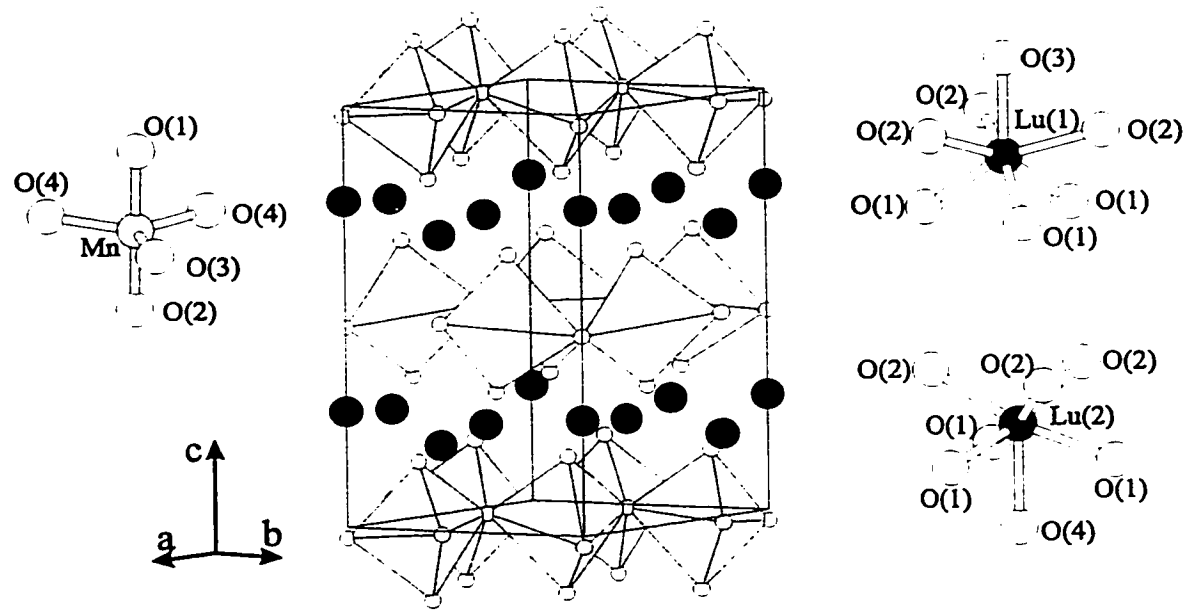

Figure 3.4: Room temperature crystal structure of $LuMnO_3$ as determined from powder neutron diffraction data. The polyhedra present the trigonal bipyramidal coordination of Mn^{3+} by oxygen (white). The Lu^{3+} cations (black) separate the paramagnetic layers. The coordination polyhedra of Mn, Lu(1) and Lu(2) are shown on the left and right side of the crystal structure. The coordinate system is applicable to all figures.

$DI = < r_a > / < r_e > = 0.920$ [2]. The trigonal bipyramids are linked by corners in the ab-plane, due to the buckling of the coordination polyhedra the Mn^{3+}-Mn^{3+} exchange path is not perfectly planar, but the Mn^{3+} sublattice is. The combined manganese and oxygen sublattices form a slightly off-planar honeycomb pattern in the ab-plane. The axial oxygen ions are linked to the rare earth ions in the layers above and below the Mn-sheets. Both Lu^{3+} sites are sevenfold coordinated by

[2]The axial bonds are not perfectly perpendicular to the equatorial plane, but close enough to use $< r_a > / < r_e >$ as a valid distortion index.

oxygen and are best described as monocapped octahedra. The bond length distribution for these two non-equivalent monocapped octahedra is rather narrow and thus assures a regular coordination polyhedron. The closest exchange path between adjacent Mn^{3+} cations in the ab-plane is via one oxygen ion, the geometric distance between two adjacent Mn^{3+} cations is 3.496(3)Å, whereas the bond path is approximately 4.04Å. The interplanar exchange path is very complicated and involves the Mn-O-Lu-O-Mn bonding sequence. The direct Mn^{3+}-Mn^{3+} distance is 6.027(1)Å, whereas the shortest bond path is already on the order of 8.5Å. The exchange paths are presented in figure 3.5.

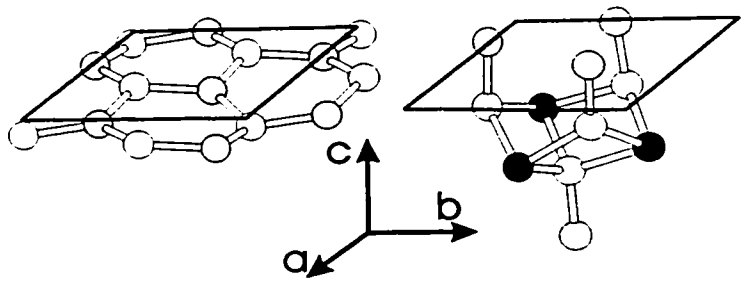

Figure 3.5: Magnetic exchange paths. Left: In-plane Mn^{3+}-O^{2-} frame work. Right: Interlayer magnetic exchange path for $LuMnO_3$. Legend: Mn^{3+} in grey, Lu^{3+} in black and O^{2-} in white.

3.3.2 $ScMnO_3$ at Room Temperature

$ScMnO_3$ and $LuMnO_3$ are isostructural, where more details regarding the crystal structure of $ScMnO_3$ can be found in the literature [GBJ+95]. For sake of comparison, the structural parameters as derived from single crystal x-ray diffraction data, the agreement factors, the atomic coordinates, bond distances, bond angles and bond valence sums are presented in table 3.2. These results are in agreement

with neutron powder diffraction results reported in [BG99] which are discussed in section 3.4. The Mn-O distortion index for $ScMnO_3$ is $< r_a > / < r_e >$=0.958 and is considerably closer to unity than for $LuMnO_3$. At room temperature a perfectly equilateral triangular sublattice of Mn^{3+}-ions is found. The intraplanar Mn^{3+}-Mn^{3+} distance is 3.364(3)Å, whereas the Mn^{3+}-O^{2-}-Mn^{3+} bond path is 3.92Å. The interplanar Mn^{3+}-Mn^{3+} distance is 5.914(1)Å and the shortest bond path is 8.1Å.

In conclusion, $ScMnO_3$ and $LuMnO_3$ are isostructural at room temperature. The principal difference is the more distorted Mn-O polyhedron for $LuMnO_3$. Furthermore, it is not surprising that the Mn^{3+}-Mn^{3+} distances increase as the ionic radius of the A^{3+} cation increases.

Table 3.2: Agreement factors and refined lattice parameters for $ScMnO_3$ as determined from single crystal x-ray diffraction at room temperature. The two lower tables show the structural data, bond distances, bond angles and bond valence sums for $ScMnO_3$.

Number of reflections	:	1547	Space group	:	$P6_3cm$
Number of parameters	:	33	a [Å]	:	5.8286(6)
R1	:	0.0283	c [Å]	:	11.1738(9)
wR2	:	0.0731	V [Å^3]	:	328.80
goodness of fit	:	1.161			

Atom	x	y	z	$U_{eq.}$ [Å^2]
Sc(1)	0	0	0.2738(2)	0.24(18)
Sc(2)	1/3	2/3	0.2312(2)	0.27(11)
Mn	0.3335(1)	0	0	0.28(6)
O(1)	0.3031(6)	0	0.1683(9)	0.35(18)
O(2)	0.6358(6)	0	0.3328(9)	0.13(17)
O(3)	0	0	0.4675(14)	0.30(22)
O(4)	1/3	2/3	0.0240(11)	0.29(14)

	distance [Å]		angle [°]
Mn-O(1)	1.877(10)	O(1)-Mn-O(2)	179.9(2)
Mn-O(2)	1.889(10)	O(1)-Mn-O(3)	95.2(5)
Mn-O(3)	1.977(3)	O(2)-Mn-O(3)	84.9(5)
Mn-O(4) × 2	1.961(2)	O(3)-Mn-O(4)	120.78(3)
<Mn-O>	1.93(5)	O(4)-Mn-O(4)	118.2(9)
$\sum$radii	1.96		
Mn-Mn (intraplanar)	3.364(3)		
Mn-Mn (interplanar)	5.914(1)	Atom	bond valence sum
		Sc(1)	2.951
Sc(1)-(O1) ×3	2.124(7)	Sc(2)	2.829
Sc(1)-(O2) ×3	2.223(4)	Mn	3.153
Sc(1)-(O3)	2.16(2)		
Sc(2)-(O1) ×3	2.155(4)		
Sc(2)-(O2) ×3	2.179(6)		
Sc(2)-(O4)	2.31(1)		

3.4 Magnetic Structure and Spin-Reorientation Transition in $ScMnO_3$

The investigation of the magnetic properties and the magnetic structure determination for $ScMnO_3$ has been published in a separate article. This article is presented on the following pages and is an integral part of the investigation of the solid solution $Lu_xSc_{(1-x)}MnO_3$.

Magnetic Structure and Spin Reorientation Transition in $ScMnO_3$

M. Bieringer and J. E. Greedan[1]

Brockhouse Institute for Materials Research and Department of Chemistry, McMaster University, Hamilton, ON L8S 4M1, Canada

Received August 27, 1998; in revised form November 17, 1998; accepted December 20, 1998

The magnetic structure of $ScMnO_3$ was investigated using polycrystalline samples. Bulk magnetic measurements were carried out revealing a Neel temperature of 130 K, followed by two maxima at 58 K and 40 K. The high-temperature data indicate strong antiferromagnetic coupling between Mn^{3+} ions in the form of a large, negative $\theta = -943(7)$ K. Powder neutron diffraction as a function of temperature disclosed magnetic long-range ordering below 130 K, where the chemical and magnetic unit cell have the same volume. A 120° magnetic structure was found consistent with the triangular Mn^{3+} sublattice and frustrated antiferromagnetic nearest neighbor coupling. The orientation of the magnetic spins is temperature dependent below 70 K. *c* 1999 Academic Press

Key Words: **geometrical frustration; antiferromagnetism; spin reorientation.**

INTRODUCTION

Rare earth manganese oxides of composition $AMnO_3$ have been studied extensively. These oxides form an orthorhombic perovskite structure for large A, Pr^{3+}-Dy^{3+}, but hexagonal structures for smaller A, Ho^{3+}-Lu^{3+} (1). The hexagonal structure is described in $P6_3cm$ and is a distorted form of the $YAlO_3$ structure with A in sevenfold monocapped octahedral coordination and Mn in fivefold trigonal bipyramidal coordination. For the hexagonal structure a linear relationship exists between the rare earth cationic radii and the unit cell parameters a and c. To extend the series, $InMnO_3$ and $ScMnO_3$ are of interest as both In^{3+} and Sc^{3+} have smaller radii than Lu^{3+}. $InMnO_3$ has been found to have an anomalously long c-axis which has been rationalized in terms of the difference in electronic configurations between In^{3+} and the trivalent lanthanides. $ScMnO_3$ was first reported by Koehler *et al.* (2) but the structural analysis was not detailed. A later study by Norrestam (3) using single crystal data was not conclusive regarding the space group. The structure of $ScMnO_3$ was eventually established by Greedan *et al.* (4) in $P6_3cm$ and is thus isostructural with the remaining $AMnO_3$ phases.

The magnetic structure of the A = Ho, Er, Tm, and Lu members of the series were determined by Koehler *et al.* (2) and a noncollinear 120° structure is found, consistent with the edge-shared triangular Mn^{3+} sublattice which is seen clearly in Fig. 1. The moments lie in the hexagonal plane. In $HoMnO_3$ an inplane spin reorientation occurs at temperatures below the Néel temperature but no such effect is seen for the other series members. The Néel temperature increases monotonically with decreasing c-axis length from $T_N = 76$ K for A = Ho to $T_N = 96$ K for A = Lu. From susceptibility and heat capacity measurements, Xu *et al.* determined a $T_N = 129$ K for $ScMnO_3$ (5). The magnetic structure of $InMnO_3$ is quite different from the remaining $AMnO_3$ phases as ordering of a long but finite range sets in below 120 K and there is clearly a c-axis doubling not found in the other series members (4).

As to-date, studies of $ScMnO_3$ have been sparse, this work reports magnetic susceptibility data over a wide temperature range, 5 to 600 K, on powder and single crystal samples and neutron diffraction studies of the magnetic structure.

EXPERIMENTAL

Preparation of $ScMnO_3$

Polycrystalline $ScMnO_3$ was prepared using Sc_2O_3 and Mn_2O_3 or Sc_2O_3 and MnO_2 which resulted in the same product. The well-homogenized mixture was pressed into pellets, which were reacted on a Pt-foil in an alumina boat for a total of 70 h at 1280°C in air, which included several regrinding and refiring stages. The product formation was followed using a Guinier-Hägg camera. The dark gray product was covered with a greenish layer, which was removed. A small excess of approximately 4% Mn_3O_4 was detected. The preparation of single crystals can be found elsewhere (4).

Magnetic Measurements

Magnetic measurements were performed using a Quantum Design MPMS SQUID magnetometer in a temperature

[1]To whom correspondence should be addressed.

0022-4596/99 $30.00

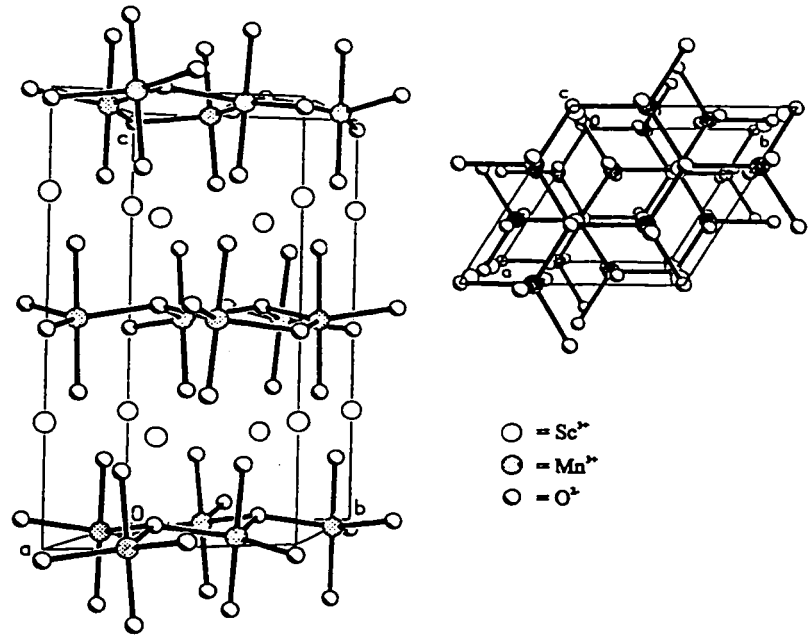

FIG. 1. Crystal structure of $ScMnO_3$.

range from 5 to 350 K and an applied magnetic field of 0.05 T. High-temperature measurements were carried out between 300 and 600 K using a furnace. Magnetic susceptibilities were measured using polycrystalline samples in order to obtain averaged data.

X-ray powder Diffraction

Powder diffraction data were obtained using a Guinier-Hägg camera having $CuK\alpha_1$ radiation (λ = 1.54056 Å) and silicon as an internal standard.

The final polycrystalline product was investigated using a Nicolet I2 automated powder X-ray diffractometer having radiation $CuK\alpha_{1,2}$ with λ = 1.5418 Å. The data were collected at room temperature over the diffraction angle range $10° \leq 2\theta \leq 90°$; the step size was chosen to be $\Delta 2\theta = 0.03°$. The collected data have been refined using the Rietveld refinement program Fullprof version 3.5. The single crystal X-ray diffraction data have already been published elsewhere (4).

Neutron Diffraction

All neutron powder diffraction experiments were carried out on the C2 diffractometer operated by the Neutron Program for Materials Research of the National Research Council of Canada at the Chalk River Nuclear Laboratory. The neutron wavelength was λ = 1.32587 Å.

The experiments were performed using an approximately 2 g sample in a vanadium can sealed under He gas with an indium wire gasket. Twenty-one data sets were collected between 10 and 130 K covering a 2θ-range from 10° to 90° (800 data points). The Rietveld refinement was performed using the program Fullprof version 3.5 (7). Three phases were included in the refinement, namely the chemical and magnetic structures of $ScMnO_3$ and the chemical structure of Mn_3O_4.

RESULTS AND DISCUSSION

Crystal Structure

The unit cell of $ScMnO_3$ contains six formula units and crystallizes in space group $P6_3cm$ (No. 185).

Figure 1 shows the unit cell. The stacking can be described as alternating Sc^{3+} layers and O-Mn-O layers separated by O^{2-} layers along the c-axis. With respect to the Mn^{3+} layers the stacking occurs in an ···ABAB··· fashion, which is a rather rare stacking sequence for ternary hexagonal transition metal oxides.

Mn^{3+} is located in site 6*c* and forms a 2-dimensional net which is perfectly planar triangular. Two different sites are occupied by Sc^{3+}. Sc(1) is located in site 2*a* and Sc(2) in site

TABLE 1
Crystallographic Data for Polycrystalline $ScMnO_3$ from X-Ray Powder Diffraction Refinement

Crystal system	Hexagonal
Space group	$P6_3cm$
Unit cell dimensions (Å)	$a = 5.8364(2)$
	$c = 11.1812(5)$
Volume (Å^3)	329.84(2)
Z	6
Density (calc) (Mg/m^3)	4.490
Formula weight (g/mol)	147.90

4*b*. The Sc^{3+} ions form a net in the *a*–*b* plane which is slightly nonplanar.

The coordination of Mn^{3+} by O^{2-} gives rise to a distorted trigonal bipyramid, and these trigonal bipyramids are tilted with respect to the unit cell axis *c*. Sc^{3+} is sevenfold coordinated in both sites and forms monocapped octahedra when coordinated by O^{2-}.

The room-temperature powder neutron data were refined for two phases, namely $ScMnO_3$ and Mn_3O_4. Twenty-three parameters were refined including six background parameters, the cell constants and scale factors for both phases, the zero point as well as profile parameters, and nine atomic parameters for $ScMnO_3$. The amount of Mn_3O_4 present was refined to be 5.4(6) wt%. The atomic parameters for $ScMnO_3$ are given in Table 2, the unit cell constants can be obtained from Table 1. The final agreement factors are $R_p = 4.53$, $R_{wp} = 6.01$, and $\chi^2 = 5.20$. The structure of $ScMnO_3$ deduced using single crystal data (4) and the polycrystalline sample, using X-ray and neutron diffraction data which are published in this work, are in agreement. Thus this serves as support for the correctness of the assumed model for the powder sample.

Magnetic Susceptibilities

Figure 2 shows the magnetic susceptibility for polycrystalline $ScMnO_3$ using a field strength of 0.05 T. Three

TABLE 2
Atomic Coordinates and Equivalent Isotropic Displacement Parameters for Polycrystalline $ScMnO_3$ at Room Temperature from Neutron Powder Data Refinement

	x	y	z	$U(eq)$ (Å^2)
Sc(1)	0	0	0.2793(12)	0.39(4)
Sc(2)	1/3	2/3	0.2335(10)	0.39(4)
Mn	0.3333(2)	0	0	0.50
O(1)	0.3995(15)	0	0.1645(13)	0.11(6)
O(2)	0.6381(16)	0	0.3307(14)	0.11(6)
O(3)	0	0	0.4788(15)	0.11(6)
O(4)	1/3	2/3	0.0248	0.11(6)

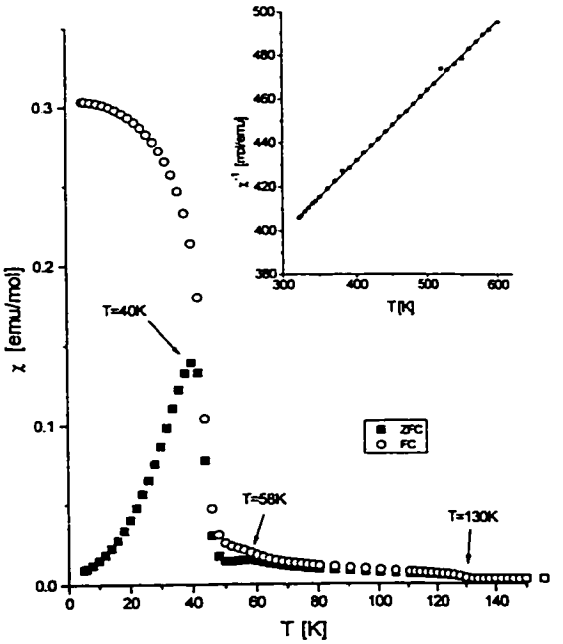

FIG. 2. Magnetic susceptibility for polycrystalline $ScMnO_3$ using a magnetic field of 0.05 T, solid squares, zero field cooling data; open circles, field cooling data. The inset shows the Curie–Weiss fit for the temperature range from 320 to 600 K.

significant features are present, namely an inflection point at 130 K, a broad maximum at 58 K, and a maximum at 40 K.

The Néel temperature is 130 K, below which magnetic long range ordering occurs. Note the FC-ZFC divergence below 130 K which indicates the presence of weak ferromagnetism due to sublattice canting. The broad maximum at 58 K is due to spin reorientation. The transition at 40 K is due to spin canting. It should be mentioned that this feature is not caused by the Mn_3O_4 impurity. This was evaluated from a study carried out earlier on different samples which showed the presence of a larger Sc_2O_3 impurity but no Mn_3O_4 impurity. All samples showed a maximum at 40 K. Furthermore, magnetic susceptibility data acquired using single crystals showed a maximum at 40 K as well. The high-temperature data, collected in a separate experiment, are shown as an inset in Fig. 2. The Curie–Weiss law was found for the temperature range 320–600 K, a temperature independent term being of no significance.

$$\chi = \frac{C}{T - \theta_c}. \qquad [1]$$

where χ is the molar magnetic susceptibility, C is the Curie constant, and θ_c is the Weiss temperature.

Accounting for 4 wt% of Mn_3O_4, the Curie constant for $ScMnO_3$ was found to be 2.85(3) emu K/mol, giving an effective magnetic moment of 4.78(4) μ_B which is close to the theoretical spin only value of 4.9 μ_B for Mn^{3+}. The Weiss temperature is $\theta_c = -943(7)$ K indicating strong antiferromagnetic coupling.

Xu *et al.* published a Néel temperature of 129 K determined from magnetic data and heat capacities (5) and is therefore close to our value. These authors did not measure the temperature range below 77 K where additional transitions are found.

Magnetic Structure

The magnetic structure of $ScMnO_3$ is expected to reflect the geometric frustration inherent in the triangular lattice with strong antiferromagnetic exchange. This situation is shown in Fig. 3.

Neutron diffraction experiments have been employed in order to determine the magnetic structure of $ScMnO_3$. Data were collected for 21 temperatures between 10 and 130 K. Figure 4 shows the low angle region of the powder neutron diffractograms obtained at several temperatures emphasizing the changing intensities of the most prominent magnetic Bragg reflections and finally the disappearance of the magnetic Bragg peaks at 130 K. The diffractograms below 130 K show additional peaks, which are due to magnetic long-range ordering. Upon lowering the temperature, the intensity of the $(101)_{mag}$ peak increases until a temperature of 70 K is reached; below 70 K the intensity decreases again and remains constant below 40 K. However, the $(100)_{mag}$ peak appears below 70 K and its intensity increases until a temperature of 40 K is reached. Between 40 and 10 K the intensity of the $(100)_{mag}$ reflection does not change significantly. All magnetic peaks can be indexed on the chemical unit cell. Therefore, the propagation vector is $q = [000]$.

Below 45 K the $(100)_{mag}$ reflection shows a shoulder on the high-angle side, which is due to the strongest magnetic reflection of Mn_3O_4, which is present as a small impurity phase. The disappearance of this reflection above 40 K is in agreement with the ordering temperature of 42.5 K for Mn_3O_4 (6). The presence of the shoulder at low-temperature complicates the refinement of the magnetic structure which will be discussed in the next paragraph.

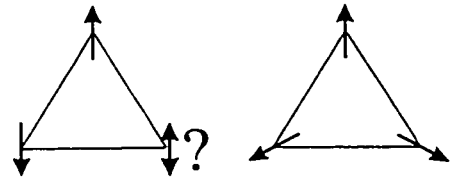

FIG. 3. Triangular arrangement of magnetic moments and the impossibility of satisfying all antiparallel alignments simultaneously. Right-hand side 120° structure.

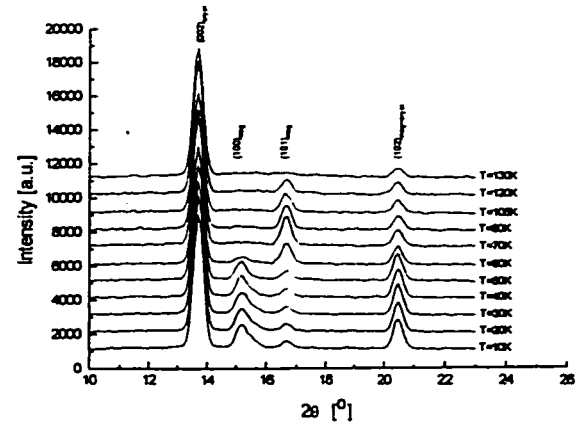

FIG. 4. Neutron powder diffraction patterns for $ScMnO_3$ at different temperatures, showing magnetic long rang order at low temperatures, $\lambda = 1.32587$ Å.

The varying intensity ratio of the $(100)_{mag}$ peak and the $(101)_{mag}$ reflection is due to spin reorientation in the **a**–**b** plane. Close to the Neel temperature a broad background can be seen.

Magnetic Short-Range Order

To estimate the correlation length associated with two-dimensional magnetic short-range order the neutron powder data were fitted to a Warren lineshape (8),

$$P_{2\theta} = Kmt \frac{F_{hk}^2(1 + \cos^2 2\theta)}{2(\sin\theta)^{3/2}} \frac{(L)^{1/2}}{\pi\lambda} F(a). \qquad [2]$$

where $a = (2\sqrt{\pi}L/\lambda)(\sin\theta - \sin\theta_0)$. K is a constant, m is the multiplicity, F_{hk} is the two-dimensional structure factor, λ is the wavelength, L is a two-dimensional correlation length, and θ_0 is the peak position. The function $F(a)$ is tabulated.

The results are shown in Fig. 5. The strongly overlapping $(002)_{cryst}$ was modeled using a gaussian lineshape. From the 130 K data set only the $(102)_{cryst}$ peak was excluded. Whereas, for lower temperatures the $(101)_{mag}$ reflection was excluded as well. Below 80 K too many peaks are present and no fit using the Warren function was carried out. A nearly temperature-independent correlation length of 13(2) Å for the temperature range 80–130 K was found.

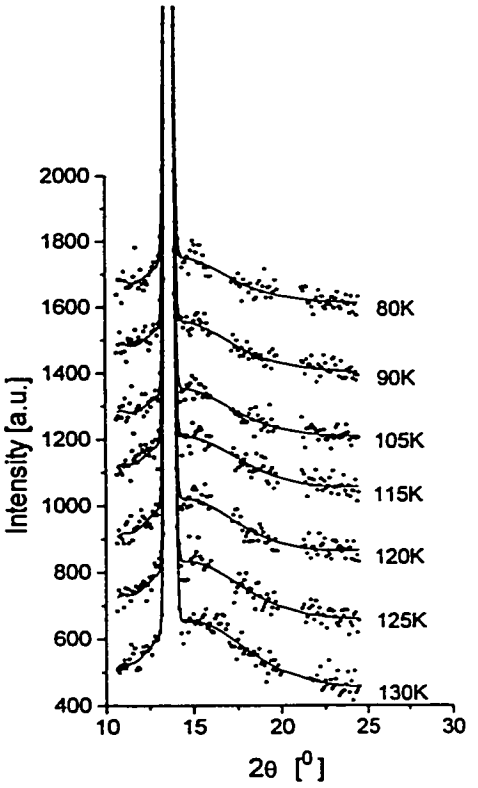

FIG. 5. Powder neutron diffraction data. Two-dimensional magnetic short-range order. The symbols are experimental data and the solid lines represent fits to a Warren line shape.

Refinement of the Magnetic Structure

All neutron diffraction refinements were done for three phases, namely the crystallographic structure for $ScMnO_3$, the magnetic structure for $ScMnO_3$, and Mn_3O_4 as a minor impurity phase. When refining the neutron powder diffraction data sets for various temperatures, 15 parameters were refined including the unit cell parameters, the zero point, the scale factors, the magnetic moments, and six background parameters.

The data were collected over a 2θ-range from 10° to 90°. The orientation of the magnetic moments is strongly correlated to the intensity ratio of the $(100)_{mag}$ and the $(101)_{mag}$ reflections as was shown with neutron powder pattern simulations. Due to the presence of Mn_3O_4 the $(100)_{mag}$ peak is broadened at low temperature. Refinements were carried out using different strategies. In one case the refinement was carried out at 70 K and for all remaining data sets the peak shape parameters were held constant. During an alternative refinement procedure the $(100)_{mag}$ peak was excluded from the refinements. Between 10 and 70 K the same results were found for both procedures, but at higher temperatures the orientations for the magnetic moments differed such that the first procedure resulted in smaller angles, ϕ. This is caused by the broad background underneath the $(100)_{mag}$ and $(101)_{mag}$ peak which could not be modeled properly. This problem is illustrated in Fig. 6 where the calculated profile includes a small peak at the $(100)_{mag}$ position when none is present in the data. For the above-mentioned reasons the $(100)_{mag}$ peak was excluded from the Rietveld refinements. Below 35 K the region $23° < 2\theta < 24°$ is excluded from the refinements, because of the presence of a magnetic peak due to Mn_3O_4 which is negligible above 30 K.

Initially, a 120° spin arrangement was assumed with the moments lying in the a–b plane, using space group $P1$ and a 120° rotation matrix. Figure 7 shows the initial model for the magnetic moments and the definition of the spin orientation ϕ. Powder neutron diffraction patterns of the magnetic phase were simulated assuming out-of-plane spin canting angles of 5° and 10°; the resulting patterns are too

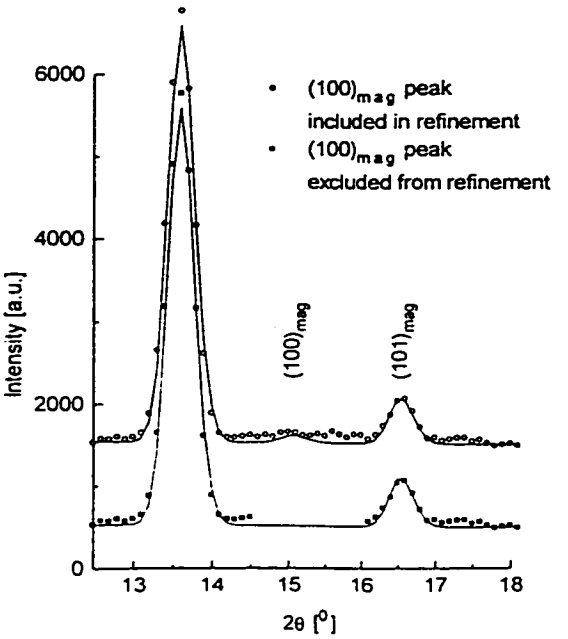

FIG. 6. Neutron powder diffraction patterns for $ScMnO_3$ at 120 K. Illustration of incorrect fitting of $(100)_{mag}$ peak as a consequence of the broad background present.

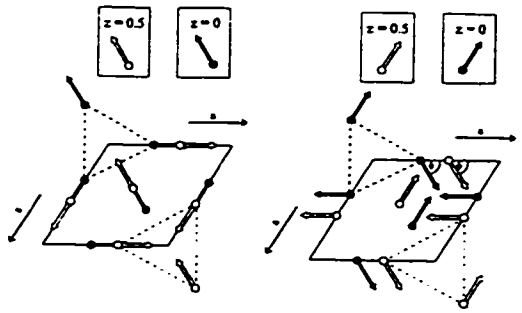

FIG. 7. Description of the magnetic structure of $ScMnO_3$ at two different temperatures; (right) low-temperature form and (left) high-temperature form. The 120° constraint is retained after reorientation of the magnetic moments in the basal plane. Only the Mn^{3+} positions are shown.

similar to the noncanted case to be distinguished by powder neutron diffraction techniques. Nonetheless, magnetic susceptibility data indicate weak ferromagnetism and support the presence of spin canting. Consequently, the neutron powder refinements were carried out assuming no canting of the spins.

For several temperatures the refined powder neutron diffraction data are shown in Fig. 8, and Table 3 shows the results for all refinements. The results for the orientations and magnitudes of the magnetic moments in $ScMnO_3$ are shown in Fig. 9. At 10 K the magnetic moments are almost aligned with the a-axis, i.e., $\phi = 15(3)°$, at 40 K the spins start to reorient simultaneously in the a–b plane. At 70 K the reorientation reaches an angle of $\phi = 80(9)°$, and therefore the spins are oriented almost perpendicularly with respect to the low-temperature case. The reorientation process occurs between 50 and 70 K, which is in agreement with the broad feature at 58 K for the magnetic susceptibility. The magnitude of the magnetic moment at 10 K is 3.40(7) μ_B and decreases rapidly above 90 K. Upon warming the sample, the unit cell parameter a increases, whereas the c-axis remains constant between 10 and 130 K (Fig. 10). The crystallographic structure of $ScMnO_3$ does not change

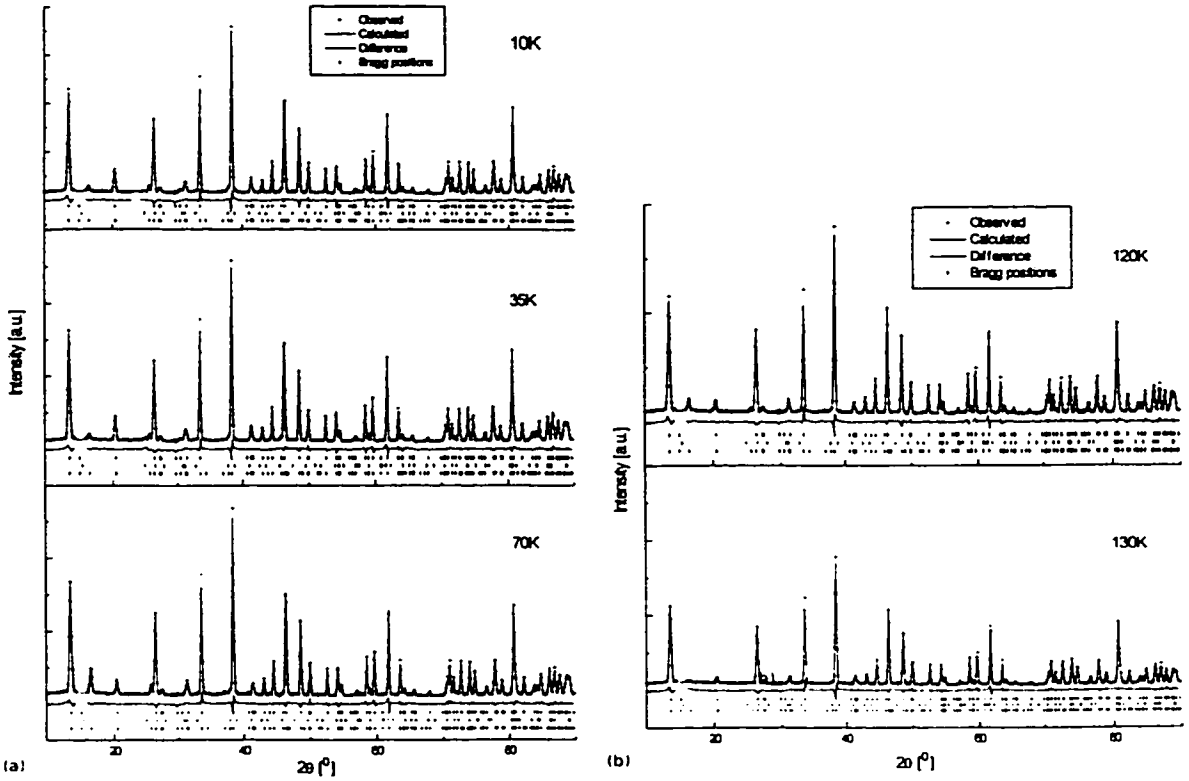

FIG. 8. Refined neutron powder diffraction patterns for (a) T = 10, 35 and 70 K and (b) T = 120 and 130 K. For all graphs the tick marks at the top refer to the crystallographic structure of $ScMnO_3$, in the middle to Mn_3O_4, and at the bottom to the magnetic structure of $ScMnO_3$.

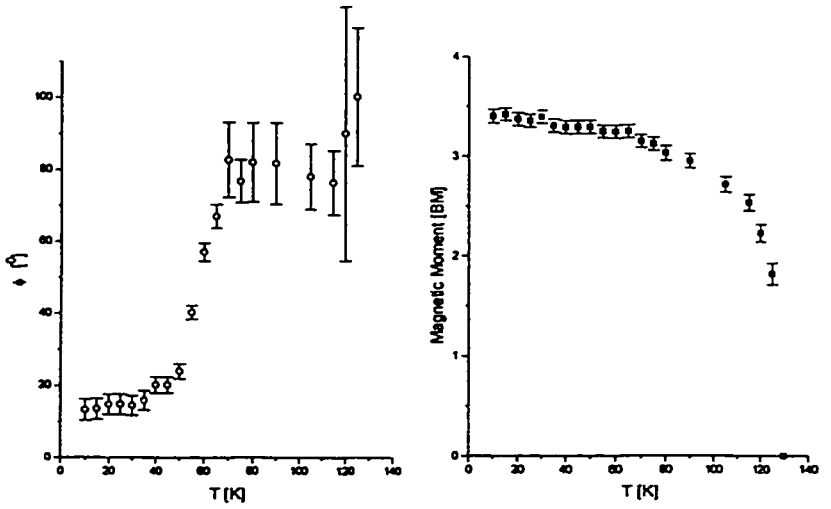

FIG. 9. The left figure shows the reorientation of the magnetic moments of Mn^{3+} in $ScMnO_3$ in the basal plane as a function of the temperature. The right figure shows the temperature dependence of the magnitude of the magnetic moment.

as a function of temperature as confirmed by carrying out full refinements at various temperatures.

CONCLUSIONS

Magnetic measurements carried out on $ScMnO_3$ over a wide temperature range, 5–600 K, show the presence of strong antiferromagnetic exchange, $\theta_c = -943(7)$ K, and three transitions, one at 130 K, a second, broad transition at 58 K, and a maximum at 40 K. Neutron diffraction experiments confirm that the 130 K transition represents the Néel temperature below which a 120° magnetic structure is found. This result is consistent with previous work on isostructural $LnMnO_3$ phases, Ln = Ho–Lu. The 120° structure arises due to the frustration inherent in the layered triangular Mn^{3+} sublattice and the very strong antiferromagnetic exchange already noted. The transition at 58 K is revealed by neutron diffraction to involve a spin reorientation of the moments within the a–b plane. At 10 K the Mn^{3+} spins are almost parallel to the a–a crystallographic axes but at 50 K they begin to reorient to an angle of 80 with respect to the a-axes which is complete at 70 K. This is similar to the behavior of $HoMnO_3$. Koehler *et al.* (2) reported a 120° structure for the magnetic moments in $ScMnO_3$, and an angle $\phi = 24°$ at 4.2 K, however, no temperature dependence of ϕ has been reported since.

The two-dimensional magnetic short-range order between 80 and 130 K can be described with a nearly temperature-independent correlation length of 13(2) Å.

The origin of the weak ferromagnetism and the maximum at 40 K in the ZFC magnetic susceptibility data mentioned earlier could be due to out-of-plane spin canting

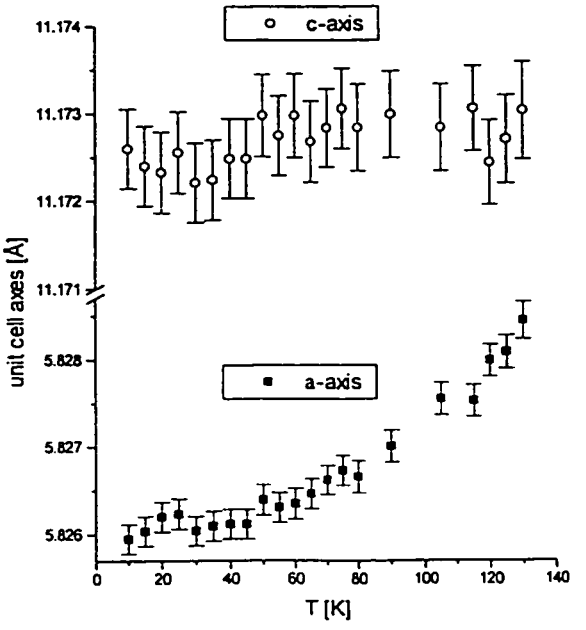

FIG. 10. Unit cell axes lengths for $ScMnO_3$ as a function of temperature

TABLE 3
Three Phase Neutron Powder Diffraction Refinement for $ScMnO_3$ at Low Temperatures

T [K]	M [μ_B]	ϕ [°]	Magnetic-R[a]	R_p[b]	R_{wp}[c]
10	3.40(7)	12(3)	12.8	5.16	6.67
15	3.40(7)	13(3)	13.3	5.32	6.71
20	3.36(7)	14(3)	11.2	5.23	6.76
25	3.34(7)	14(3)	13.0	5.26	6.78
30	3.39(7)	14(3)	12.3	5.20	6.64
35	3.28(7)	15(3)	13.7	5.21	6.65
40	3.29(7)	20(2)	12.6	5.20	6.63
45	3.29(7)	20(2)	12.6	5.20	6.63
50	3.27(7)	23(2)	13.7	5.43	6.90
55	3.23(7)	40(2)	11.9	5.28	6.67
60	3.23(7)	57(3)	12.8	5.42	6.95
65	3.23(7)	67(4)	11.7	5.24	6.75
70	3.14(7)	82(9)	11.2	5.00	6.44
75	3.11(7)	77(6)	13.1	5.22	6.60
80	3.01(8)	82(12)	12.4	5.66	7.14
90	2.93(8)	82(13)	16.0	5.55	7.12
105	2.69(8)	78(10)	13.6	5.55	7.08
115	2.51(9)	76(10)	18.9	5.55	6.97
120	2.20(10)	92(37)	19.5	5.51	7.00
125	1.81(12)	100(19)	30.9	5.66	7.17
130				6.07	7.59

[a] $\text{Magnetic} - R = 100 \dfrac{\sum_k |I_{ok} - I_{ck}|}{\sum_k |I_{ok}|}$.

[b] $R_p = 100 \dfrac{\sum_i |y_i - y_{ci}|}{\sum_i |y_i|}$.

[c] $R_{wp} = 100 \sqrt{\dfrac{\sum_i w_i [y_i - y_{ci}]^2}{\sum_i w_i y_i^2}}$.

and was predicted by Kawamura for a layered triangular lattice (9).

A more detailed study would require large single crystals in order to perform neutron diffraction experiments and to investigate possible spin canting in $ScMnO_3$. Unfortunately, the crystal growth showed only a very slow growing rate along the c-direction, resulting in extremely thin crystals (5 μm). Slower cooling during the crystal growth resulted only in crystals with larger dimensions in the a–b plane. Therefore, the spin canting problem cannot be solved in the near future.

ACKNOWLEDGMENTS

We thank N. P. Raju for assistance with the SQUID magnetometer and H. Dabkowska for helpful discussions. M. Bieringer is grateful for financial support from the "Deutscher Akademischer Austauschdienst". J. E. Greedan acknowledges support from the Natural Sciences and Engineering Research Council of Canada.

REFERENCES

1. H. L. Yakel, W. C. Koehler, E. F. Bertaut, and E. F. Forrat, *Acta. Crystallogr.* 16, 957–962 (1963).
2. W. C. Koehler, H. L. Yakel, E. O. Wollan, and J. W. Cable, *Phys. Lett.* 9(2), 93–95 (1964).
3. Rolf Norrestam, *Acta Chem. Scand.* 19, 1009–1010 (1965).
4. J. E. Greedan, M. Bieringer, J. F. Britten, D. M. Giaquinta, and H.-C. zur Loye, *J. Solid State Chem.* 116, 118–130 (1995).
5. H. W. Xu, J. Iwasaki, T. Shimizu, H. Satoh, and N. Kamegashira, *J. Alloys Compounds* 221, 274–279 (1995).
6. B. Boucher, R. Buhl, and M. Perrin, *J. Phys. Chem. Solids*, 32, 2429–2437 (1971).
7. Juan Rodriguez-Carvajal, "Fullprof Manual version 3.5."
8. B.E. Warren, *Phys. Rec.* 59, 693 (1941).
9. Hikaru Kawamura, *J. Phys. Soc. Jpn.* 54(9), 3220–3223 (1985).

3.5 $Lu_xSc_{(1-x)}MnO_3$

3.5.1 Unit Cell Constants for $Lu_xSc_{(1-x)}MnO_3$

For all samples of the series $Lu_xSc_{(1-x)}MnO_3$ Guinier x-ray diffraction patterns were taken in order to determine the phase purity and in particular to investigate the unit cell constant evolution as a function of the composition. The room temperature unit cell constants a and c are presented in figure 3.6. In particular

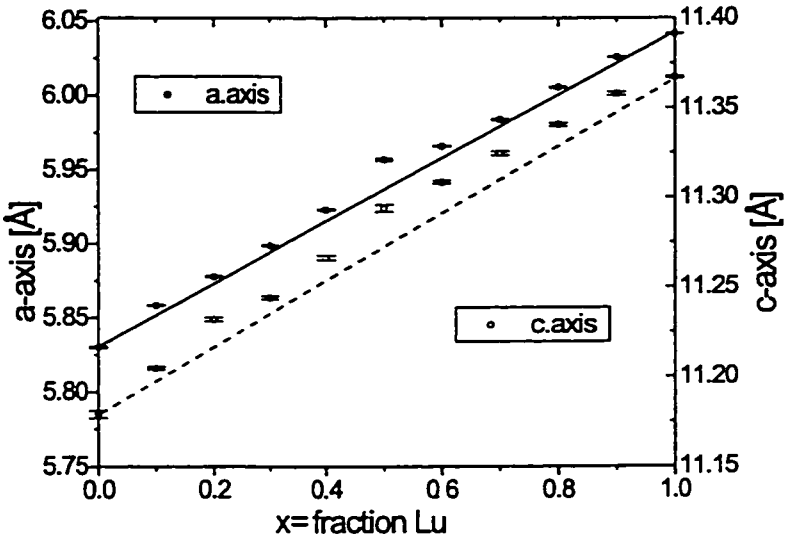

Figure 3.6: Unit cell constants for the series $Lu_xSc_{(1-x)}MnO_3$ determined using the Guinier x-ray camera, λ=1.540598Å. The unit cell constants for the end members are connnected with straight lines emphasizing the deviations from linearity.

the c-axis parameters show a non-linear behaviour as a function of x, whereas the a-axis constants show a much smaller deviation from linearity. Impurities were not detected by means of powder x-ray diffraction techniques.

3.5.2 Neutron Diffraction for $Lu_xSc_{(1-x)}MnO_3$ at Low Temperature

The low temperature neutron powder diffraction data obtained with diffractometer C2 have been analyzed using the Rietveld refinement program FullProf [RC98]. No crystallographic transitions are observed upon cooling. Table 3.3 summarizes the atomic positions for Mn^{3+} and the total agreement factors R_p and R_{wp} for 3 different samples measured at different temperatures. Figure 3.7 shows a refined neutron diffraction data set for $LuMnO_3$ at 4K. Between 28 and 30 pa-

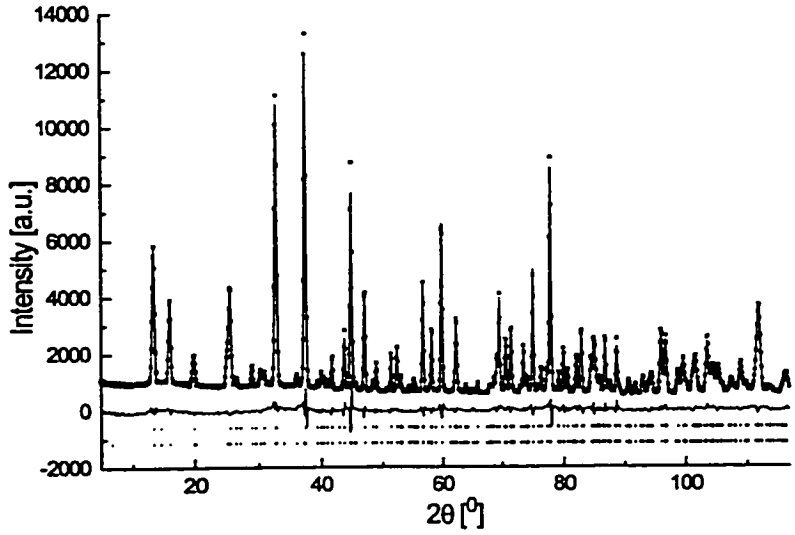

Figure 3.7: Neutron powder diffraction refinement for $LuMnO_3$ at T=4K, λ = 1.328591(48)Å. The stars are experimental data, the best fit and difference are shown as solid lines. The upper tick marks correspond to the crystallographic phase the lower tick marks correspond to the magnetic phase.

rameters were refined for each powder neutron diffraction pattern. The refinements include 6 background coefficients, the zero shift parameter, scale factor, unit cell

Table 3.3: Mn^{3+} x-parameters and agreement factors for neutron powder diffraction refinements for $Lu_xSc_{(1-x)}MnO_3$.

	x=1.0			x=0.9			x=0.8		
T[K]	x(Mn)	R_p	R_{wp}	x(Mn)	R_p	R_{wp}	x(Mn)	R_p	R_{wp}
4	0.336(2)	4.40	5.75	0.339(2)	3.16	4.13	0.336(3)	6.02	7.98
20	0.338(2)	4.21	5.60	0.338(2)	3.29	4.25	0.337(3)	5.97	7.99
50	0.337(2)	4.31	5.68	0.338(2)	3.26	4.23	0.337(3)	6.04	8.03
80	0.337(3)	4.58	5.92	0.338(3)	3.40	4.43	0.333(3)	6.14	8.06
120	0.331(3)	4.14	5.40	0.330(3)	3.38	4.37	0.330(3)	6.20	8.07

constants, all atomic positions and isotropic temperature factors, peak shape parameters, asymmetry parameters and magnetic moments where applicable [3]. Table 3.3 shows that the Mn^{3+} positions are within experimental uncertainty of x=1/3 for all three samples for all temperatures studied. Consequently, the distortion of the magnetic sublattice from that of essentially perfect equilateral triangular topology can be ruled out as the origin for the onset of a spin-reorientation transition found for the Sc^{3+}-containing members of the $Lu_xSc_{(1-x)}MnO_3$ series.

3.6 Bulk Magnetic Properties

Bulk magnetic measurements were carried out using a Quantum Design SQUID magnetometer. Covering the temperature range 5K to 600K magnetic susceptibility measurements were performed using a magnetic field strength of 0.05T. The Néel temperatures for the solid solution were extracted and hysteresis behaviour was investigated. Figure 3.8 shows the magnetic susceptibility for $ScMnO_3$ as a function of the temperature. The sample was cooled in the absence of the magnetic field and data (ZFC) were collected while warming up. The field cooled (FC) data were

[3]No magnetic phase was used for the refinements for the 120K data sets.

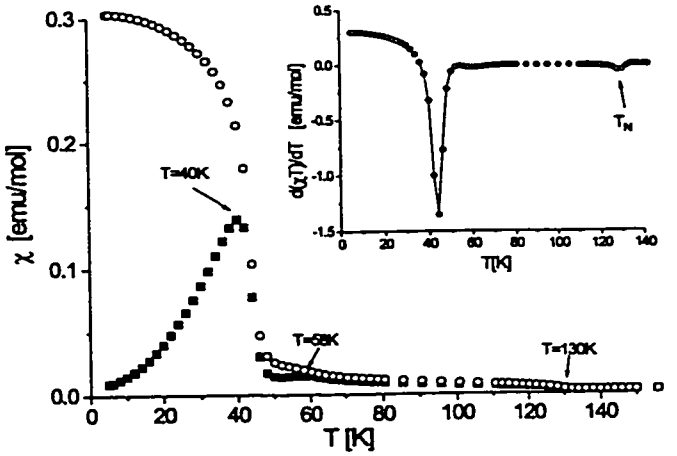

Figure 3.8: Magnetic susceptibility data for $ScMnO_3$ (H=0.05T). The solid squares represent the zero field cooled (ZFC) data and the open circles are the field cooled (FC) data. The inset shows the derivative $\frac{\partial(\chi T)}{\partial T}$.

recorded after cooling the sample in the presence of the magnetic field (H=0.05T). Any deviations between the two traces indicate hysteresis behaviour and the presence of cooperative magnetism. The inflection point at 130K is due to magnetic long range ordering. The exact Néel temperature is determined according to Fisher [Fis62] by taking the numerical derivative according to equation 3.6.1.

$$C_M(T) = A \frac{\partial}{\partial T} (\chi(T)T) \tag{3.6.1}$$

The broad maximum on the χ versus T plot at approximately 58K coincides with a magnetic transition. Only $ScMnO_3$ shows this maximum, which will be discussed in section 3.8. The intense maximum at approximately 40K is due to spin canting and will be dealt with in section 3.13. In general the divergence of ZFC and FC data indicates the presence of a ferromagnetic component, which is observable just below the Néel temperature. The transition can be located using equation 3.6.1. The

derivative gives a transition temperature of 44K. It is noteworthy, that the magnetic ordering temperature of the ferrimagnet Mn_3O_4 is T_C=41K [JN74]. However, the maximum seen at 44K for $ScMnO_3$ is not related to the possible presence of Mn_3O_4. Samples which were prepared with excess Sc_2O_3 showed the same maximum in the χ versus T curves at approximately 44K as samples with excess of Mn_2O_3. The presence of Mn_3O_4 was confirmed from powder diffraction experiments for the Mn-excess sample. Whereas the Mn-deficient samples did not show any evidence of Mn_3O_4. Furthermore, single crystals of $ScMnO_3$ showed the same maximum at approximately 44K.

3.6.1 Evolution of the Néel temperatures

Figure 3.9 shows the evolution of the Néel temperatures for $Lu_xSc_{(1-x)}MnO_3$ as a function of x. The Néel temperatures were determined from magnetic susceptibility measurements using equation 3.6.1. The gradual evolution of the Néel temperatures suggests that the magnetic coupling constants change gradually as the Lu-Sc substitution is carried out. Fundamental changes in the exchange paths or significant changes of the topology of the magnetic sublattice are not expected. The Néel temperatures show a downward curvature as a function of the composition. This is consistent with the upward curvature for the c-axis parameter as a function of x noted earlier (see figure 3.6). The Néel temperature should be correlated with the interplanar superexchange pathways which will in turn correlate with the c-axis parameter.

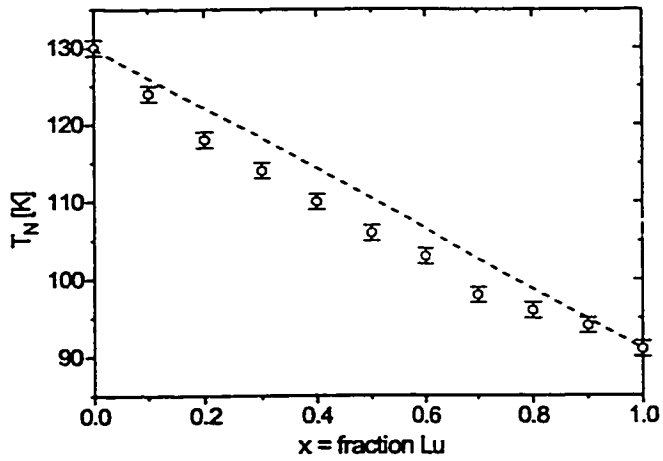

Figure 3.9: Presentation of the Néel temperatures as a function of the composition x in $Lu_xSc_{(1-x)}MnO_3$. The dashed line serves as a reference in order to emphasize the downward curvature. These data are compiled in table 3.4.

3.6.2 Hysteresis Behaviour for $Lu_xSc_{(1-x)}MnO_3$

Figure 3.10 shows the magnetic susceptibilities for several members of the series $Lu_xSc_{(1-x)}MnO_3$. The features are much less pronounced for the Lu^{3+}-rich compounds. Note the gradual increase for the low temperature susceptibilities as the Sc-content increases. At T=5K $ScMnO_3$ shows a 6-times larger magnetic susceptibility for the field cooled data than $Lu_{0.5}Sc_{0.5}MnO_3$ (compare figures 3.8 and 3.10). Furthermore, the initial divergence just below T_N is larger for the Sc-rich forms. The divergence indicates a ferromagnetic component, which might be due to spin-canting. The perfectly planar 120° spin structure does not allow for a ferromagnetic net moment, however a small magnetic component along the z-direction could create this moment.

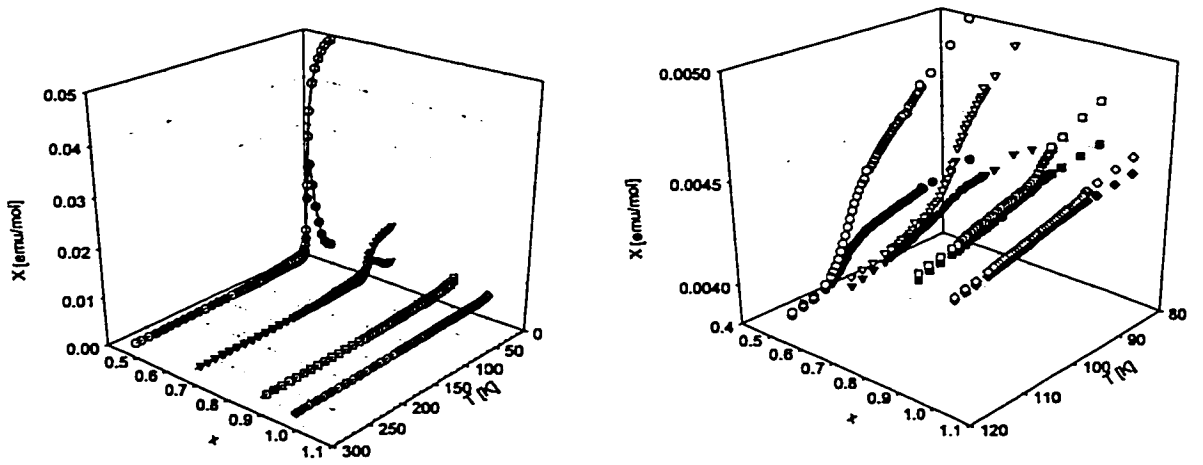

Figure 3.10: Magnetic susceptibility data for $Lu_xSc_{(1-x)}MnO_3$ (x=1.0, 0.9, 0.7 and 0.5). The left image shows the temperature range 0K to 300K, whereas the right graph shows the same data with more detail in the temperature range 80K to 120K. The zero field cooled data are shown as solid symbols and the field cooled data as open symbols. Obviously the degree of divergence increases as the Sc^{3+} content is increased.

3.6.3 Curie-Weiss Regime

For the temperature range ≈400K to ≈600K the χ^{-1} versus T data were fitted to equation 3.6.2.

$$\chi = \frac{C}{T - \theta} \tag{3.6.2}$$

In the above C is the Curie constant and θ is the Weiss temperature. The assumptions and limitations of the Curie-Weiss law are presented in the introduction on page 3. The Curie-Weiss plots can be found in Appendix B (page 190). The effective magnetic moments μ_{eff} and Weiss temperatures θ for $Lu_xSc_{(1-x)}MnO_3$ are summarized in table 3.4. Despite some scattering, the Weiss temperatures, θ, scale with the composition, x. All effective magnetic moments are very close to the expected effective magnetic moment for spin only Mn^{3+} (S=2), $\mu_{eff}(S.O.)= 4.90\mu_B$.

Table 3.4: Effective magnetic moments and Weiss temperatures obtained from Curie-Weiss fits (equation 3.6.2) for the series $Lu_xSc_{(1-x)}MnO_3$. The Néel temperatures were determined from low temperature bulk magnetic measurements.

x	:	μ_{eff} [μ_B]	θ [K]	T_N [K]	θ/T_N
1.0	:	4.76(4)	-552(13)	91	-6.1
0.9	:	4.95(6)	-560(24)	94	-6.0
0.8	:	4.93(6)	-537(21)	99	-5.5
0.6	:	5.01(6)	-757(15)	103	-7.3
0.5	:	4.95(7)	-787(10)	106	-7.4
0.4	:	4.82(6)	-825(16)	110	-7.5
0.2	:	4.82(5)	-919(16)	118	-7.8
0.0	:	4.78(4)	-943(7)	129	-7.3

The largely negative Weiss temperatures indicate strong antiferromagnetic coupling between Mn^{3+} ions, while the large ratios θ/T_N indicate severe magnetic frustration. Furthermore, the more negative Weiss temperatures for the Sc-rich compounds agree with the stronger antiferromagnetic coupling constants as the Mn^{3+}-Mn^{3+} distances decrease.

3.7 Magnetic Ordering

3.7.1 $ScMnO_3$ versus $LuMnO_3$

All members of the series $AMnO_3$ show magnetic long range order. The ground state is described as a 120° structure, resulting in a net magnetic moment of zero per triangle. All spins are constrained to the ab-plane. Figure 3.11 shows the 120° structure and defines the magnetic moment orientation, ϕ. However, a small vector component along the c-axis due to spin canting can not be ruled out. Neutron diffraction experiments showed a spin-reorientation transition for $ScMnO_3$

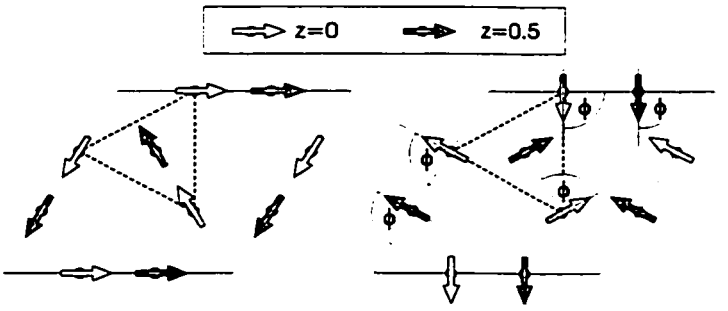

Figure 3.11: Illustration of the 120°structure and definition of the magnetic moment orientation ϕ. The left figure shows ϕ=0°, the right figure shows ϕ=90°.

at approximately 60K. The temperature of the reorientation process spans approximately 20K [BG99]. In contrast no spin-reorientation transition was reported for $LuMnO_3$ [KWYC64] and no spin-reorientation was found in this study. This difference is surprising when considering the structural similarities for $ScMnO_3$ and $LuMnO_3$. The only obvious differences between the above mentioned compounds are the lattice parameters and the less distorted Mn-O_5 polyhedron for $ScMnO_3$. Sc^{3+} is significantly smaller than Lu^{3+} thus causing smaller unit cell constants.

The following section presents the investigation of the magnetic structures for the series $Lu_xSc_{(1-x)}MnO_3$. Powder neutron diffraction experiments were carried out using the high resolution diffractometer, C2, at Chalk River and low resolution diffractometer, D1B, at ILL in Grenoble.

3.8 The Spin-Reorientation Transition

3.8.1 Magnetic Structure of $LuMnO_3$

Powder neutron diffraction experiments show the onset of magnetic Bragg peaks below 94K. This finding is in agreement with the Néel temperature of T_N=91K

as determined from dc-magnetic susceptibility data and the earlier reported ordering temperature of 91K [KWYC64]. The magnetic moment develops smoothly as the temperature is decreased and reaches a maximum value of 3.4BM. The relative intensities of the magnetic Bragg peaks do not change as a function of temperature, thus indicating that the magnetic structure does not undergo any changes. Figure 3.12 shows the neutron diffraction patterns collected on diffractometer D1B at ILL (Grenoble) using a wavelength of λ=2.5248(6)Å. For each data set the magnetic

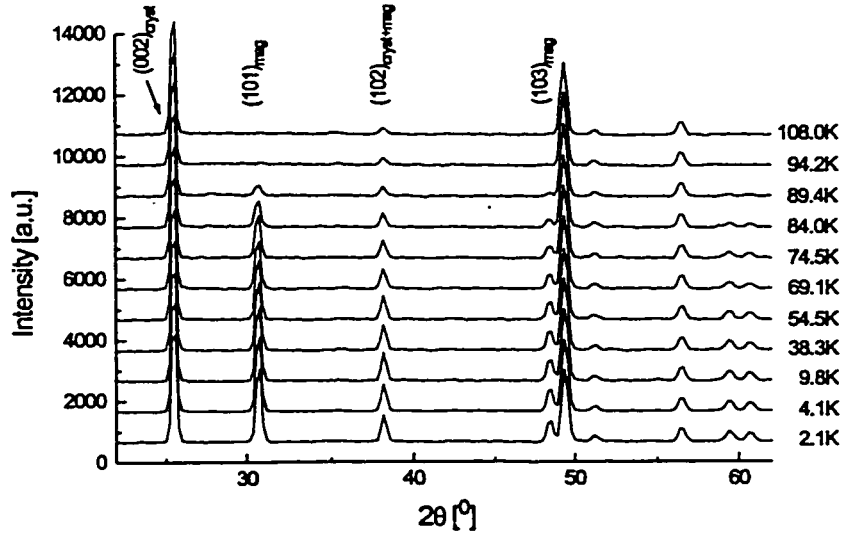

Figure 3.12: Neutron powder diffraction data for $LuMnO_3$ (λ=2.5248(6)Å).

structure was refined using FullProf [RC98]. The resolution and 2θ-range of D1B are not sufficient to permit simultaneous refinement of crystal and magnetic structures. Therefore, crystal structure models obtained from refinements of high resolution data at 4K, 20K, 50K, 80K and 120K were assumed and not refined. In any case the positional parameters do not change significantly with temperature. The magnetic structures obtained from the limited number of high resolution data sets were

not significantly different from those found using the D1B data sets. Figure 3.13 shows the evolution of the magnetic moments as a function of temperature. For

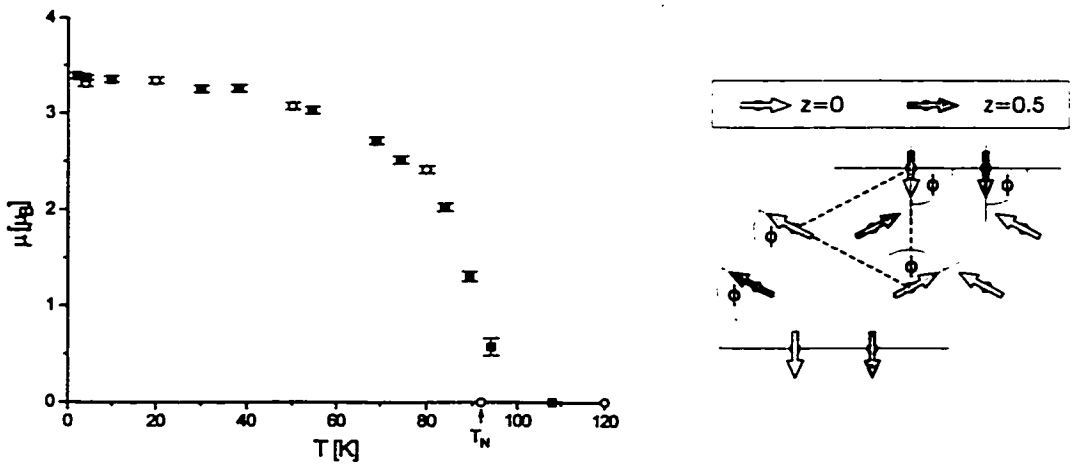

Figure 3.13: left: Evolution of the magnetic moments as determined from Rietveld refinements of the magnetic phase in $LuMnO_3$. Open circles correspond to high resolution data collected on C2, the solid squares correspond to diffractometer D1B. right: Representation of the magnetic structure of $LuMnO_3$ between T=2.1K and T_N=91K, where ϕ is 90°.

$LuMnO_3$ the magnetic moment orientation was not refined but was set to an angle ϕ=90°. This is a valid procedure, since the $(100)_{mag}$ reflection showed a zero intensity, which is only consistent with ϕ=90° and 270°. The orientation of the magnetic moments is in contrast to the value of ϕ=55° (at T =4.2K) reported by Koehler [KWYC64]. The correctness of ϕ=90° is confirmed by two independent neutron diffraction experiments in conjunction with the refinement of a reasonable crystal structure. Furthermore, the evolution of ϕ for the solid solution $Lu_xSc_{(1-x)}MnO_3$ supports our value. The crystal structure of our sample was refined to a high level of precision, whereas earlier reports considered only the room temperature structure

and used different samples for structural studies [YKBF63] and magnetic investigations [KWYC64].

3.8.2 Magnetic Structure of $Lu_{0.9}Sc_{0.1}MnO_3$

The magnetic structure of $Lu_{0.9}Sc_{0.1}MnO_3$ was investigated using the powder diffractometer D1B at ILL (λ=2.5248(6)Å), and the higher resolution data diffractometer C2 at Chalk River (λ=1.328591(48)Å). Figure 3.14 shows the neutron diffraction patterns as a function of the temperature. At low temperatures the

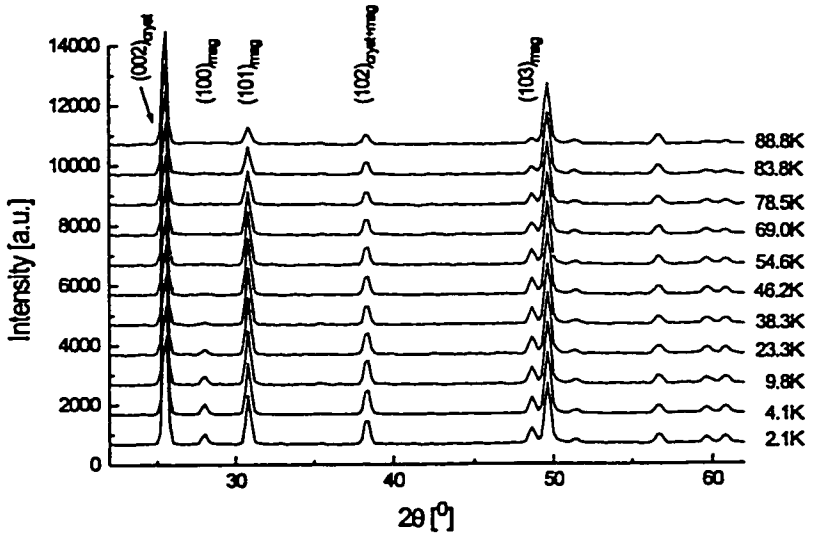

Figure 3.14: Powder neutron diffraction patterns for $Lu_{0.9}Sc_{0.1}MnO_3$, collected on instrument D1B at ILL (λ=2.5248(6)Å). Note the presence of the $(100)_{mag}$ reflection at low temperature.

magnetic $(100)_{mag}$ reflection has a non-zero intensity, thus indicating a different magnetic moment orientation than for $LuMnO_3$ where this peak has zero intensity. The temperature dependence is remarkable, as upon warming the $(100)_{mag}$ reflection disappears at 46K and for higher temperatures the diffraction patterns resemble

those for $LuMnO_3$. Therefore, above 46K, the magnetic structure is similar to that of $LuMnO_3$. As an example the refined data set for T=38.3K is shown in figure 3.15. The C2 data sets were particularly important in determining the crystallographic

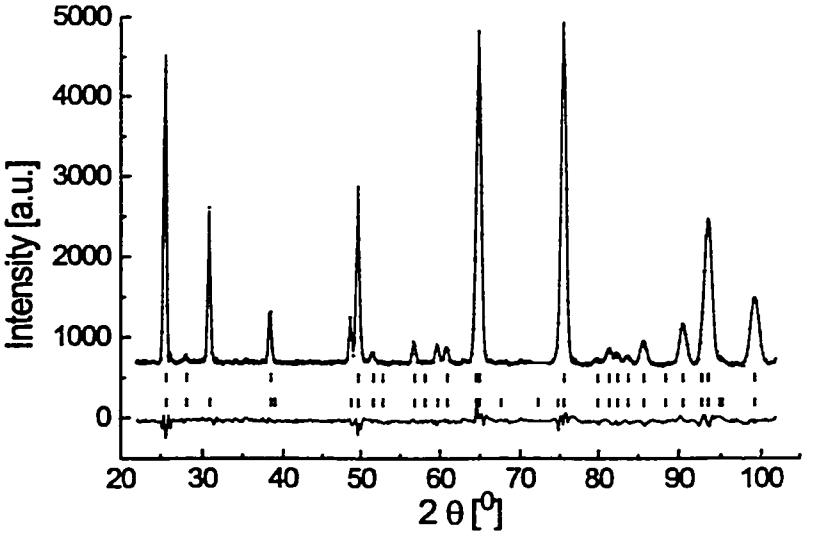

Figure 3.15: Refined powder neutron diffraction data set for $Lu_{0.9}Sc_{0.1}MnO_3$ at T=38.3K (λ=2.5248(6)Å). The stars represent the observed data, the best fit is shown as a solid line and the difference is shown as a line below the pattern. The tick marks indicate the Bragg positions, where the upper marks correspond to the crystallographic phase and the lower marks indicate the magnetic phase. The region 71-73° is excluded due to an instrumental artifact.

structure of $Lu_{0.9}Sc_{0.1}MnO_3$ as a function of temperature and do not indicate any structural change below the Néel temperature. The two phase refinements were carried out using FullProf. The temperature variation of the magnetic moment magnitude and orientation are shown in figure 3.16. The refinements clearly show the spin-reorientation to occur at temperatures below 46K. The magnetic moments have an effective orientation of ϕ=60° at 2.1K and reach the ϕ=90° limit at approximately T=46K. The orientation of the magnetic moments was fixed to 90° for all

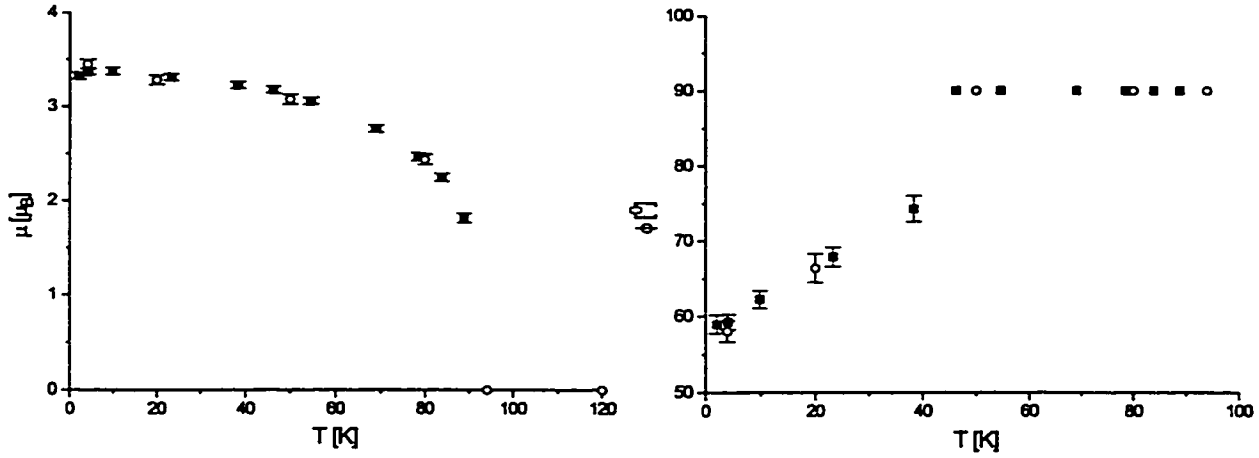

Figure 3.16: left: Evolution of the magnetic moments as determined from Rietveld refinements of the magnetic phase in $Lu_{0.9}Sc_{0.1}MnO_3$. Open circles correspond to high resolution data obtained on C2, the solid squares correspond to data sets from diffractometer D1B. right: Orientation of the magnetic moments as a function of the temperature for $Lu_{0.9}Sc_{0.1}MnO_3$.

data sets above 46K, since the $(100)_{mag}$ reflection was absent. The magnitude of the magnetic moment evolves smoothly as a function of temperature and with no anomaly at the spin-reorientation transition. The disappearance of the magnetic Bragg peaks above 89K is in agreement with the Néel temperature T_N=94K.

3.8.3 Magnetic Structure of $Lu_{0.8}Sc_{0.2}MnO_3$

Neutron powder diffraction data for $Lu_{0.8}Sc_{0.2}MnO_3$ were collected on C2 using wavelengths of λ=1.328591(48)Å (for high resolution) and λ=2.37101(11)Å for monitoring the thermal evolution of the magnetic structure. As for the case of $Lu_{0.9}Sc_{0.1}MnO_3$ an intensity variation of the $(100)_{mag}$ and the $(101)_{mag}$ Bragg peaks was observed at low temperatures, figure 3.17. However, the present sample

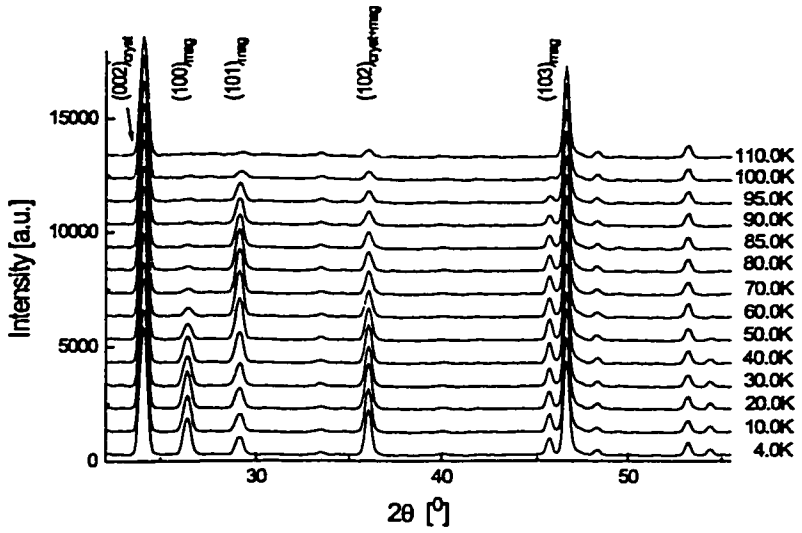

Figure 3.17: Powder neutron diffraction patterns for $Lu_{0.8}Sc_{0.2}MnO_3$, collected on instrument C2 at Chalk River (λ=2.37101(11)Å). Note the presence of the $(100)_{mag}$ reflection at low temperature.

which is richer in Sc^{3+} shows more variation, indicating that the associated spin-reorientation transition covers a larger angular range. The magnetic structures were refined assuming a crystallographic model obtained as described in the previous section. The results of the refinements for $Lu_{0.8}Sc_{0.2}MnO_3$ are summarized in figure 3.18, which shows the evolution of the magnetic moment magnitude and its orientation as a function of the temperature. Again, the moment variation is smooth as for $LuMnO_3$ and $Lu_{0.9}Sc_{0.1}MnO_3$ inspite of the spin-reorientation. This transition spans the ϕ-range from 20° to 70° over a temperature interval of approximately 60K, these results are very similar to those for pure $ScMnO_3$ in terms of $\Delta\phi$ with a slightly broader ΔT.

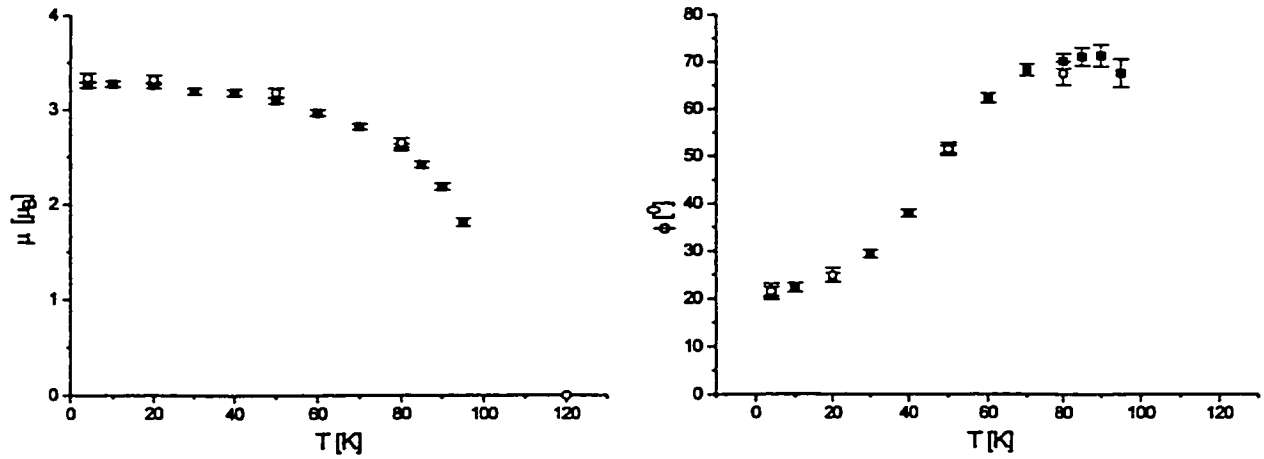

Figure 3.18: left: Evolution of the magnetic moment magnitude as determined from Rietveld refinements of the magnetic phase in $Lu_{0.8}Sc_{0.2}MnO_3$. Open circles correspond to high resolution data λ=1.328591(48)Å, the solid squares correspond to data collected with λ=2.37101(11)Å. right: Orientation of the magnetic moments as a function of the temperature for $Lu_{0.8}Sc_{0.2}MnO_3$.

3.8.4 Magnetic Structures of $Lu_xSc_{(1-x)}MnO_3$ x=0.4 and 0.2

The magnetic structures of the solid solution $Lu_xSc_{(1-x)}MnO_3$ with the compositions x=0.4, 0.8, 0.9 and 1.0 were determined from low temperature powder neutron diffraction data. The magnetic phases were refined according to the crystallographic models investigated earlier. The evolution of the magnetic moment magnitude is identical for all samples and will not be presented again. However, the magnetic moment reorientations differ slightly as a function of x. Figure 3.19 compares the orientation of the magnetic moments of different compositions on a common temperature scale. In summary, $LuMnO_3$ does not show any spin-reorientation transition, whereas $Lu_{0.9}Sc_{0.1}MnO_3$ shows a very limited ϕ range for the reorientation process. As the Sc^{3+} content is increased the spin-reorientation

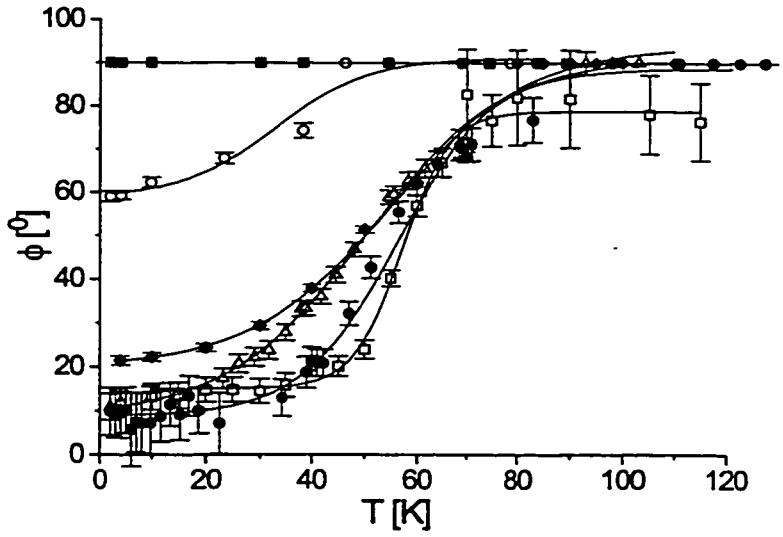

Figure 3.19: Orientation of the magnetic moments as a function of the temperature for $Lu_xSc_{(1-x)}MnO_3$. Where the different x-values are presented using the following symbols ■=1.0, ○=0.9, ♦=0.8, △=0.4, ●=0.2, □=0.0, the lines are only to guide the eye.

process covers almost 90° and sharpens with respect to the temperature dependence. $ScMnO_3$ shows a spin-reorientation transition which is completed within 20K, whereas the spin-reorientation for composition x=0.8 occurs over almost 60K. The lower temperature for the spin-reorientation transition as well as the fact that the transition is broadened can explain that no maximum in the χ versus T data is observed. Only the sharpest transition for $ScMnO_3$ shows a weak maximum at T=58K. All Sc^{3+} containing samples show an in-plane spin-reorientation transition and the variable temperature range of this transition can be rationalized in terms of A-cation disorder. The smaller ϕ angle for the Lu-rich samples can be explained with a two phase model, which will be presented in section 3.12.1.

3.9 Critical Exponents

The critical exponent β can be determined from neutron diffraction experiments. Knowing the magnetic moments from the refined magnetic structures, these can be correlated with the reduced temperature $t = (T_N - T)/T_N$ using equation 3.9.1,

$$M = A \left(\frac{T_N - T}{T_N}\right)^{\beta} \tag{3.9.1}$$

where β is the critical exponent and A is a scaling factor. On a $\log(M)$ versus $\log(-t)$ plot the slope in the vicinity of the critical temperature represents the exponent β (equation 3.9.2).

$$\log(M) = log(A) + \beta \log\left(\frac{T_N - T}{T_N}\right) \tag{3.9.2}$$

Figure 3.20 shows the fit of equation 3.9.1 to magnetic moments determined from neutron diffraction studies. The resulting critical exponents β for 6 samples are summarized in table 3.5. Gaulin [Gau94] pointed out the strong correlation between the Néel temperature and the exponent β. Ideally, a large number of temperatures should be measured close to the ordering temperature, such that the data density increases as the Néel temperature is approached, thus allowing the fitting of several decades in reduced temperature. However, the number of data points for the experiments presented in this section is too limited, due to limited experimental time, such that the Néel temperatures were not fitted. Instead the Néel temperatures were taken from the dc-magnetic susceptibility measurements (see section 3.6.1). The results indicate agreement with the SO(3) universality class as well as with the $Z_2 \times S_1$ rotational group, both of which predict critical exponents β=0.25. Clearly the results

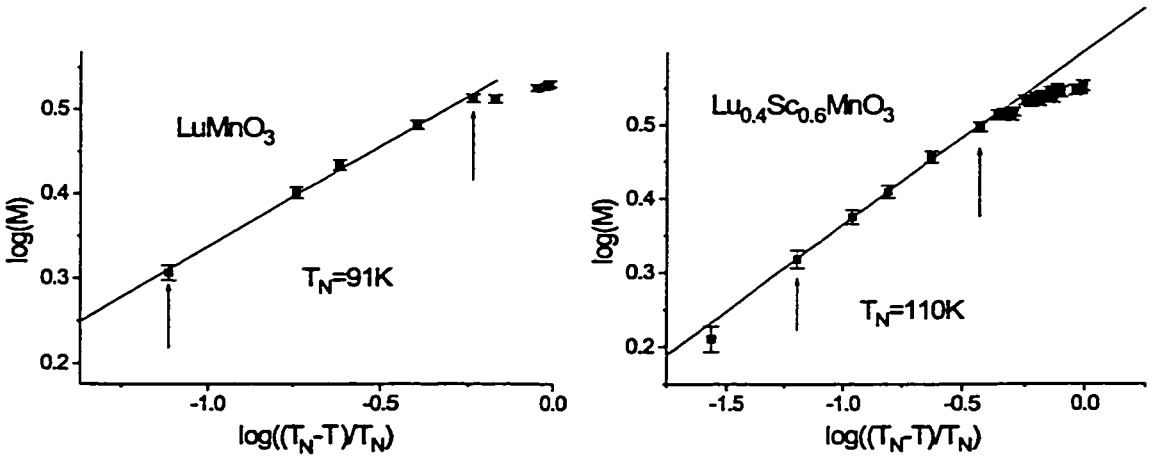

Figure 3.20: Determination of β (slope of the linear fit) from the magnetic moments and reduced temperature. The arrows indicate the range of data used to carry out the fit.

presented in table 3.5 are very different from the expected critical exponents as predicted for the 3d-Heisenberg model ($\beta = 0.346(9)$) and for the 2d-Heisenberg model ($\beta = 0.326$). Therefore, it is concluded that the triangular antiferromagnets of the series $Lu_xSc_{(1-x)}MnO_3$ can be described either by the SO(3) or $Z_2 \times S_1$ universality class. As β alone can not distinguish between these two cases, additional critical exponents (α, γ and ν) are required for this purpose. The critical exponents β for the series $Lu_xSc_{(1-x)}MnO_3$ are in agreement with other triangular antiferromagnets [CP97].

Table 3.5: Critical exponents β for $Lu_xSc_{(1-x)}MnO_3$.

x	β	T_N [K]
1.0	0.24(1)	91
0.9	0.25(1)	94
0.8	0.23(1)	99
0.4	0.24(1)	110
0.2	0.20(1)	118
0.0	0.23(1)	130

3.10 Magnetic Short Range Order

As the temperature is increased until the Néel temperature is reached a broad background underneath the magnetic diffraction peaks develops in the powder neutron diffraction patterns. This broad and asymmetric feature is due to 2-dimensional magnetic short range order. By fitting the experimental data to the so called Warren-line shape the magnetic correlation lengths can be determined. Based on Laue's qualitative treatment [Lau32] of diffraction peaks caused by 2-dimensional lattices Warren presented a generalized quantitative description of diffraction from randomly stacked 2-dimensional layers [War41]. In general powder diffraction peaks of small two dimensional domains show a considerable degree of anisotropy, where the maximum of these diffuse peaks is shifted towards higher angle with respect to the corresponding sharp Bragg peak. Due to the steep rise on the low angle side and the more gradual decrease at the high angle side of the peak the Warren-line shape can be easily recognized. In contrast, if the domains are 3-dimensional, a symmetrical gaussian or lorentzian line shape will be observed and the magnetic correlation lengths can be extracted from the FWHM after allowing for instrumental resolution. Figure 3.21 compares the two different peak shapes, and obviously,

the asymmetry of the Warren-line shape is a good indication of a 2-dimensional system. The Warren-line shape is described in equation 3.10.1.

$$P_{2\theta} = K\ m\frac{F_{hk}^2\,(1+\cos^2 2\theta)}{2\,(\sin\theta)^{3/2}}\frac{(\xi_{2D})^{1/2}}{\pi\lambda}F(a) \qquad (3.10.1)$$

where a=$(2\pi\sqrt{\pi}L/\lambda)(\sin\theta - \sin\theta_0)$, K is a constant, m is the multiplicity, F_{hk} is the two-dimensional structure factor, λ is the wavelength, ξ_{2D} is a two-dimensional correlation length, and θ_0 is the peak position. The function $F(a)$ is tabulated [War41]. Powder neutron diffraction data with sufficient counting statistics were collected for $ScMnO_3$ and $LuMnO_3$. The thermodiffractometry carried out for the intermediate compositions of the solid solution are not of good enough quality in order to fit function 3.10.1 to the data. The data for $LuMnO_3$ collected at 120K (figure 3.21) are used to show that the observed broad feature can be best fit using the Warren line shape 3.10.1. Figure 3.21 shows the fits of experimental data using gaussian functions and the asymmetric Warren line shape. The gaussian peaks can not describe the experimental data satisfactorily, whereas the Warren line shape accounts very well for the strong asymmetry. The fit corresponds to the 2-dimensional (10) reflection and the 2-dimensional Warren correlation length for $LuMnO_3$ is ξ_{2D} = 15(1)Å for temperatures of 80 K and 120K. For $Lu_{0.8}Sc_{0.2}MnO_3$ magnetic correlation lengths of ξ_{2D} = 15(2)Å were found at temperatures of 100K and 110K, at lower temperatures no meaningful fits were obtained, due to noisy data. The same result was found for $ScMnO_3$ [BG99], wherein the authors reported a temperature-independent Warren correlation length of ξ_{2D} = 13(2)Å for the temperature range 80K to 130K. Therefore, the end-members of the solid solution $Lu_xSc_{(1-x)}MnO_3$ show identical behaviour exhibiting 2-dimensional magnetic short range order at

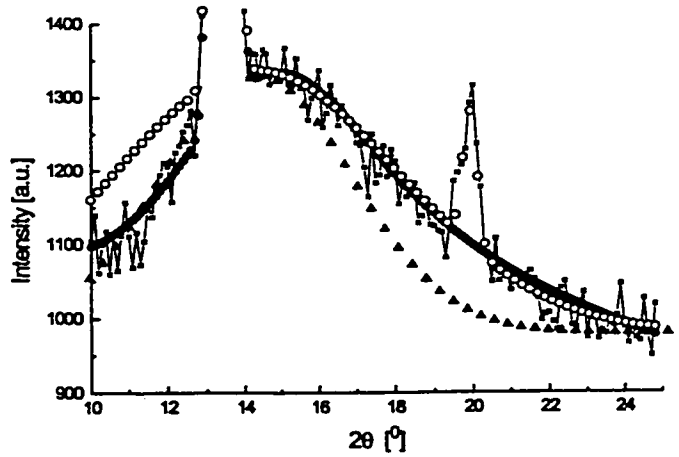

Figure 3.21: Neutron diffraction data, $\lambda = 1.328591(48)$Å, collected for $LuMnO_3$ at 120K. The stars represent the experimental data, the open circles and solid triangles are fits to gaussian functions ($y = \frac{A}{\sigma\sqrt{2\pi}} \exp\left(\frac{-(x-x_o)^2}{2\sigma^2}\right)$) which have been adjusted such that these fit the high angle and the low angle side of the broad peak, respectively. The densely plotted solid circles present the fit for the Warren line shape, equation 3.10.1.

temperatures well above T_N. The remaining neutron diffraction data are not of sufficient quality to determine magnetic correlation lengths. However, the data clearly show the same feature, namely the broad asymmetric peak at the diffraction angle for the $(10)_{mag}$ reflection. As expected the Warren line shape is most intense in the vicinity of the Néel temperature. Figure 3.22 shows the neutron diffraction patterns for x=1.0, 0.4 and 0.2 clearly indicating the presence of 2-dimensional magnetic short range order.

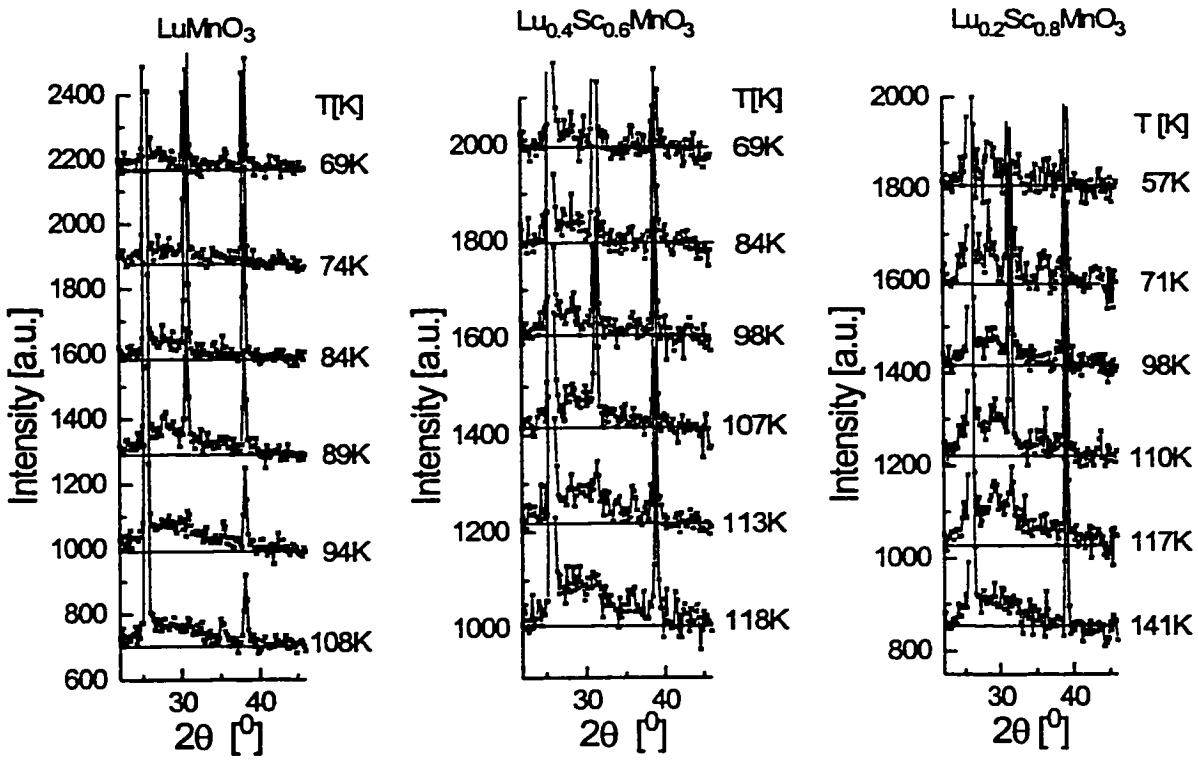

Figure 3.22: Magnetic short range order for $Lu_xSc_{(1-x)}MnO_3$ with x=1.0, 0.4 and 0.2. The powder neutron diffraction data were collected using a wavelength of λ=2.5248(6)Å. For each sample the counting time for each temperature was the same, consequently the intensities can be compared. Whereas, the data for different samples are not normalized with respect to each other.

3.11 Comparison with Reported Properties

In 1964 Koehler et al. reported [KWYC64] the magnetic structures for $LuMnO_3$, $TmMnO_3$, $ErMnO_3$ and $HoMnO_3$ including the specification of the angle between the magnetic moment and the hexagonal a-axis. Table 3.6 summarizes the data reported in 1964. First of all, the results reported in the previous paragraph for $ScMnO_3$ and the results in table 3.6 are not too far apart. However, the spin-reorientation transition was not reported in 1964. We prepared several samples

Table 3.6: Results for the series $AMnO_3$ as reported by Koehler et al. [KWYC64]. T_N is the Néel temperature determined from powder neutron diffraction studies. ϕ is the angle between the crystallographic a-axis and the orientation of the magnetic moment. All values refer to T=4.2K. Numbers in parantheses refer to samples with impurities.

Compound	T_N [K]	ϕ [°]	μ [μ_B]
$ScMnO_3$	(120)	(24)	(4.0)
$LuMnO_3$	91	55	3.7(2)
$TmMnO_3$	(86)	(45)	(3.8)
$ErMnO_3$	79	70	3.5(2)
$HoMnO_3$	76	0	3.5(2)

showing identical behaviour in terms of magnetic properties. Thus the results presented in the previous sections are considered reliable. Furthermore, Koehler et al. reported an unidentified impurity in their sample. In particular the Néel temperature of 120K, versus 129K, is very concerning. Our value for T_N has been confirmed by heat capacity measurements reported by Xu et al. [XIS+95]. Koehler's results for $LuMnO_3$ are very different from the findings presented in the previous section. We found a magnetic moment orientation of 90°, whereas Koehler et al. [KWYC64] reported an angle of 55°.

3.12 Alternative Magnetic Structure Models

This discussion is focused on the equivalence of different magnetic structure models with respect to neutron powder diffraction experiments. The assumed model consists of only one magnetic phase, which is described by the 120° rotation matrix of the spins in a given layer, the magnitude of the magnetic moment and the orientation of a reference spin via the angle ϕ. The angle ϕ can take any value between 0° and

90°. Furthermore, if the Mn^{3+}-ion is located at position 1/3,0,z the diffraction patterns for ϕ, -ϕ and ϕ+180° are identical. In addition different chiralities for the spin structures for different layers of paramagnetic ions need to be considered. The chirality problem will be dealt with in the next paragraph.

3.12.1 One Phase versus Multiple Phase Models

Instead of using the angle ϕ as a continuous parameter a two phase model can be used to describe the neutron diffraction patterns, where each phase has only one value for the magnetic moment orientation, i.e. phase "A" has the value ϕ_A=0° and phase "B" has the value ϕ_B=90°. Now the volume fractions of these two phases are related to the continuous angle ϕ by equation 3.12.1 and 3.12.2 as derived in Appendix A.1,

$$A_{fraction} = \frac{\cos(\phi)}{\sin(\phi) + cos(\phi)} \approx \frac{90° - \phi}{90°} \tag{3.12.1}$$

$$B_{fraction} = \frac{\sin(\phi)}{\sin(\phi) + cos(\phi)} \approx \frac{\phi}{90°} \tag{3.12.2}$$

where the approximation introduces a maximum error of ±0.04. The two phase model implies a spin-flop mechanism between the two magnetic phases, which occurs over the determined temperature range. However, the model can be extended to a larger number of phases. Assuming 30° increments for ϕ between different phases, a model with 4 phases is required and consequently, 4 coefficients (a,b,c,d) for the phase fractions need to be determined. The 30° model is consistent with the 6-fold symmetry of the crystallographic phase and allows the angles ϕ=0° and ϕ=90°. Since there are 4 unknowns (a,b,c,d) but only 2 known parameters (ϕ and a+b+c+d=1) there is no unique solution. These three above mentioned models for the description

of the magnetic phase are indistinguishable by means of powder neutron diffraction experiments. Only single crystal diffraction experiments will be able to determine the correct model. However, since earlier results [KWYC64] were reported in terms of a one phase model and a continuous angle ϕ the results here are presented in the same manner. In any case the angle ϕ can always be converted to the two phase model via equations 3.12.1 and 3.12.2.

3.12.2 The Problem of Chirality

A truly equilateral triangular antiferromagnetic sublattice has two degenerate chiral solutions. For the $\cdots$AAA$\cdots$ stacking sequence the interlayer magnetic exchange constant will couple the magnetic moments between the paramagnetic layers in such a way that if the magnetic moment orientation and the chirality of one layer is defined the second layer is defined as well. However, the $AMnO_3$ phases show a $\cdots$ABAB$\cdots$ stacking sequence. Due to the inherent geometric magnetic frustration between the two magnetic layers the chirality of the layer A is independent of the chirality in layer B. Consequently, 4 different combinations of chiralities are possible, namely A(+)B(+), A(+)B(-), A(-)B(+) and A(-)B(-), where A and B are the layers at z=0 and z=0.5 respectively, and (+) and (-) refer to the chiralities. Despite the fact that a considerable body of work concerning triangular lattices exists, no analysis which takes chirality into explicit account has been published to date. The 4 chiral models can be extracted from table 3.7 and two combinations are illustrated in figure 3.23 for the case ϕ=0°. It is important to investigate the limitations of powder neutron diffraction experiments in distinguishing between triangular magnetic states with different chiralities. For this purpose neutron powder diffraction patterns were simulated for all four magnetic structures as a function of

Table 3.7: Definition of the magnetic sublattices for the 120° magnetic structures on a triangular lattice. ϕ covers the angular range 0° to 90°.

Atom	x	y	z	layer	spin orientation [°]	
					+ chirality	- chirality
Mn(1)	1/3	0	0	A	ϕ	ϕ
Mn(2)	0	1/3	0	A	ϕ+120°	ϕ+240°
Mn(3)	-1/3	-1/3	0	A	ϕ+240°	ϕ+120°
Mn(4)	-1/3	0	1/2	B	ϕ	ϕ
Mn(5)	0	-1/3	1/2	B	ϕ+120°	ϕ+240°
Mn(6)	1/3	1/3	1/2	B	ϕ+240°	ϕ+120°

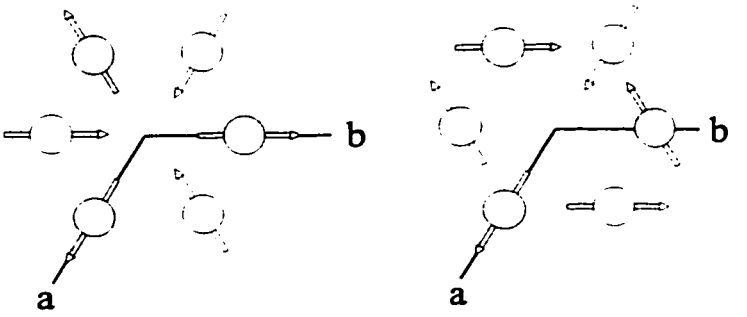

Figure 3.23: Projections of the chiral magnetic structures A(+)B(+) (left) and A(-)B(-) right. The grey and white atoms are located at z=0(A) and z=0.5(B), respectively.

the spin angle ϕ. The layer combination A(+)B(+) shows a significant change for the intensities of the magnetic diffraction peaks as ϕ is varied, and this is the model used for all results presented in the earlier section. In particular the intensities for the $(100)_{mag}$ [4] and $(101)_{mag}$ [5] reflections are sensitive to the magnetic moment orientation. Simulated diffraction patterns for the three remaining spin structures do not show any intensity variations as a function of ϕ. In fact the intensities of the

[4]The $(100)_{mag}$, consists of the $(1\bar{1}0)$, (010) and (100) reflections
[5]The $(101)_{mag}$, consists of the (101), $(10\bar{1})$, (011), $(01\bar{1})$, $(1\bar{1}1)$ and $(1\bar{1}\bar{1})$ reflections

individual magnetic reflections $(1\bar{1}0)_{mag}$, $(010)_{mag}$ and $(100)_{mag}$ change as a function of ϕ. However, only the sum of these reflections is observed, which does not change as a function of ϕ, because the intensity changes of the individual reflections compensate each other. This is true for all coinciding diffraction peaks in the powder patterns. The left side of figure 3.24 shows the integrated intensities for two magnetic reflections for the above mentioned combinations of chiralities. The right figure shows the intensities of indiviual diffraction peaks and the sum of all contributing diffraction peaks for one reflection position. From these simulated powder

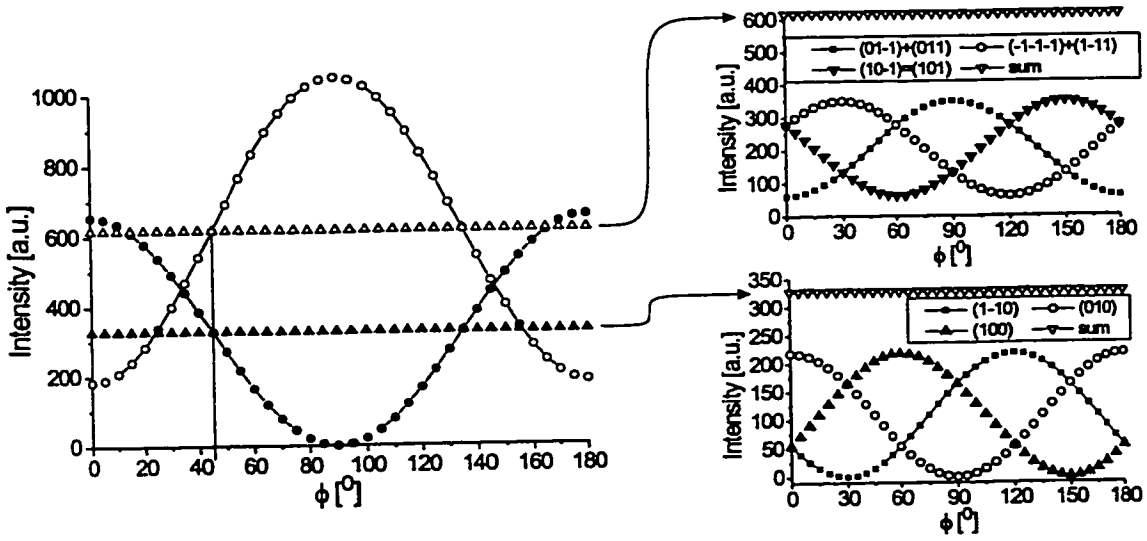

Figure 3.24: The left figure shows the integrated intensities for two sets of magnetic reflections for different chiralities. Solid symbols = $(100)_{mag}$ and related reflections, open symbols = $(101)_{mag}$ and related reflections. The circles represent the A(+)B(+) combination, whereas the triangles represent the three remaining combinations. The right figure shows the individual contributions to the magnetic Bragg peaks as well as the summation of these intensities for the chiral combination A(-)B(-).

patterns it can be concluded, that if an in-plane spin-reorientation process is recognized from powder neutron diffraction experiments the chirality combination must be A(+)B(+). Furthermore, neutron diffraction patterns for the models A(+)B(-), A(-)B(+) and A(-)B(-) are identical with the A(+)B(+) case with ϕ=45° [6]. Consequently, if a refinement is carried out with the magnetic structure model A(+)B(+) a resulting spin orientation $\phi \neq 45°$ indicates that the chirality is indeed A(+)B(+). This is the case for $LuMnO_3$ since a magnetic moment orientation of $\phi = 90°$ is found. The variable value for ϕ for $ScMnO_3$ indicates that $ScMnO_3$ is of A(+)B(+) type as well. In conclusion, above 70K the magnetic structures of $LuMnO_3$ and $ScMnO_3$ are identical, whereas at low temperature (below 40K) $ScMnO_3$ shows a spin arrangement, which is perpendicular to the state found for $LuMnO_3$.

3.13 Spin canting

The ZFC-FC divergence for the magnetic susceptibility below T_N indicates the presence of a ferromagnetic component for the Sc^{3+}-rich members of the solid solution $Lu_xSc_{(1-x)}MnO_3$. This is most likely due to a small extent of out-of-plane spin canting. The absence of an inversion center between the triangular layers is compatible with possible spin canting. Figure 3.25 illustrates the difference between the truly planar and the canted magnetic structures. Figure 3.26 compares simulated neutron powder diffraction patterns for an out-of-plane spin canting of 5° with no spin canting and a refined neutron powder diffraction data set. The very small differences between the two simulated patterns are far below the statistical uncertainties of the refined data set, shown on the right of figure 3.26. Consequently,

[6] For $x \neq 1/3$ the simulated neutron diffraction patterns will be fundamentally different.

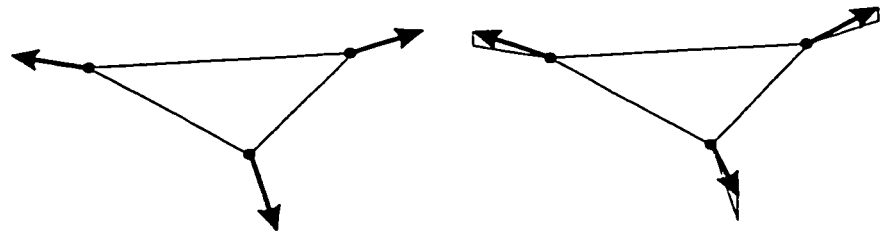

Figure 3.25: Comparison of the truly planar 120° magnetic structure (left) with the spin-canted structure (right).

a small spin canting angle can not be determined from powder neutron diffraction data. As the large ZFC-FC divergence in the magnetic susceptibility data occurs at the same temperature for all samples which show this feature, it is suggested that its origin is the same for all of these samples.

3.14 Conclusion

This work shows that all members of the solid solution $Lu_xSc_{(1-x)}MnO_3$ ($0 \leq x \leq 1.0$) show long range magnetic ordering with Néel temperatures between 91K ($LuMnO_3$) and 130K ($ScMnO_3$). The Néel states are consistent with the large spin quantum number, S=2, for Mn^{3+}. The magnetic structures are best described by a 120° spin structure, where all magnetic moments are constrained to the ab-plane. Detailed crystallographic analysis confirmed that the Mn^{3+} sublattice consists of edge sharing equilateral triangles, thus presenting a highly frustrated topology for antiferromagnetic exchange coupling. All compounds, except $LuMnO_3$, show an in-plane spin-reorientation transition. Therefore, it is concluded that the presence of Sc^{3+} causes this transition. As the concentration of Sc^{3+} is increased the angular range for the reorientation process increases and the transition occurs over a

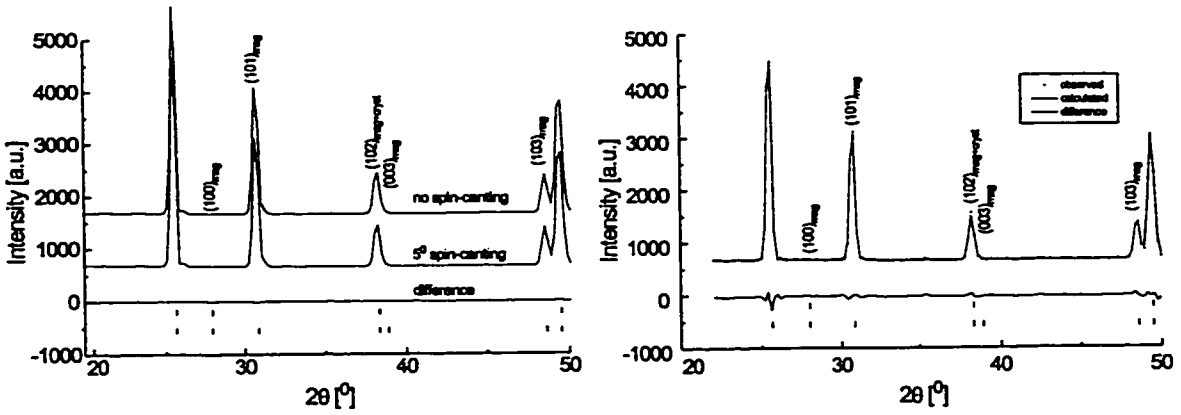

Figure 3.26: Left: Comparison of simulated powder neutron diffraction patterns for $LuMnO_3$ without spin canting and 5° spin canting. Right: Refined powder neutron diffraction data set for $LuMnO_3$ at 4.1K. The simulated patterns are calculated using the instrumental parameters as used for the experimental data collected on diffractometer D1B ($\lambda \approx 2.52$Å).

narrower temperature range. It is believed that the Sc^{3+}-Lu^{3+} disorder broadens the transition temperature range. The spin-reorientation transition is accompanied by a large ZFC-FC divergence at 44K in the magnetic susceptibility data. As this large divergence is not temperature dependent, the origin of this feature is considered to be the same for all samples. Furthermore, for all samples a much smaller ZFC-FC divergence is found just below the Néel temperature, again the divergence is largest for $ScMnO_3$ and rather small for $LuMnO_3$. Spin-canting is the likely origin for this hysteresis behaviour. It was pointed out, that powder neutron diffraction experiments can not detect a small canting angle, single crystal neutron diffraction experiments are required for a final conclusion.

In the vicinity of the Néel temperatures 2-dimensional magnetic short range order is found, where the temperature independent magnetic correlation lengths are

approximately 13-15Å for all samples. Only the extent of short range order varies as a function of temperature, with the highest intensities close to the Néel temperature.

The critical exponents β=0.23(3) confirm that the solid solution $Lu_xSc_{(1-x)}$-MnO_3 does not belong to any conventional universality class. Instead, at least over the range of reduced temperature investigated, the SO(3) and $Z_2 \times S_1$ universality classes are consistent with the critical behaviour.

The magnetic sublattice has a chirality of A(+)B(+), while all remaining chiral combinations do not agree with the neutron diffraction data for the investigated compounds. Only the A(+)B(+) model leads to different intensities for the magnetic reflections for different magnetic moment orientations.

A comparison of a single phase magnetic model with multiple phase models has been presented. However, the models can not be distinguished with powder neutron diffraction data.

Only two compounds of the hexagonal $AMnO_3$ series were known to exhibit an in-plane spin-reorientation transition, namely $HoMnO_3$ [KWYC64] and $ScMnO_3$ [BG99]. The present work showed that even small amounts of Sc^{3+} in the solid solution $Lu_xSc_{(1-x)}MnO_3$ conserves this transition. No detailed analysis regarding the Ho^{3+} compound has been carried out. To date, there is no explanation, why the Sc^{3+} containing and the Ho^{3+} compounds show this transition, whereas $LuMnO_3$ does not. Since Lu^{3+} is of intermediate size it is concluded that the A^{3+}-cation size is not the origin of this transition. The investigation of the solid solution $Lu_xHo_{(1-x)}MnO_3$ is proposed in order to investigate the spin-reorientation transition in $HoMnO_3$. A detailed study regarding the crystal structure and the orientation of the magnetic

moment and the possible presence of spin canting may help to resolve this puzzle. However, $ScMnO_3$ shows a more isotropic Mn-O_5 coordination than the Lu analogue. It is possible that this is important for the spin-reorientation transition. The suggested presence of spin-canting supports the decrease in anisotropy. A detailed crystallographic study of the Ho analogue should be carried out in order to gain a deeper understanding.

Chapter 4

The Square Planar Antiferromagnets A_2BO_4

4.1 Introduction

This chapter focuses on compounds which form the K_2NiF_4 structure. K_2NiF_4 itself was first reported in (1892) [Pou92] and the structure was first recognized in 1953 [Bal53] followed by a detailed analysis by Balz and Plieth [BP55] in 1955. Formally, the K_2NiF_4 structure can be considered an intergrowth of the rock salt and perovskite structures, both structure types are very common for metal oxides and a tremendous amount of research has been devoted to transition metal oxide perovskites. It is not surprising that there exists also a large number of oxides which form the K_2NiF_4 structure. Figure 4.1 shows the K_2NiF_4 structure and the two building blocks, namely, the perovskite as well as the rock salt structures. The figure is idealized such that only geometric constraints are considered, when charge repulsion is taken into account the rock salt layers lose the perfect planarity. However, the $\sqrt{2}$ relation between the rock salt and perovskite layers is readily seen. Furthermore, the coordination number of K^+ is reduced to 9 due to the intergrowth with the rock salt layer. This structure is described in space group $I4/mmm$ and

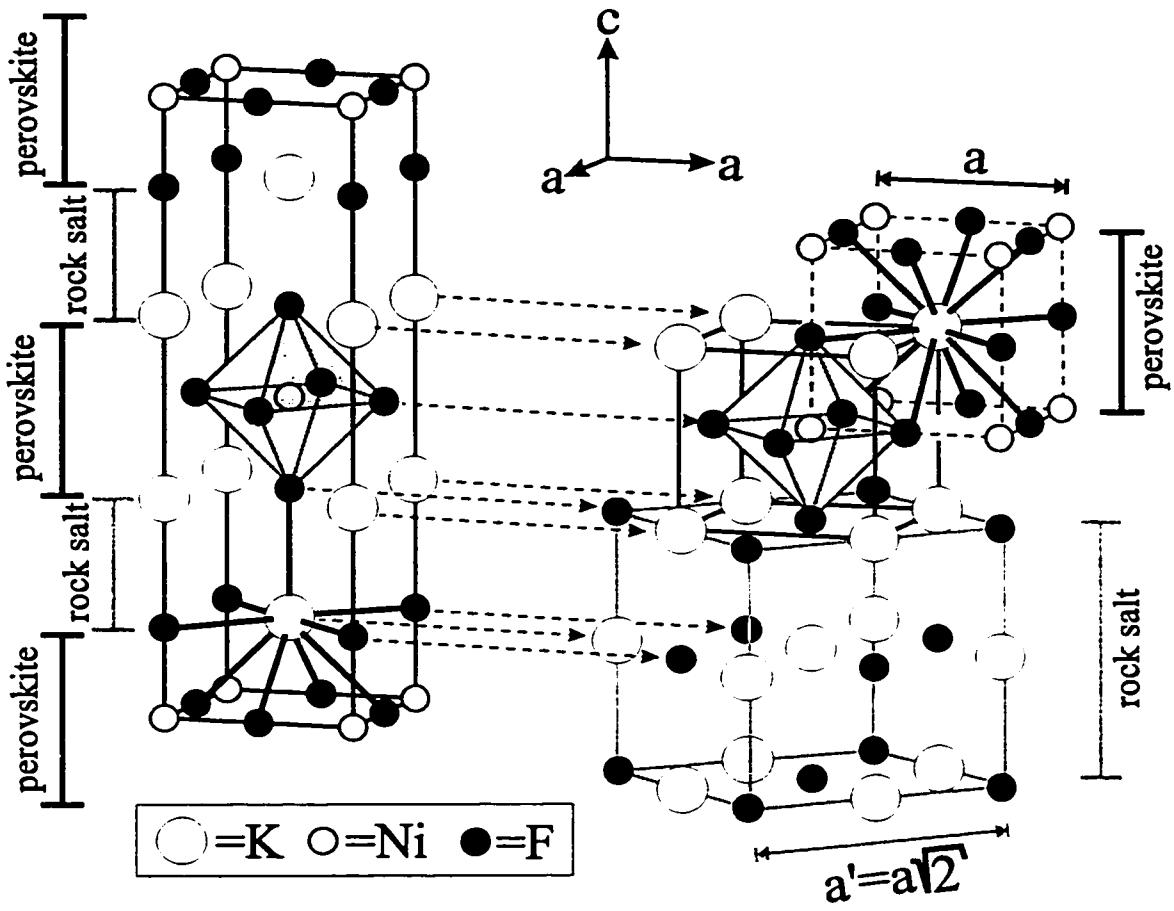

Figure 4.1: Left: Idealized K_2NiF_4 structure, the individual layers are indicated on the left of the crystal structure. The right side illustrates the interface between $KNiF_3$ (perovskite phase) and KF (rock salt phase) layers. The perovskite phase is shown with two different origins, where the upper presentation is the A-setting (dashed line), here the twelve fold coordination of K^+ is emphasized and the lower perovskite unit cell is the B-setting (solid black lines) with the central Ni-F_6 octahedron. The whole unit cell of rock salt (in grey) is shown at the bottom, whereas the corresponding layers in K_2NiF_4 only consists of half the unit cell. Due to the interface between the two crystallographic systems the coordination of K^+ is only 9 in K_2NiF_4. The dashed arrows connect corresponding atoms and are meant as a guide.

has an ideal a:c ratio of 1:3.4142. The structure does not permit any buckling of the Ni-F_6 octahedra, which is in contrast to the wide variety of lower symmetry perovskite phases, which are based on cooperative tilting of octahedra [Gla72], [Woo97a], [Woo97b]. The K_2NiF_4 structure can accommodate additional anions at the interface, which is due to a rather large interstitial site between K^+ and Ni^{2+}. If the B ion has a variable oxidation state this can cause severe problems in terms of oxidation of samples. In analogy to the Goldschmidt tolerance factor for perovskites Poix [Poi80] introduced a tolerance factor t for the K_2NiF_4 structure type.

$$t = \frac{\psi_A}{\sqrt{2}\beta_B} \tag{4.1.1}$$

where β_B is the sum of the Shannon radii [Sha76] of cation B and oxygen, ψ_A is a parameter which can be determined from equation 4.1.2

$$\beta_B + \sqrt{2}\psi_A = 0.99615V^{1/3} \tag{4.1.2}$$

V is the unit cell volume and tetragonal K_2NiF_4-phases are stable for $1.02 > t > 0.85$. There is a whole family of oxides which are based on the intergrowth of rock salt and perovskite phases. The perovskite layers can be extended and are separated by rock salt layers. These compounds are called Ruddlesden Popper phases and follow the stochiometric relation $AO \cdot (ABO_3)_n = A_{(n+1)}B_nO_{(3n+1)}$, where n is an integer between 0 and ∞. Obviously n=1 is the K_2NiF_4 phase and the pure perovskites are the members with n=∞. Several members of the Ruddlesden Popper phases are shown in figure 4.2. The Ruddlesden-Popper phases are very interesting since GMR was reported for several Mn-containing phases with n=2, similar to Mn based perovskites which also show CMR. Contrastingly, none of these properties are known for n=1 phases. Moreover, at least one family of high temperature superconductors

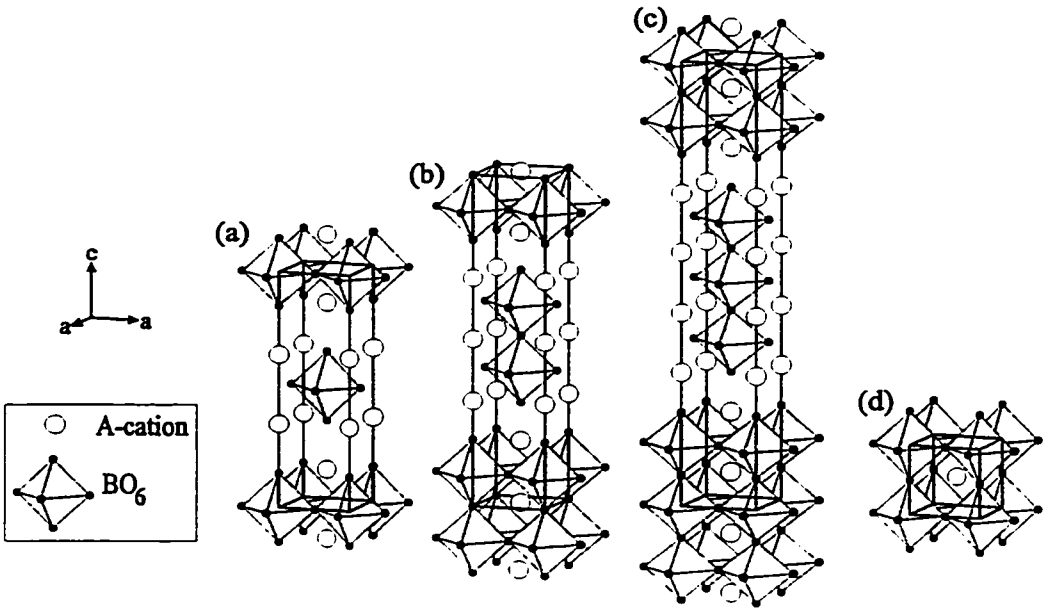

Figure 4.2: Ruddlesden Popper phases (a) A_2BO_4 (n=1), (b) $A_3B_2O_7$ (n=2), (c) $A_4B_3O_{10}$ (n=3) and (d) perovskite (n=∞)

is based on the K_2NiF_4 structure. Overall this class of compounds has been and continues to be a very fertile field of research. The details of CMR, GMR and high T_c superconductivity are not completely understood and the Ruddlesden-Popper phases are considered very good model compounds with the potential to gain understanding of the above mentioned properties. It is understood that the mixed oxidation states of Mn contribute to the drastic changes in resistivity in GMR and CMR materials.

4.2 $BaLaMnO_4$ Background

$BaLaMnO_4$ was first reported in 1977 by Benabad et al. [BDSlF77]. Here the unit cell constants a=3.902(5)Å and c=13.27(1)Å and their evolution for the

substitutional solid solution $Ba_{(1-x)}La_{(1+x)}MnO_4$ were reported but not a detailed structure. $BaLaMnO_4$ forms the K_2NiF_4 structure (space group $I4/mmm$), where Ba^{2+} and La^{3+} are randomly disordered on the A-cation site, Mn^{3+} is located at the B-cation site, thus being octahedrally coordinated by oxygen. The Mn-O_6 octahedra are linked via corners in the ab-plane and well separated by the rock-salt layer along the c-axis. Only the d^4-ion Mn^{3+} (S=2) is paramagnetic, therefore the magnetic sublattice can be described as square planar, where the 2-dimensional sheets extend in the ab-plane. Furthermore, a certain extent of geometric frustration is expected due to the stacking sequence of the Mn^{3+} layers, forming a body centered array of paramagnetic ions on the magnetic sublattice as clearly shown in figure 4.1 on page 104. As mentioned earlier the interface between the perovskite and rock-salt building blocks has rather large interstitial sites, thus being able to accommodate additional anions. In 1988 Jorgensen et al. [JDP+88] investigated $La_2CuO_{4+\delta}$ ($0 \leq \delta \leq 0.13$) and in 1989 [JDP+89] $La_2NiO_{4+\delta}$ ($0 \leq \delta \leq 0.13$), the temperature dependent structure is of K_2NiF_4 type at high temperature, but shows phase separation with lower symmetry phases at low temperatures. Later the phase diagram for oxygen excess $La_2NiO_{4+\delta}$ ($0 \leq \delta \leq 0.17$) was extended by Rice and Buttrey [RB93]. The possible changes in crystal chemistry are shown in figure 4.3, which shows the occupation of an interstitial site and the distortion of the original oxygen sublattice [CCC+90].

4.3 The Jahn-Teller Effect

The Jahn-Teller theorem states that a non-linear molecule in an electronic state with orbital degeneracy will distort so as to lower its symmetry and remove

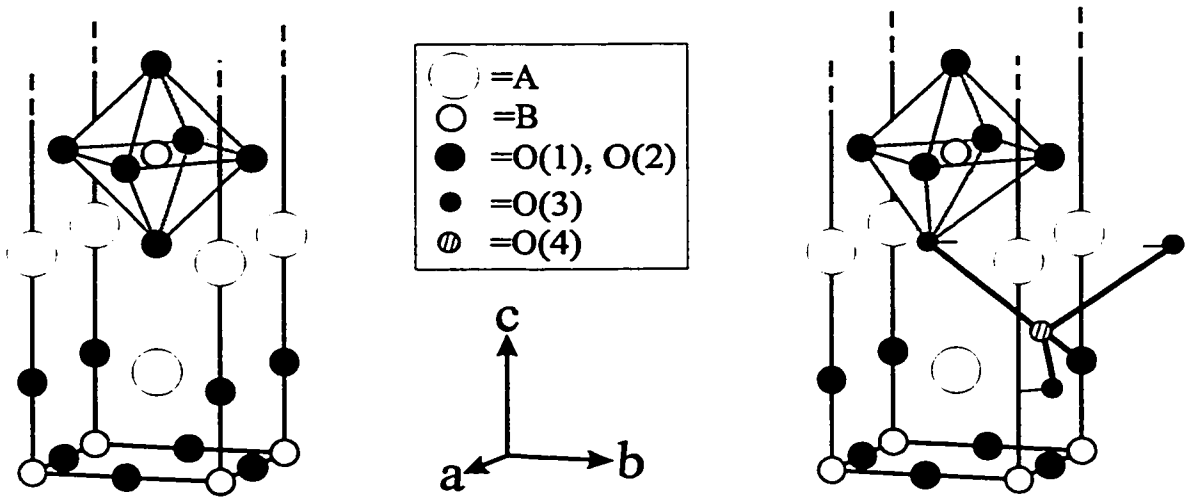

Figure 4.3: Oxidation of the K_2NiF_4 structure through interstitial oxygen as shown for $La_2NiO_{4+\delta}$ [JDP+88], [CCC+90]. The left figure shows part of the unit cell of the original structure in space group $I4/mmm$. The right figure shows the displacement of oxygen atoms and the creation of a new crystallographic site O(3) (the dashed lines indicate the displacement) and the new site O(4). The crystallographic symmetry is lowered to the orthorhombic space group $Fmmm$. The coordinate system refers to the original $I4/mmm$ structure, the orthorhombic structure has $\sqrt{2}\times$ larger a and b unit cell axes.

the orbital degeneracy [Cox92]. This can be accomplished by distorting octahedral coordinations by lengthening two M-O bonds. The Jahn-Teller effect is confined to localized electrons and results in tetragonal distortion of an octahedral coordination for high spin d^4, low spin d^7 and d^9 configurations. Mn^{+3} is a d^4-ion, thus representing the classical case of a Jahn-Teller ion. The significance of the Jahn-Teller effect for $SrLaMnO_4$ can be demonstrated by comparison with isostructural compounds of composition $SrLaMO_4$, where M is Cr^{3+} (d^3), Mn^{3+} (d^4), Fe^{3+} (d^5) and Co^{3+} (d^6). The bond distances [FCDS81] and the distortion indices, DI (equation 4.3.1),

for the M-O_6 octahedra are summarized in table 4.1.

$$DI = \frac{< M - O_{ax} >}{< M - O_{eq} >} \tag{4.3.1}$$

Where $< M - O_{ax} >$ and $< M - O_{eq} >$ are the mean axial and equatorial transition metal oxygen bond distances, respectively. All four compounds show tetragonal

Table 4.1: Bond distances for different transition metal oxide octahedra as found in the K_2NiF_4 structure. $SrLaMnO_4$ shows the largest tetragonal distortion, which is attributed to the Jahn-Teller effect as expected for a d^4 ion. Data taken from [FCDS81]. The tolerance factors t for the K_2NiF_4 structure (equation4.1.1) are also shown [GR84].

	:	M-O_{eq} [Å]	M-O_{ax} [Å]	DI	t
$SrLaCrO_4$	:	1.926	2.09	1.08	0.928
$SrLaMnO_4$	:	1.898(1)	2.29(5)	1.21	0.901
$SrLaFeO_4$	:	1.940	2.143	1.10	0.922
$SrLaCoO_4$	:	1.903	2.027	1.07	0.989

elongation for the Mn-O_6 octahedra, which can be correlated to Poix's tolerance factor, t. All compounds have tolerance factors of less than one, the resulting mismatch between the perovskite and rock salt layers causes a compression of the equatorial Mn-O bonds [GR84]. However, the largest distortion is found for the Mn^{3+} compound, which is due to the Jahn-Teller effect.

4.4 Sample Preparation

Samples covering the compositional range $0.00 \leq x \leq 1.00$ were prepared for the series $Ba_xSr_{(1-x)}LaMnO_4$. Furthermore, oxidized samples for the system $BaLaMnO_{(4+\delta)}$ were synthesized, where δ spans the range 0 to 0.2. Reduced forms of $BaLaMnO_4$ were prepared as well.

4.4.1 Polycrystalline Samples

All samples of the series $Ba_xSr_{(1-x)}LaMnO_4$ were prepared from $BaCO_3$ (99.7% Baker Chemical Co.), $SrCO_3$ (99.5% Baker Chemical Co.), La_2O_3 (99.99% Rhone-Poulenc) and Mn_2O_3 (99.9% CERAC). Residual water in $BaCO_3$ and $SrCO_3$ was determined by weight loss at 600°C in air, the used masses were adjusted accordingly. La_2O_3 was prefired at approximately 1050°C in air. Stochiometric amounts of the starting materials were ground and mixed in an alumina mill in acetone. The pressed pellets were placed on Pt-foil in an Al_2O_3 boat and fired for 24h at 1350°C in high purity Ar. All samples had a homogeneous grey to black color and were poor electronic conductors.

$$xBaCO_3 + (1-x)SrCO_3 + \frac{1}{2}La_2O_3 + \frac{1}{2}Mn_2O_3 \xrightarrow{1350°C} Ba_xSr_{(1-x)}LaMnO_4 + CO_2 \tag{4.4.1}$$

Preparation of Oxidized Samples

The polycrystalline $BaLaMnO_4$ samples were pelletized, wrapped in Pt-foil and were heated to 500°C in a sealed glass tube in the presence of stochiometric amount of CrO_3. According to equation 4.4.2 the chromium trioxide decomposes and the released oxygen can react with $BaLaMnO_4$ according to reaction 4.4.3

$$2CrO_3 \xrightarrow{500°C} Cr_2O_3 + \frac{3}{2}O_2 \tag{4.4.2}$$

$$BaLaMnO_4 + \frac{\delta}{2}O_2 \xrightarrow{500°C} BaLaMnO_{(4+\delta)} \tag{4.4.3}$$

Preparation of Reduced Samples

$BaLaMnO_4$ samples were reduced using H_2-gas of different partial pressure and at different temperatures. The unit cell constants of the resulting products were

monitored and correlated with the reaction conditions but the absolute degree of reduction could not be obtained. Reaction 4.4.4 summarizes the overall reactions.

$$BaLaMnO_4 + \delta H_2 \xrightarrow{T_p} BaLaMnO_{(4-\delta)} + \delta H_2O \qquad (4.4.4)$$

4.4.2 Single Crystals

Several attempts to grow single crystals were undertaken. All single crystal growth experiments were carried out with oxides instead of carbonates. Crystallization from the melt using the Bridgeman technique failed due to decomposition. Experiments were carried out using arc melting as well as melting in sealed Mo-crucibles. The products obtained from the sealed Mo-containers showed the presence of very small crystals, which all turned out as multiply intergrown species. None of the obtained crystals was of good enough quality for single crystal x-ray diffraction experiments.

4.5 $BaLaMnO_4$

Several samples of $BaLaMnO_4$ were prepared and the quality of the samples was investigated using high resolution x-ray diffraction with the Guinier Hägg camera and bulk magnetic properties which are very sensitive to possible oxidation of the products (see section 4.7.2). The unit cell parameters and volume for $BaLaMnO_4$ are a=3.8989(3)Å, c=13.264(1)Å and V=201.6(2)Å^3. These values are in reasonable agreement with Benabad's values of a=3.907(5)Å, c=13.27(1)Å and V=202.7(6)Å^3 [BDSlF77]. Powder x-ray and neutron diffraction patterns obtained at room temperature clearly indicate that $BaLaMnO_4$ crystallizes in space group $I4/mmm$ with the K_2NiF_4 structure. The Guinier x-ray pattern for $BaLaMnO_4$ is shown in figure

4.4, all except one minor diffraction peak can be indexed on the K_2NiF_4 structure. Several samples of $BaLaMnO_4$ were prepared, some of these showed a small extent

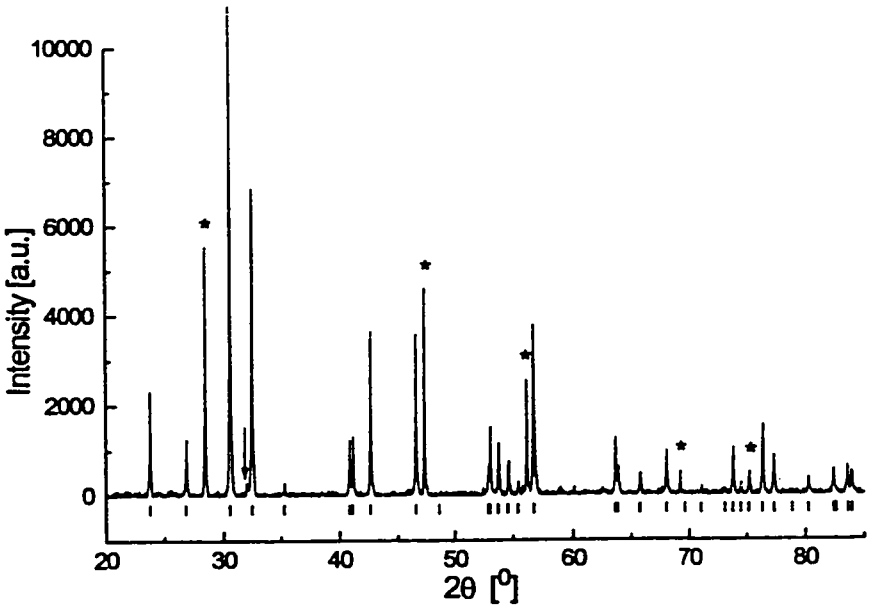

Figure 4.4: Guinier x-ray diffraction pattern for $BaLaMnO_4$ λ=1.54060Å yielding unit cell constants of a=3.8989(3)Å and c=13.264(1)Å. The expected peak positions are indicated by the tick marks below the pattern. The stars indicate the diffraction lines due to Si, which is used as an internal standard. The arrow indicates the only non-indexed diffraction line. Several other small spikes and broad features are artifacts on the photographic film.

of oxidation as determined from magnetic susceptibility data, furthermore the lattice parameters for the c-axis varied as a function of oxygen content. However, for all analyzed samples atomic emission spectroscopy (ICP-technique) yielded molar cation ratios of 0.99(2):1.02(2):1.00(2) for Ba:La:Mn. Attempts to determine the oxygen stochiometry in $BaLaMnO_4$ using thermal gravimetric analysis failed. Oxidizing in pure oxygen at 1100°C as well as reduction in pure hydrogen at 1000°C did not succeed to convert the sample to a fully oxidized or reduced form, only partial

conversion took place. Experiments were not reproducible which is attributed to the inherent stability of the K_2NiF_4 phase, a small amount of oxygen can be accepted in the crystal structure, but complete oxidation was not achieved [1]. Therefore the oxygen stochiometry needs to be determined by other means. A small degree of oxidation and reduction was achieved and the unit cell constant evolution was correlated with the nominal stochiometry. Results regarding these experiments are presented in section 4.5.4.

4.5.1 Neutron Diffraction Experiments

Room temperature Neutron diffraction experiments were carried out at IPNS at Argonne National Laboratory on instrument SEPD. The excellent resolution and d-spacing range accessible with SEPD allows reliable structure determinations from powder data. The refined neutron powder diffraction pattern is shown in figure 4.5. Figure 4.6 illustrates the crystal structure, the cation coordination and the potential exchange paths between Mn^{3+}-ions. The statistics describing the refinement, the crystallographic parameters, bond lengths and bond distances are presented in table 4.2. As a consequence of the three perpendicular mirror planes all O^{2-}-Mn^{3+}-O^{2-} angles are 90° or 180°, consequently the Mn^{3+} coordination is well described by the distortion index, $DI = < r_a > / < r_e > = 1.145(1)$, which indicates tetragonal elongation for the Mn-O_6 octahedron in $BaLaMnO_4$. The distortion index reflects the extent of Jahn-Teller distortion due to electronic repulsion. The Ba^{2+} and La^{3+} cations are randomly disordered on the A cation site. The bond valence sums determined for Ba^{2+} and La^{3+} are 2.846 and 2.093, respectively. Using equation 1.6.13

[1] $BaLaMnO_4$ can only be dissolved slowly in hot aqua regia, the drastic conditions required to dissolve the compound confirm the stability of the phase.

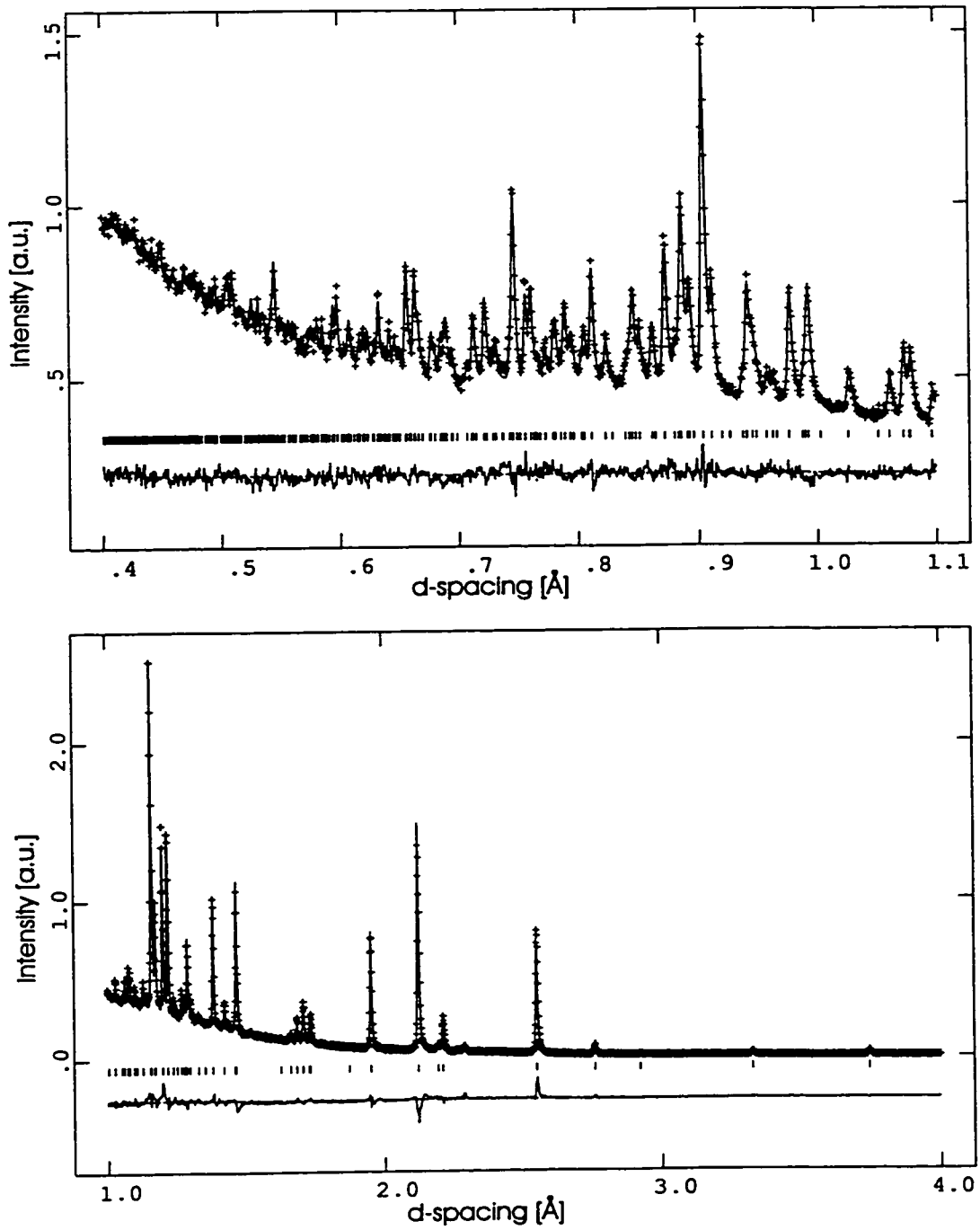

Figure 4.5: Powder neutron diffraction refinement for $BaLaMnO_4$, the data were obtained at room temperature at IPNS.

Table 4.2: Agreement factors, crystallographic parameters and bond lengths for $BaLaMnO_4$ as determined from Rietveld refinement of powder neutron diffraction data at room temperature.

Number of data points	:	5402	Space group	:	$I4/mmm$
Number of parameters	:	25	a [Å]	:	3.90252(6)
R_{wp}	:	6.83	c [Å]	:	13.2660(3)
R_p	:	3.88	V [Å^3]	:	202.036(6)
$reduced\chi^2$	:	3.73			

Atom	x	y	z	$U_{iso}/U_e \times 100$	Occupancy
Ba(1)	0	0	0.35735(10)	0.80(7)	0.495(3)
La(2)	0	0	0.35735(10)	0.80(7)	0.495(3)
Mn(3)	0	0	0	0.72(7)	0.990(7)
O(4)	0	0	0.16841(14)	3.829(11)	1
O(5)	1/2	0	0	1.87(11)	1

	distance [Å]		angle [°]
Mn-O(4) × 2	2.2341(19)	O(5)-Ba-O(4a)	134.12(2))
Mn-O(5) × 4	1.95126(3)		
<Mn-O>	2.05	Atom	bond valence sum
$\sum$radii	1.96	Ba^{2+}(1)	2.846
		La^{3+}(2)	2.093
Mn-Mn (intraplanar)	3.90252(6)	Mn^{3+}	2.944
Mn-Mn (interplanar)	7.184(1)		
Ba(1)-(O4a)	2.5065(21)		
Ba(1)-(O4) ×4	2.78057(31)		
Ba(1)-(O5) ×4	2.7182(9)		

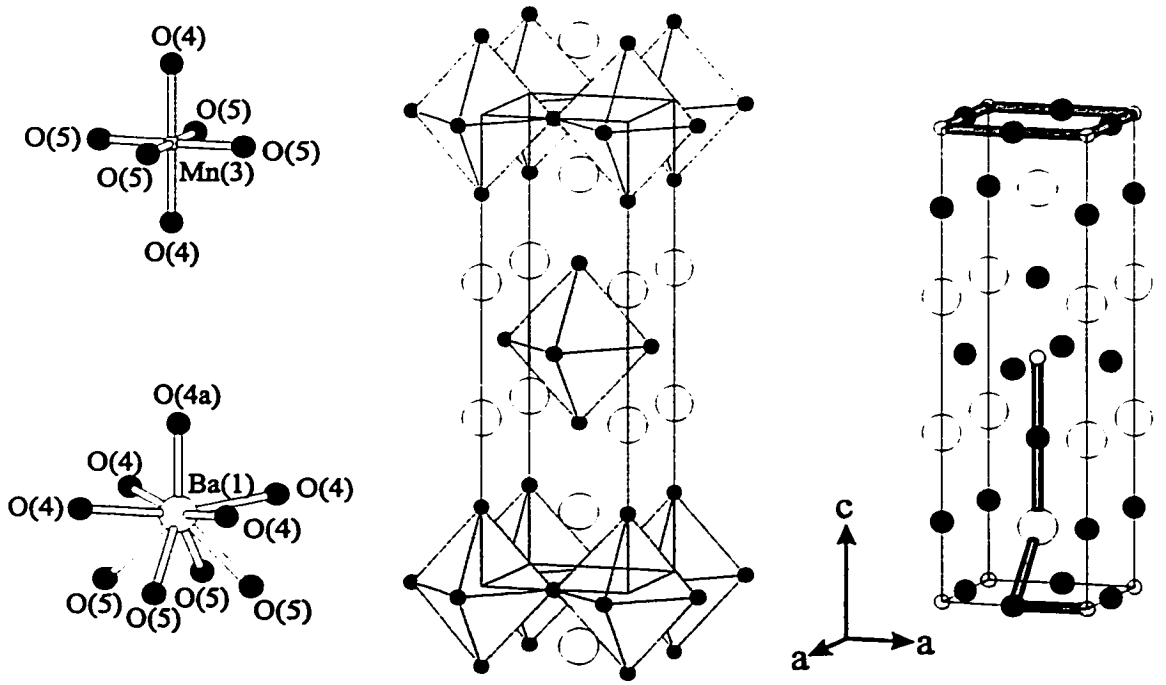

Figure 4.6: Room temperature crystal structure of $BaLaMnO_4$ according to powder neutron diffraction refinements. Left: coordination polyhedra; center: crystallographic unit cell with Mn-O_6 octahedra, the open circles are (Ba,La) cations, the solid circles are oxygen ion; right potential magnetic exchange paths in bold.

(page 34) the following site occupations of 0.49 and 0.51 are determined for Ba^{2+} and La^{3+}, respectively. The bond valences are very sensitive to the value of r_o used for the calculations and an error of at least 0.02 for the occupations is estimated. Therefore, the result is in agreement with the cation ratio determined from atomic emission spectroscopy and justifies the constraint of a 1:1:1 ratio for Ba:La:Mn as used during the refinement.

As can be seen in figure 4.6 magnetic exchange paths between Mn^{3+} ions are simple within the ab-plane. The Mn^{3+}-O^{2-}-Mn^{3+} bond path is linear. In contrast the interplanar magnetic exchange is complicated since three mediating ions

are involved and one angle is close to 120°. The sign for the exchange coupling is difficult to predict and only weak interactions due to the complexity of the path as well as the long distances are expected.

4.5.2 Magnetic Susceptibility

$BaLaMnO_4$ was measured in the temperature range 5K to 600K using an external magnetic field of 0.01T. The obtained data are shown in figure 4.7. Obviously

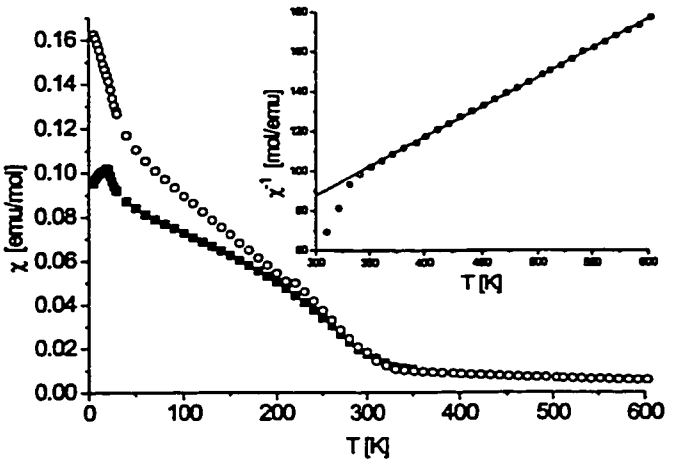

Figure 4.7: Magnetic susceptibility data for $BaLaMnO_4$ (solid squares = ZFC, open circles = FC). The cusp at 21K might be caused by a glassy state. The divergence below 300K is due to ferromagnetism originating from a very small degree of oxidation of the sample. The inset shows the inverse magnetic susceptibility data at high temperature, where the solid line represents the best fit to the Curie-Weiss law.

$BaLaMnO_4$ shows a small degree of zero field cooled (ZFC) - field cooled (FC) divergence below 300K. This ferromagnetic response can be explained with a small degree of oxidation of the sample. As the sample is oxidized a small fraction of Mn^{3+} is substituted by Mn^{4+}. Goodenough's rules predict ferromagnetic exchange for Mn^{3+}-O-Mn^{4+}, as found for the sample. Whereas, the crystallographic system

containing only Mn^{3+} will not show any evidence of ferromagnetic exchange. The refinement of neutron diffraction data as well as the phase purity as determined from x-ray Guinier diffraction patterns support that only a minor fraction of the sample might be oxidized. Furthermore, evidence is gained from the high temperature (see section 4.7.2) bulk magnetic susceptibility data. The Weiss temperature θ is slightly positive thus indicating that ferromagnetic exchange interactions are present, as a purely antiferromagnetic system will give a negative Weiss temperature. The value of θ=5(2)K as well as the small magnetization at 5K are too small to consider a major phase as ferromagnetically ordered. The Curie-Weiss fit for the high temperature inverse susceptibility data reveals an effective magnetic moment of μ_{eff}=5.18(3)BM, whereas the expected spin-only value is μ_{so}=4.90BM. The c-axis parameters of $BaLaMnO_4$ is slightly shorter than reported by [BDSlF77] which supports that the present $BaLaMnO_4$ sample is slightly oxidized. Caution is required with the Curie-Weiss fit, because the onset of zero field - field divergence is close to 300K and thus close to the fitting range, most likely the reported error for μ_{eff} is underestimated.

The lack of a sharp maximum in the χ versus T data suggests that no antiferromagnetic long range order is established. However, the observed ferromagnetic response could mask a possible antiferromagnetic feature. Finally, powder neutron diffraction experiments will clarify if antiferromagnetic long range ordering takes place at low temperatures. However, the cusp in the ZFC data at approximately 21K, suggests magnetic short range order. The presence of a cusp is very often found for spin glasses [Myd93]. Consequently, the spin glass state is considered a possible magnetic ground state for $BaLaMnO_4$.

4.5.3 Low Temperature Neutron Diffraction

Neutron diffraction experiments on powders were carried out on several samples, none of which showed any evidence of magnetic long range ordering at liquid helium temperature. Neither new Bragg peaks nor changes in the intensities of any peaks were observable. This finding rules out magnetic long range ordering for $BaLaMnO_4$. The diffraction patterns at low temperature show the evolution of a broad maximum, which indicates the possible presence of magnetic short range order. However, the broad feature is very weak and barely above noise level. Consequently, no detailed analysis concerning the nature of the ordering can be carried out. This includes the correlation lengths as well as the dimensionality of these magnetic domains. Figure 4.8 shows the powder neutron diffraction data for $BaLaMnO_4$. All the above results point at the inhibition of magnetic long range ordering, which is in contrast to the behaviour of $SrLaMnO_4$ (see section 4.6 and [KAKA88]). Upon increasing the effective A-cation size, i.e. substituting Sr^{2+} by Ba^{2+}, a lower Néel temperature is excepted. This is due to the increased distances between paramagnetic ions and the resulting weakening of the coupling between magnetic moments. Surprisingly, $BaLaMnO_4$ does not show any magnetic long range ordering.

4.5.4 Oxidized and Reduced $BaLaMnO_4$

A systematic study was carried out in order to gain understanding regarding the reduction and oxidation behaviour of $BaLaMnO_4$. Upon oxidation the c-axis parameter decreases, whereas the a-axis constant increases. Partial oxidation of $BaLaMnO_4$ can be achieved easily at elevated temperatures, the unit cell evolution of $BaLaMnO_{(4+\delta)}$ are shown in figure 4.9. The decrease of the c-axis parameter upon

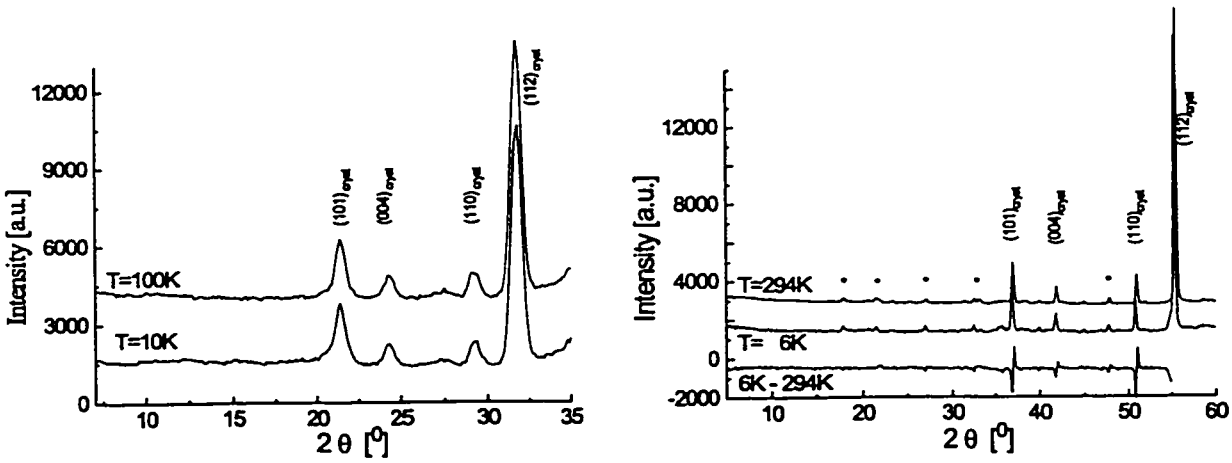

Figure 4.8: The left side shows powder neutron diffraction data for $BaLaMnO_4$ collected at McMaster University nuclear reactor (λ=1.392Å). The patterns at 10K and 100K are identical, allowing the conclusion that no long range magnetic ordering takes place. The right figure shows neutron diffraction data collected at Chalk River (λ=2.3692Å), again there is no difference between the 6K and the room temperature data sets. The stars indicate a minor impurity which has not been identified.

oxidation can be rationalized in terms of substitution of Mn^{3+} with the smaller Mn^{4+} cation [2]. Whereas, the a-axis parameter increases due to the additional oxygen in the structure. A minimum c-axis parameter of approximately 13.0Å is found, suggesting that the crystal structure can not accommodate more oxygen than δ=0.1, thus the upper compositional limit of $BaLaMnO_{4.1}$ is proposed. This is comparable with the values found for $La_2CuO_{4+\delta}$ (δ_{max}=0.13) and $La_2NiO_{4+\delta}$ (δ_{max}=0.17) [JDP+88] [RB93].

Reduction of $BaLaMnO_4$ in hydrogen at elevated temperatures showed an increase of the c-axis parameter, this is in agreement with the observations for the oxidized samples. As reduction occurs Mn^{3+} is substituted by the larger Mn^{2+} cation

[2]The sums of the ionic radii are 1.995Å and 1.880Å (for Mn^{3+}-O^{2-}) and (Mn^{4+}-O^{2-}), respectively [Sha76]

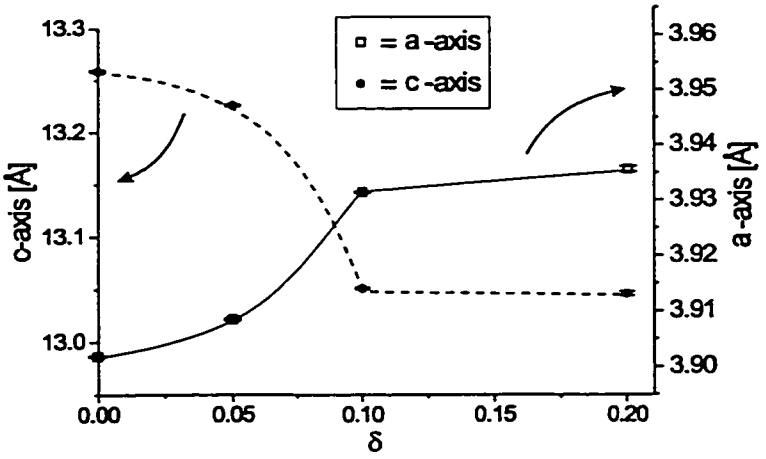

Figure 4.9: Evolution of the a-axis and c-axis parameter for $BaLaMnO_{(4+\delta)}$. The samples were prepared according to reaction 4.4.2, δ is the nominal oxygen excess. The lines serve to guide the eye.

[3]. Again the a-axis increases slightly for reduced compounds. No quantification of the reduction could be carried out but the upper limit for the c-axis is approximately 13.52Å.

4.5.5 Neutron Diffraction Study on $BaLaMnO_{(4\pm\delta)}$

The nominally stochiometric $BaLaMnO_4$ phase was oxidized at 500°C for 12 hours in pure oxygen ($BaLaMnO_{4+\delta}$). A reduced sample was prepared under the same conditions in pure hydrogen ($BaLaMnO_{4-\delta}$). High resolution neutron diffraction experiments were carried out at IPNS at room temperature. The obtained diffraction patterns are shown in figure 4.10. For all three samples all peaks except one were indexed on the tetragonal unit cells, where the d-spacings of the non-indexed peaks (indicated by stars) show the same reduction - oxidation dependence

[3]The sum of the ionic radii is 2.160Å for Mn^{2+}-O^{2-} [Sha76].

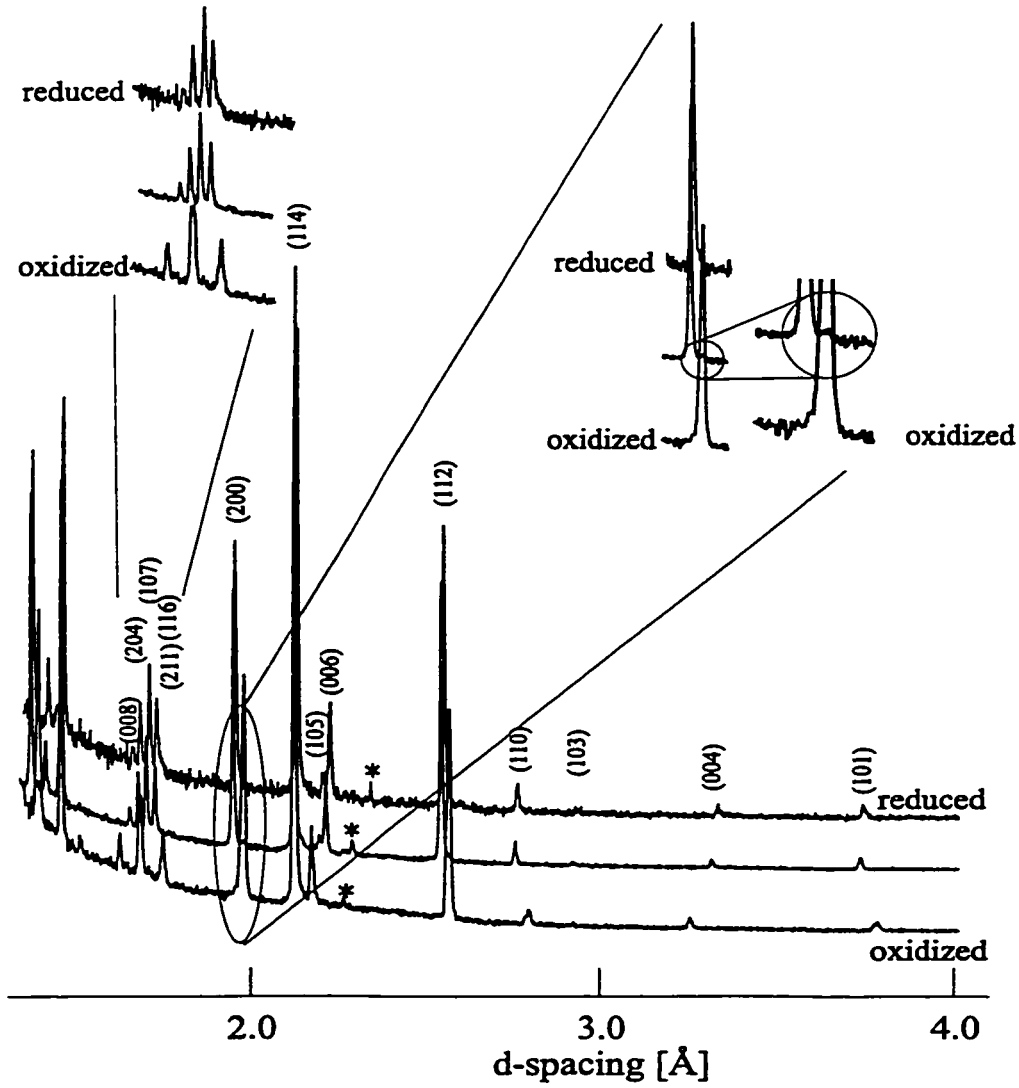

Figure 4.10: Neutron diffraction patterns for $BaLaMnO_4$ (in the middle) an oxidized form (bottom pattern) and a reduced sample of $BaLaMnO_4$. The $BaLaMnO_4$ sample and the reduced sample show very similar diffraction patterns, the only variations are due to differences in the unit cell constants. The oxidized form shows fewer peaks which is due to peak overlap. The reduced form has larger a and c-axis parameters, whereas the oxidized sample has a longer a-axis and a shorter c-axis. The insets show the presence of small peaks of the oxidized sample in the nominally stochiometric $BaLaMnO_4$ sample. The stars indicate an unidentified impurity.

than the (00ℓ) peaks of the tetragonal phase. Furthermore, the nominally stochiometric sample shows indication of the presence of a small fraction of the oxidized phase, the right inset of figure 4.10 emphasizes this. The minute amount of the oxidized phase can explain the ferromagnetic response for this sample. As the sample is reduced both unit cell parameters increase, whereas oxidation results in an elongated a-axis and a smaller c-axis. The unit cell constants for these samples are presented in table 4.3. The oxidized sample seems to show fewer diffraction peaks

Table 4.3: Unit cell constants as determined from neutron diffraction experiments at room temperature for a nominally stochiometric sample of $BaLaMnO_4$, an oxidized sample ($BaLaMnO_{4+\delta}$) and a reduced sample ($BaLaMnO_{4-\delta}$).

	a [Å]	c [Å]	V [Å^3]
$BaLaMnO_4$	3.90252(6)	13.2660(3)	202.036(6)
$BaLaMnO_{4-\delta}$	3.9089(1)	13.3243(5)	203.59(2)
$BaLaMnO_{4+\delta}$	3.9553(1)	13.0230(5)	203.74(2)

which is due to peak overlap caused by the unit cell constant evolution. The inset on the left hand of figure 4.10 shows the resulting peak overlap including two barely resolved reflections for the oxidized sample. The reduced sample, $BaLaMnO_{4-\delta}$, was refined in space group $I4/mmm$. The Rietveld refinement is shown in figure 4.11 and the crystallographic data are presented in table 4.4. The reduction is achieved via the formation of oxygen defects, resulting in a stochiometry of $BaLaMnO_{3.88}$. The molar ratio for Ba:La is 0.52:0.48 as determined from the bond valence sums and equation 1.6.13.

The oxidized sample shows broad background signals underneath the intense peaks. Several attempts to refine the structure in $I4/mmm$, $Bmab$ and $Fmmm$ (according to [JDP+89] and [RB93]) were undertaken, but the broad features prevented

Table 4.4: Agreement factors, crystallographic parameters and bond lengths for $BaLaMnO_{4-\delta}$ as determined from Rietveld refinement of powder neutron diffraction data at room temperature.

Number of data points	:	5499	Space group	:	$I4/mmm$
Number of parameters	:	30	a [Å]	:	3.9089(1)
R_{wp}	:	8.95	c [Å]	:	13.3243(5)
R_p	:	5.41	V [Å^3]	:	203.59(2)
$reduced\chi^2$	:	1.377			

Atom	x	y	z	$U_{iso}/U_e \times 100$	Occupancy
Ba(1)	0	0	0.35648(16)	1.03(8)	0.5
La(2)	0	0	0.35648(16)	1.03(8)	0.5
Mn(3)	0	0	0	1.17(12)	1
O(4)	0	0	0.16968(21)	3.88(12)	1
O(5)	1/2	0	0	2.38(12)	0.944(13)

	distance [Å]	Atom	bond valence sum
Mn-O(4) × 2	2.2608(28)		
Mn-O(5) × 4	1.9544(1)	Ba^{2+}(1)	2.796
<Mn-O>	2.06	La^{3+}(2)	2.061
		Mn^{3+}	2.884
Mn-Mn (intraplanar)	3.9089(1)		
Mn-Mn (interplanar)	7.213(1)		
Ba(1)-(O4a)	2.4891(32)		
Ba(1)-(O4) ×4	2.7859(5)		
Ba(1)-(O5) ×4	2.7343(15)		

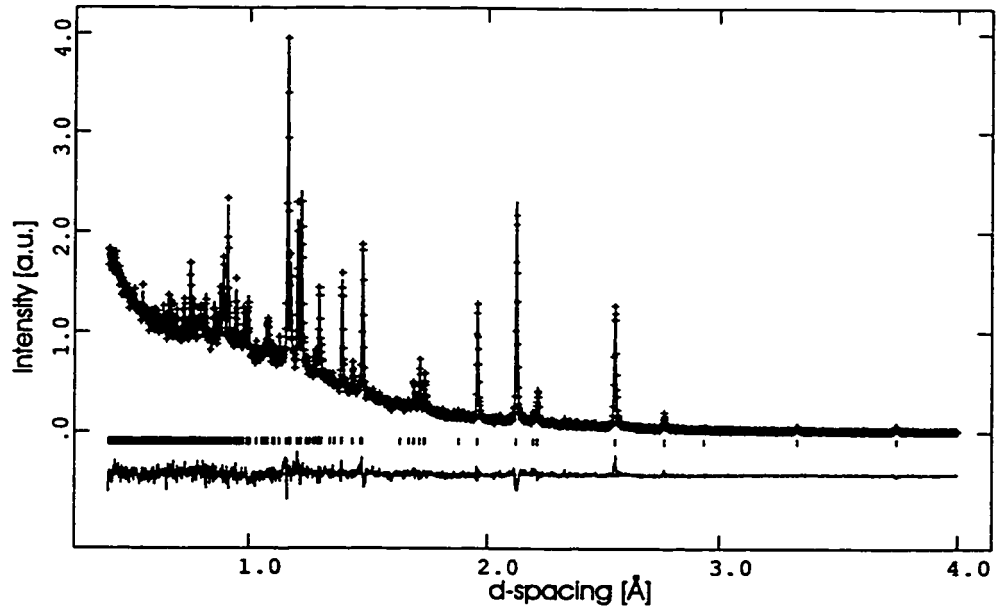

Figure 4.11: Powder neutron diffraction refinement for $BaLaMnO_{4-\delta}$, the data were obtained at room temperature at IPNS.

a meaningful refinement. It is suggested that a small amount of differently oxidized phases are present, causing a distribution of unit cell constants, which appear as a broad background. This is supported by high resolution x-ray diffraction data showing approximately twice the peak widths for the oxidized sample than for the Si standard lines.

4.6 $SrLaMnO_4$

In 1988 Kawano et al. [KAKA88] reported the magnetic properties of $SrLaMnO_4$. From neutron diffraction data the authors determined a magnetic moment of $0.8(2)\mu_B$ for the Mn^{3+}-sublattice. The neutron diffraction patterns presented in the publication contradict this result. The powder neutron pattern resembles

the neutron diffraction pattern of our sample collected at McMaster nuclear reactor. Despite the lack of high angle diffraction data (essentially only the data from 10 to 35° in 2θ are available) a magnetic moment of $3.3(2)\mu_B$ is estimated. This value was determined using the crystallographic model of $Ba_{0.05}Sr_{0.95}LaMnO_4$ for $SrLaMnO_4$ and the refinement of only 4 parameters (zero point, scale factor, background offset and magnetic moment magnitude). The model for the magnetic structure (see figure 4.18) involves a $\sqrt{2}$ relation between the a-axis for the magnetic and the crystallographic unit cell, the magnetic moments are oriented along the crystallographic c-axis [KAKA88] and [MTA$^+$95]. Furthermore, simulations with a magnetic moment magnitude of $0.8\mu_B$ reveal that the magnetic diffraction peaks barely exceed the noise level, whereas the data of Kawano et al. clearly indicate the presence of intense magnetic Bragg peaks. The main criterion for the determination of the magnetic moments are the intensities of the magnetic Bragg peaks $(100)_{mag}$ and $(101)_{mag}$ compared with the nuclear peak $(112)_{cryst}$. Figure 4.12 compares the simulated neutron diffraction patterns for magnetic moment magnitudes of $0.8\mu_B$ and 3.3 μ_B with experimental data obtained at McMaster nuclear reactor and the data Kawano et al. published. Obviously the value of $0.8\mu_B$ for the magnetic moment of Mn^{3+} is not correct. Whereas, the simulated pattern for $3.3\mu_B$, the McMaster data set as well as the data set published by Kawano et al. agree very well. Furthermore, our estimated value is in agreement with the series $Ba_xSr_{(1-x)}LaMnO_4$. It should be mentioned that the Néel temperature of 180K reported by Kawano et al. is very questionable as well. The McMaster sample revealed a transition temperature of T_N=128K, which again is in agreement with other results presented in this chapter, the unit cell constants of the prepared samples are a=3.7934(3)-3.7979(3) Å and

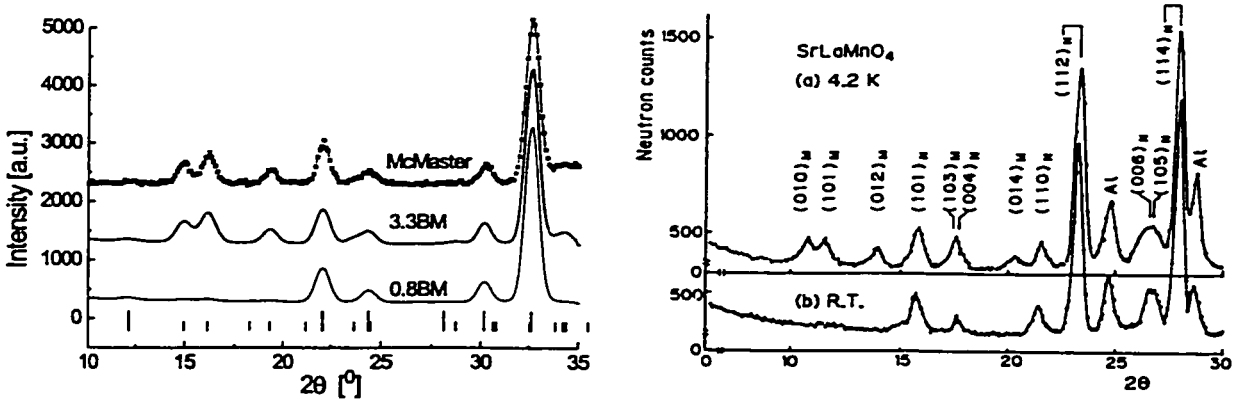

Figure 4.12: Comparison of simulated neutron diffraction patterns (solid lines) with actual data set for $SrLaMnO_4$ as obtained at McMaster nuclear reactor at 10K (λ=1.392Å). The right figure shows neutron diffraction patterns taken from [KAKA88] ($\lambda \approx 1.0$Å) (reproduced with permission).

c=13.102(1)-13.134(1)Å. The magnetic moments as estimated from powder neutron diffraction experiments (McMaster nuclear reactor) are shown in figure 4.13. For $SrLaMnO_4$ Moritomo et al. [MTA+95] reported a Néel temperature of ≈120K for a single crystal with unit cell constants of a=3.80Å and c=13.17Å. The antiferromagnetic transition seen in the magnetic susceptibility data and the absence of ferromagnetism suggest that this sample is stochiometric. Magnetic susceptibility data of the McMaster sample showed a small extent of ferromagnetic response, confirming, that the slightly smaller c-axis constant as found for that sample is due to a small degree of oxidation. However, Benabad et al. [BDSlF77] reported a=3.804(5)Å and c=13.10(1)Å, again the short c-axis parameter might be due to partial oxidation.

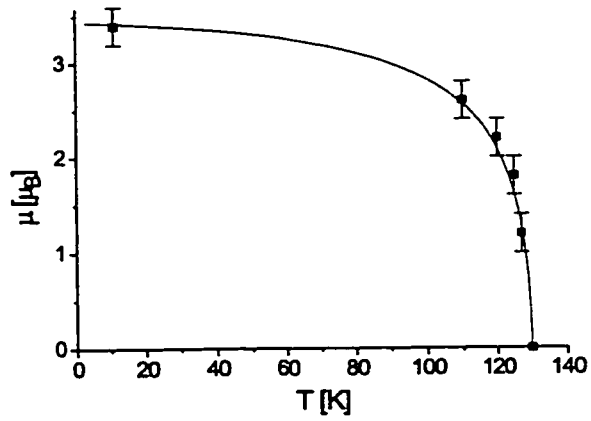

Figure 4.13: Evolution of the magnetic moment for $SrLaMnO_4$ as determined from powder neutron diffraction data, λ=1.392Å. Due to the limited 2θ range (10 to 35°) the indicated error bars are rather large. The solid line serves to guide the eye.

4.7 The Solid Solution $Ba_xSr_{(1-x)}LaMnO_4$

The fact that $SrLaMnO_4$ shows magnetic long range ordering at low temperature and the lack of such ordering for $BaLaMnO_4$ raises the question at what Ba^{2+} concentration the magnetic long range order disappears. The substitutional solid solution $Ba_xSr_{(1-x)}LaMnO_4$ is investigated in order to investigate the limiting x value for a Néel state.

4.7.1 Evolution of Unit Cell Constants

The unit cell dimensions of the series $Ba_xSr_{(1-x)}LaMnO_4$ were determined from x-ray powder data collected with a high resolution Guinier Hägg camera as well as with high resolution neutron diffraction data collected at IPNS. The evolution of the unit cell axes a and c as a function of Ba-content is shown in figure 4.14. The unit cell constants evolve fairly smoothly as a function of the composi-

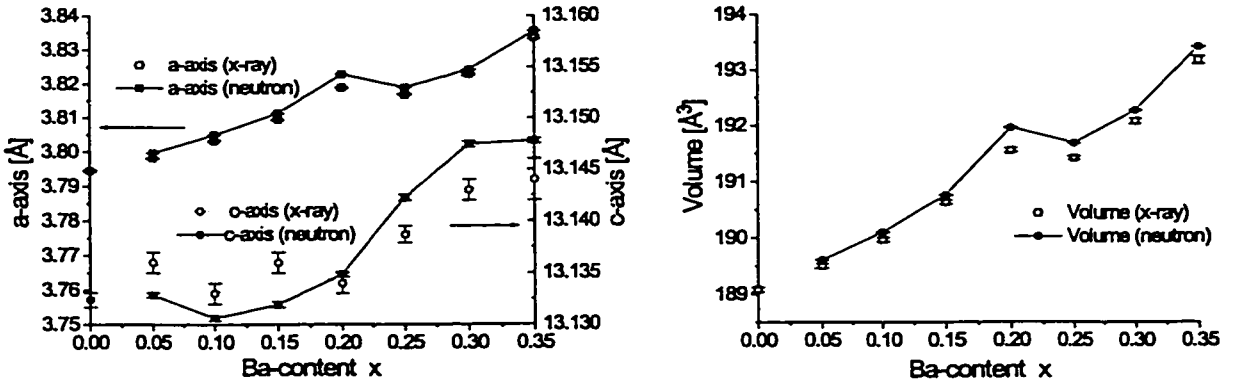

Figure 4.14: Unit cell constant evolution at room temperature for the series Ba_x-$Sr_{(1-x)}LaMnO_4$. The right figure shows the unit cell volume as a function of the composition x. The agreement between the results obtained from high resolution x-ray and neutron data is very good.

tion. However, at x=0.25 an inflection point is found which is of major importance. Most likely, phase segregation takes place for $x \geq 0.25$. However, this phase segregation involves two very similar phases which are not easy to identify. This result will be supported by magnetic measurements, and temperature dependent neutron diffraction measurements. Furthermore, oxidation of one of the accompanying phases can not be ruled out. From the unit cell constants the tolerance factors for all compounds are determined using equation 4.1.1. The results are presented in table 4.5 and the tolerance factors indicate that the K_2NiF_4 structure is stable for all compositions. The correctness of the overall cation stochiometry for all compounds was confirmed with atomic emission spectroscopic measurements. The Ba^{2+} concentration as determined from atomic emission spectroscopy is shown in table 4.6. However, the nominal compositions x=0.25, 0.30 and 0.35 show the presence of an impurity phase.

Table 4.5: Tolerance factors ($t_{(Poix)}$) determined with equation 4.1.1 and unit cell constants for the series $Ba_xSr_{(1-x)}LaMnO_4$.

x	:	t_{Poix}	a [Å]	c [Å]	V [Å^3]
0.00	:	0.934	3.804(5)	13.10(1)	189.6(6)
0.05	:	0.934	3.7982(2)	13.136(1)	189.50(3)
0.10	:	0.935	3.8033(2)	13.133(1)	189.97(3)
0.15	:	0.937	3.8095(2)	13.136(1)	190.63(3)
0.20	:	0.939	3.8190(2)	13.134(1)	191.56(3)
0.25	:	0.939	3.8169(2)	13.1387(8)	191.41(3)
0.30	:	0.941	3.8229(3)	13.143(1)	192.07(4)
0.35	:	0.943	3.8337(4)	13.144(2)	193.18(7)
1.00	:	0.971	3.8988(3)	13.259(1)	201.55(5)

4.7.2 Magnetic Susceptibility Measurements

Low Temperature Magnetism

Bulk magnetic susceptibility measurements were carried out for the compounds $Ba_xSr_{(1-x)}LaMnO_4$ ($0.05 \leq x \leq 0.35$) using a magnetic field of 0.01T. The data sets are shown in figure 4.15, where for sake of comparison all data are plotted on a common scale. The χ versus T curves all show maxima in the temperature range 50K to 100K. The maxima represent the Néel temperatures, these ordering temperatures are consistent with the disappearance of magnetic Bragg peaks (figure 4.21 on page 141). In contrast the determination of Néel temperatures using the derivative $\partial(\chi T)/\partial T$ (equation 3.6.1 on page 73) yielded values which were approximately 10K lower than the maxima for the χ versus T plots. Obviously the Néel temperatures decrease as the Ba^{2+} content is increased. This finding is expected for a solid solution. Furthermore, magnetic susceptibilities increase and the maxima become less distinct as Sr^{2+} is substituted by Ba^{2+}, this is accompanied by

Table 4.6: Comparison of nominal Ba concentration in $Ba_xSr_{(1-x)}LaMnO_4$ with molar fraction of Ba as determined from atomic emission spectroscopy.

x nominal	x AES
0.00	0.00
0.05	0.06(2)
0.10	0.11(2)
0.15	0.15(2)
0.20	0.21(2)
0.25	0.23(2)
0.30	0.29(2)
0.35	0.34(2)
1.00	1.00

the onset of field cooled - zero field cooled divergence. As a result for the sample of nominal composition $Ba_{0.30}Sr_{0.70}LaMnO_4$ the maximum appears only as a shoulder. The Néel temperatures for x=0.20, 0.25 and 0.30 are essentially identical and it is suggested that the magnetically ordered phases for these compositions have a similar stochiometry. This is supported by the presence of impurities. A phase segregation into a Ba-rich and a Ba-poor phase can explain this finding. It should be mentioned that a sample with composition $Ba_{0.35}Sr_{0.65}LaMnO_4$ shows a typical ferromagnetic response, no sharp maximum is seen, but a 10 to 20-fold increase in magnetic susceptibility with respect to the remaining samples is found at low temperature. Consequently, for this compound no information regarding magnetic ordering can be extracted from bulk magnetic measurements, as the ferromagnetic response would mask a possible antiferromagnetic ordering temperature. In order to determine possible magnetic ordering powder neutron diffraction experiments are required. At a later point (section 4.8.2) neutron diffraction data will be presented

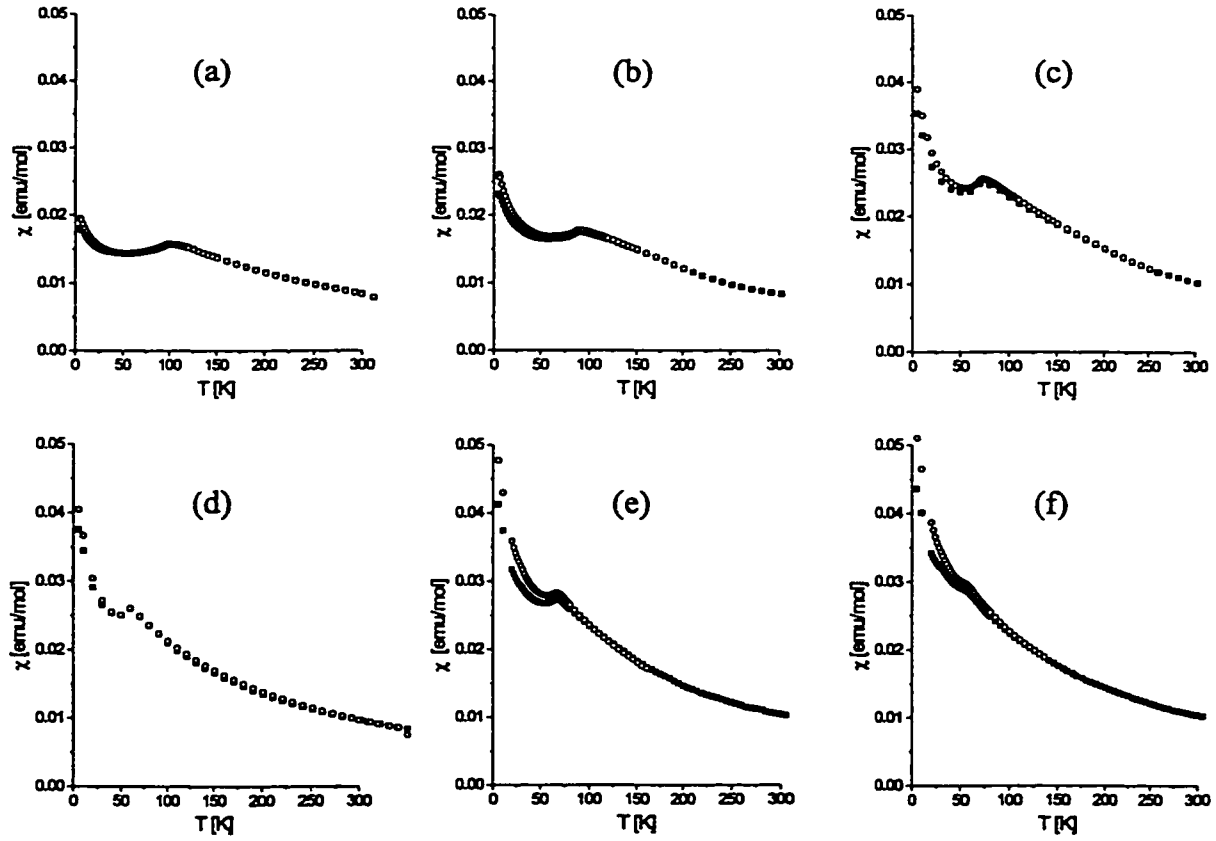

Figure 4.15: Magnetic susceptibility data for $Ba_xSr_{(1-x)}LaMnO_4$ (solid squares = ZFC, open circles = FC) using a magnetic field of 0.01T. Where (a) x=0.05, (b) x=0.10, (c) x=0.15, (d) x=0.20, (e) x=0.25 and (f) x=0.30.

for all of these samples. It turns out that magnetic susceptibility measurements are particularly sensitive to oxygen excess in the system $Ba_xSr_{(1-x)}LaMnO_4$. According to the Goodenough rules Mn^{4+} and Mn^{3+} couple ferromagnetically for a 180° bridging angle, while Mn^{3+}-O-Mn^{3+} couple antiferromagnetically. Therefore, the presence of ferromagnetic fractions in the samples is indicative for small degrees of oxidation, but at the same time it prevents a meaningful analysis of the antiferromagnetic phase from bulk susceptibility data.

The Curie Weiss Regime

The effective magnetic moments and Weiss temperatures as determined from high temperature magnetic susceptibility data are summarized in table 4.7, no temperature independent term was required for the fits. The Curie-Weiss plots

Table 4.7: Effective magnetic moments and Weiss temperatures obtained from Curie-Weiss fits (≈350K to 600K) (equation 3.6.2) and Néel temperatures from low temperature data for the series $Ba_xSr_{(1-x)}LaMnO_4$.

x	:	μ_{eff} [μ_B]	θ [K]	T_N
0.05	:	5.06(2)	-89(6)	100(5)
0.10	:	4.53(3)	-40(7)	92(2)
0.15	:	4.61(3)	-10(1)	74(2)
0.20	:	4.85(2)	-8(4)	65(5)
0.25	:	5.22(10)	-39(4)	66(2)
0.30	:	5.38(3)	-48(1)	58(2)
1.00	:	5.18(3)	5(2)	-

can be found in Appendix C (page 194). $Ba_{0.35}Sr_{0.65}LaMnO_4$ does not show any Curie-Weiss behaviour in the accessible temperature range (maximum T is 600K), consequently no effective magnetic moment and no Weiss temperature are available.

4.8 Magnetic Long Range Order

4.8.1 Powder Neutron Diffraction Studies

Low temperature powder neutron diffraction experiments were carried out on diffractometer C2 in Chalk River. The temperature range 10K to 240K was covered in order to follow the sublattice magnetization for magnetic long range ordered states and to identify possible crystallographic changes. In particular the

tetragonal distortion of the Mn-O_6 octahedra as a function of temperature was investigated and the results will be presented in section 4.10.

4.8.2 Thermodiffractometry

Figure 4.16 shows temperature dependent neutron diffraction patterns for polycrystalline $Ba_{0.05}Sr_{0.95}LaMnO_4$. Below 100K additional Bragg peaks are observed which are of magnetic origin, these peaks can be indexed on a magnetic unit cell with unit cell constants $a_{mag} = \sqrt{2} \times a_{cryst}$, the "magnetic reciprocal lattice translation vector" is $\underline{k} = (1/2, 1/2, 0)$. The appearance of additional Bragg reflections coincides with the Néel temperature of T_N=95K as determined from bulk magnetic susceptibility data (see section 4.7.2). At T=100K only a very broad maximum centered close to the $(100)_{mag}$ peak position is observed. This broad feature is due to magnetic short range order, which will be dealt with in section 4.9. At temperatures considerably higher and lower than the Néel temperature the broad feature is less pronounced, this supports that this signal is of magnetic origin.

4.8.3 Magnetic Ordering

The neutron diffraction patterns were analysed using the Rietveld refinement package FullProf [RC98]. Above the Néel temperature only the crystallographic phase was refined using 24 parameters, including background, zero shift, peak shape and asymmetry, atomic positions, temperature factors and the unit cell constants. The low temperature data sets were described using an additional magnetic phase. The magnetic phase requires a larger unit cell, with a $\sqrt{2}$ relation between the crystallographic and magnetic unit cell axes a. The second phase only required one additional parameter for the refinement (in total 25 parameters),

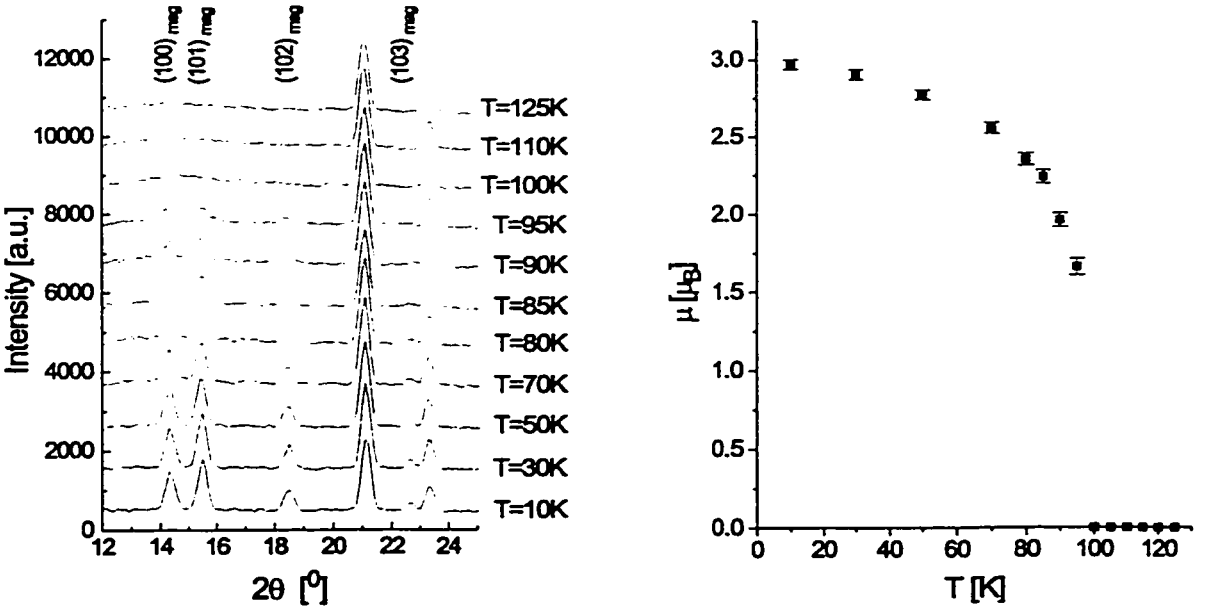

Figure 4.16: Neutron diffraction patterns (λ=1.32632(7)Å) for $Ba_{0.05}Sr_{0.95}LaMnO_4$. The Miller indices refer to the corresponding unit cells, where the magnetic unit cell constant $a_{mag} = \sqrt{2} \times a_{cryst}$. The right figure shows the evolution of the magnetic moment magnitude as a function of the temperature as refined from the full powder diffraction data sets.

namely the magnetic moment magnitude. Figure 4.17 shows a refined data set for $Ba_{0.05}Sr_{0.95}LaMnO_4$ at 10K, the crystallographic and magnetic Bragg peaks are indexed on the corresponding unit cells. All magnetic peaks with indices (00ℓ) are absent, indicating that the magnetic moment component is zero in the ab-plane. Consequently, the spins are aligned along the c-axis and no magnetic moment orientation was refined. The magnetic structure is shown in figure 4.18. The refined magnetic moment shows a smooth moment magnitude evolution as a function of the temperature with a saturation at approximately $3.0\mu_{BM}$ below 20K. The temperature dependence is shown on the right side of figure 4.16, the R-values and magnetic

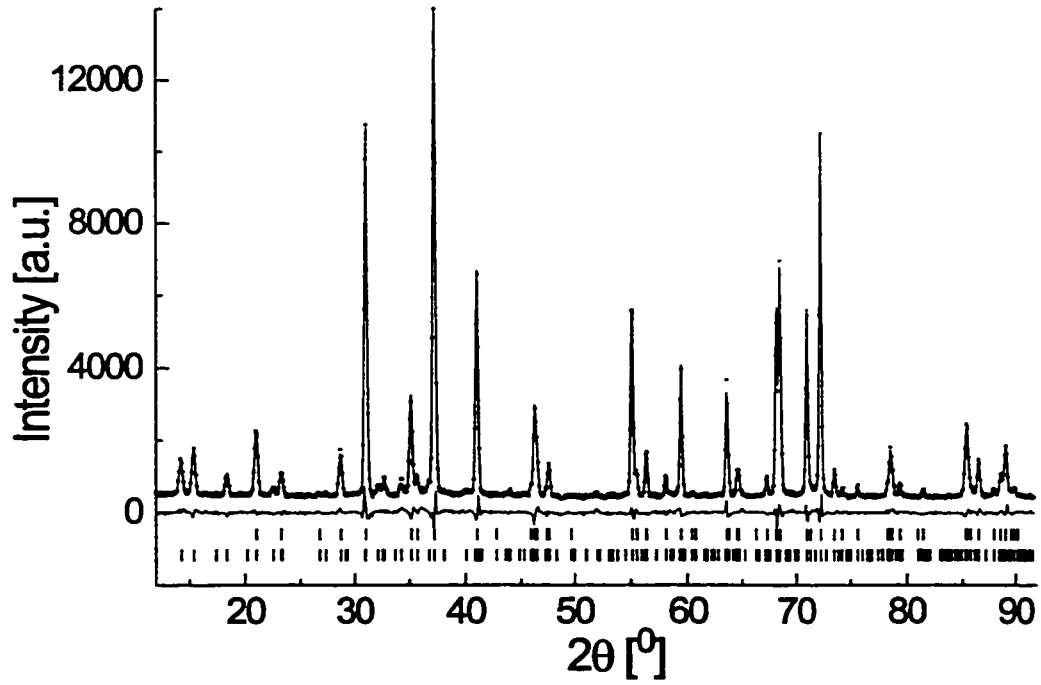

Figure 4.17: Neutron powder diffraction pattern for $Ba_{0.05}Sr_{0.95}LaMnO_4$ at T=10K, λ=1.32587Å. The crystallographic and magnetic phases were refined simultaneously, the crosses are experimental data, the best fit and difference plot are shown as solid lines. The upper and lower tick marks correspond to the expected Bragg peaks for the crystallographic and magnetic phase respectively.

moments are tabulated in table C.1 in appendix C. Note, that the expected magnetic moment of $4.0\mu_{BM}$ is not reached, which is not uncommon for frustrated systems.

The magnetic structures of all members of the series $Ba_xSr_{(1-x)}LaMnO_4$ were determined using the same procedure. All members with x smaller than 0.25 show magnetic long range order as is easily deduced from the the thermodiffractometric experiments. Furthermore, all magnetically ordered members form the same spin structure, which is shown in figure 4.18. However, the derived magnetic saturation moments show an astonishing behaviour. The saturation values decrease

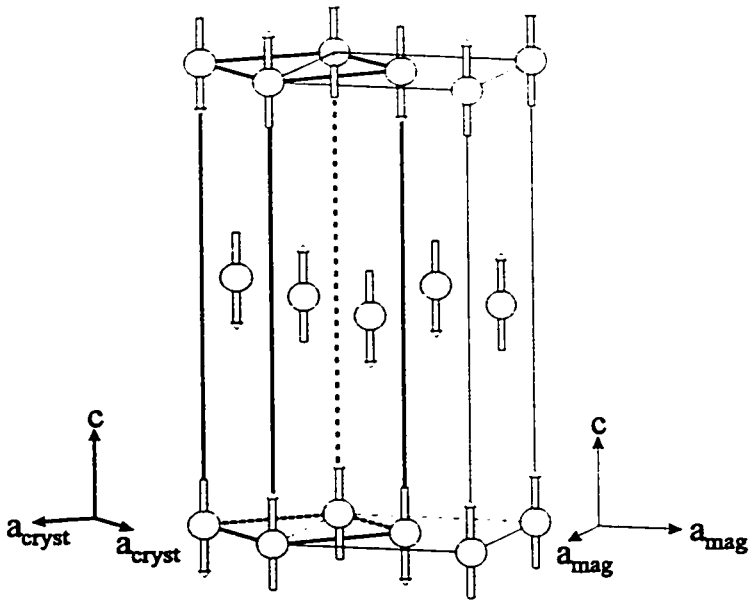

Figure 4.18: Representation of the magnetic structure for the series $Ba_xSr_{(1-x)}LaMnO_4$ with x<0.25, only the Mn^{3+} positions and the corresponding magnetic moment orientations are indicated. The magnetic ordering vector is k=(1/2,1/2,0). The crystallographic unit cell is out-lined in bold on the left, the magnetic unit cell is shown on the right.

sharply with increasing x as seen in figure 4.19. The finding of such strongly reduced magnetic moments is surprising as only a substitution of diamagnetic cations is involved, the Mn^{3+} ion concentration is the same for all compounds. Consequently, the same magnetic moments would be expected for all members of the solid solution $Ba_xSr_{(1-x)}LaMnO_4$. Some reduction of the Néel temperature with increasing x might be expected as Ba^{2+} is larger than Sr^{2+} and as a result the unit cell constants increase with increasing x. As was shown on page 129 the orbital overlap between Mn^{3+} and O^{2-} should diminish which causes weaker magnetic exchange coupling and thus a decreased ordering temperature. A smaller magnetic moment than the

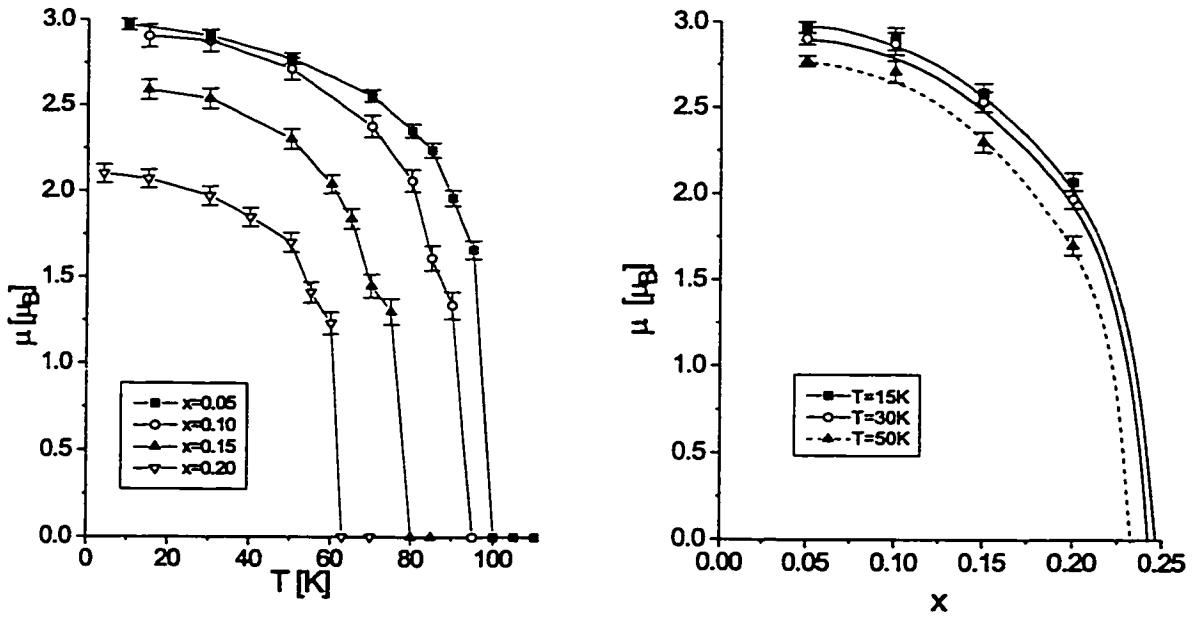

Figure 4.19: The left figure shows the evolution of magnetic moment magnitude as a function of the temperature T for 4 different compositions. The right figure shows the x-dependence of the magnetic moments for 15K, 30K and 50K. The lines are only a guide for the eye. However, the extrapolated magnetic moments are consistent with the lack of ordering at x=0.25.

value expected from the number of unpaired electrons is common for magnetically frustrated systems. Since a systematic reduction of μ_{BM} as a function of x is found it is concluded that the degree of magnetic frustration increases as Sr^{2+} is substituted by Ba^{2+}. The origin of this behaviour is not understood and requires more detailed crystallographic studies as a function of composition x and temperature T. In order to estimate the disappearance of magnetic long range order the low temperature magnetic moments are plotted as a function of the composition x. These data are shown on the right side of figure 4.19. Connecting the data points for each temperature and extrapolating with a smooth function yields x-intercepts of less

than 0.25. It should be pointed out, that there is no mathematical or physical basis for this extrapolation, but from this qualitative estimate it can be concluded that the lack of magnetic long range order for x=0.25 is not unreasonable. All R-values and magnetic moments are tabulated in appendix C.

4.9 Magnetic Short Range Order

Two-dimensional short range order can be identified from a broad asymmetric peak where the peak maximum is shifted towards larger diffraction angles with respect to the corresponding Bragg peak. The Warren-line shape is described by equation 4.9.1.

$$P_{2\theta} = K\ m\frac{F_{hk}^2\,(1+\cos^2 2\theta)}{2\,(\sin\theta)^{3/2}}\frac{(\xi_{2D})^{1/2}}{\pi\lambda}F(a) \qquad (4.9.1)$$

where a=$(2\pi\sqrt{\pi}L/\lambda)(\sin\theta - \sin\theta_0)$, K is a constant, m is the multiplicity, F_{hk} is the two-dimensional structure factor, λ is the wavelength, ξ_{2D} is a two-dimensional correlation length, and θ_0 is the peak position. The function $F(a)$ is tabulated [War41]. Using equation 4.9.1 a 2-dimensional correlation length of $\xi_{2D} = 21(3)$Å is determined for $Ba_{0.05}Sr_{0.95}LaMnO_4$. The 2-dimensional correlation length is temperature independent for the temperature range 100K to 125K. The fits to the Warren line shape for the $(10)_{mag}$ reflection are shown in figure 4.20. The asymmetry of the broad feature underneath the $(100)_{mag}$ and $(101)_{mag}$ reflections indicates 2-dimensional domains. The powder neutron diffraction data for four samples are compared in figure 4.21, the x-axis is compressed in order to make the broad feature associated with 2-dimensional magnetic short range order recognizable. It is apparent that only the data sets for sample $Ba_{0.05}Sr_{0.95}LaMnO_4$ are of good enough quality to quantify the 2-dimensional magnetic correlation lengths. All samples show broad

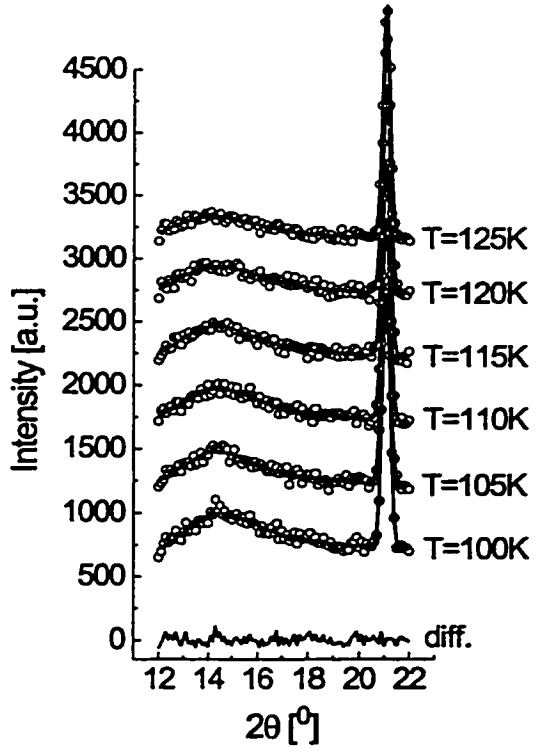

Figure 4.20: Warren fits for the broad 2-dimensional $(10)_{mag}$ reflection for $Ba_{0.05}$-$Sr_{0.95}LaMnO_4$. The Bragg peak at $2\theta \approx 21°$ is the $(101)_{cryst}$ reflection. The open circles are the observed powder neutron diffraction data, $\lambda = 1.326$Å, and the solid lines are the best fits to the Warren function, equation 4.9.1. The solid line at the bottom of the figure shows the differences between the observed data and the best fit for the 100K data set.

asymmetric peaks at temperatures close to T_N this result is in accordance with the findings for $Ba_{0.05}Sr_{0.95}LaMnO_4$. It is concluded that the observed magnetic short range order is best described by 2-dimensional magnetic domains for all members of $Ba_xSr_{(1-x)}LaMnO_4$ ($0.05 \leq x \leq 0.20$).

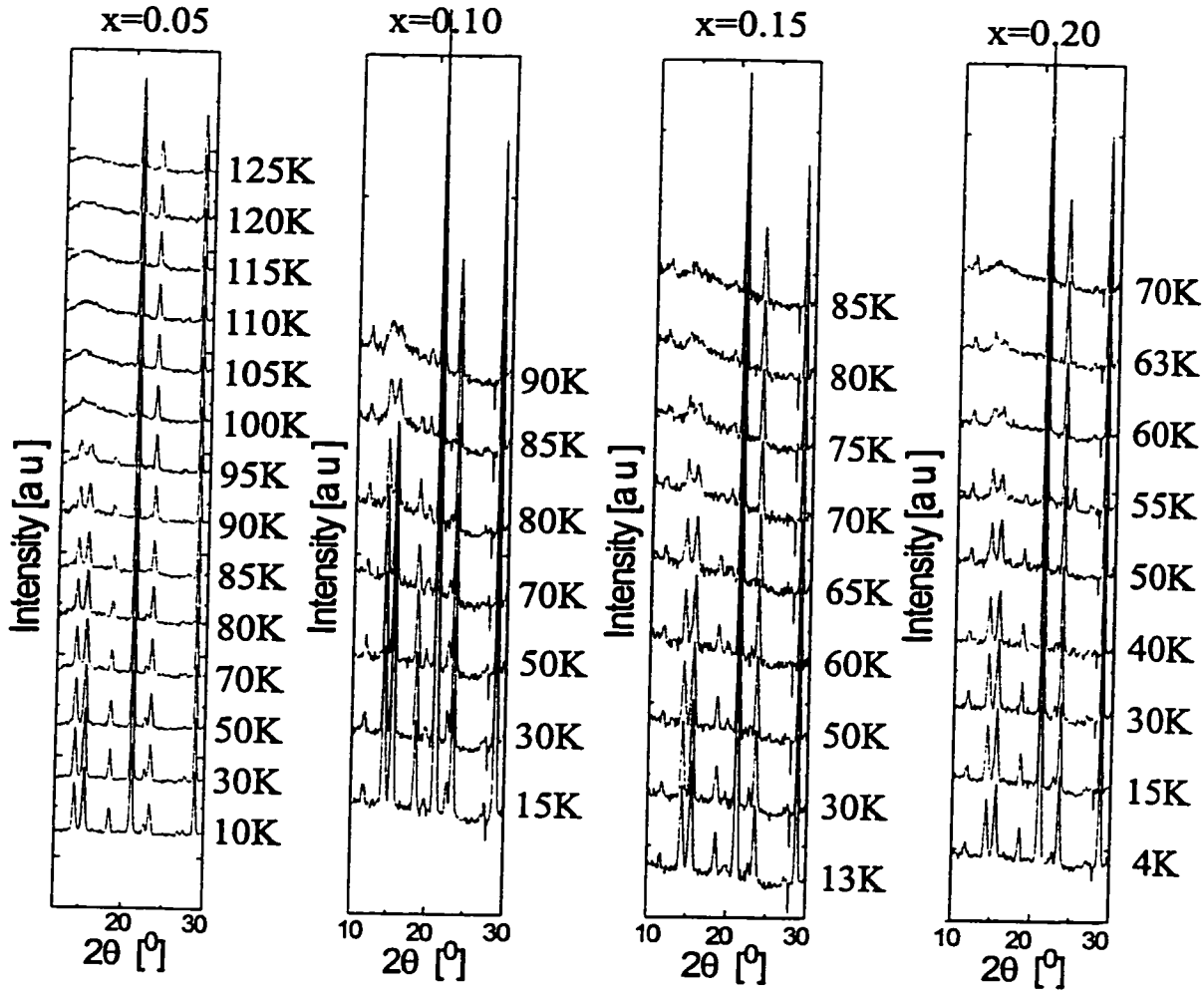

Figure 4.21: Neutron powder diffraction data for four samples of the series Ba_x-$Sr_{(1-x)}LaMnO_4$, the data sets are stacked upwards with increasing temperatures. Magnetic short range order, identified by a broad feature in the vicinity of 15°, is established well below the Néel temperature, the feature is most intense around T_N and diminishes slowly above the ordering temperatures. All data sets were collected on diffractometer C2 at Chalk River using a neutron wavelength $\lambda \approx 1.3$Å.

4.10 Disappearance of Magnetic Long Range Ordering

The lack of magnetic ordering for $Ba_xSr_{(1-x)}LaMnO_4$ for x> 0.20 requires the investigation of intraplanar and interplanar magnetic exchange.

The magnetic exchange coupling is a strong function of the orbital overlap between Mn^{3+} and O^{2-}, it was already mentioned that the K_2NiF_4 structure type shows a distorted B-O_6 environment. This distortion is in part due to the tolerance factor, t, if t is less than one the B-O_6 octahedra show elongation along the c-axis. Furthermore, the Jahn-Teller effect can enhance this distortion. The tolerance factors for $SrLaCoO_4$, $SrLaCrO_4$ and $SrLaFeO_4$ span the range 0.989 - 0.922, whereas the distortion indices, DI, span the range 1.07 - 1.10. In contrast $SrLaMnO_4$ with t=0.901 shows a significantly larger distortion index of $DI = 1.21$. This elongation is attributed to the Jahn-Teller effect. Despite a tolerance factor of t=0.971 $BaLaMnO_4$ shows significant distortion, $DI = 1.145$, which is again attributed to the Jahn-Teller effect of Mn^{3+}. No quantitative results can be extracted but the qualitative result is very reasonable. Obviously, this tetragonal elongation will weaken the interplanar exchange. Figure 4.22 shows the evolution of the distortion index for the Mn-O_6 octahedra for the series $Ba_xSr_{(1-x)}LaMnO_4$. All analyzed compounds show a pronounced temperature dependence for the tetragonal distortion. It should be emphasized that the distortion indices for the compositions x=0.20, 0.25 and 0.30 are identical within experimental error. Throughout the series broadened diffraction lines are found, however, at x=0.25 the FWHM is largest, whereas for x=0.30 the high angle data even show line splitting. It is concluded that the samples are not

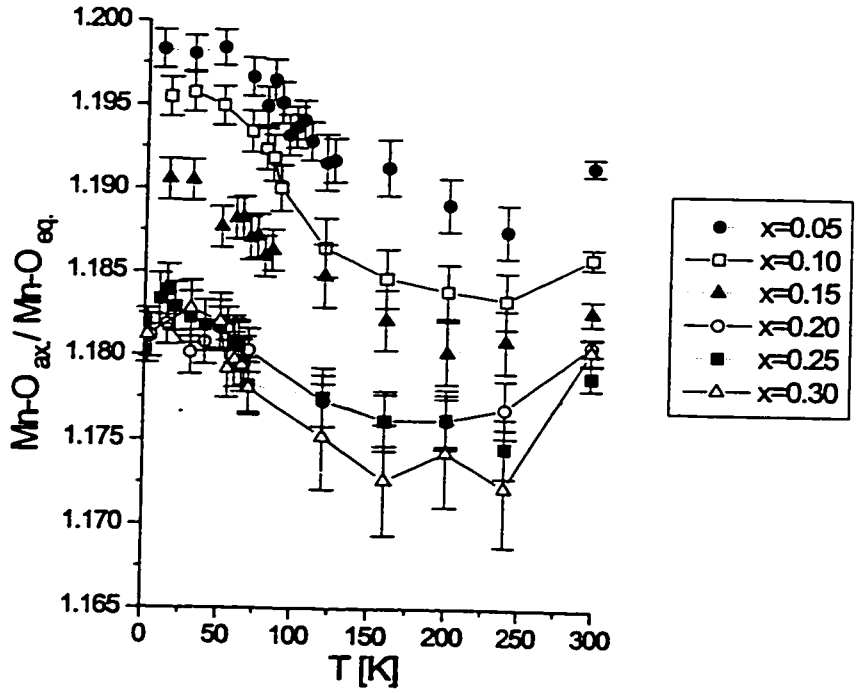

Figure 4.22: Evolution of the octahedral distortion for the series $Ba_xSr_{(1-x)}LaMnO_4$ ($0.05 \leq x \leq 0.30$ as a function of temperature.

single phase and based on the Néel temperatures and distortion indices it is suggested that the nominal composition x=0.25 and x=0.30 are closer to the composition x=0.20. It should be mentioned that all samples except $Ba_{0.05}Sr_{0.95}LaMnO_4$ show slight line broadening for the high resolution x-ray diffraction experiments. The refined magnetic moments at low temperatures are all identical within error for x=0.20, 0.25 and 0.30. A phase segregation into Ba-rich and Ba-poor fractions could explain the magnetic ordering found for x=0.25 and x=0.30, where the Ba-poor fraction seems to be the major phase with a composition close to x=0.20 and the Ba-richer phases are best described by a distribution of compositions. A similar phase segregation was reported for $Sr_2NdMn_2O_7$ [BGL+96] [BGK+97] [BGL+97].

Furthermore, the proposed interplanar exchange path (see figure 4.6 on page 116) includes the large A cation, thus weakening the magnetic exchange coupling between layers. Consequently, for the Ba-rich samples a weaker interlayer coupling than for the Sr-rich samples is expected.

The intraplanar exchange interactions are fairly simple and only the Mn^{3+}-Mn^{3+} distances increase and the intraplanar exchange interactions decrease as Sr^{2+} is substituted by Ba^{2+} .

The lengths of the potential magnetic exchange paths are summarized in table 4.8. Both exchange paths, intraplanar and interplanar, lengthen as a function

Table 4.8: Intraplanar and interplanar magnetic exchange path lengths for Ba_x-$Sr_{(1-x)}LaMnO_4$ as derived from Rietveld refinements of high resolution powder neutron diffraction data obtained on diffractometer SEPD at room temperature.

x	interplanar exchange path [Å]	intraplanar exchange path [Å]
0.05	9.256(5)	3.7997(1)
0.10	9.260(5)	3.8050(1)
0.15	9.266(5)	3.8114(1)
0.20	9.278(5)	3.8229(1)
1.00	9.410(5)	3.9025(1)

of x. The ratio of interlayer over intralayer distances as a function of the composition, x, is plotted in figure 4.23. Which indicates that the intraplanar exchange path lengthens more rapidly than the interplanar pathway. Furthermore, the solid line indicating the extrapolated behaviour based on the compositional range $0.05 \leq x \leq 0.20$ does not intercept with the value found for $BaLaMnO_4$, suggesting that drastic changes between x=0.20 and x=1.00 take place.

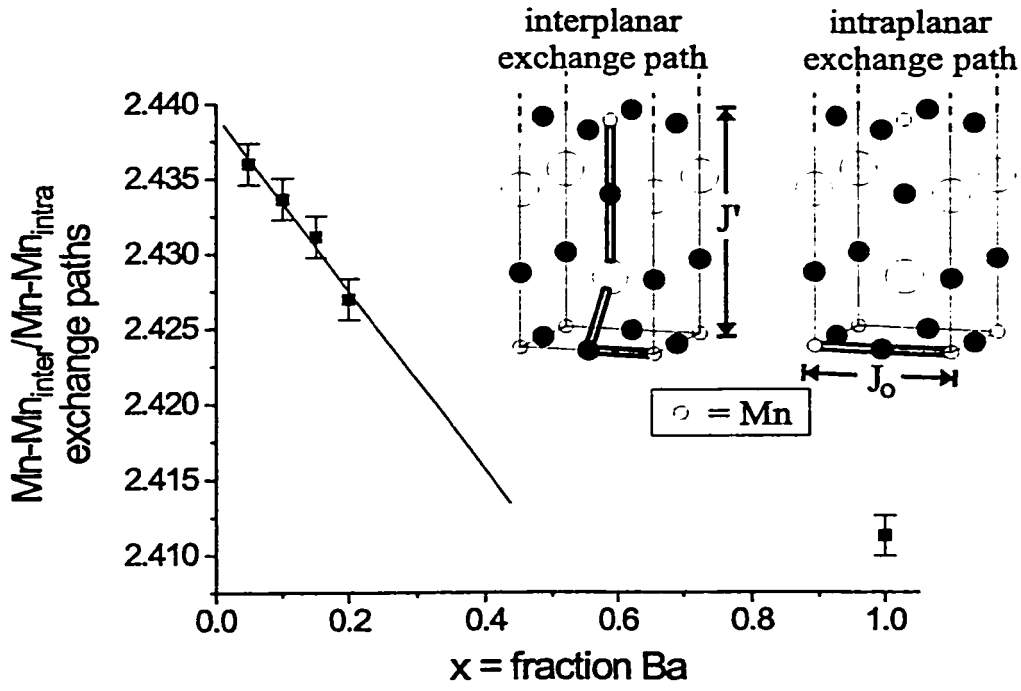

Figure 4.23: Evolution of the exchange path ratio for interplanar over intraplanar distances for the series $Ba_xSr_{(1-x)}LaMnO_4$ at room temperature. The solid line is meant as a guide to the eye. The insets show the magnetic exchange paths.

It is well known that quasi 2-dimensional magnetic systems only show magnetic ordering for a non-zero interplanar coupling constant. However, for very weak interplanar exchange coupling mean-field theory suggests that the ordering temperature T_N is a function of the 2-dimensional magnetic correlation length ξ_{2D}, equation 4.10.1 [dJ90],

$$T_N \approx \xi_{2D}^2 \, J' \frac{S^2}{k} \tag{4.10.1}$$

where J' is the interlayer magnetic exchange constant and k is the Boltzmann constant. It is argued that this limit is reached for the series $Ba_xSr_{(1-x)}LaMnO_4$, such that for x> 0.20 the 2-dimensional magnetic correlation length converges towards

zero and thus no magnetic long range ordering is found for the investigated temperature intervals. The results presented in section 4.9 support small 2-dimensional magnetic correlation lengths, even $Ba_{0.05}Sr_{0.95}LaMnO_4$ with T_N=100(5)K shows only a magnetic correlation length of approximately 21Å in the vicinity of the ordering temperature. Therefore, it is suggested that there is a minimum interplanar coupling constant and a minimum 2-dimensional magnetic correlation length to form a Néel ground state for the square planar lattice.

This qualitative explanation requires additional work in order to quantify critical coupling constants for interplanar to intraplanar interactions which can inhibit magnetic long range order. Furthermore, the cusp in the magnetic susceptibility data for $BaLaMnO_4$ supports the above suggestions, the disorder on the A-cation site (Ba, La disorder) in conjunction with geometric frustration for a body centered lattice could cause the formation of a spin glass state ground state. It is proposed to confirm the potential spin glass ground state with muon spin relaxation measurements and ac-susceptibility measurements.

4.11 Critical Exponents

The critical exponent β is determined from the sublattice magnetization as determined from powder neutron diffraction experiments. Figure 4.24 shows the log(M) versus log(t) plot, where t is defined according to equation 1.2.12 on page 9. According to equation 4.11.1 β is the slope of the linear regression shown in figure 4.24.

$$\log(M) = log(A) + \beta \log\left(\frac{T - T_N}{T_N}\right) \qquad (4.11.1)$$

Strictly speaking equation 4.11.1 is only valid in the vicinity of the critical point

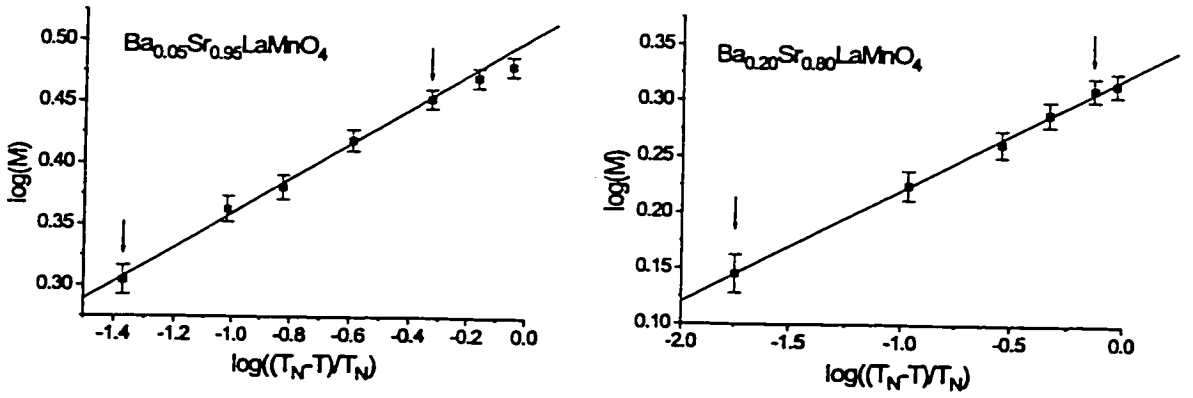

Figure 4.24: Determination of critical exponents β. Two examples are shown, the downwards pointing arrows indicate the range of fitted data. The correlation coefficients are better than 0.99 for all fits.

(here the Néel temperature), however it seems that the data presented here are linear throughout the whole temperature range on the log-log plots. The data density for the determination of the critical exponents is not sufficient to obtain absolute values with high confidence level. The errors presented in table 4.9 are only based on the linear regression algorithm and are most likely underestimated. However, since all data sets were treated in an identical manner, including the use of Néel temperatures as derived from bulk magnetic susceptibility data, the results presented here are useful for the purpose of comparison. Table 4.9 summarizes the critical exponents for the series $Ba_xSr_{(1-x)}LaMnO_4$. As the Ba^{2+} content is increased β decreases. Of all standard models the 2-dimensional Ising magnet predicts a critical exponent (β=0.125) which is closest to the above values for β. The gradual evolution of the critical exponents indicates deviation from the standard model. This in conjunction with the disappearance of magnetic ordering at Ba concentrations larger than 0.2 and the geometric conditions for magnetic frustration require caution when assigning

Table 4.9: Critical exponents β determined using the Néel temperatures shown in the 3rd column and equation 4.11.1.

x	β	T_N [K]
0.00	-	128
0.05	0.141(5)	100
0.10	0.142(6)	92
0.15	0.113(6)	74
0.20	0.101(2)	65

a particular model to this system. These results are in agreement with the findings for K_2NiF_4 β values of 0.15-0.18 [BSS71] [BGS73]. These values are reasonably close to the values found for $Ba_{0.05}Sr_{0.95}LaMnO_4$ and $Ba_{0.10}Sr_{0.90}LaMnO_4$. However, the lower values for the Ba^{2+}-richer compounds may indicate an important change for the ordered state which finally results in the loss of magnetic long range ordering for x>0.20.

4.12 Comparison with K_2NiF_4 and K_2MnF_4

In 1962 LeGrand and Plumier reported on the antiferromagnetic ordering of the Ni^{2+} magnetic moments in K_2NiF_4 with a Néel temperature of 180K [LP62]. In 1964 Plumier commented on broadened magnetic diffraction peaks of the type (h0ℓ) ($\ell \neq 0$), concluding that stacking faults and an orthorhombic distortion might be responsible for the broadened lines [Plu64]. The first single crystal investigation of the magnetic structure was published in 1969 [BGS69]. Two dimensional ordering was concluded from rod shaped diffraction features between 180K and 91.1K, whereas at 97.1K a magnetic phase transition to a 3-dimensional antiferromagnetically ordered structure is observed. Furthermore a critical exponent $\beta = 0.15(1)$ [BGS73] was

reported as well. Although K_2NiF_4 and K_2MnF_4 are nearly Heisenberg antiferromagnets, a small amount of Ising-like anisotropy is present, the easy axis being the c-axis. From neutron diffraction experiments Shirane [SB77] found for both compounds critical exponents which are in agreement with 2-d Ising systems. These findings serve as a support for the results for the solid solution $Ba_xSr_{(1-x)}LaMnO_4$. Obviously the K_2NiF_4 structures represent systems which are at the borderline between 2-dimensional and 3-dimensional magnetic behaviour. Therefore, even small crystallographic changes can cause major changes for the magnetic properties. This has been shown for the system $Ba_xSr_{(1-x)}LaMnO_4$, where the Ba^{2+}-Sr^{2+} substitution can inhibit magnetic long range ordering, which occurs despite the fairly high Néel temperature of approximately 128K for $SrLaMnO_4$.

4.13 Conclusion

$BaLaMnO_4$ and $SrLaMnO_4$ were prepared as polycrystalline samples. $SrLaMnO_4$ shows magnetic long range ordering below 128K, such that all magnetic moments are oriented along the crystallographic c-axis. In contrast $BaLaMnO_4$ does not show any evidence of magnetic long range ordering. The substitutional solid solution $Ba_xSr_{(1-x)}LaMnO_4$ was prepared and it has been shown that magnetic long range ordering only occurs for $x < 0.25$. All long range ordered states show identical magnetic structures. However, neutron diffraction experiments show that the magnetic moment magnitude decreases as the Ba concentration is increased. The effective magnetic moments as determined from high temperature magnetic susceptibility data are consistent with Mn^{3+} in $Ba_xSr_{(1-x)}LaMnO_4$. In the vicinity of the

Néel temperatures 2-dimensional magnetic short range ordering is found. Fits revealed that the 2-dimensional magnetic correlation lengths, ξ_{2D}, are temperature independent. The critical exponents for the sublattice magnetization, β, indicate that the magnetic systems are best described as 2-dimensional Ising antiferromagnets. However, the critical exponents decrease from 0.14 to 0.10 as the Ba content is increased from x=0.05 to x=0.20. Samples with x=0.25, x=0.30 and x=0.35 raised questions concerning the phase purity. High resolution synchrotron x-ray experiments are required in order to investigate a possible phase segregation, consisting of very similar phases. Slightly oxidized samples did not show any magnetic long range ordering for x>0.20. It is noted that the Néel temperatures for the slightly oxidized and non-oxidized samples for x< 0.25 are very similar. The ordering temperatures for the oxidized samples were obtained from powder neutron diffraction experiments, the ferromagnetic response prevented the determination of the Néel temperatures from bulk magnetic susceptibility data. Additional oxygen seems to stabilize the crystal structure and can prevent potential phase segregation. The lack of magnetic long range ordering for x>0.20 is attributed to very weak interplanar magnetic interactions, such that the ordering becomes a function of the 2-dimensional magnetic correlation length, ξ_{2D}. ξ_{2D} decreases with the addition of Ba^{2+} until no long range ordering is observed. It is suggested that there are threshold values for the intraplanar exchange coupling constant, J_o, and the interplanar exchange constant, J', below which no Néel ground state is established.

$BaLaMnO_4$ shows indications of magnetic short range order and even a possible spin glass ground state. The existence of a spin glass state should be

investigated using muon spin relaxation measurements and ac-susceptibility measurements.

Chapter 5

The Tetrahedral Antiferromagnet Li_4MgReO_6

5.1 Introduction

In 1973 a new magnetic ground state for frustrated antiferromagnets was proposed by Anderson [And73]. For the case of a S=1/2 system Anderson suggested a model involving the formation of spin singlets, based on the pairing of adjacent spins, which satisfies the antiferromagnetic coupling condition. It is easy to imagine that there exists a large number of combinations of nearest neighbor singlet pair formations. Consequently, no magnetic long range order is established, but a high degree of degeneracy is achieved by forming linear combinations of individual spin configurations which lowers the total energy. In analogy to the chemical bonding models of Pauling this was called the resonating valence bond (r.v.b.) model. This also represents a spin liquid type ground state, since no "condensation" into either a Néel state or a frozen spin or spin glass state occurs. The different spin configurations of a spin liquid are separated by a zero energy barrier. In 1974 Fazekas and Anderson [FA74] published a detailed analysis of the triangular lattice for S=1/2 spins. It has been pointed out that a high degree of anisotropy is favorable for the

formation of the spin liquid type ground state (see section 1.4.1).

Since 1974 several magnetic systems have been investigated experimentally, in a search for real spin liquids, including $LiNiO_2$ [HNI91], $LiCoO_2$, $NaTiO_2$ [CFH+98] and $SrCr_4Ga_8O_{19}$ [UKK+94] where interesting data concerning the spin dynamics at low temperatures were obtained. In the latter the paramagnetic Cr^{3+} ions are located on a Kagome lattice (corner shared triangular lattice) as well as in layers of edge sharing triangles. Lately, the jarosite family has attracted attention, since this is the first example of a Kagome structure with no disorder present, thus representing an interesting model compound for spin liquid behavior [WH96].

Another interesting ground state, already mentioned, is the spin glass state, where the magnetic moments freeze randomly upon cooling the sample below a characteristic temperature. It is noteworthy, that short range order might be present on the magnetic sublattices (see section 1.4.1). Spin glasses were investigated extensively in the 1970's, in particular dilute metallic spin glasses were considered, whereas interest in spin glasses of magnetic insulators developed in the 1980's. For most cases site disorder on the magnetic sublattice is considered a necessary requirement for the formation of a spin glass ground state. In the two broad classes of spin glasses positional disorder is a prominent feature as the concentration of the magnetic ion on its sublattice is below the appropriate percolation limit. There does exist a small class of insulating magnetic materials in which the magnetic sublattice appears to be fully occupied, i.e. with defect levels at or near the limit of detection by diffraction methods, and thus, with concentration levels well above any percolation threshold, which nonetheless exhibit spin glass like behavior. In such materials the magnetic sublattice is geometrically frustrated and the nearest neighbor exchange

spin coupling is antiferromagnetic. An example is the pyrochlore oxide, $Y_2Mo_2O_7$ [RGS88].

Many of the candidate spin liquid materials mentioned above crystallize in an ordered variant of the NaCl structure, with a 1:1 ratio of magnetic to non-magnetic ions, e.g. $LiNiO_2$, $LiCoO_2$ and $NaTiO_2$. In these cases, order on the cation sublattice results in a geometrically frustrated magnetic sublattice, layers of edge-sharing equilateral triangles. It is of interest to investigate other ordered NaCl structures with different magnetic to non magnetic ion ratios. One such example is the α-Li_2SnO_3 structure type. In this case the Sn^{4+} sublattice consists of layers with honeycomb topology. Cation ordering on half of the sites in such a lattice would result in an edge-sharing triangular layer or a tetrahedral sublattice depending on the layer spacing. The problem, then, is to find a combination of ions which are likely to exhibit charge ordering and one of which is a S=1/2 ion. A solution to the problem may be the material Li_4MgReO_6 in which Re^{6+} ($5d^1$, S=1/2) is paired with Mg^{2+}. This compound was first reported in 1963 along with Li_5ReO_6, which is apparently isostructural, but a detailed crystal structure of Li_4MgReO_6 was not presented [SHP63]. Somewhat later Lang [Lan66] considered the symmetry of different stacking sequences of the Re^{6+} containing layers and suggested monoclinic C2/m and C2/c and trigonal space groups, $P3_112$ and $P3_212$, but again no detailed structure. The availability of only x-ray powder samples has been an impediment to a structure solution. An additional issue with a Re^{6+} material is whether the d-electron will remain localized. ReO_3 is well-known to be metallic, but the ordered perovskite Sr_2MgReO_6 is insulating [FRG65]. Given the level of dilution of Re^{6+} in the proposed cation-ordered structure one would expect Li_4MgReO_6 to be insulating

and magnetic as well.

This chapter presents the preparation of polycrystalline Li_4MgReO_6, and the crystallographic structure of Li_4MgReO_6 as derived from powder neutron diffraction data. Of central interest is the geometry of the Re^{6+} sublattice and the significance of disorder of magnetic as well as non-magnetic ions in the structure. The results of a detailed study of the magnetic properties including bulk magnetic susceptibility and time dependent relaxation experiments are presented. The observations are supplemented by heat capacity, low temperature neutron diffraction and muon spin relaxation experiments which are crucial in the characterization of the magnetic ground state.

5.2 Preparation of Polycrystalline Li_4MgReO_6

Li_2O was prepared at 650°C under vacuum from $LiOH \cdot H_2O$ (≥99.9% Smith Chemicals) according to the following reaction:

$$2LiOH \cdot H_2O \longrightarrow Li_2O + 2H_2O \tag{5.2.1}$$

Li_4MgReO_6 was prepared from Li_2O, MgO (Cerac, 99.99%), Re_2O_7 (Cerac, 99.9%) and Re (Cerac, 99.99%). Stochiometric amounts of the starting materials were ground and placed in a Pt crucible, which was placed in a sealed and evacuated quartz tube. The synthesis was carried out for 24h at 650°C according to reaction (5.2.2).

$$2Li_2O + MgO + \frac{3}{7}Re_2O_7 + \frac{1}{7}Re \longrightarrow Li_4MgReO_6 \tag{5.2.2}$$

All preparative steps were carried out in a glove box (Ar atmosphere). After completion of the reaction a very small amount of white deposit (Li_2O or MgO) was

found on the walls of the quartz tube. The polycrystalline product is black and homogeneous. A two probe resistance measurement indicated insulating behavior.

5.3 Space Group Assignment for Li_4MgReO_6

The phase purity and space group of Li_4MgReO_6 were determined from powder x-ray diffraction patterns obtained with a Guinier Hägg camera where Si was used as an internal standard. The diffraction peaks were indexed on a monoclinic unit cell using the unit cell search routine VISSER (vers. 9) [Vis69]. Based on 20 reflections, the space group C2/m was determined. The unit cell parameters as found with the indexing routine were refined using the least square minimization program LSUDF, yielding the following parameters: a=5.0941(3)Å, b=8.809(2)Å, c=5.0801(8)Å and β=109.875(1)°. The unit cell as well as the space group found for Li_4MgReO_6 agree with Li_5ReO_6 [BH84].

5.4 Crystallographic Structure of Li_4MgReO_6

5.4.1 Refinement of Li_4MgReO_6 from Powder Diffraction Data

X-ray diffraction experiments on polycrystalline samples can only provide limited information regarding structural details as the x-ray diffraction pattern of Li_4MgReO_6 is dominated by Re, whereas the lighter elements contribute very little intensity. In order to investigate the structure of Li_4MgReO_6 in more detail neutron powder diffraction experiments were carried out at Argonne National Laboratory on the time of flight instrument, SEPD. The high resolution and small d-spacings accessible with SEPD in conjunction with the distinct coherent neutron scattering

lengths of the elements provide significant advantages with respect to the x-ray powder study.

The refinements were carried out sequentially such that the occupancies were refined at an intermediate stage but held constant during the final cycle. Using the refinement package GSAS [LD94] the 32 refined parameters included atomic positions, temperature factors, occupation factors, background parameters, cell constants, the absorption coefficient and preferred orientation parameters. The unit cell parameters determined from the neutron powder diffraction data are reasonably close to the values found with the Guinier x-ray camera, the unit cell dimensions and the agreement factors for the Rietveld refinement are reported in table 5.1. Figure 5.1 shows the Rietveld refinement of the neutron powder pattern obtained at room temperature. The occupancies were refined such that all sites are fully

Table 5.1: Agreement factors and refined lattice parameters for Li_4MgReO_6 as determined from Rietveld refinement of powder neutron diffraction data at room temperature.

Number of data points	:	5299	a [Å]	:	5.0979(3)
Number of parameters	:	32	b [Å]	:	8.8163(5)
R_{wp}	:	5.53	c [Å]	:	5.0815(3)
R_p	:	3.66	β [°]	:	109.835(2)
Reduced χ^2	:	1.86	V [Å^3]	:	214.83(2)
Space group	:	C2/m			

occupied and that the Li^+ and Mg^{2+} ratio was refined as well. All possible combinations of cation mixing on the cation sites were tested. The Re^{6+} site did not allow any substitution by Li^+ or Mg^{2+}, therefore in the final refinement cycles the occupation factors were refined such that no Li and/or Mg was allowed on the Re site. The structural parameters obtained from Rietveld analysis of time of flight

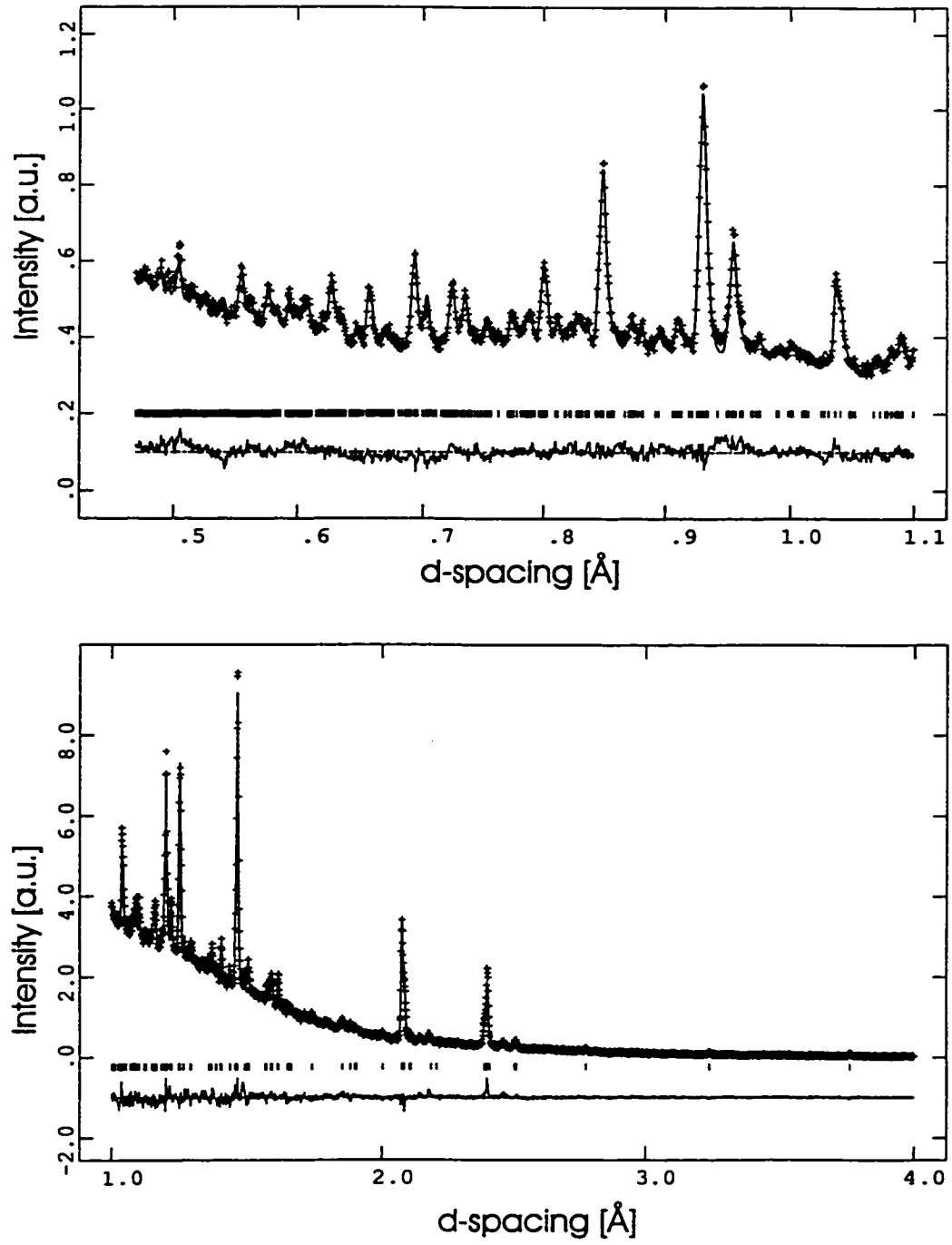

Figure 5.1: Powder neutron diffraction refinement for Li_4MgReO_6, the data were obtained at room temperature at IPNS.

neutron powder data are presented in table 5.2. The stochiometry derived from

Table 5.2: Li_4MgReO_6 structural data from Rietveld refinement of neutron powder data for space group C2/m.

Atom	x	y	z	$U_i/U_e \cdot 100$	Occupancy
Li(1)	0	0.6660	0	6.4(7)	0.74(2)
Mg(1)	0	0.6660	0	6.4(7)	0.26(2)
Li(2)	1/2	0.315(5)	1/2	6.4(7)	0.84(2)
Mg(2)	1/2	0.315(5)	1/2	6.4(7)	0.16(2)
Li(3)	0	1/2	1/2	6.4(7)	0.80(2)
Mg(3)	0	1/2	1/2	6.4(7)	0.20(2)
Re(4)	0	0	0	1.01(6)	1.0000
O(5)	0.2598(7)	0.3445(3)	0.7603(5)	0.78(5)	1.0000
O(6)	0.2658(9)	1/2	0.2297(8)	1.12(8)	1.0000

the occupation factors[1] is $Li_{3.96}Mg_{1.04}ReO_6$ which is in reasonable agreement with the nominal composition of Li_4MgReO_6. The crystal structure of Li_4MgReO_6 is shown in figure 5.2 and is isostructural with Li_5ReO_6, which was determined from single crystal x-ray data [BH84]. Both structures are based on that of α-Li_2SnO_3. All cations are in slightly distorted octahedral environments. Figure 5.3 shows the cation coordination and the corresponding bond distances and bond angles are summarized in table 5.3. The Li,Mg(2)-O_6 octahedron shows significant asymmetric distortion. This distortion is caused by two short Li,Mg(2)-Re distances. Charge repulsion moves the Li,Mg(2) ions away from the hexavalent Re ions, whereas the less distorted Li,Mg(1)-O_6 and Li,Mg(3)-O_6 octahedra are located in symmetrical Re^{6+} environments. The cation-oxygen octahedra are edge shared, consequently, the structure is well described as an ordered rock salt structure. The cation distribution

[1]The reported errors for the occupation factors are estimates based on results from earlier refinement cycles. The occupancies were held constant during the final cycle.

Table 5.3: Bond distances and bond angles for Li_4MgReO_6 at room temperature.

	distance [Å]		angle [°]
Re(4)-O(5) ×4	1.9619(24)	O(5a)-Re-O(5b)	91.37(15)
Re(4)-O(6) ×2	1.932(4)	O(5a)-Re-O(5c)	88.63(15)
<Re-O>	1.952	O(5a)-Re-O(5d)	180.00
		O(5a)-Re-O(6a)	90.48(11)
		O(6a)-Re-O(6b)	180.00
Li,Mg(1)-O(5) ×2	2.0834(31)	O(5e)-Li,Mg(1)-O(5f)	93.18(10)
Li,Mg(1)-O(5) ×2	2.1090(26)	O(5e)-Li,Mg(1)-O(5g)	90.64(9)
Li,Mg(1)-O(6) ×2	2.0658(30)	O(5e)-Li,Mg(1)-O(5h)	174.89(13)
<Li,Mg(1)-O>	2.086	O(5e)-Li,Mg(1)-O(6b)	93.63(13)
		O(6b)-Li,Mg(1)-O(6c)	89.78(17)
Li,Mg(2)-O(5) ×2	2.101(7)	O(5e)-Li,Mg(2)-O(5f)	93.7(8)
Li,Mg(2)-O(5) ×2	2.074(32)	O(5e)-Li,Mg(2)-O(5i)	94.4(19)
Li,Mg(2)-O(6) ×2	2.20(4)	O(5e)-Li,Mg(2)-O(5k)	95.9(8)
<Li,Mg(2)-O>	2.125	O(5f)-Li,Mg(2)-O(5k)	165.9(26)
		O(5e)-Li,Mg(2)-O(6d)	173.7(14)
		O(5e)-Li,Mg(2)-O(6e)	90.63(16)
Li,Mg(3)-O(5) ×4	2.0479(26)	O(5m)-Li,Mg(3)-O(5e)	84.02(13
Li,Mg(3)-O(6) ×2	2.233(4)	O(5m)-Li,Mg(3)-O(5i)	180.00
<Li,Mg(3)-O>	2.110	O(5m)-Li,Mg(3)-O(5n)	95.98(13)
		O(5m)-Li,Mg(3)-O(6b)	89.83(10)
		O(6b)-Li,Mg(3)-O(6e)	179.980(0)

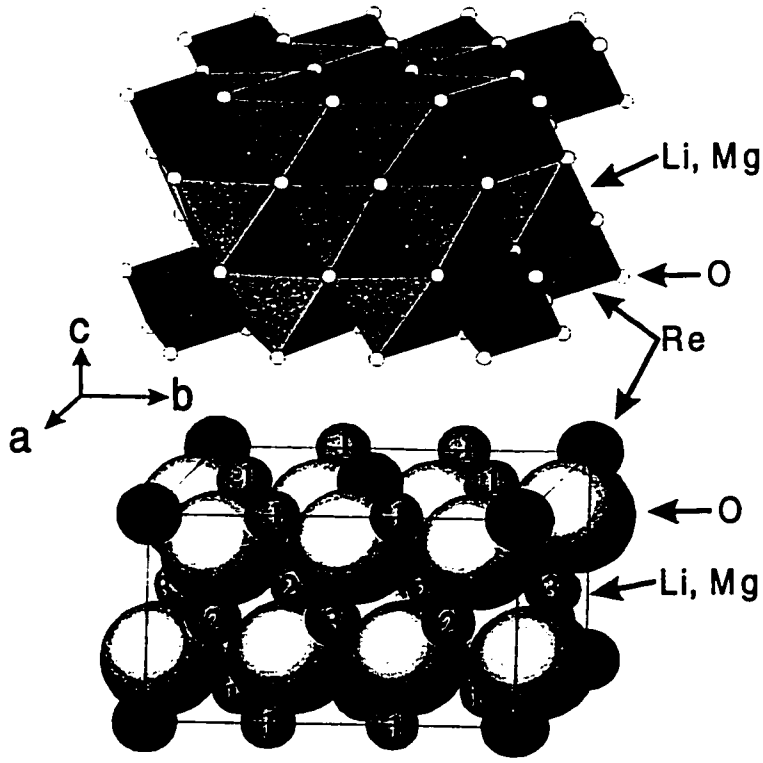

Figure 5.2: The crystal structure of Li_4MgReO_6 can be described as an ordered NaCl structure having a monoclinic unit cell. The numbers indicate the sites according to table 5.2.

can be described in terms of layers, which are stacked perpendicular to the ab-plane. The first layer contains Li^+ and Mg^{2+} ions only. Every other layer accommodates Li^+, Mg^{2+} and Re^{6+} ions. Therefore, in terms of stacking, the Re^{6+} containing layers are separated by Li^+, Mg^{2+} containing sheets, see figure 5.2. Lang described the structure as a 2-dimensional honey comb structure [Lan66]. However, the shortest Re-Re distance is found along the stacking direction, e.g. the crystallographic c-axis. Since the Re-Re distances in the ab-plane are only slightly larger than along

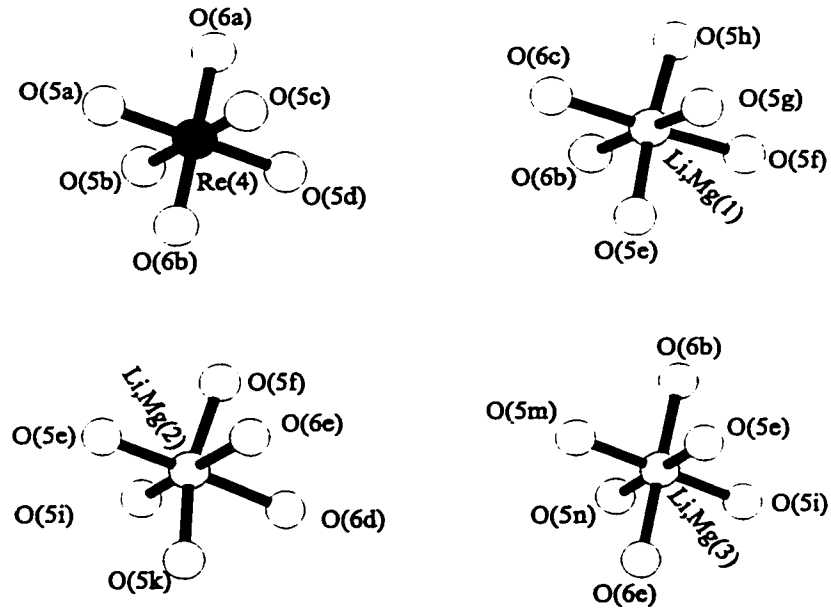

Figure 5.3: Representation of coordination polyhedra in Li_4MgReO_6. All octahedra show a small extend of distortion.

the stacking direction the Re^{6+} network is better described as a 3-dimensional sublattice. The Li^+, Mg^{2+} cations are randomly disordered on their sites with a Li^+ to Mg^{2+} ratio close to 4:1 as required by the stochiometry, see table 2, whereas, the Re^{6+}-site does not show any disorder. The separation of the (Li^+, Mg^{2+})-sublattice from the Re-sublattice can be rationalized in terms of charge ordering. The high charges on the Re^{6+} ions can be accommodated best in the structure by permitting only mono- and divalent cations in the vicinity of Re^{6+}, thus excluding Re^{6+} from these sites. The main focus of this work is the magnetism associated with the Re^{6+} sublattice, therefore it is particularly important to look at the topology of that sublattice. The Re^{6+}-ions form tetrahedra with edge lengths between 5.08Å and 6.55Å. These distorted tetrahedra share faces throughout the structure, thus presenting a

highly frustrated situation for antiparallel alignment of spins. The Re^{6+}-sublattice is presented in figure 5.4, one tetrahedral face is shaded in order to emphasize the connectivity of the Re^{6+} tetrahedra by faces. The triangular faces in the ab-plane are nearly equilateral with angles of 59.962° and 60.075°. The tetrahedra are more distorted in the c-axis stacking direction giving triangular face angles of 54.787°, 70.165° and 55.048°.

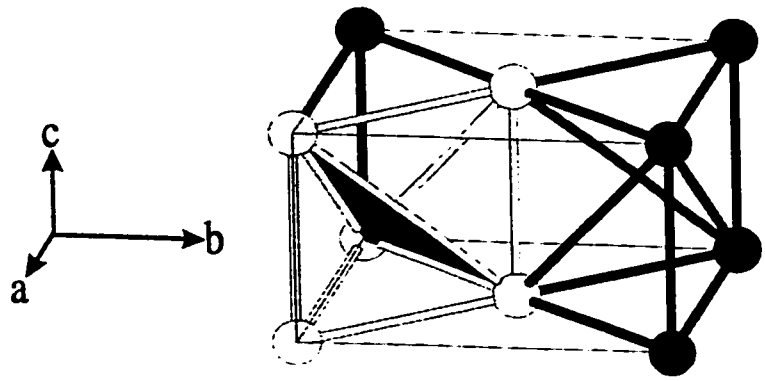

Figure 5.4: Three dimensional highly frustrated Re^{6+}-sublattice in Li_4MgReO_6. Only Re^{6+} cations are shown, the light atoms and lines with the shaded triangle are chosen to emphasize the face sharing tetrahedral sublattice.

5.4.2 Potential Magnetic Exchange Paths for Re-Re Interactions

There are 5 different Re-Re distances for each Re^{6+}-tetrahedron 5.0815(3)Å [001], 5.0978(3)Å [100], 5.0920(6)Å [110], 5.8506(3)Å [101] and 6.5546(3)Å [221]. The tetrahedral Re^{6+} framework is indicated in figure 5.4 and the distances are shown in figure 5.5. The formal exchange path consists of a Re-O-(Li, Mg)-O-Re link. Due to the fact that all cations are octahedrally coordinated and all octahedra share edges there exist two basic types of exchange pathways. First, there are 6

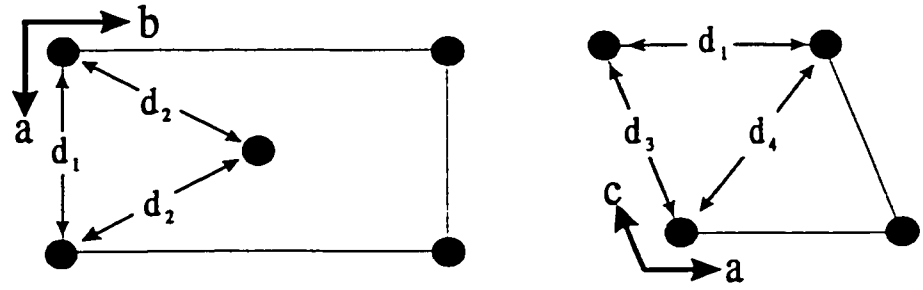

d_1=5.0978(3)Å d_3=5.0815(3)Å

d_2=5.0920(6)Å d_4=5.8506(3)Å

Figure 5.5: Re-Re distances in Li_4MgReO_6.

similar Re-O-(Li, Mg)-O-Re links between 2 Re ions. Due to the distortion of the octahedra these 6 paths are not equivalent, but are very similar. Alternatively the exchange could occur via Re-O-O-Re, where there are three different possible paths between neighboring Re ions in the a-b layers. However, the O-O distances are rather large (2.7-3.1Å) and there is no reason to believe that there is any contact (overlap) between neighboring O^{2-} ions. The potential magnetic exchange paths can be seen in figure 5.6.

5.4.3 Bond Disorder in Li_4MgReO_6

For the longest time spin glass behavior was considered to depend on disorder within the crystallographic lattice. The system presented here does not show any Re^{6+} disorder according to the Rietveld refinement carried out on the neutron powder diffraction data. However, the (Li, Mg) sites show disorder thus creating bond disorder, that means that the exchange paths and the orbital overlap depend

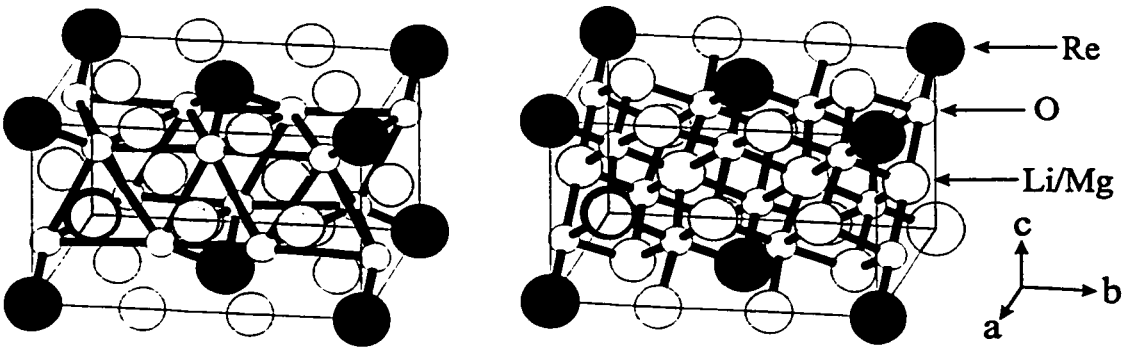

Figure 5.6: The left figure shows the Re-O-O-Re exchange paths and the right hand figure illustrates the Re-O-(Li,Mg)-O-Re exchange paths for magnetic coupling between Re cations in Li_4MgReO_6.

on the local environment of each of the Re^{6+} cations.

5.5 Magnetic Susceptibility

Using magnetic fields of 0.1T and 1T the magnetic susceptibility of polycrystalline Li_4MgReO_6 was measured. No features indicating long range order are present. However at low temperature hysteresis behavior is found. The magnetic susceptibility data are presented in figure 5.7 and 5.8. The data do not show the typical maximum in χ versus T for antiferromagnetic long range ordering. Furthermore, the true Curie-Weiss region is not reached until about 350K and the data for the temperature range 350K to 500K were fitted to the Curie-Weiss law,

$$\chi = \frac{C}{T - \theta} \tag{5.5.1}$$

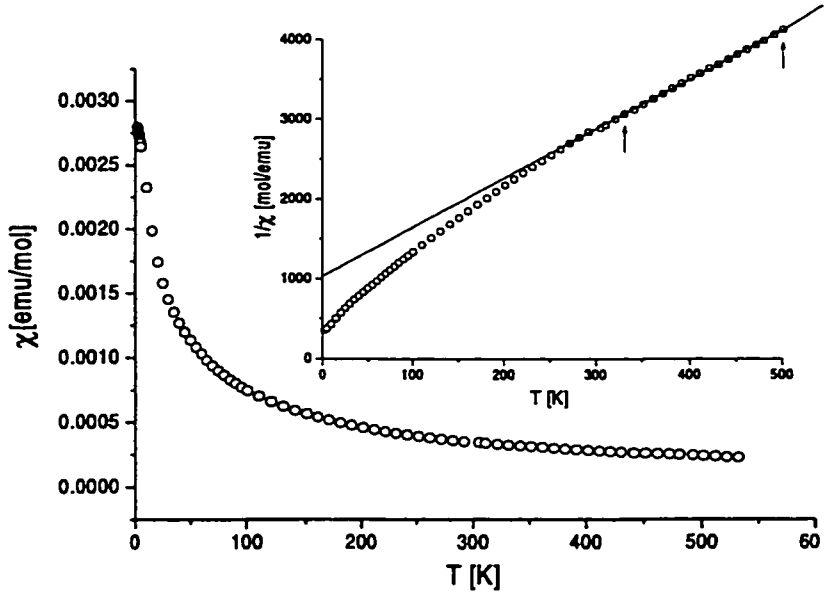

Figure 5.7: Magnetic susceptibility measurements carried out using H=1T. The inset shows the Curie-Weiss plot.

where C is the Curie constant and θ the Weiss temperature. The fit revealed θ = -166(3)K indicating strong antiferromagnetic coupling. The effective magnetic moment was determined to μ_{eff} = 1.14(1)BM, whereas the spin only value for Re^{6+} is 1.73BM. The low value of μ_{eff} may reflect admixture of an orbital component due to the rather large spin-orbit coupling expected for a 5d series ion. Using EPR experiments the anisotropic g-values for Re^{6+} in $(Mo,Re)O_3$ were determined to be very close to 1.6 and almost isotropic [Por79]. For g=1.6 the expected effective magnetic moment is 1.39BM, which is much closer to the experimental value for Li_4MgReO_6. At low temperatures a divergence between zero field and field cooled magnetic susceptibilities is seen. The divergence sets in at 12K as can be seen in figure 5.8. No indication of long range magnetic ordering is present, both traces

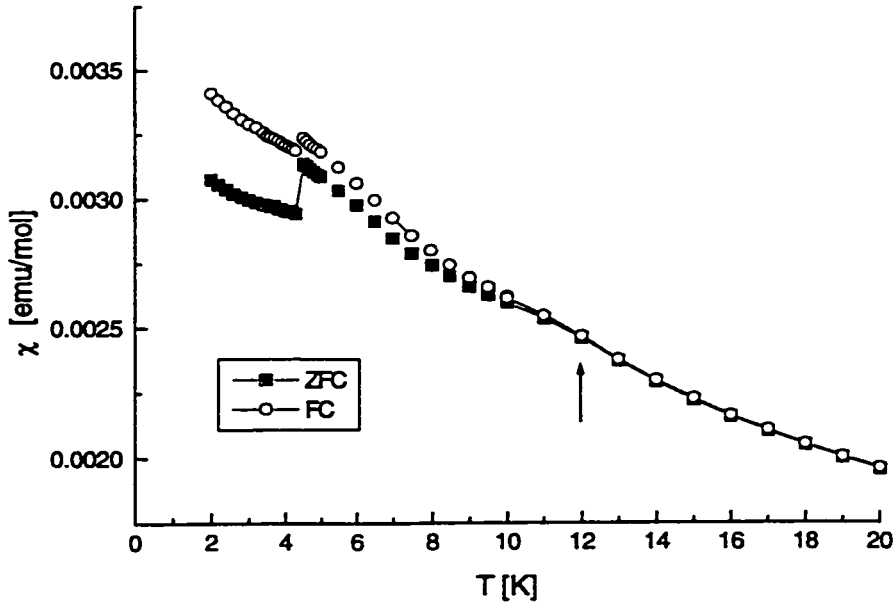

Figure 5.8: Magnetic susceptibility measurements for Li_4MgReO_6, carried out at low temperatures using a magnetic field of 0.1T. The divergence of ZFC-FC data is indicated with an arrow. The step at 4.2K is discussed in the text.

increase monotonically with decreasing temperatures, showing only changes in the slopes. No cusp, which is often found for spin glasses, is present, however a cusp is not a necessary requirement for a spin glass. At 4.2K a step in the χ versus T curves is observed, which is caused by a delay during the measurement, which is due to the refilling of the He reservoir in the SQUID magnetometer. While the He reservoir is refilled the temperature control is lost and temperatures close to 12K can be reached, therefore the data measured after this delay and temperature instability do not represent a true ZFC experiment. Therefore, the step is an experimental artifact but at the same time it emphasizes the time dependence of the magnetization. The inflection point at 12K and the divergence below that temperature clearly indicate hysteresis behaviour, which supports the presence of cooperative magnetism. In

order to investigate this hysteresis relaxation measurements were carried out at 5K, 10K and 20K. The sample was cooled to 5K in zero field. As soon as T=5K was reached a magnetic field of H=0.1T was switched on and the magnetization was monitored as a function of time for approximately 5 hours. Before measuring the next temperature the sample was warmed to T=50K in order to be far above the glass transition temperature of 12K. At 5K and 10K a bi-exponential saturation behavior is observed, whereas at 20K no saturation is seen. The dc-magnetic relaxation measurements are shown in figure 5.9. This clearly supports the above statement

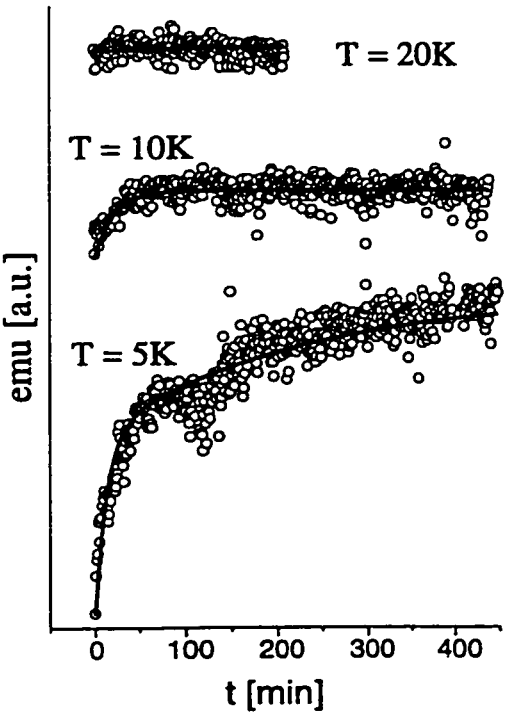

Figure 5.9: Magnetic relaxation measurements at 5K, 10, and 20K using an external magnetic field of H=0.1T. The data sets acquired at 5K and 10 are fitted using a bi-exponential relaxation function. All three data sets are on the same scale.

regarding cooperative magnetism below 12K. In addition the magnetization versus magnetic field strength data (figure 5.10) show a linear behavior for 10K and 15K, the lack of saturation confirms the absence of ferromagnetic components. The slight curvature at 5K is consistent with that expected for the S=1/2 Brillouin function. The type of magnetic ordering can not be extracted from bulk magnetic measure-

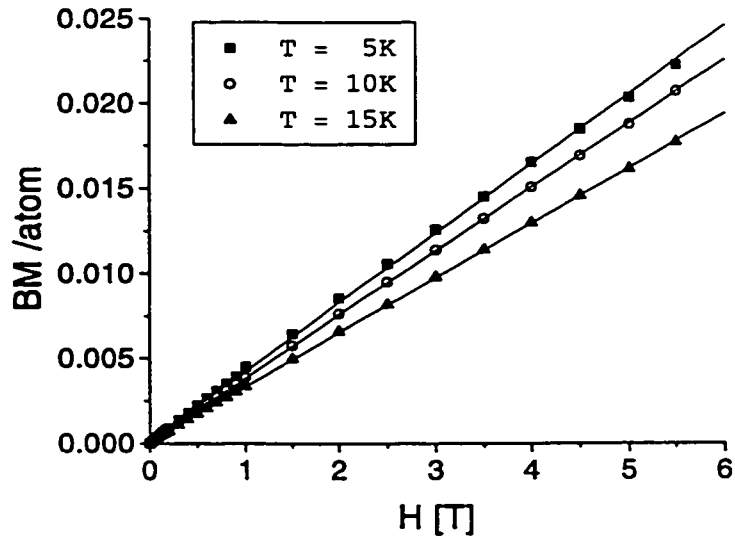

Figure 5.10: Magnetization measurements at 5K, 10, and 15K. Note that only the 5K data deviate from the straight line.

ments. However, neutron diffraction and muon spin relaxation measurements will help to determine the true magnetic ground state.

5.6 Neutron Diffraction at Low Temperatures

Neutron powder diffraction experiments were carried out at 4K and 40K. The powder diffraction patterns for 4K and 40K are identical as can be seen in figure 5.11. If the inflection point at 12K in the magnetic susceptibility data were due to

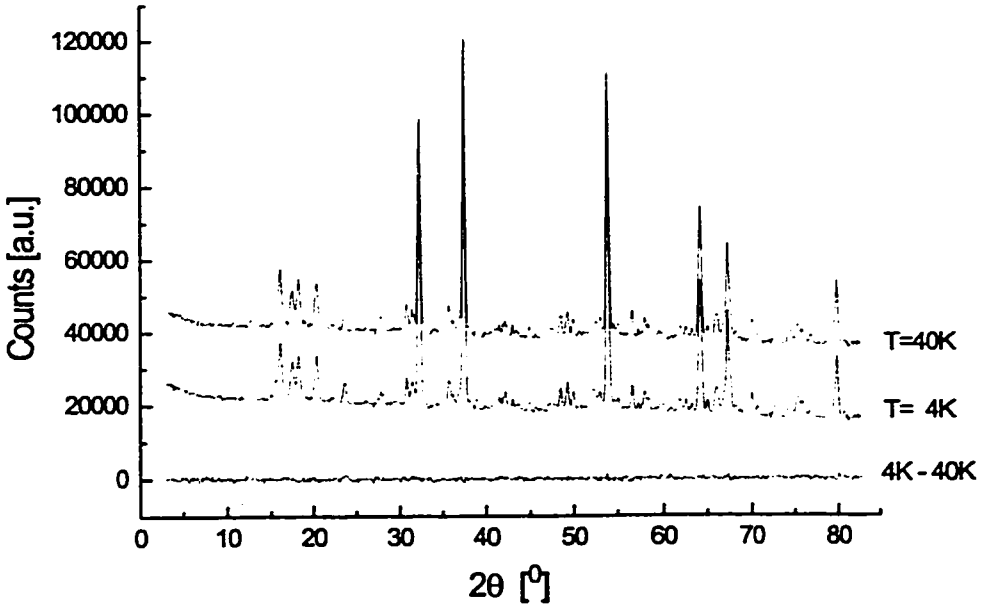

Figure 5.11: Powder neutron diffraction data obtained at low temperatures. The data sets at 40K and 4K are identical, indicating that no magnetic long range order is present in the sample. Data obtained on powder diffraction instrument C2 at Chalk River (λ=1.3259Å).

magnetic long range order, the neutron powder patterns would show magnetic Bragg peaks at 4K, or the intensities of the crystallographic peaks should change due to the magnetic contribution. However, no differences are found for these measurements, thus indicating that no magnetic long range order is present down to 4K as already expected from bulk magnetic data. Furthermore, the absence of broad features at 4K suggests that no magnetic short range order is detectable at this temperature. However, due to the weak magnetic moment of Re^{6+} (S=1/2) and the fact that the sample resembles a fairly dilute magnetic system, potential broad features might be too weak to be observable. It is noteworthy that room temperature experiments, carried out under the same conditions, showed identical neutron diffraction patterns

as the low temperature data sets. However, the poor counting statistics do not allow a full refinement of the crystallographic structure. For that reason the structure was refined from time of flight neutron diffraction data.

5.7 Heat Capacity Measurements

The specific heat in zero field of the sample in the form of a pellet was measured using the pulse method in the temperature range 0.6-30K in a quasiadiabatic calorimeter and a commercial Heliox sorption pumped ^{3}He cryostat. The sample was mounted on a thin sapphire plate with apiezon grease for better thermal contact. Underneath the sapphire plate a strain gauge heater and a RuO_2 temperature sensor were attached. The specific heat of the sample was obtained by subtracting the contribution of the addendum, measured separately, from the total measured heat capacity. The heat capacity data for the temperature range 0.6K to 6K are shown in figure 5.12. The measurement was carried out up to 30K, but the data were unacceptably noisy above 6K. Nonetheless, there was no evidence of a lambda anomaly up to 30K. The data for the temperature range 0.5K to 6K were fitted to equation (5.7.1)

$$C_p = \gamma T + \beta T^3 \tag{5.7.1}$$

where γT describes the electronic contribution and βT^3 the lattice contribution to the heat capacity. Since Li_4MgReO_6 is an insulator, as determined from two probe resistivity measurements, it is assumed that the electronic contribution to the heat capacity is entirely due to the inherent magnetism. For spin glasses a linear temperature dependence of the magnetic heat capacity is expected [Myd93]. The following coefficients are found for Li_4MgReO_6: γ = 0.070(2) J mol^{-1}K^{-2} and β

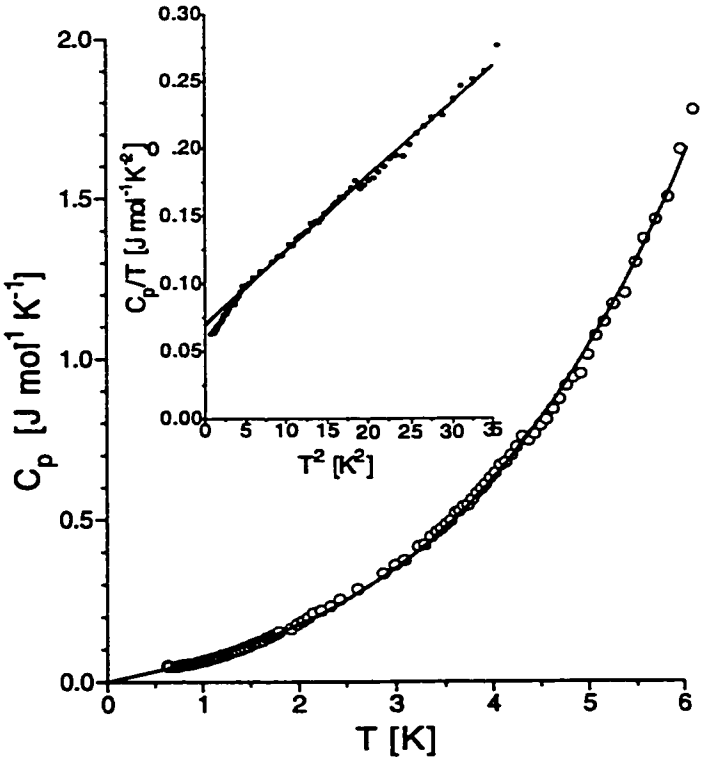

Figure 5.12: Heat capacity measurements at low temperatures. The experiment was carried out using the pulse method.

= 0.0054(8) J mol^{-1}K^{-4}. The inset in figure 5.12 shows C_p/T versus T^2, which is linear as required according to equation (5.7.1), the slope represents β and the extrapolated ordinate-intercept gives γ. The magnetic entropy S_m was obtained by extrapolating C_m/T to 0K and to T_f=12K and integrating over this temperature range according to equation (5.7.2).

$$S_m = \int_0^T \frac{C_m}{T'} dT' \tag{5.7.2}$$

The total magnetic entropy is 0.84 J mol^{-1}K^{-1}. Whereas, the expected magnetic entropy is R ln(2) = 5.76 J mol^{-1}K^{-1}, thus the experimental magnetic entropy below

T_f accounts for only 14% of the expected entropy. This result is not surprising, as it is well known for spin glasses that most of the magnetic entropy removal takes place above the glass transition temperature [Myd93], [FH91].

5.8 Muon Spin Relaxation

The muon spin relaxation (μSR) experiments were carried out on the M13 surface μ^+ beamline at the TRIUMF facility, Vancouver, Canada. The zero field (ZF) experiments were performed at temperatures between 125K and 2.5K. Additional measurements were carried out at 2.5K in a longitudinal field (LF) of 0.01T and 0.1T. Several ZF/LF-μSR spectra collected at 2.5K are shown in figure 5.13; clearly the relaxation behavior changes drastically upon increasing the longitudinal field strength. The two component form of the spin relaxation, along with the decoupling of the relaxation upon application of a longitudinal field are characteristic features of a (quasi)-static distribution of internal magnetic fields, such as would be present in a spin glass. In contrast long range magnetic order (AFM or FM) would have resulted in muon spin precession in zero applied field. The ZF and H=0.01T data show pronounced relaxation during the first 200ns. The data at longer times seem to flatten out for the 0.01T experiment, which also indicates that the internal fields are essentially static. Upon increasing the longitudinal field strength to 0.1T the relaxation disappears completely and only a flat plateau is found. ZF-μSR experiments were performed as a function of temperature between 2.5K $\leq$ T $\leq$ 12.5K, these data show a marked temperature dependence (figure 5.14). As the temperature is decreased below 12.5K, the muon spin relaxation data show pronounced relaxation behavior, which is in agreement with the inflection point at 12K for dc-magnetic

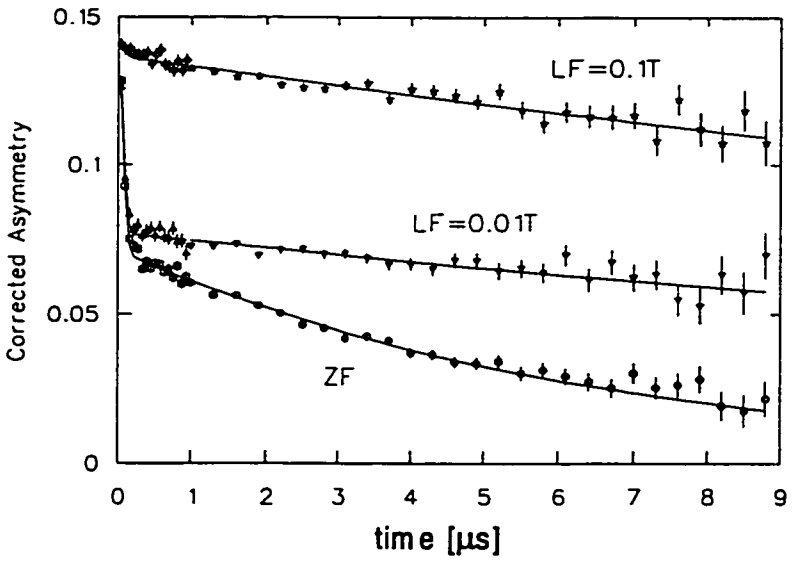

Figure 5.13: Muon spin relaxation spectra for Li_4MgReO_6 as a function of a longitudinal magnetic field taken at 2.5K.

susceptibility data reported earlier. The gaussian relaxation is in agreement with the behavior expected for a dense distribution of (quasi)-static randomly oriented spins. This fact is in agreement with fully occupied Re^{6+} sites, in contrast to an exponential or square root exponential behavior as expected for a dilute spin system. Furthermore, the increasing amplitude of the gaussian relaxation function with decreasing temperature suggests a clustered spin glass, where the clusters grow in size as the temperature is lowered. The ZF data were fitted to a phenomenological fitting function (5.8.1), in which the relaxation without the typical (Kubo-Toyabe) 1/3 recovery was modeled using the following fitting function.

$$\begin{aligned} Asym_{cor} = A\left[(1-O_{frac})\exp\left(-\Delta^2 t^2\right)\exp\left(-\lambda_s t\right)\right] + \\ +A\left[O_{frac}\frac{2}{3}\exp\left(-\sigma_f^2 t^2\right) + O_{frac}\frac{1}{3}\exp\left(-\lambda_t t\right)\right] \end{aligned} \tag{5.8.1}$$

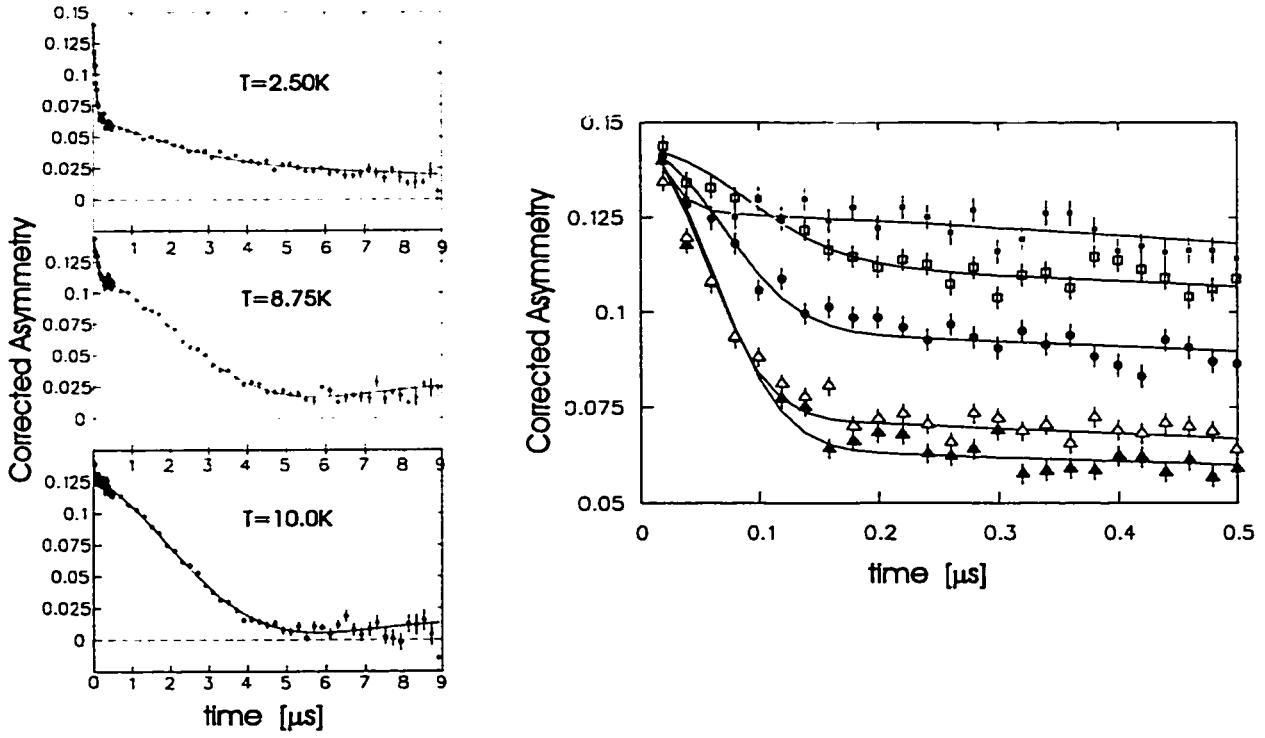

Figure 5.14: Muon spin relaxation spectra for Li_4MgReO_6. The left side shows three different temperatures, 10K, 8.75K and 2.50K for the time intervals 0 to 10 μs. The graph on the right shows the details for the first 0.5μs for taken at 5 different temperatures, the solid lines are the best fits. ■=10K, □=8.75K, •=7.50K, Δ=5.00K, ▲=2.50K.

Where t = time in μs and A is the asymmetry of the counter which accounts for the efficiencies of the forward and backward counters and the properties of muon decay. $Asym_{cor}$ is the corrected asymmetry, O_{frac} denotes the volume fraction of frozen spins and Δ, λ_s, σ_f and λ_t are inverse relaxation times. The first bracket in equation (5.8.1) describes the non-ordered fraction of the sample, where the source of relaxation is nuclear dipolar fields. This is mainly described by the gaussian function, however, a multiplicative exponential term was included which improved the fit.

The exponential function could reflect the possible existence of multiple muon sites, which explains the deviation from a truly gaussian relaxation function appropriate to a single muon site. The parameters Δ and λ_s are temperature independent and were determined from fits at 125K. These parameters were held fixed for the low temperature fits. The second bracket in equation (5.7.2) describes the volume fraction of frozen spins (fraction of quasi-static electronic spins) using a gaussian type function with a characteristic inverse relaxation time σ_f and an exponential term with parameter λ_t for the 1/3-tail in the ordered state. For the temperature range 2.5K $\leq$ T $\leq$ 10K the inverse relaxation times σ_f were found to be in the range 10 to 13μs^{-1}. Using equation (5.8.2)

$$B_{local} = \frac{\sigma_f}{\gamma_\mu} \tag{5.8.2}$$

and the value γ_μ = 861.5Mrad s^{-1} T^{-1} for the gyromagnetic ratio for a muon, we obtain an averaged characteristic internal magnetic field of approximately 0.014T. The size of the field indicates that the Re^{6+} electronic moments must be the source of the internal field as any nuclear dipolar fields would be much smaller and temperature independent. The observed characteristic local field is in agreement with the fact that the muon spin relaxation is completely decoupled upon application of an external longitudinal field of 0.1T whereas the smaller longitudinal field of 0.01T was not able to significantly decouple the relaxation (except for that due to nuclear dipolar fields in the non-ordered volume fraction). The freezing of the magnetic moments at low temperatures clearly indicates that the ground state of Li_4MgReO_6 is best described as a spin glass and not as a spin liquid state. For each temperature the volume fraction of frozen spins, O_{frac}, was determined from the fits of function (5.8.1), these results are shown in figure 5.15. The gradual increase of the ordered

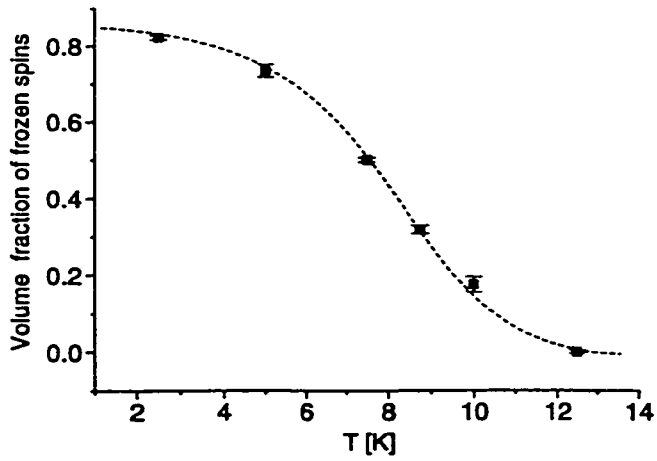

Figure 5.15: Volume fraction of frozen spins as a function of temperature as derived from muon spin relaxation measurements. The broken line is to guide the eye.

fraction below 12K allows the conclusion that the spin glass freezing consists of an island growth process. The volume fraction of frozen spins levels off slightly above 0.8, however, due to systematic errors the true value might be closer to 1.0 (for example in underestimating the fraction of muons landing in the sample holder). The sample is considered to be completely frozen at 2.5K.

5.9 Conclusions

The crystal structure and magnetic properties of Li_4MgReO_6 were investigated. As expected Li_4MgReO_6 is an electrical insulator with localized magnetic moments of S=1/2 for Re^{6+}. Li_4MgReO_6 crystallizes in space group C2/m, having a 3 dimensional network of Re^{6+} ions. The Re^{6+} sublattice is best described as a distorted face sharing tetrahedral framework. Magnetic bulk measurements show hysteresis behavior below 12K, thus indicating cooperative magnetism at low

temperature. From low temperature powder neutron diffraction experiments magnetic long range order can be ruled out for Li_4MgReO_6. μSR experiments clearly indicate a spin glass ground state, where the spin freezing process is completed at approximately 2.5K. We found an averaged characteristic internal magnetic field of approximately 0.014T. Usually, spin glasses are identified by a.c. susceptibility measurements, however due to the small concentration of the weak magnetic moment of Re^{6+} (S=1/2) no useful data were obtained. Heat capacity measurements from 0.5K to 6K show a linear in temperature magnetic term and that most of the entropy removal occurs above T_f, thus supporting the finding of a spin glass ground state. The spin glass ground state is attributed to the high degree of geometric magnetic frustration inherent on the Re^{6+} sublattice. Furthermore, bonding disorder due to Mg^{2+}, Li^{+} disorder favors the spin glass ground state over a Néel state. The absence of spin liquid behaviour is in agreement with the lack of anisotropy for Li_4MgReO_6. Each magnetic exchange path is complicated and involves in total five ions, a simple model based on super-exchange can not describe the magnetic interactions.

Chapter 6

Conclusion and Further Work

Three different systems exhibiting geometric magnetic frustration have been presented. The frustration is caused by antiferromagnet exchange between nearest neighbours on triangular, tetrahedral and body centered lattices. All of the above show frustration in three dimensions. The triangular antiferromagnets of composition $AMnO_3$ can be described as triangular bipyramids, where this topology is a result of the $\cdots$ABAB$\cdots$ stacking sequence. The square planar antiferromagnets $Ba_xSr_{(1-x)}LaMnO_4$ show frustration along the c-direction, whereas the 2-dimensional sheets are not frustrated. Furthermore, the magnetic sublattice of Li_4MgReO_6 consists of face-sharing tetrahedra.

All investigated systems have only one paramagnetic ion each, thus these are very good model compounds for the investigation of lattice topology and magnetic frustration. The magnetic ions have spin quantum numbers of S=2 (Mn^{3+}) for the triangular and the square planar antiferromagnetic phases. In contrast the tetrahedral system has a spin quantum number of S=1/2 (Re^{6+}). It was shown that magnetic systems with a large spin quantum number establish Néel ground states, whereas Li_4MgReO_6 with a small spin quantum number forms a spin glass ground

state.

The two different substitutional solid solutions $Ba_xSr_{(1-x)}LaMnO_4$ and $Lu_xSc_{(1-x)}MnO_3$ showed very different results as a function of the exchange diamagnetic ions. The properties of the triangular system show a continuous behaviour, the in-plane spin-reorientation transition evolves gradually as a function of the Lu:Sc ratio. In contrast the $Ba_xSr_{(1-x)}LaMnO_4$ system shows the disappearance of magnetic long rang order as x exceeds 0.20. Here a fundamental change of the magnetic ground state is observed.

The triangular antiferromagnets show an easy-plane anisotropy, as evidenced from the confinement of the magnetic moments to the ab-plane. In contrast the square planar system shows an easy-axis anisotropy. All magnetic moments are aligned with the crystallographic c-axis.

Additional experiments are required in order to answer open questions. The triangular antiferromagnets showing an in-plane spin-reorientation transition should be compared with a solid solution $Lu_xHo_{(1-x)}MnO_3$. A spin-reorientation transition was reported for the pure Ho compound [KWYC64], but no details were given.

The square planar antiferromagnet $BaLaMnO_4$ should be further investigated. In particular the investigation of a potential spin glass ground state below 21K should be probed with muon spin relaxation and ac-susceptibility measurements.

Li_4MgReO_6 has been studied comprehensively and the spin glass state has been identified as the magnetic ground state. However, there is a large group of potential spin glasses based on Li_4MgReO_6, namely the Sr, and Ca analogues. Furthermore, the dilution of the paramagnetic Re^{6+} with diamagnetic Mo^{6+} is considered interesting in terms of freezing temperature evolution and the formation of

potential spin-clusters.

It has been shown that the chirality of a given magnetic structure can be determined under favorable conditions. This has been illustrated for the triangular antiferromagnets $AMnO_3$.

Appendix A

Mathematical Proofs

A.1 $A_{fraction}$ as a function of ϕ

$$A + B = 1 \Rightarrow B = 1 - A \tag{A.1.1}$$

A and B are perpendicular vectors, thus C is the resulting vector upon vector addition of A and B. Another way of looking at this problem is to consider A and B as the fractions of the total scale factor of the magnetic fraction of the sample,

$$C = \sqrt{A^2 + B^2} \tag{A.1.2}$$

$$C = B\ \cos(\phi) \tag{A.1.3}$$

$$C = A\ \sin(\phi) \tag{A.1.4}$$

$$A\ \sin(\phi) = B\ \cos(\phi) \tag{A.1.5}$$

$$A = B\frac{\cos(\phi)}{\sin(\phi)} \tag{A.1.6}$$

$$A = (1 - A)\frac{\cos(\phi)}{\sin(\phi)} \tag{A.1.7}$$

$$A\left(1 + \frac{\cos(\phi)}{\sin(\phi)}\right) = \frac{\cos(\phi)}{\sin(\phi)} \tag{A.1.8}$$

$$A = \frac{\cos(\phi)}{\sin(\phi) + \cos(\phi)} \tag{A.1.9}$$

The fraction B can easily be obtained from equation A.1.1 and A.1.6

$$B = \frac{\sin(\phi)}{\sin(\phi) + \cos(\phi)} \tag{A.1.10}$$

Appendix B

Triangular Antiferromagnets

The following tables contain the agreement factors and magnetic phase information for neutron powder diffraction refinements carried out for the solid solution $Lu_xSc_{(1-x)}MnO_3$. [1] The agreement factors are defined on page 32.

[1]Instrument D1B is the 400 wire low resolution powder diffractometer at Institute Laue-Langevin in Grenoble. Diffractometer C2 is the high resolution 800 wire diffractometer in Chalk River.

Table B.1: Agreement factors for Rietveld refinements of neutron powder diffraction data for the crystallographic and magnetic phases of $LuMnO_3$.

T[K]	M [μ_B]	ϕ [°]	Magnetic-R [%]	R_p [%]	R_{wp} [%]	Instrument
2.1	3.39(3)	90	6.58	2.38	3.11	D1B
4.0	3.31(4)	90	14.4	4.40	5.75	C2
4.1	3.37(3)	90	6.90	2.01	2.80	D1B
9.8	3.36(3)	90	6.33	2.56	3.42	D1B
20.0	3.34(4)	90	13.4	4.21	5.60	C2
30.0	3.26(4)	90	4.48	2.45	3.21	D1B
38.3	3.26(4)	90	5.68	2.45	3.25	D1B
50.0	3.08(4)	90	17.5	4.31	5.61	C2
54.5	3.03(4)	90	7.28	2.50	3.24	D1B
69.1	2.71(4)	90	9.23	2.45	3.17	D1B
74.5	2.52(4)	90	6.31	2.55	3.32	D1B
80.0	2.42(4)	90	23.9	4.58	5.92	C2
84.0	2.03(4)	90	9.82	2.53	3.34	D1B
89.4	1.31(5)	90	30.2	2.56	3.36	D1B
94.2	0			2.67	3.47	D1B
108.0	0			2.69	3.46	D1B
120.0	0			4.14	5.40	C2

Table B.2: Agreement factors for Rietveld refinements of neutron powder diffraction data for the crystallographic and magnetic phases of $Lu_{0.9}Sc_{0.1}MnO_3$.

T[K]	M [μ_B]	ϕ [°]	Magnetic-R [%]	R_p [%]	R_{wp} [%]	Instrument
2.1	3.33(4)	59(1)	7.33	2.59	3.37	D1B
4.0	3.45(5)	58(1)	20.9	3.16	4.13	C2
4.1	3.39(3)	59(1)	5.91	1.95	2.78	D1B
9.8	3.38(4)	62(1)	6.31	2.46	3.29	D1B
20.0	3.28(5)	66(2)	22.2	3.29	4.25	C2
23.3	3.31(4)	68(1)	6.24	2.41	3.16	D1B
38.3	3.23(4)	74(2)	6.23	2.37	3.15	D1B
46.2	3.17(4)	90	5.89	2.36	3.12	D1B
50.0	3.07(5)	90	24.8	3.26	4.23	C2
54.6	3.06(4)	90	6.98	2.49	3.21	D1B
69.0	2.77(4)	90	7.89	2.46	3.20	D1B
78.5	2.47(4)	90	7.64	2.45	3.27	D1B
80.0	2.44(5)	90	30.0	3.30	4.43	C2
83.8	2.25(4)	90	9.69	2.46	3.24	D1B
88.8	1.82(5)	90	13.8	2.46	3.46	D1B
120.0				3.38	4.37	C2

Table B.3: Agreement factors for Rietveld refinements of neutron powder diffraction data for the crystallographic and magnetic phases of $Lu_{0.8}Sc_{0.2}MnO_3$.

T[K]	M [μ_B]	ϕ [°]	Magnetic-R [%]	R_p [%]	R_{wp} [%]	Instrument
4	3.26(3)	21(1)	5.15	6.91	9.16	C2
10	3.27(3)	22(1)	5.67	6.93	9.09	C2
20	3.26(3)	24(1)	6.02	6.78	8.98	C2
30	3.20(3)	29(1)	6.00	6.99	9.36	C2
40	3.18(3)	38(1)	8.01	7.20	9.49	C2
50	3.10(3)	51(1)	7.33	6.88	9.16	C2
60	2.97(3)	62(1)	10.1	7.02	9.28	C2
70	2.82(3)	68(1)	9.98	6.68	8.74	C2
80	2.60(3)	70(2)	11.8	6.97	9.21	C2
85	2.42(3)	90	14.2	7.00	9.18	C2
90	2.19(4)	90	17.2	7.08	9.20	C2
95	1.81(4)	90	23.7	7.33	9.56	C2
100	0			7.28	9.55	C2
110	0			7.31	9.62	C2

Table B.4: Agreement factors for Rietveld refinements of neutron powder diffraction data for the crystallographic and magnetic phases of $Lu_{0.4}Sc_{0.6}MnO_3$.

T[K]	M [μ_B]	ϕ [°]	Magnetic-R [%]	R_p [%]	R_{wp} [%]	Instrument
2.1	3.57(6)	11(3)	19.6	2.36	3.22	D1B
4.1	3.53(5)	12(3)	17.1	2.02	2.89	D1B
9.8	3.52(6)	13(3)	13.5	2.36	3.21	D1B
23.2	3.50(6)	17(2)	20.5	2.45	3.31	D1B
26.1	3.52(6)	21(2)	16.9	2.66	3.45	D1B
29.0	3.45(6)	22(2)	15.8	2.73	3.55	D1B
31.7	3.50(6)	24(2)	22.0	2.72	3.64	D1B
35.0	3.44(6)	28(2)	9.29	2.57	3.50	D1B
38.0	3.46(5)	33(2)	18.6	2.61	3.50	D1B
38.8	3.41(5)	33(2)	21.2	2.40	3.25	D1B
41.8	3.44(5)	36(2)	15.5	2.69	3.50	D1B
44.5	3.40(5)	41(2)	21.7	2.78	3.69	D1B
48.0	3.41(5)	47(2)	11.5	2.74	3.52	D1B
54.6	3.29(5)	59(2)	17.2	2.34	3.14	D1B
55.6	3.25(5)	60(2)	22.1	2.67	3.38	D1B
58.4	3.27(5)	63(2)	20.2	2.63	3.54	D1B
61.5	3.26(5)	66(2)	16.7	2.72	3.45	D1B
69.0	3.14(5)	70(2)	18.5	2.36	3.17	D1B
84.0	2.86(5)	69(3)	19.5	2.33	3.16	D1B
93.0	2.57(5)	90	17.5	2.32	3.12	D1B
98.0	2.37(5)	90	23.9	2.27	3.10	D1B
103.0	2.08(6)	90	32.6	2.40	3.23	D1B
107.0	1.62(7)	90	40.0	2.35	3.17	D1B
113.0	0			2.36	3.15	D1B
118.0	0			2.67	3.45	D1B

Table B.5: Agreement factors for Rietveld refinements of neutron powder diffraction data for the crystallographic and magnetic phases of $ScMnO_3$.

T[K]	M [μ_B]	ϕ [°]	Magnetic-R [%]	R_p [%]	R_{wp} [%]	Instrument
10	3.40(7)	12(3)	12.8	5.16	6.67	C2
15	3.40(7)	13(3)	13.3	5.32	6.71	C2
20	3.36(7)	14(3)	11.2	5.23	6.76	C2
25	3.34(7)	14(3)	13.0	5.26	6.78	C2
30	3.39(7)	14(3)	12.3	5.20	6.64	C2
35	3.28(7)	15(3)	13.7	5.21	6.65	C2
40	3.29(7)	20(2)	12.6	5.20	6.63	C2
45	3.29(7)	20(2)	12.6	5.20	6.63	C2
50	3.27(7)	23(2)	13.7	5.43	6.90	C2
55	3.23(7)	40(2)	11.9	5.28	6.67	C2
60	3.23(7)	57(3)	12.8	5.42	6.95	C2
65	3.23(7)	67(4)	11.7	5.24	6.75	C2
70	3.14(7)	82(9)	11.2	5.00	6.44	C2
75	3.11(7)	77(6)	13.1	5.22	6.60	C2
80	3.01(8)	82(12)	12.4	5.66	7.14	C2
90	2.93(8)	82(13)	16.0	5.55	7.12	C2
105	2.69(8)	78(10)	13.6	5.55	7.08	C2
115	2.51(9)	76(10)	18.9	5.55	6.97	C2
120	2.20(10)	92(37)	19.5	5.51	7.70	C2
125	1.81(12)	100(19)	30.9	5.66	7.17	C2
130				6.07	7.59	C2

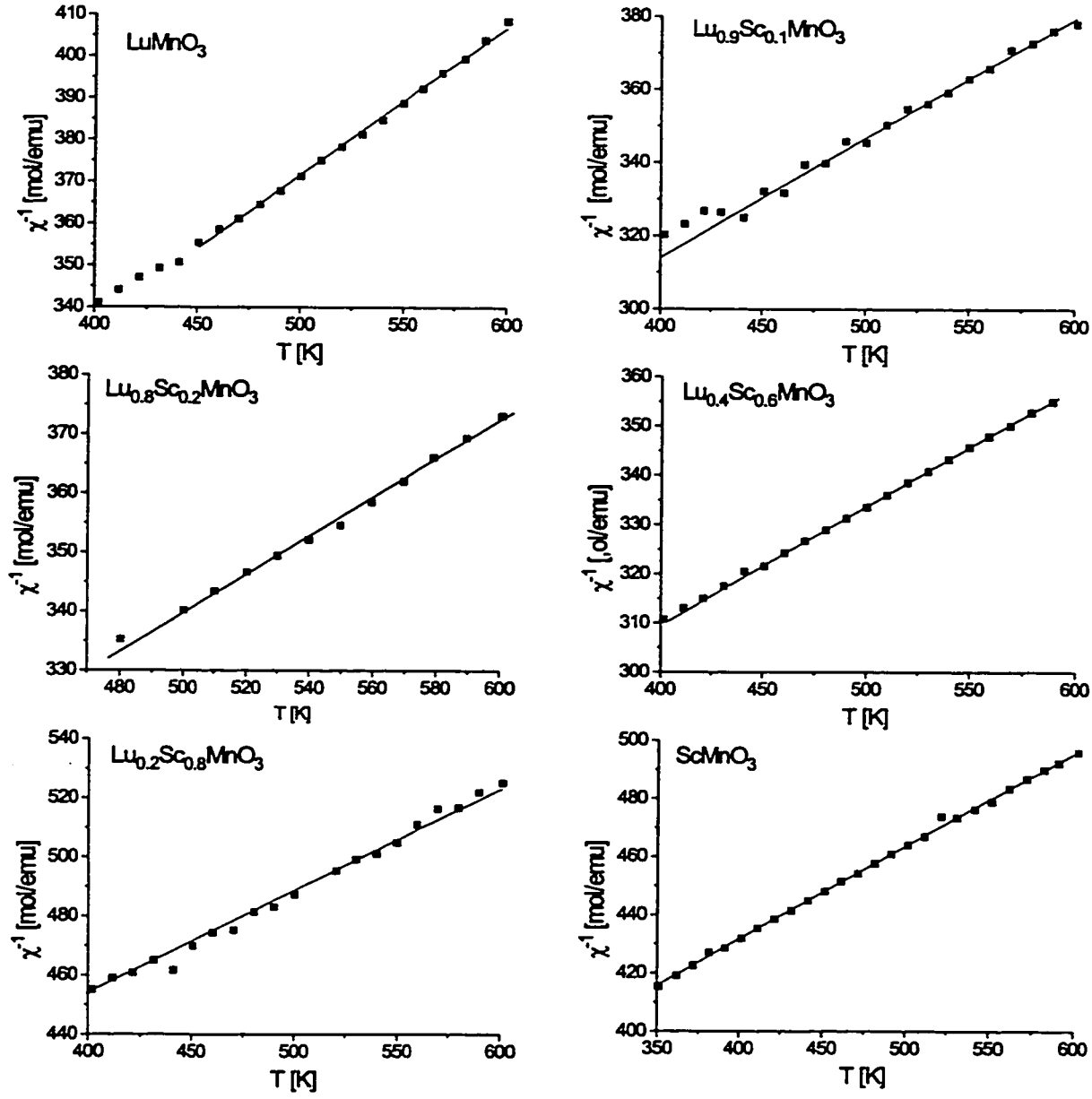

Figure B.1: Curie-Weiss plots for the series $Lu_xSc_{(1-x)}MnO_3$ (H=0.05T).

Appendix C

Square Planar Antiferromagnets

The following tables present the agreement factors and magnetic phase information for neutron powder diffraction refinements carried out for the solid solution $Ba_xSr_{(1-x)}LaMnO_4$. [1] The agreement factors are defined on page 32.

Table C.1: Agreement factors for Rietveld refinements of neutron powder diffraction data for the crystallographic and magnetic phases of $Ba_{0.05}Sr_{0.95}LaMnO_4$.

T[K]	M [μ_B]	Magnetic-R [%]	R_p [%]	R_{wp} [%]	Instrument
10	3.02(6)	16.5	4.65	5.99	C2
30	2.95(5)	16.2	4.44	5.92	C2
50	2.84(5)	15.4	4.27	5.64	C2
70	2.63(5)	21.3	4.40	5.75	C2
80	2.51(4)	25.5	4.55	5.90	C2
85	2.31(6)	25.0	4.65	6.12	C2
90	2.02(6)	32.1	4.65	6.06	C2
95	1.73(6)	35.7	4.66	6.23	C2
100			4.61	6.02	C2
105			4.32	5.61	C2
110			4.42	5.80	C2
125			4.69	6.08	C2
295			3.94	6.27	SEPD

[1] Diffractometer C2 is the high resolution 800 wire diffractometer in Chalk River. SEPD is the high resolution time of flight diffractometer at IPNS in Argonne.

Table C.2: Agreement factors for Rietveld refinements of neutron powder diffraction data for the crystallographic and magnetic phases of $Ba_{0.10}Sr_{0.90}LaMnO_4$.

T[K]	M [μ_B]	Magnetic-R [%]	R_p [%]	R_{wp} [%]	Instrument
15	2.79(5)	16.4	4.42	5.82	C2
30	2.76(5)	16.2	4.47	5.83	C2
50	2.59(5)	18.2	4.48	5.92	C2
70	2.24(5)	22.7	4.45	5.89	C2
80	1.92(5)	30.0	4.62	6.05	C2
85	1.45(6)	45.8	4.85	6.45	C2
90			5.03	6.67	C2
295			4.39	7.59	SEPD

Table C.3: Agreement factors for Rietveld refinements of neutron powder diffraction data for the crystallographic and magnetic phases of $Ba_{0.15}Sr_{0.85}LaMnO_4$.

T[K]	M [μ_B]	Magnetic-R [%]	R_p [%]	R_{wp} [%]	Instrument
15	2.48(5)	22.2	3.55	4.77	C2
30	2.43(5)	20.9	3.49	4.79	C2
50	2.19(5)	25.7	3.41	4.72	C2
60	2.02(5)	28.1	3.44	4.66	C2
65	1.81(6)	33.1	3.56	4.80	C2
70	1.42(7)	48.7	3.53	4.79 C2	
75	1.27(7)	54.5	3.58	4.88	C2
80	0.99(9)	60.2	3.42	4.67	C2
85			3.54	4.74	C2
295			4.28	7.34	SEPD

Table C.4: Agreement factors for Rietveld refinements of neutron powder diffraction data for the crystallographic and magnetic phases of $Ba_{0.20}Sr_{0.80}LaMnO_4$.

T[K]	M [μ_B]	Magnetic-R [%]	R_p [%]	R_{wp} [%]	Instrument
4	2.07(5)	26.8	4.74	6.47	C2
15	2.05(5)	25.0	4.67	6.30	C2
30	1.95(5)	27.6	4.83	6.50	C2
40	1.83(5)	29.9	4.81	6.44	C2
50	1.68(5)	35.8	4.89	6.44	C2
55	1.40(6)	46.2	4.88	6.45	C2
60	1.20(6)	50.9	4.88	6.47	C2
63	1.09(7)	53.3	4.94	6.52	C2
70			4.93	6.43	C2
295			3.94	6.38	SEPD

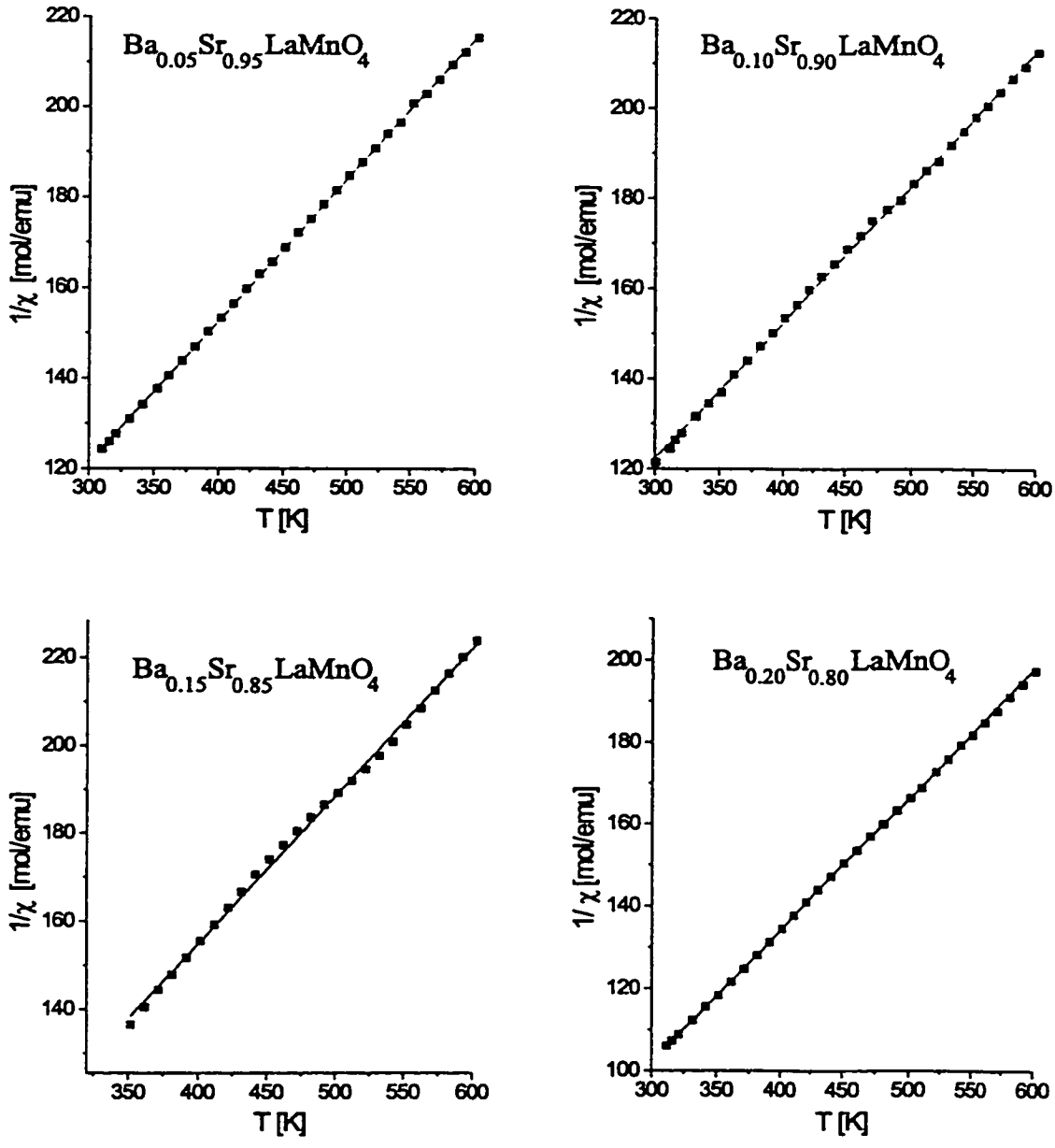

Figure C.1: Curie-Weiss plots for the series $Ba_xSr_{(1-x)}LaMnO_4$ (H=0.01T).

Bibliography

[AM76] N.W. Ashcroft and N.D. Mermin. *Solid State Physics.* Saunders College, Philadelphia, 1976.

[And73] P.W. Anderson. *Mat. Res. Bull.*, 8:153–160, 1973.

[ASJMJCRP92] A.Salinas-Sanchez, J.L.Garcia-Monoz, J.Rodrigues-Carvajal, and R.Saez-Puche. *J. Solid State Chem.*, 100:201–211, 1992.

[AW82] A. Albinati and B.T.M. Willis. *J. Appl. Cryst.*, 15:361–374, 1982.

[BA85] I.D. Brown and D. Altermatt. *Acta Cryst.*, B41:244–247, 1985.

[Bac75] G.E. Bacon. *Neutron Diffraction.* Claredon Press, Oxford, 3 edition, 1975.

[Bal53] D. Balz. *Naturwissenschaften*, 40:241, 1953.

[BDSlF77] A. Benabad, A. Daoudi, R. Salmon, and G. le Flem. *Journal of Solid State Chemistry*, 22:121–126, 1977.

[BG99] M. Bieringer and J.E. Greedan. *Journal of Solid State Chemistry*, 143:132–139, 1999.

[BGK+97] P.D. Battle, M.A. Green, N.K. Kasmir, J.E. Millburn, L.E. Spring, S.P. Sullivan, M.J. Rosseinsky, and J.F. Vente. *J. Mater. Chem.*, 7(6):977–988, 1997.

[BGL+96] P.D. Battle, M.A. Green, N.S. Laskey, J.E. Millburn, P.G. Radaelli, M.J. Rosseinsky, S.P. Sullivan, and J.F. Vente. *Phys. Rev. B.*, 54(22):15967–15976, 1996.

[BGL+97] P.D. Battle, M.A. Green, N.S. Laskey, J.E. Millburn, M.J. Rosseinsky, S.P. Sullivan, and J.F. Vente. *Chem. Mater.*, 9:552–559, 1997.

[BGS69] R.J. Birgenau, H.J. Guggenheim, and G. Shirane. *Physical Review Letters*, 22(14):720–723, 1969.

[BGS73] R.J. Birgenau, H.J. Guggenheim, and G. Shirane. *Physical Review B*, 8(1):304–311, 1973.

[BH84] T. Betz and R. Hoppe. *Z. Anorg. Allg. Chem.*, 512:19–33, 1984.

[BK94] A.J. Berlinsky and C. Kallin. *Hyperfine Interactions*, 85:173–179, 1994.

[BM97] N.E. Brese and M.O'Keeffe. *Acta Cryst.*, B47:192, 197.

[BP55] D. Balz and K. Plieth. *Zeitschrift für Elektrochemie*, 59(6):545–551, 1955.

[Bre94] J.H. Brewer. *Encyclopedia of Applied Physics*, 11:23–78, 1994.

[BRGK96] S.L. Brock, N.P. Raju, J.E. Greedan, and S.M. Kauzlarich. *Journal of Alloys and Compounds*, 237:9–19, 1996.

[Bro92] I.D. Brown. *Acta Cryst.*, B48:553–572, 1992.

[BSS71] R.J. Birgenau, J. Skalyo, and G. Shirane. *Physical Review B*, 3(5):1736–1749, 1971.

[BY86] K. Binder and A.P. Young. *Reviews of Modern Physics*, 58(4):801–970, 1986.

[CCC+90] C. Chaillout, J. Chenavas, S.W. Cheong, Z. Fisk, M. Marezio, B. Morosin, and J.E. Schirber. *Physica C*, 170:87–94, 1990.

[CD88] A.K. Cheetham and P. Day. *Solid State Chemistry, Techniques.* Oxford Science Publications. Clarendon Press, Oxford, 1988.

[CFH+98] S.J. Clarke, A.J. Fowdes, A. Harrison, R.M. Ibberson, and M.J. Rosseinsky. *Chem. Mater.*, 10:372–384, 1998.

[Cho86] D. Chowdhury. *Spin Glasses and Other Frustrated Systems.* Princeton Series in Physics. Princeton University Press, Princeton, 1986.

[Col89] Malcolm F. Collins. *Magnetic Critical Scattering.* Oxford Series on Neutron Scattering in Condensed Matter. Oxford University Press, Oxford, 1989.

[Cox87] S.F.J. Cox. *J. Phys. C: Solid State Phys.*, 20:3187–3319, 1987.

[Cox92] P.A. Cox. *Transition Metal Oxides.* Clarendon Press, Oxford, 1992.

[CP97] M.F. Collins and O.A. Petrenko. *Can. J. Phys.*, 75:605–655, 1997.

[CPR58] G. Caglioti, A. Paoletti, and F.P. Ricci. *Nucl. Instrum.*, 3:223–228, 1958.

[CvD77] R.L. Carlin and A.J. van Duyneveldt. *Magnetic Properties of Transition Metal Compounds.* Inorganic Chemistry Concepts. Springer-Verlag, New York, 1977.

[Des94] Quantum Design. Fundamentals of magnetism and magnetic measurements, 1994.

[DG76] C. Domb and M.S. Green. *Phase Transitions and Critical Phenomena*, volume 5a. Academic Press, London, 1976.

[dJ90] L.J. de Jongh. *Magnetic Properties of Layered Transition Metal Compounds*, page 19. Kluwer Academic Publishers, Boston, 1990.

[DJW82] R.B.v. Dreele, J.D. Jorgensen, and C.G. Windsor. *J. Appl. Cryst.*, 15:581–589, 1982.

[dRY97] P. Dalmas de Reotier and A. Yaouanc. *Journal of Physics, Condensed Mater*, 9:9113–9166, 1997.

[ea96] R.M. Barnett et al. *Physical Review D*, 54:1, 1996.

[FA74] P. Fazekas and P.W. Anderson. *Philos. Mag.*, 30:423–440, 1974.

[FCDS81] G. Le Flem, Ph. Courbin, C. Delmas, and J.-L. Soubeyroux. *Z. anorg. allg. Chem.*, 476:69–88, 1981.

[FDH82] G. Le Flem, G. Demazeau, and P. Hagenmuller. *Journal of Solid State Chemistry*, 44:82–88, 1982.

[FH91] K.H. Fischer and J.A. Hertz. *Spin Glasses.* Cambridge University Press, Cambridge, 1991.

[Fis62] M. Fisher. *Phil. Mag.*, 17:1731, 1962.

[FRG65] A. Ferretti, D.B. Rogers, and J.B. Goodenough. *J. Phys. Chem. Solids*, 26:2007–2011, 1965.

[Gau94] B.D. Gaulin. *Magnetic Systems with Competing Interactions (Frustrated Spin Systems).* World Scientific, Singapore, 1994. edited by H.T. Diep.

[GBJ+95] J.E. Greedan, M. Bieringer, J.F.Britten, D.M. Giaquinta, and H.-C. zur Loye. *Journal of Solid State Chemistry*, 116:118–130, 1995.

[Gla72] A.M. Glazer. *Acta Cryst.*, B28:3384, 1972.

[Gme79] E. Gmelin. *Thermochimica Acta*, 29:1–39, 1979.

[Gme87] E. Gmelin. *Thermal Analysis Highlights*, volume 8^{th} ICTA. Elsevier Science Publisher, Bratislava, Czechoslovakia, 1987.

[Gol26] V.M. Goldschmidt. *Mat.-Naturv. Kl.*, 2:117, 1926.

[Goo55] J.B. Goodenough. *Physical Review*, 100(2):564–573, 1955.

[Goo63] John B. Goodenough. *Magnetism and the Chemical Bond.* Interscience Publishers, New York, 1963.

[GR84] P. Ganguly and C.N.R. Rao. *Journal of Solid State Chemistry*, 53:193–216, 1984.

[Gre94] J.E. Greedan. *Encyclopedia of Inorganic Chemistry.* Wiley, New York, 1994.

[GzL92] D.M. Giaquinta and H.-C. zur Loye. *J. Am. Chem. Soc.*, 114:10952–10953, 1992.

[GzL94] D.M. Giaquinta and H.-C. zur Loye. *Chem. Mater.*, 6:365–372, 1994.

[HJ39] O. Halpern and M.H. Johnson. *Phys. Rev.*, 55:898–923, 1939.

[HNI91] K. Hirota, Y. Nakazawa, and M. Ishikawa. *P. Phys.: Condens. Matter*, 3:4721–4730, 1991.

[HUI+79] R.S. Hayano, Y.J. Uemura, J. Imazato, N. Nishida, T. Yamazaki, and R. Kubo. *Physical Review B*, 20(3):850–859, 1979.

[IKNM91] M. Isobe, N. Kimizuka, M. Nakamura, and T. Mohri. *Acta Cryst.*, C47:423–424, 1991.

[IO70] Y.A. Izyumov and R.P. Ozerov. *Magnetic Neutron Diffraction.* Plenum Press, New York, first edition, 1970.

[JDP+88] J.D. Jorgensen, B. Dabrowski, S. Pei, D.G. Hinks, L. Soderholm, B. Morosin, J.E. Schirber, E.L. Venturini, and D.S. Ginley. *Physical Review B*, 38(16):11337–11345, 1988.

[JDP+89] J.K. Jorgensen, B. Dabrowski, S. Pei, D.R. Richards, and D.G. Hinks. *Physical Review B*, 40(4):2187–2199, 1989.

[JFC+89] J.D. Jorgensen, J. Faber, J.M. Carpenter, R.K. Crawford, F.R. Haumann, R.L. Hitterman, R. Kleb, G.E. Ostrowski, F.J. Rotella, and T.G. Worlton. *J. Appl. Cryst.*, 22:321–333, 1989.

[JI98] JCPDS-ICDD. Pcpdfwin, 1998. Powder Diffraction Files.

[JN74] G.B. Jensen and O.V. Nielsen. *J. Phys. C: Solid State Phys.*, 7:409–424, 1974.

[KAKA88] S. Kawano, N. Achiwa, N. Kamegashira, and M. Aoki. *Journal de Physique*, C8(12):829, 1988.

[Kan59] J. Kanamori. *J. Phys. Chem. Solids*, 10:87–98, 1959.

[Kaw85] H. Kawamura. *Journal of the Physical Society of Japan*, 54(9):3220–3223, 1985.

[Kaw88] H. Kawamura. *J. Appl. Phys.*, 63(8):3086–3088, 1988.

[Kit76] C. Kittel. *Introduction to Solid State Physics.* John Wiley and Sons, Inc., New York, 1976.

[KPS66] L.N. Komissarova, B.I. Pokrovskii, and I.S. Shaplygin. *Izvestiya Akademii Nauk SSSr, Neorganicheskie Materialy*, 2(2):275–280, 1966.

[Kra34] H.A. Kramers. *Physica*, 1:182–192, 1934.

[KW98] P. Karen and P.M. Woodward. *Journal of Solid State Chemistry*, 141:78–88, 1998.

[KWYC64] W.C. Koehler, E.O. Wollan, H.L. Yakel, and J.W. Cable. *Phys. Lett.*, 9:93–95, 1964.

[Lac87] P. Lacorre. *J. Phys. C: Solid State Phys.*, 20:L775–L781, 1987.

[Lan66] G. Lang. *Z. Anorg. Allg. Chem.*, 348:246–256, 1966.

[Lau32] M.v. Laue. *Zeits. f. Krist.*, 82:127, 1932.

[LD94] A.C. Larson and R.B.v. Dreele. *GSAS General Structure Analysis System.* LANSCE, Los Alamos National Laboratory, Los Alamos, 1994.

[LP62] E. LeGrand and R. Plumier. *Physica Status Solidi*, 2:317–320, 1962.

[MAKT96] Y. Moritomo, A. Asamitsu, H. Kuwahara, and Y. Tokura. *Nature*, 380(14):141–144, 1996.

[Mas90] T.E. Mason. *Critical Behavior of $CsMnBr_3$.* PhD thesis, McMaster University, , Hamilton, Ontario, Canada, 1990.

[MDC+99] L.B. McCusker, R.B. Von Dreele, D.E. Cox, D. Louer, and P Scardi. *Journal of Applied Crystallography*, 32:36–50, 1999.

[MMRR96] R. Mahesh, R. Mahendiran, A.K. Raychaudhuri, and C.N.R. Rao. *Journal of Solid State Chemistry*, 122:448–450, 1996.

[M.O89] M.O'Keeffe. *Structure and Bonding*, 71:161–190, 1989.

[MTA+95] Y. Moritomo, Y. Tomioka, A. Asamitsu, Y. Tokura, and Y. Matsui. *Phys. Rev. B*, 51(5):3297–3300, 1995.

[Myd93] J.A. Mydosh. *Spin Glasses, An Experimental Introduction.* Taylor & Francis, London, 1993.

[Nor65] R. Norrestam. *Acta Chem. Scand.*, 19(4):1009–1010, 1965.

[OKKS76] A. Oles, F. Kajzar, M. Kucab, and W. Sikora. *Magnetic Structures, Determined by Neutron Diffraction.* Panstwowe Wydawnictwo Naukowe, Warszawa, 1976.

[Plu64] R. Plumier. *Journal of Applied Physics*, 35(3):950–951, 1964.

[Poi69] P. Poix. *C. R. Acad. Sc. Paris*, t. 268(C):1139–1140, 1969.

[Poi80] P. Poix. *Journal of Solid State Chemistry*, 31:95–102, 1980.

[Por79] A.C. Porte. *Transition-Metal Ions - 'Electron Spin Resonance'.* Alden Press, Oxford, 1979.

[Pou92] M.C. Poulenc. *C.R. hebd. Seances Acad. Sci.*, 114:746, 1892.

[PV70] R. Pauthenet and C. Veyret. *Journal de Physique*, 31(1):65–72, 1970.

[Rao99] C.N.R. Rao. *J. Mater. Chem.*, 9:1–14, 1999.

[RB93] D.E. Rice and D.J. Buttrey. *Journal of Solid State Chemistry*, 105:197–210, 1993.

[RC93] J. Rodriguez-Carvajal. *Physica B*, 192:55–69, 1993.

[RC98] Juan Rodrguez-Carvajal. Fullprof-rietveld, profile matching & integrated intensities refinement of x-ray and/or neutron data (powder and/or single-crystal), 1998. Version 3.5d Oct98-LLB-JRC.

[RG97] C.N.R. Rao and J. Gopalakrishnan. *New Directions in Solid State Chemistry*. Cambridge University Press, Cambridge, second edition, 1997.

[RGR87] R.A. Mohan Ram, P. Ganguly, and C.N.R. Rao. *Journal of Solid State Chemistry*, 70:82–87, 1987.

[RGS88] J.N. Reimers, J.E. Greedan, and M. Sato. *Journal of Solid State Chemistry*, 72:390–394, 1988.

[RGSR88] C.N.R. Rao, P. Ganguly, K.K. Singh, and R.A. Mohan Ram. *Journal of Solid State Chemistry*, 72:14–23, 1988.

[Rie69] H.M. Rietveld. *J.Appl. Cryst.*, 2:65, 1969.

[RP57] S.N. Ruddlesden and P. Popper. *Acta. Cryst.*, 10:538, 1957.

[SB77] G. Shirane and R.J. Birgenau. *Physica*, 86-88B:639, 1977.

[Sea92] V.R. Sears. *Neutron News*, 3(3):26–37, 1992.

[Sha76] R.D. Shannon. *Acta. Cryst. A*, 32:751, 1976.

[SHP63] R. Scholder, K.L. Huppert, and P.P. Pfeiffer. *Angew. Chem. Int. Edit.*, 2:375, 1963.

[SI90] A. Skowron and I.D.Brown. *Acta Cryst.*, C46:527–531, 1990.

[SJ89] G.H. Stout and L.H. Jensen. *X-ray Structure Determination.* John Wiley & Sons, New York, second edition, 1989.

[SP86] K. Sköld and D.L. Price. *Neutron Scattering*, volume 23 A of *Methods in Experimental Physics.* Academic Press, Inc., New York, 1986.

[SP87] K. Sköld and D.L. Price. *Neutron Scattering*, volume 23 A of *Methods in Experimental Physics.* Academic Press, Inc., New York, 1987.

[Squ96] G.L. Squires. *Introduction to the Theory of Thermal Neutron Scattering.* Dover, Cambridge, 1996.

[TMM+84] C.W. Tompson, D.F.R. Mildner, M. Mehregany, J. Sudol, R. Berliner, and W.B. Yelon. *J. Appl. Cryst.*, 17:385–394, 1984.

[UKK+94] Y.J. Uemura, A. Keren, K. Kojima, L.P. Le, G.M. Luke, W.D. Wu, Y. Ajiro, T. Asano, Y. Kuriyama, M. Mekata, and H. Kikuchi. *Physical Review Letters*, 73:3306–3309, 1994.

[Vil79] J. Villain. *Z. Physik B*, 33:31–42, 1979.

[Vis69] Visser. J. appl. cryst., 1969. version 9.

[Wan72] B.M. Wanklyn. *Journal of Materials Science*, 7:813–821, 1972.

[War41] B.E. Warren. *Phys. Rev.*, 59:693–698, 1941.

[WB99] A.S. Wills and I.D. Brown. Valist, 1999. CEA France.

[Wes92] A.R. West. *Grundlagen der Festkörperchemie.* Verlag Chemie, Weinheim, FRG, 1992.

[WH96] A.S. Wills and A. Harrison. *J. Chem. Soc. Faraday Trans.*, 92(12):2161–2166, 1996.

[Wil92] A.J.C. Wilson, editor. *International Tables for Crystallography*, volume C of *The International Union of Crystallography*. Kluwer Academic Publishers, Dordrecht, Holland, 1992.

[Woo97a] P.M. Woodward. *Acta Cryst.*, B53:32–43, 1997.

[Woo97b] P.M. Woodward. *Acta Cryst.*, B53:44–66, 1997.

[XIS+95] H.W. Xu, J. Iwasaki, T. Shimizu, H. Satoh, and N. Kamegashira. *Journal of Alloys and Compounds*, 221:274–279, 1995.

[YKBF63] H.L. Yakel, W.C. Koehler, E.F. Bertaut, and E.F. Forrat. *Acta. Cryst.*, 16:957, 1963.

[You93] R.A. Young. *The Rietveld Method*. International Union of Crystallography. Oxford University Press, Oxford, 1993.

[Zen51a] C. Zener. *Physical Review*, 83(2):299–301, 1951.

[Zen51b] C. Zener. *Physical Review*, 82(3):403–405, 1951.

[Zen51c] C. Zener. *Physical Review*, 81(4):440–444, 1951.